2025

Biophysical view of electrocatalysis of immobilized DyP-type peroxidases for improved biotechnological applications

Catarina Boloto Barbosa Nobre

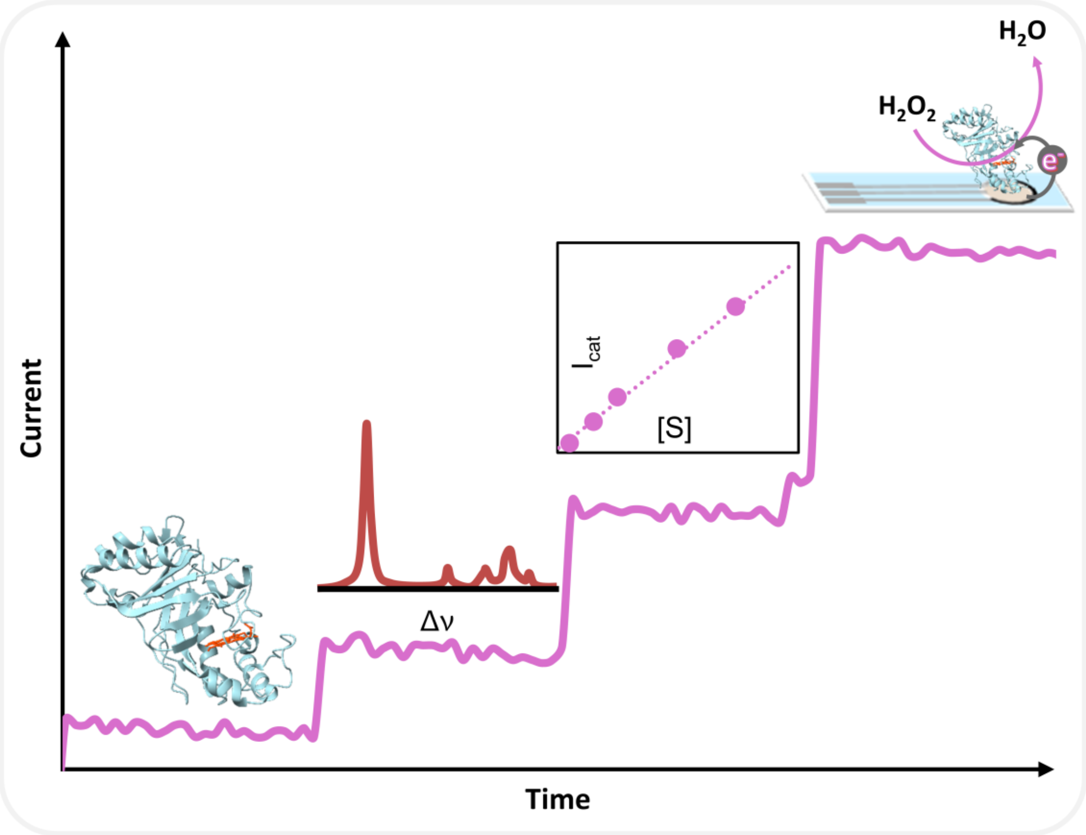

Dissertation presented to obtain the

Ph.D degree in Molecular Biosciences

Speciality Biochemistry

Oeiras, March 2025

INSTITUTO DE TECNOLOGIA QUÍMICA E BIOLÓGICA ANTÓNIO XAVIER | UNIVERSIDADE NOVA DE LISBOA

Biophysical view of electrocatalysis of immobilized DyP-type peroxidases for improved biotechnological applications

Catarina Boloto Barbosa Nobre

Dissertation presented to obtain the Ph.D. degree in Molecular Biosciences

Instituto de Tecnologia Química e Biológica António Xavier

Universidade Nova de Lisboa

Supervisor: Dr. Smilja Todorovic

Co-Supervisor: Prof. Lígia O. Martins

Oeiras, March 2025

Second Edition, March 2025

Laboratory for Raman BioSpectroscopy

Instituto de Tecnologia Química e Biológica António Xavier

Universidade Nova de Lisboa

Av. da República, Oeiras

Acknowledgments

I would like to start by expressing my gratitude to my supervisors. To Smilja Todorovic who gave me the opportunity to join her lab and pursue my research under her guidance. Her mentorship has been fundamental in advancing my scientific knowledge, especially through every challenge and lesson, she has encouraged me to push my boundaries. I am especially grateful for the numerous opportunities she provided me, all of which broadened my knowledge and perspective. Her patience and trust in me, especially during times when I doubted myself, have been invaluable. To Ligia O. Martins for her technical expertise throughout this work. Her insightful feedback as the hands-on support were fundamental to achieved the objectives of this work and the opportunities. Additionally, I also want to thank her for the opportunity to make international and intersectoral secondments, which allowed me to gain new skills and perspectives that enriched my research. Thank you both for your guidance and encouragement throughout my journey.

I would also like to extend my deepest gratitude to Célia M. Silveira, who over the past five years has been like the big sister I never had. Her guidance, encouragement, invaluable lessons, and challenges she has set for me have played a crucial role in my personal and professional growth. I owe her more thanks than words can capture on paper.

I am grateful as well to my thesis committee members, Abel Oliva and João Vicente, for their insightful feedback and collaborative support throughout this project.

I want to thank to the Microbial & Enzyme Technology lab for all its support and attention. In particular, I extend my thanks to Diogo Silva and Carolina F. Rodrigues, for their contributions over the years.

I would like to thank all the wonderful colleagues and people I have met over these four years. Each of you has contributed to my growth as a scientist and as a person, and I am immensely grateful for your impact on my journey.

À minha mãe, irmão e a toda a minha família por todo o apoio e carinho desde sempre.

Gostaria de agradecer também ao Rodrigo Barbosa Nobre que inexplicavelmente se tornou metade de mim. Obrigada, por todos os risos e pelo apoio.

Finally, I thank for the financial support provided by FCT - *Fundação para a Ciência e a Tecnologia*, through the MOSTMICRO-ITQB R&D Unit (UIDB/04612/2020, UIDP/04612/2020), LS4FUTURE Associated Laboratory (LA/P/0087/2020 and my PhD fellowship 2020/05017/BD (https://doi.org/10.54499/2020.05017.BD) and to the European Union's Horizon 2020 Research and Innovation Program, through TIMB^3 and B-LigZymes projects (grant agreements No. 810856 and 824017, respectively).

Para o meu pai, que sempre me apoiou e que sei que, de algum modo, estará sempre comigo.

Abstract

Dye-decolorizing Peroxidases (DyP) are recently discovered heme-containing enzymes that share no similarity with classical peroxidases in terms of their sequence or structure. DyPs couple the reduction of hydrogen peroxide (H_2O_2) with the oxidation of structurally different substrates, including synthetic azo and anthraquinone dyes, phenolic and nonphenolic lignin units, and kraft lignin, among others. Due to their catalytic properties, ease of production, and stability, these enzymes have great potential for biotechnological applications, e.g., biocatalysts in electrochemical biosensors for H_2O_2 detection or dye remediation of wastewater generated by industries.

This thesis describes the construction of third-generation electrochemical H_2O_2 biosensors based on immobilized DyPs. The herein developed DyP-constructs are characterized through an approach that we term *rational design*, in which we employ spectroelectrochemistry to monitor the immobilized enzymes along the biosensor construction and fine-tune the process. In parallel, we also developed DyP-constructs following an *empirical approach*, using a trial-and-error strategy that provides no structural insights into the immobilized enzymes. We evaluated the analytical performance of all constructs and selected the best performing one.

To identify potential biocatalyst candidates, we explore wild-type (WT) DyPs from various organisms, including *Streptomyces coelicolor* (ScoDyP), *Thermobifida fusca* (TfuDyP), *Cellulomonas bogoriensis* (CboDyP), *Saccharomonospora viridis* (SviDyP), *Escherichia coli* (Yfex), *Thermobifida cellulosilytica* (TceDyP), and *Pseudomonas putida* (PpDyP). Additionally, we also evaluate several variants, including *in silico* developed variants of PpDyP (FireProt and PROSS), generated for improved thermal stability properties in solution and distal variants for PpDyP and CboDyP (R214W/I and R307W/I, respectively) designed by point mutations to target a reduction potential upshift. Resonance Raman (RR) spectroscopy and UV-visible (UV-vis) absorption spectroelectrochemistry were used to investigate structural and redox properties of DyPs in solution, which critically define their possible application

in biotechnology. We demonstrated that the reduction potential of the different WT DyPs is comparable and that the substitution of the highly conserved arginine in the distal side of the heme pocket in the so-called distal variants influences the reduction potential in a case-dependent manner. RR spectroscopy demonstrated that SviDyP, ScoDyP, CboDyP, PpDyP, the distal variants of CboDyP, PpDyP (R214W), and *in silico* PpDyP variants are, as judged by their solution properties, the most promising candidates. This conclusion is mainly based on the analysis of the RR spectra of each DyP in physiological conditions, which reveals that these enzymes show a catalytically competent active site structure.

To construct a functional third-generation biosensor, it is important that the enzymes preserve their native solution properties upon immobilization on the electrode surface. In this work, the most promising enzymes, identified by solution properties, are immobilized on biocompatible silver electrodes functionalized with alkanethiol self-assembled monolayers (SAM). Structural and redox properties of the immobilized enzymes are evaluated by surface-enhanced RR (SERR) spectroscopy and their electrocatalytic properties by electrochemistry. Among the studied electrode/DyP constructs, only WT CboDyP and WT PpDyP, together with PpDyP *in silico* variants, show preserved native structure upon attachment to the electrode. However, only WT PpDyP and its *in silico* variants reveal preserved redox properties and electrocatalytic activity for H_2O_2 in the immobilized state. The PpDyP *in silico* variant-based constructs are exceptionally fit for the development of H_2O_2 biosensors since they exhibit a good dynamic range (1 - 275 μM), short response times (< 3 s) and superior sensitivity (1,150 - 1,420 $mA \cdot M^{-1} \cdot cm^2$). Their performance is comparable to that of our previously developed biodevice based on WT PpDyP. Moreover, the PpDyP *in silico* variant-based constructs show improved long-term stability compared to the previously reported device.

Following the empirical approach, WT PpDyP and WT CboDyP are also immobilized onto different carbon nanotube-modified glassy carbon electrodes. The only modified electrode that shows activity towards H_2O_2 among all tested nanotubes is the construct developed using single-walled nanotubes-ink. Although these devices can be considered for developing H_2O_2 biosensors, they reveal almost half of the sensitivity compared to those that resulted from the rational design approach, which made us discard the constructs characterized through the empirical strategy in the subsequent work.

Next, we set to translate the bulk silver electrode-based constructs into compact, disposable, and user-friendly devices using WT PpDyP immobilized on nanostructure-modified screen-printed electrodes (SPEs). To increase enzyme loading, metal nanostructures, including gold nanoparticles (AuNP), silver nanopillars (AgNPi), and silver nanoparticles (AgNP), are electrodeposited or drop-casted onto commercial carbon (C-SPE) and gold (Au-SPE) electrodes. The enzyme structure is further analyzed by RR spectroscopy, while electrocatalytic activity is evaluated using electrochemical methods. Among all configurations tested, the PpDyP/SAM/AuNP/C-SPE shows the best performance, with a dynamic range of 30 - 475 μM H_2O_2 and a sensitivity of 230 $mA \cdot M^{-1} \cdot cm^{-2}$ in open-air conditions. Devices incorporating PpDyP PROSS also exhibited comparable analytical performance. All these devices are suitable for on-site H_2O_2 detection in air-exposed samples, such as physiological fluids. In terms of analytical performance, i.e., sensitivity, dynamic range response, and LOD, the WT PpDyP and PpDyP PROSS biosensors outperform HRP/SPE-based devices and several other sensors constructed using artificial peroxidases reported in the literature. The PpDyP-based devices stand out for the simplicity of fabrication and measuring setup, as they allow the determination of H_2O_2 in air-exposed samples. Additionally, the constructs' design allows customization to enhance specific traits, like sensitivity, thermal stability, or resistance to substrate inhibition, due to the ease of producing and genetic modification of the DyP biocatalyst. Taken together, we demonstrate that the best-performing devices developed in this work, i.e., PpDyP/SAM/AuNP/C-SPE (for a miniaturized format) or PpDyP *in silico* variants/SAM/Ag (for a bulk format), can be a valuable alternative to devices for H_2O_2 detection and quantification that rely on HRP. Moreover, DyP-based devices could be interesting for detecting other small hydroperoxides.

Keywords: Dye-decolorizing Peroxidases; Third-generation Biosensors; Hydrogen Peroxide; resonance Raman, Surface Enhanced resonance Raman; Direct Electron Transfer; Immobilized Enzymes; Screen-printed Electrodes

Resumo

Dye-decolorizing peroxidases (DyPs) são enzimas hémicas descobertas há relativamente pouco tempo que se diferem das peroxidases clássicas a nível da sua sequência e estrutura. As DyPs acoplam a redução de peróxido de hidrogénio (H_2O_2) com a oxidação de diferentes compostos incluindo corantes sintéticos azo e antraquinônicos, unidades fenólicas e não fenólicas de lignina, *kraft lignin*, entre outros. Devido às suas propriedades catalíticas e de estabilidade, estas enzimas têm um grande potencial para serem usadas em aplicações biotecnológicas como, por exemplo, biocatalizadores em biossensores eletroquímicos para a deteção de H_2O_2 ou para serem usadas na remoção de corantes tóxicos das águas residuais produzidas por diferentes indústrias (e.g., têxtil, papel, farmacêutica, entre outras).

Esta tese descreve a construção de um biossensor de terceira geração para a deteção de H_2O_2 desenvolvido usando DyPs imobilizadas em elétrodos modificados. Os bio-dispositivos desenvolvidos aqui são caracterizados por uma abordagem a que designamos *rational design,* em que a espectroeletroquímica é usada para monitorizar as características redox e estruturais das DyPs imobilizadas no decorrer da construção do biossensor. Em paralelo, outros bio-dispositivos foram caracterizados usando uma *emprical approach*, i.e. uma estratégia de tentativa-e-erro, em que as técnicas espectroscópicas não se conseguem realizar ao mesmo tempo que as técnicas de eletroquímica e como resultado não se obtém informação estrutural das proteínas imobilizadas. O desempenho analítico de todos os bio-dispositivos foi avaliado por eletroquímica e aquele que demostrou melhor desempenho para a deteção de H_2O_2 foi o dispositivo escolhido para estudos futuros.

Para identificar o melhor biocatalizador, explorámos as enzimas nativas [*wild-type* (WT)] de diferentes organismos, sendo esses *Streptomyces coelicolor* (ScoDyP), *Thermobifida fusca* (TfuDyP), *Cellulomonas bogoriensis* (CboDyP), *Saccharomonospora viridis* (SviDyP), *Escherichia coli* (Yfex), *Thermobifida cellulosilytica* (TceDyP) e *Pseudomonas putida* (PpDyP). Ao mesmo tempo averiguámos também diferentes variantes, incluindo variantes geradas *in silico* da

PpDyP (FireProt e PROSS), para terem uma estabilidade térmica em solução melhorada e também variantes distais da PpDyP e CboDyP (R214W/I e R307W/I) que foram especificamente desenhadas para terem um potencial de redução mais positivo. A espectroscopia de ressonância de Raman (RR) e a espectroeletroquímica de UV-vis foram usadas para estudar as propriedades estruturais e redox em solução das enzimas. O estudo destas propriedades é importante uma vez que estas têm uma grande influência sobre a utilização de DyPs em aplicações biotecnológicas. Neste trabalho demostrámos que os potenciais de redução das DyPs estudadas apresentam valores muito comparáveis entre si. Também observámos que a substituição da Arg, que é conservada no lado distal do hemo (variantes distais), influencia o potencial redox de maneiras diferentes dependendo da enzima a ser estudada. Pela espectroscopia de RR identificámos que os candidatos mais promissores para aplicações biotecnológicas são WT: SviDyP, ScoDyP, CboDyP, PpDyP, os variantes distais da CboDyP, assim como o PpDyP R214W, e também as variantes *in silico* da PpDyP*.* Estas enzimas foram escolhidas uma vez que, em condições fisiológicas identificamos maioritariamente a presença de espécies cataliticamente ativas nos seus espectros.

De modo a desenvolver um biossensor funcional de terceira geração, é crucial que as enzimas aquando da sua imobilização na superfície do elétrodo preservem as suas características nativas observadas em solução, nomeadamente propriedades catalíticas e estruturais. Os biocatalizadores identificados como sendo os mais promissores foram imobilizados em elétrodos de prata funcionalizados com monocamadas auto-montadas (SAM) de alcanotióis de modo criar um ambiente compatível para a imobilização das enzimas no seu estado nativo (igual ao seu estado em solução). Neste caso, as propriedades estruturais e redox das enzimas imobilizadas foram avaliadas por espectroscopia de ressonância de Raman amplificada por superfície (SERR), e as propriedades electrocatalíticas por eletroquímica. Entre os dispositivos enzima/elétrodo produzidos, os únicos que mantiveram a sua estrutura nativa quando imobilizados foram: WT CboDyP, WT PpDyP, PpDyP R214W e as variantes *in silico* da PpDyP. Destes dispositivos, apenas os da WT PpDyP e as suas variantes *in silico* demostraram preservação das propriedades redox e atividade electrocatalítica para H_2O_2. Os variantes *in silico* da PpDyP são excelentes candidatos para a produção de biossensores para H_2O_2 pois, da sua avaliação de desempenho, observamos que os bio-dispositivos têm uma boa gama linear (1 - 275 μM), um tempo curto de resposta (< 3 s) e uma sensibilidade elevada (1 150 - 1 420 $mA \cdot M^{-1} \cdot cm^{2}$) para o H_2O_2. Apesar do seu desempenho idêntico ao dispositivo previamente fabricado usando a WT PpDyP, os dispositivos aqui desenvolvidos apresentam uma maior estabilidade de armazenamento.

Em paralelo, as enzimas WT PpDyP e WT CboDyP foram também imobilizadas na superfície de elétrodos de carbono vítreo modificados com diferentes nanotubos de carbono. De todas as configurações testadas apenas as preparadas com *single-walled nanotubes ink* apresentaram atividade catalítica. Tendo em conta que o seu desempenho analítico relativamente à sensibilidade é menos de metade da sensibilidade detectada nos dispositivos acima referidos que são caracterizados pelo *rational design*, os elétrodos modificados com DyP/nanotubos de carbono não foram considerados para os futuros estudos.

De seguida, o dispositivo em que a WT PpDyP foi imobilizada em electrodos de prata funcionalizados com SAM que foi desenvolvido no que designamos de elétrodo de laboratório, foi convertido num formato compacto, descartável e simples de usar. Para tal, a WT PpDyP foi imobilizada em *screen-printed electrodes* (SPE) modificados previamente com nanoestruturas, que foram usadas para aumentar a quantidade de enzima imobilizada na superfície do elétrodo. Para tal foram usadas nanopartículas de ouro (AuNP), nanopilares de prata (AgNPi) e nanopartículas de prata (AgNP) que foram (electro)depositadas na superfície de elétrodos de carbono (C-SPE) ou ouro (Au-SPE). Em paralelo, tal como para os elétrodos de laboratório, a estrutura da enzima foi estudada por espectroscopia de RR, enquanto a atividade electrocatalítica foi estudada por métodos eletroquímicos. De todas as configurações testadas, a PpDyP/SAM/AuNP/C-SPE apresentou o melhor desempenho, tendo inclusive feito a deteção de H_2O_2 em amostras expostas ao ar, com uma gama linear de 30 - 475 μM

H_2O_2 e uma sensibilidade de 230 $mA \cdot M^{-1} \cdot cm^{-2}$. Quando a PpDyP PROSS foi usada em vez da WT PpDyP, os dispositivos relevaram um desempenho analítico comparável. No que toca ao seu desempenho analítico, os dispositivos produzidos neste estudo são melhores que dispositivos reportados na literatura desenvolvidos com *horseradish peroxidase* (HRP)/SPE e outros sensores fabricados com peroxidases artificiais, e ao contrário destes dispositivos, o biossensor desenvolvido com a PpDyP (PROSS) não implica a alteração das amostras em estudo. Neste estudo confirmámos também que os nossos dispositivos podem ser usados em amostras complexas como fluidos corporais. Os biosensores produzidos neste estudo têm ainda a vantagem de permitirem a sua personalização para um objetivo especifico, como maior sensibilidade, a estabilidade térmica, bem como a resistência à inibição pelo substrato, uma vez que as DyPs têm uma produção fácil e são passíveis a uma rápida e fácil modificação genética. No final deste trabalho conseguimos demonstrar que os dispositivos aqui desenvolvidos têm um otímo desempenho analítico seja no formato miniaturizado, PpDyP (PROSS)/SAM/AuNP/C-SPE ou no formato de laboratório, PpDyP *in silico*/SAM/Ag, e que podem ser alternativas a bio-dispositivos que são fabricados com a HRP.

Palavras chave: *Dye decolorizing Peroxidases*; Biossensores de Terceira Geração; Peróxido de Hidrogénio; Ressonância de Raman; Ressonância de Raman amplificada por Superfície; Transferência Eletrónica; Enzimas Imobilizadas; *Screen-printed Electrodes*

Publications

Lidia Zuccarello, **Catarina Barbosa**, Smilja Todorovic, Célia M. Silveira. Electrocatalysis by Heme Enzymes - Applications in Biosensing. *Catalysts* 11: 218, 2021. Doi: 10.3390/catal11020218.

Célia M. Silveira, Lidia Zuccarello, **Catarina Barbosa**, Giorgio Caserta., Ingo Zebger, Peter Hildebrandt, Smilja Todorovic. Molecular Details on Multiple Cofactor Containing Redox Metalloproteins Revealed by Infrared and Resonance Raman Spectroscopies. *Molecules* 26: 4852, 2021. Doi: 10.3390/molecules26164852.

Lidia Zuccarello, **Catarina Barbosa**, Edilson Galdino, Nicola Lončar, Célia M. Silveira, Marco W. Fraaije, Smilja Todorovic. SERR Spectroelectrochemistry as a Guide for Rational Design of DyP-Based Bioelectronics Devices. *International Journal of Molecular Sciences* 22: 7998, 2021. Doi: 10.3390/ijms22157998.

Catarina Barbosa, Carolina F. Rodrigues, Nicola Lončar, Lígia O. Martins, Smilja Todorovic, Célia M. Silveira. Spectroelectrochemistry for Determination of the Redox Potential in Heme Enzymes: Dye-Decolorizing Peroxidases. *BBA Advances* 5: 100112, 2024. Doi: 10.1016/j.bbadva.2023.100112.

Catarina Barbosa, Maria C. Stefoni, Carolina F. Rodrigues, Lígia O. Martins, Daniel H. Murgida, Smilja Todorovic, Célia M. Silveira. Miniaturized Dyp Peroxidase-Based Biosensor for on-site Open-Air Use. *ACS Omega 10*: 8736–8744, 2025. Doi: 10.1021/acsomega.5c00461

Other publications

Giorgio Caserta; Lidia Zuccarello; **Catarina Barbosa**; Célia M. Silveira; Elin Moe; Sagie Katz.; Peter Hildebrandt, Ingo Zebger, Smilja Todorovic. Unusual Structures and Unknown Roles of Fes Clusters in Metalloenzymes Seen From a Resonance Raman Spectroscopic Perspective. *Coordination Chemistry Reviews* 452: 214287, 2022. Doi: 10.1016/j.ccr.2021.214287.

Table of contents

Figure Index

Table Index

Abbreviations and symbols

1-UDT	1-Undecanethiol
5c	5 Coordinated
5cHS	5 Coordinated High Spin
5cQS	5 Coordinated Quantum Mechanically Mixed-Spin
6c	6 Coordinated
6cHS	6c Coordinated High Spin
6cLS	6c Coordinated Low Spin
ABTS	2,2'-Azino-Bis(3-Ethylbenzothiazoline-6-Sulfonic Acid)
cAmp	Chronoamperometry
AOT	8-Amino-1-Octanethiol Hydrochloride
AUT	11-Amino-1-Undecanethiol Hydrochloride
BsDyP	Dye-Decolorizing Peroxidase from *Bacillus subtillis*
CboDyP	Dye-Decolorizing Peroxidase from *Cellulomonas bogoriensis*
CCD	Charge Coupled Device
CNT	Carbon-Nanotubes
Cpd	Compound
CV	Cyclic Voltammetry
DyP	Dye-Decolorizing Peroxidase
E	Potential
$E^{0'}$	Reduction Potential
ELISA	Enzyme-Linked Immunosorbent Assay
GC	Glassy Carbon
HRP	Horseradish Peroxidase
HS	High Spin
I_{cat}	Catalytic Current
I_{max}	Maximum Catalytic Current
IPTG	Isopropyl β-D-1-Thiogalactopyranoside
J_{cat}	Catalytic Current Density
J_{max}	Maximum Current Density
K_m	Michaelis-Menten Constant
K_M^{App}	Apparent Michaelis-Menten Constant
KpDyP	Dye-decolorizing peroxidase from *Klebsiella pneumoniae*
LB	Luria-Bertani Medium
LOD	Limit of Detection
LS	Low Spin

MOH	6-Mercapto-1-Hexanol
MUA	11-Mercaptoundecanoic
MUD	11-Mercapto-1-Undecanol
MWSCNT	Multi Walled Carbon Nanotubes
n	Number of Electrons
N.D.	Non-Determined
N.R.	Not Reported
NHE	Normal Hydrogen Electrode
ox	Oxidized
PAH	Polyallylamine hydrochloride
PDB	Protein Data Bank
PpDyP	Dye-decolorizing peroxidase from *Pseudomonas putida*
RE	Reference Electrode
red	Reduced
rpm	Revolutions Per Minute
RR	Resonance Raman
RSD	Relative Standard Deviation
S/N	Signal-to-Noise
SAM	Self-Assembled Monolayer
ScoDyP	Dye-Decolorizing Peroxidase from *Streptomyces coelicolor*
SD	Standard Deviation
SEM	Scanning Electron Microscopy
SERR	Surface Enhancement resonance Raman
SPE	Screen-Printed Electrodes
SviDyP	Dye-Decolorizing Peroxidase from *Scahoromonospora viridis*
SWCNT	Single-Walled Carbon Nanotube
TB	Terrific Broth Medium
TcDyP	Dye-Decolorizing Peroxidase from *Thermomonospora curvata*
TceDyP	Dye-Decolorizing Peroxidase *Thermobifida cellulosilytica*
TfuDyP	Dye-Decolorizing Peroxidase from *Thermobifida fusca*
THF	Tetrahydrofuran
UV-vis	Ultraviolet-Visible
VcDyP	Dye-Decolorizing Peroxidase from *Vibrio cholerae*
WE	Working Electrode
WT	Wild-Type
Yfex	Dye-Decolorizing Peroxidase from *Escherichia coli*
Ø	Diameter

ε	Molar Extinction Coefficient
ν_i	Raman Marker Band

Chapter 1 General Introduction

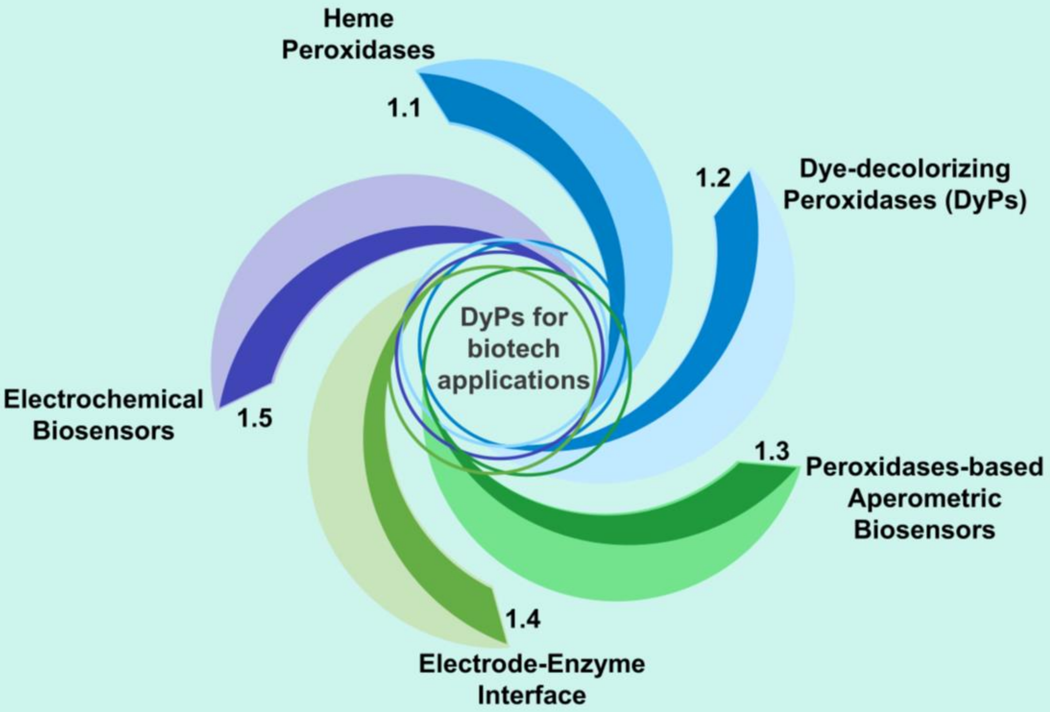

This chapter is based on:

Lidia Zuccarello, **Catarina Barbosa**, Smilja Todorovic, Célia M. Silveira. Electrocatalysis by Heme Enzymes - Applications in Biosensing. *Catalysts* 11: 218, 2021. Doi: 10.3390/catal11020218

Célia M. Silveira, Lidia Zuccarello, **Catarina Barbosa**, Giorgio Caserta., Ingo Zebger, Peter Hildebrandt, Smilja Todorovic. Molecular Details on Multiple Cofactor Containing Redox Metalloproteins Revealed by Infrared and Resonance Raman Spectroscopies. *Molecules* 26: 4852, 2021. Doi: 10.3390/molecules26164852

1.1. Heme Peroxidases

Metalloporphyrins are dispersed throughout the biosphere, playing crucial roles in the most fundamental biological processes [1-2]. Notably, they are involved in photosynthesis (chlorophyll), oxygen transport and storage (globins), electron transport (cytochrome) and catalysis (e.g., peroxidases) [1-2]. As a result, heme (iron protoporphyrin IX) is one of the most abundant and widely used cofactors. Its structure comprises the porphyrin rings connected by methine bridges, in which the central iron is coordinated by four pyrrole nitrogen atoms (Figure 1.1 A-B). Either one or both of the remaining two axial coordination sites can be occupied by an amino acid side chain, leading to five-coordinated (5c) or six-coordinated (6c) iron (Figure 1.1 C), respectively [1].

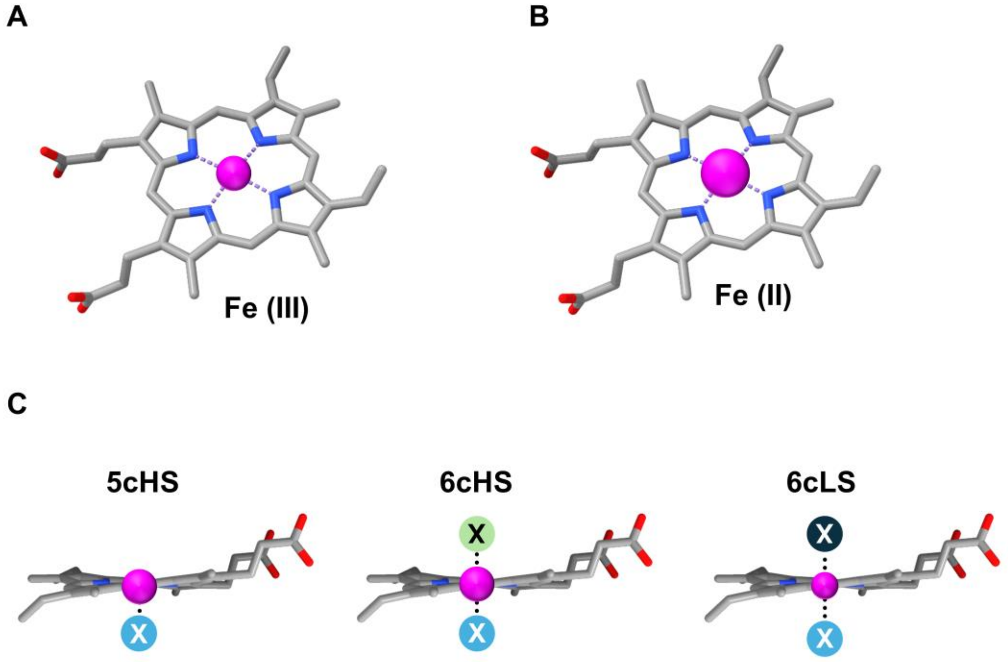

Figure 1.1 - Structure of heme *b*. Representation of (**A**) ferric Fe(III) and (**B**) ferrous Fe(II). (**C**) Types of coordination of the heme *b*. 5 coordinated high spin (5cHS, one proximal axial ligand), 6cHS (proximal axial ligand and a weak distal ligand in the 6th position) or 6c low spin (6cLS, proximal axial ligand and a distal strong ligand in the 6th position) state. The purple ball represents the iron ion, while X represents an axial ligand: blue - proximal, black- strong distal ligand, and light green - weak distal.

Heme-containing proteins perform a plethora of distinct functions due to their tenable redox chemistry. It is well known that the structure of the heme cofactor and its surroundings are important features that define the protein's reactivity and function [2,3]. Peroxidases are heme-containing enzymes that catalyze the reduction of H_2O_2 to H_2O coupled with the oxidation of a variety of structurally different substrates. They can be found in bacteria, fungi, plants and animals. Based on sequence similarity, heme peroxidases are grouped into two superfamilies: one includes the enzymes of fungal, plant and bacterial origin, and the other vertebrate enzymes belong to the peroxidase-cyclooxygenase superfamily [2,4–7]. Among the former, plant peroxidases, which will be hereinafter referred to as classical plant peroxidases, include some of the most extensively studied enzymes [4-7], e.g., horseradish peroxide (HRP). The classical plant peroxidases in the resting state configuration most commonly have a single type-*b* heme in a 5c high spin (5cHS) Fe(III) configuration. In the proximal site, they house a histidine axial ligand, whose imidazole ring is approximately perpendicular to the porphyrin plane (Figure 1.2 A) [4,5,8].

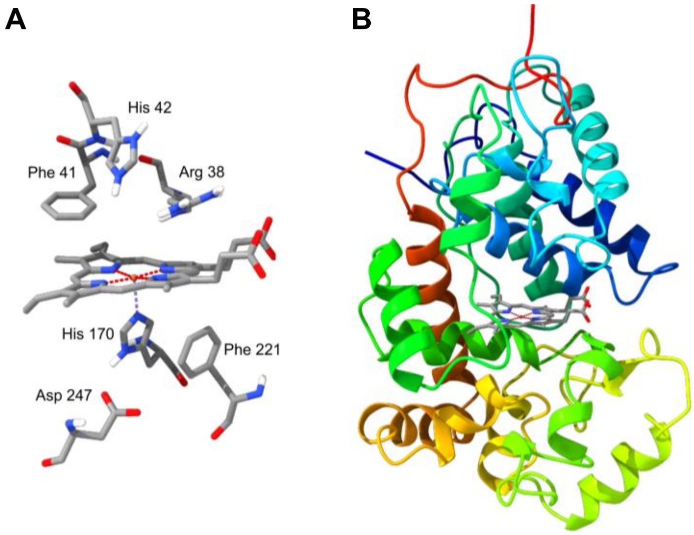

Figure 1.2 - Representation of the structure of a classical peroxidase. (**A**) Heme environment architecture in HRP C and (**B**) cartoon representation of–HRP C (Protein data bank (PDB) code: 1ATJ) crystal structure. The heme cofactor and the surronding amino acids Arg 38, Phe 41, His 42, His 170, Phe 221, and Asp 247 are represented as sticks. Image generated using Chimera X.

Although classical plant peroxidases present low sequence homology among each other (usually lower than 20%), according to their extensively characterized crystal structures [4-8], they reveal a conserved folding and secondary structure. Two distinct structural domains are formed around the heme, placing the heme in a crevice formed by two antiparallel α-helices (Figure 1.2 B) [4,7]. Additionally, some peroxidases contain an aromatic residue (either a Trp or a Phe) in the proximal side parallel to the imidazole ring of the proximal His, and in van der Waals contact with it. On the distal side of the heme, classical plant peroxidases contain a conserved His and Arg, which are crucial for the catalytic mechanism and being involved in the heterolytic cleavage of the peroxidic bond in H_2O_2. These amino acids are separated by a conserved residue with an aromatic side chain (Phe or a Trp) (Figure 1.2 A) [9].

The catalytic cycle of heme peroxidases involves several steps and the formation of two highly oxidized intermediates, Compound I (Cpd I) and Compound II (Cpd II) (Figure 1.3). In the first step of the catalytic mechanism, the ferric [Fe(III)] ion of the heme interacts with one molecule of H_2O_2 forming the transient intermediate ferric hydroperoxide [Compound 0, Cpd 0, Fe(III)-O-O-H_2, Figure 1.3 **2**] that is the precursor for the oxyferryl porphyrin radical, Cpd I, $(Fe(IV)=O)^{+\bullet}$. Protonation of the distal oxygen of Cpd 0 is necessary for converting it to Cpd I, as it helps breaking of the O-O bond to form Cpd I (Figure 1.3 **3**). The subsequent reduction of Cpd I by one substrate molecule results in the formation of Cpd II - reduced Cpd I oxyferryl iron, Fe(IV)=O (Figure 1.3 **4**), where the porphyrin radical is extinguished. Finally, Cpd II is reduced back to the resting ferric state with the concomitant one-electron oxidation of a second substrate molecule [4,5,7,9–11].

The thermodynamics and kinetics of the peroxidases' catalytic cycle are strongly influenced by the reduction potential ($E^{0'}$) of the three redox couples, namely Cpd I / Fe(III), Cpd I / Cpd II and Cpd II / Fe(III) [9,12,13]. It is known that the oxidative power of heme peroxidases depends on the (high) reduction potentials of the latter two couples, meaning that they strongly influence the possible range of oxidizable substrates by the ferric enzyme. With the help of enzyme engineering, it is possible to fine-tune the reduction potentials of the catalytic redox couples to create variants that present higher specificity for target molecules [9,12].

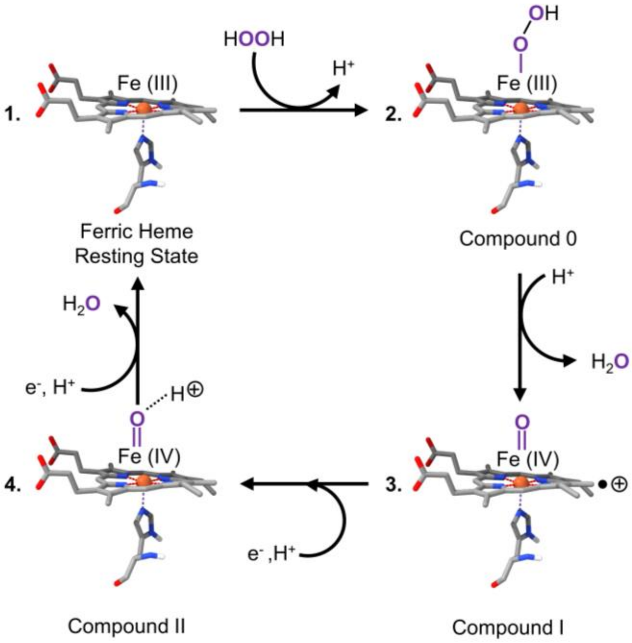

Figure 1.3 - The catalytic cycle of heme peroxidases. In the presence of H_2O_2 the ferric Fe(III)-enzyme (**1**) forms a transient reversible adduct, the ferric hydroperoxide Cpd 0 (**2**) ; protonation of Cpd 0 results in its breakdown which leads to the formation of Cpd I (oxyferryl porphyrin cation-radical) (**3**). Reduction of Cpd I by one equivalent of an electron-rich substrate (RH_2) generates the Cpd II (reduced oxyferryl porphyrin) (**4**); afterwards a second equivalent of RH_2 reacts with Cpd II to regenerate (**1**) the resting ferric enzyme.

However, measuring the $E^{0'}$ of the high-potential redox couples is a complex experimental challenge due to their instability, side reactions that can occur easily because of their high reactivity, and the small number of suitable one-electron donor reactants [9,14]. Thus, the available information regarding the reduction potential of Cpd I / Fe(III), Cpd I / Cpd II and Cpd II / Fe (III) is still fairly limited. Existing data include those on HRP [15–18], *Arthromyces ramosus* peroxidase [15,19], ascorbate peroxidase [20], and cytochrome *c* peroxidase [14,21], with $E^{0'}$ values of Cpd I / Fe(III), Cpd I / Cpd II, and Cpd I / Cpd II ranging from 883 - 954 mV, 886 -1156 mV, and 752 - 982 mV, respectively [14–21].

More information is available on the $E^{0'}$ of Fe(III) / Fe(II) ($E^{0'}_{Fe(III)\,/\,Fe(II)}$) couple, which, although not directly involved in the catalytic cycle, can influence the *in vivo* functionality of the peroxidases [9]. Actually, the fast H_2O_2-mediated two-electron oxidation of peroxidases to form Cpd I requires a stable ferric [Fe(III)] state in physiological conditions that depends on the reduction potential of the Fe(III) / Fe(II) couple [9,13,22]. Moreover, it is known that the molecular factors determinant for the

$E^{0'}_{Fe(III)\ /\ Fe(II)}$ also influence the catalytically relevant redox couples [9,23,24]. The $E^{0'}_{Fe(III)\ /\ Fe(II)}$ of heme peroxidases usually has a negative value, which indicates that the ferric state is stable under physiological conditions. This is an important requisite for the *in vivo* functionality of these enzymes because only those that have a stable Fe(III) form can be efficiently oxidized by H_2O_2 to Cpd I. The $E^{0'}$ values of Fe(III) / Fe(II) in different heme peroxidases span a range from −28 mV to −320 mV [9,25]. This high variability indicates that many factors can affect the redox properties of the heme, which include the first and second coordination spheres, and the complete heme pocket. The first coordination sphere of the heme is reflected by the axial ligands that coordinate the iron center. The second coordination sphere of the heme accounts for the electrostatic interactions between the redox center, solvent, the polar and charged residues in the proximal site, as well as the solvation of the heme group. Lastly, the overall heme pocket environment takes into consideration the effects of the protein folding around the heme pocket. Understanding the molecular factors that influence the $E^{0'}$ of peroxidases is important to enhance our knowledge of these proteins, and envision their possible biotechnological applications [9,13,23,25].

1.1.1. Peroxidases as biocatalysts

Classical plant peroxidases are a well-studied group of enzymes that are seen as attractive biocatalysts due to their broad substrate range, neutral pH optimum (pH_{opt}) and ability to catalyze different reactions such as halogenation, epoxidation, hydroxylation, and enantioselective oxidation with good yields [6,27–29]. However, their use in biotechnological applications is hampered by difficulties in their heterologous expression and limited stability [6,27–29]. Despite these drawbacks, they are used in clinical biochemistry and enzyme immunoassays [e.g., enzyme-linked immunosorbent assay (ELISA)] [28], as well as analytical systems, e.g., enzyme-based electrochemical biosensors, for the determination of H_2O_2, organic hydroperoxides and phenols, among others [28–30]. Among the plant peroxidases, HRP is probably the most commonly employed enzyme for practical analytical applications (as immobilized biocatalyst) in enzyme-based electrochemical biosensors or as a reporter in enzyme immunoassays (enzyme-labeled antibody). However, analytical systems employing other heme peroxidases from, e.g., soybean, tobacco (TOP), peanut, or sweet potato, have also been reported [29,30].

1.2. Dye-decolorizing peroxidases: a new class of enzymes

Dye-decolorizing peroxidases (DyPs) represent a relatively new member of a family of heme *b*-containing peroxidases [31–35]. They were first identified in 1999 in a basidiomycetous fungus and were named after their ability to efficiently degrade a wide range of synthetic dyes, including azo and anthraquinone dyes [36,37]. The DyP family was formally proposed in 2007, and so far, more than 50 DyP enzymes (Figure 1.4) have been characterized in bacteria, fungi, and eukarya [32].

The physiological role of DyPs is still unclear. Specific roles have been postulated for several enzymes. *Streptomyces lividans* DyP (DtpA) is thought to oxidize Cu(I) to Cu(II) so that the latter binds to the copper oxidase GlxA, which could indicate that this DyP is essential for the formation of aerial hyphae [38]. This hypothesis is based on the observation that aerial hyphae formation depends on a morphogenetic pathway involving DtpA and a radical GlxA. DtpA appears to be essential for the maturation of GlxA. This suggests that the formation of a cross-linked tyrosylcysteine cofactor is essential for its enzymatic activity [38]. The DyP from the human pathogen *Mycobacterium tuberculosis*, MtDyP, is considered a cargo of encapsulins [39]. These are conserved prokaryotic proteinaceous nanocompartments that allow for the local increase of functionally related enzymes while at the same time confining unstable reaction intermediates within the cell. The encapsulins can resist oxidative stress in low-pH environments, and due to that, it is thought that MtDyP contributes to the pathogenicity of the microorganism by helping to evade the host immune system [39].

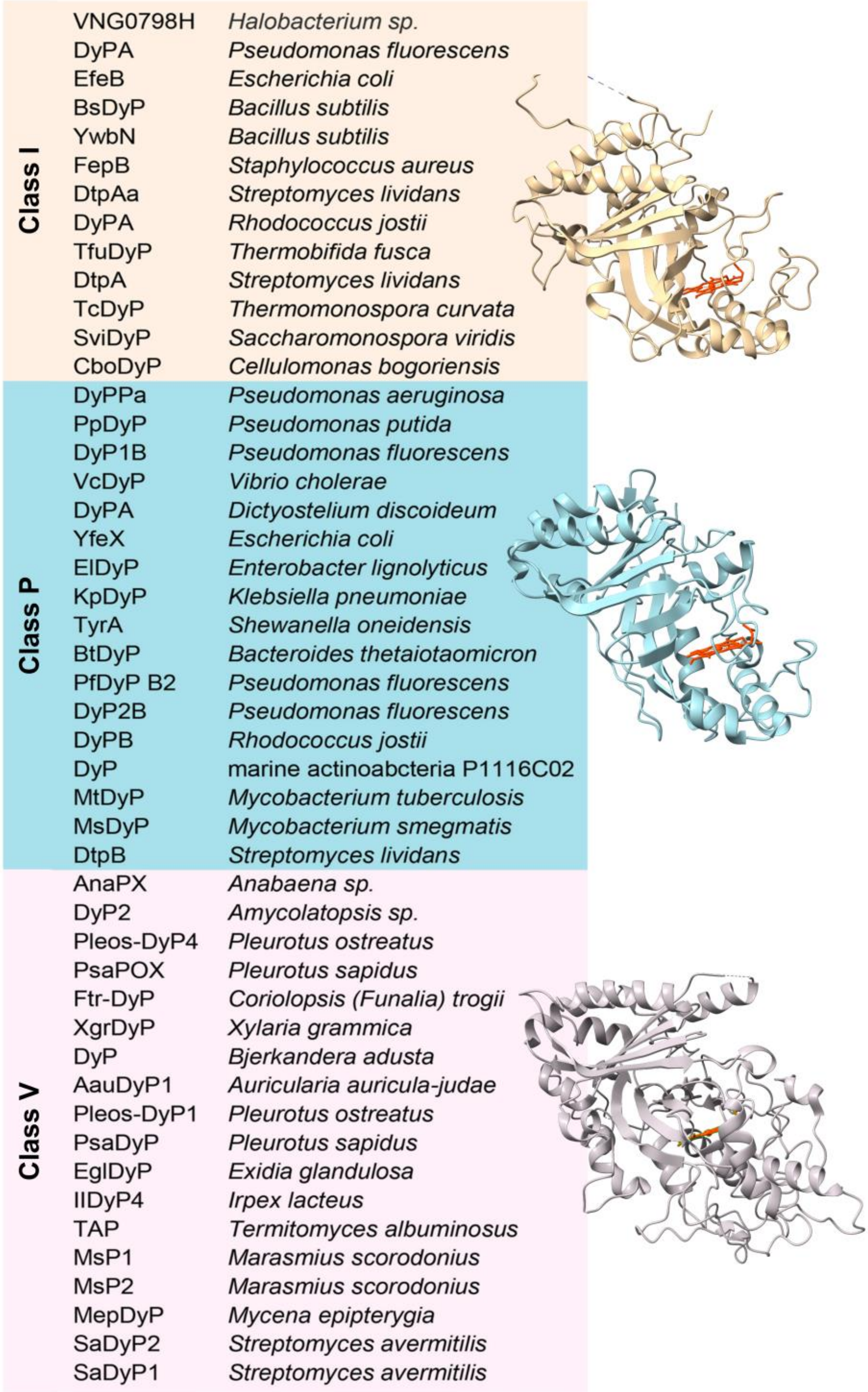

Class	Name	Organism
Class I	VNG0798H	*Halobacterium sp.*
	DyPA	*Pseudomonas fluorescens*
	EfeB	*Escherichia coli*
	BsDyP	*Bacillus subtilis*
	YwbN	*Bacillus subtilis*
	FepB	*Staphylococcus aureus*
	DtpAa	*Streptomyces lividans*
	DyPA	*Rhodococcus jostii*
	TfuDyP	*Thermobifida fusca*
	DtpA	*Streptomyces lividans*
	TcDyP	*Thermomonospora curvata*
	SviDyP	*Saccharomonospora viridis*
	CboDyP	*Cellulomonas bogoriensis*
Class P	DyPPa	*Pseudomonas aeruginosa*
	PpDyP	*Pseudomonas putida*
	DyP1B	*Pseudomonas fluorescens*
	VcDyP	*Vibrio cholerae*
	DyPA	*Dictyostelium discoideum*
	YfeX	*Escherichia coli*
	ElDyP	*Enterobacter lignolyticus*
	KpDyP	*Klebsiella pneumoniae*
	TyrA	*Shewanella oneidensis*
	BtDyP	*Bacteroides thetaiotaomicron*
	PfDyP B2	*Pseudomonas fluorescens*
	DyP2B	*Pseudomonas fluorescens*
	DyPB	*Rhodococcus jostii*
	DyP	marine actinoabcteria P1116C02
	MtDyP	*Mycobacterium tuberculosis*
	MsDyP	*Mycobacterium smegmatis*
	DtpB	*Streptomyces lividans*
Class V	AnaPX	*Anabaena sp.*
	DyP2	*Amycolatopsis sp.*
	Pleos-DyP4	*Pleurotus ostreatus*
	PsaPOX	*Pleurotus sapidus*
	Ftr-DyP	*Coriolopsis (Funalia) trogii*
	XgrDyP	*Xylaria grammica*
	DyP	*Bjerkandera adusta*
	AauDyP1	*Auricularia auricula-judae*
	Pleos-DyP1	*Pleurotus ostreatus*
	PsaDyP	*Pleurotus sapidus*
	EglDyP	*Exidia glandulosa*
	IlDyP4	*Irpex lacteus*
	TAP	*Termitomyces albuminosus*
	MsP1	*Marasmius scorodonius*
	MsP2	*Marasmius scorodonius*
	MepDyP	*Mycena epipterygia*
	SaDyP2	*Streptomyces avermitilis*
	SaDyP1	*Streptomyces avermitilis*

Figure 1.4 - List of the known DyPs (name and organism) and representative structures of Class I, BsDyP (PDB code: 7PKX); Class P, PpDyP (PDB code: 7QYQ) and Class V, AncDyPD-b (PDB code: 7ANV). Structure images generated using Chimera X, Adapted from [32].

The DyP from a parasitic fungus *Bjerkandera adusta* Dec 1, can efficiently oxidize the natural antifungal anthraquinone compound alizalin, produced by plants [40]. This suggests that this DyP could be involved in promoting parasitism in plants.

The DyP from *Halobacterium salinarum* is thought to provide additional protection to the cell against H_2O_2, when its concentration exceeds the detoxification capability of other peroxidases [41]. Based on studies using DyPs from *Exidia glandulosa, Mycena epipterygia* and *Mycetinis scorodonius*, it appears that DyPs may have a role as ligninolytic enzymes. They can oxidize several lignin-related and lignin model compounds [42]. Moreover, a transcriptomic and proteomic study of the DyP from *Enterobacter lignolyticus* showed its up-regulation when the sole carbon source was lignin [43], indicating a link between DyPs and lignin depolymerization. Nevertheless, although the physiological role is still poorly understood, it is well established that DyPs from different sources can catalyze the reduction of H_2O_2 coupled to the oxidation of structurally diverse substrates, e.g., anthraquinone-based and azo dyes, carotenoids, phenols, non-phenolic methylated aromatics, metal ions and lignin-related compounds, including phenols, kraft lignin and lignin models [31,33,35,42,44], most commonly at low pH values (3 - 5).

DyPs have been initially sub-classified into four phylogenetically distinct Classes: A, B, C and D [31]. Phylogenetic analysis has revealed that enzymes belonging to Class A contain a Tat-dependent signal sequence, which may indicate that their physiological role is outside of the cytoplasm or extracellular. According to the phylogenetic analysis, the ancestor DyP belongs to Class A. The bacterial enzymes belonging to Classes B and C are putative cytoplasmatic enzymes. Class D contains primarily fungal enzymes. A reclassification of DyPs was proposed in 2015 [33], on the grounds of structure-based sequence alignments where Classes P (primitive) and I (intermediate) replace Classes B and A, respectively. Class V (advanced) is a fusion of Class C and D (Figure 1.4). The members of Class P have the smallest molecular size, while Class V members have the largest size and higher catalytic efficiencies [33].

Nevertheless, this analysis was based on only 12 structures available at the time [32]. In 2023, the same authors revalidated their results by performing a phylogenetic analysis using all available sequences in the InterPro. They confirmed their previous results and further proposed dividing each Class into four subclasses (Figure 1.5).

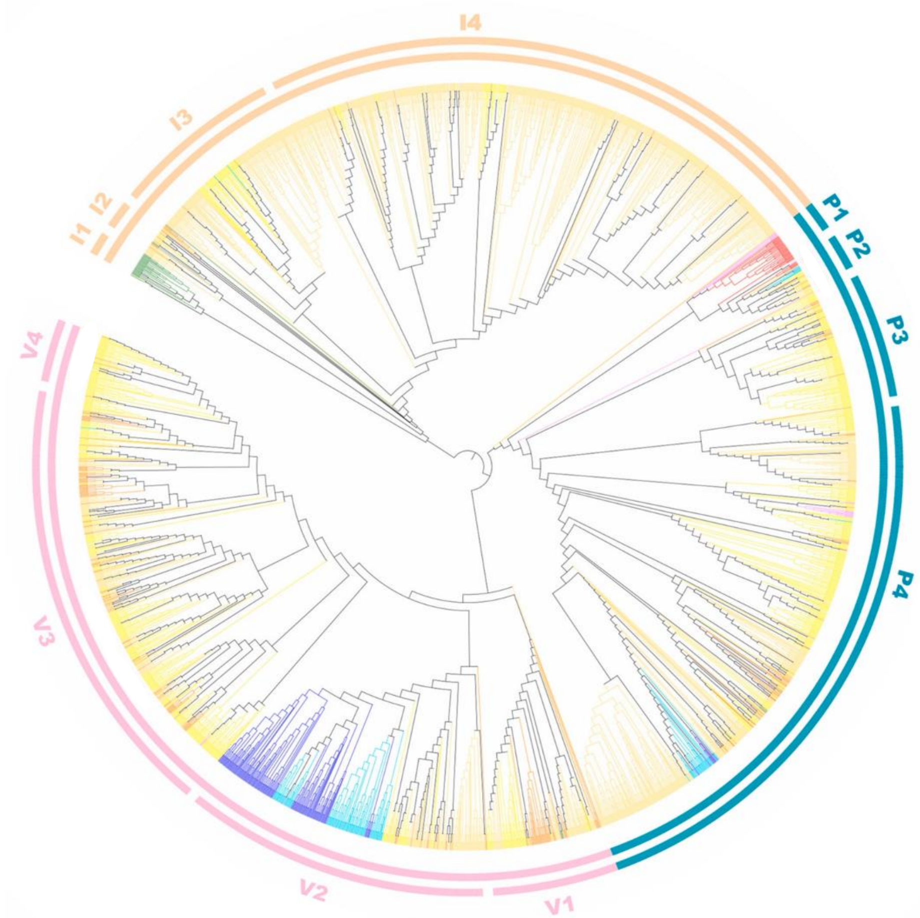

Figure 1.5 - DyPs phylogenetic tree showing the subclasses. Classes P (primitive - blue), I (intermediate - yellow) and V (advance-pink) with their respective subclasses P1 - P4, I1 - I4 and V1 - V4. Adapted from [32].

1.2.1. Structural properties of DyPs

DyPs lack sequence homology and have a different overall structure compared to classical peroxidases, which are rich in α-helixes [31–33,35]. Unlike classical peroxidases (cf. Figure 1.2), all solved DyPs structures reveal a conserved structure comprising two domains that contain α-helices and anti-parallel β-sheets that adopt a ferredoxin-like fold, which results in a buried heme cofactor within the folded α-helices and β-sheets (Figure 1.6) [31–33,35].

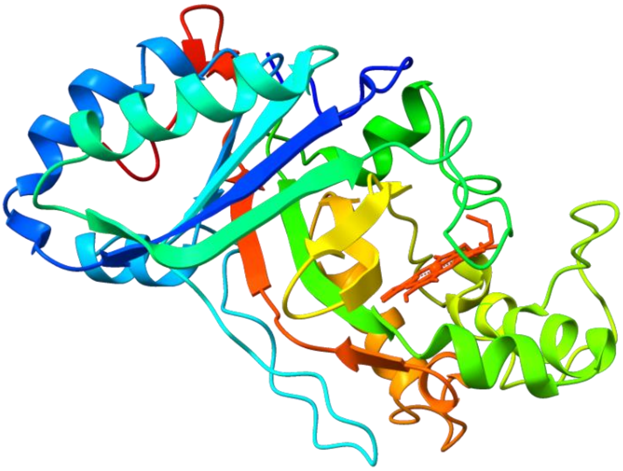

Figure 1.6 - Cartoon representation of PpDyP (PDB code: 7QYQ) monomer, with the α-helices colored in blue (α1 and α3), cyan (α2), green (α4), light green (α5 and α6), yellow (α7 and α8) and orange (α9) and the β-sheets colored in dark blue (β1), light blue (β2 and β3), cyan (β4), light green (β5), yellow (β6) and orange (β7). The image is generated using Chimera X.

DyPs typically form dimers in bacteria [45–47], while in fungi they are exclusively monomers [34,48,49]. Sequence analysis of fungal DyPs revealed that these enzymes have various C-terminated insertion sequences, which are believed to prevent enzyme dimerization. In bacterial DyPs, the dimerization is commonly due to the hydrophobic interaction between the monomers. Additionally, it has been proposed that radical formation at the protein surface may result in oligomerization as shown in the reaction of *Vibrio coloere* DyP with H_2O_2; the substitution of two Tyr residues at the dimer interface disrupted this oligomerization [50].

1.2.2. Active site structure

At the distal heme site, DyPs contain a unique GXXDG motif that lacks the highly conserved His of classical peroxidases, which acts as an acid-base catalyst in the catalytic mechanism of classical peroxidases. Instead, the currently available structures and models reveal that at the distal side, DyPs have an Asp (or Glu), an Arg, and a peripheral Phe and Asn (Ser or Gly), Figure 1.7 [31–33,35,51]. Like classical peroxidases, DyPs have a highly conserved His coordinating the iron at the proximal heme site [31–33,35,51].

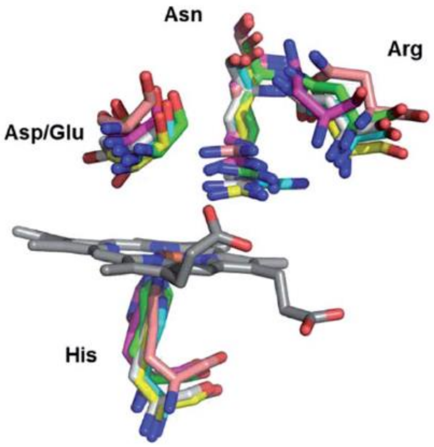

Figure 1.7- Representation of the overlaid active site of CboDyP (PDB code: 6QZO), PpDyP (PDB code: 7QYQ), TfuDyP (PDB code: 5FW4) and VcDyP (PDB code: 5DE0). This figure shows the proximal His and the conserved distal residues Asp/Glu, Asn, and Arg. Reprinted form [51].

The proposed catalytic mechanism of DyPs is based on the classical peroxidases, involving the formation of Cpd I and Cpd II (cf. Figure 1.3) [34,52–54]. However, the conserved Asp or Arg's role in the formation of Cpd I is still unanswered. Deprotonated Asp and Arg are weak bases, but they are still capable of H_2O_2 deprotonation due to the lowering of its pK_a upon binding to the heme. The Asp, which replaces the His conserved in classical peroxidases and is part of the GXXDG motif, was proposed as the key residue in the heterolytic cleavage of O-O bond by DyPs [34]. However, mutagenesis studies revealed that this is not always the case and that this residue is not crucial for activity of, e.g., *B. subtillis* BsDyP [55], *P. putida* PpDyP [56], *R. josttii* DyPB [57], and in the two enzymes identified in *S. lividans* (DtpA and DtpAa) [58,59]. The substitution of the conserved Arg results in a significant decrease in activity for some DyPs, e.g., DyPB [57], PpDyP [56] and *S. lividans* Dtp B [53]. For *V. cholerae* VcDyP, it appears that both Asp and Arg are catalytically relevant [50], while for BsDyP, none of the residues is individually essential for its peroxidase activity [55]. It is crucial to unravel the molecular factors that regulate the formation of Cpd I in DyPs to better understand these enzymes and their possible physiological roles that will accelerate their use in biotechnological applications.

1.2.3. Applications in biotechnology

As classical plant peroxidases, DyPs are versatile enzymes that can oxidize many structurally different substrates [35,44,60], which makes them promising biocatalyst for biotechnological applications [44]. On the contrary to classical plant peroxidases, DyPs appear to be highly robust, with an added advantage of being easily expressed heterologously in *E. coli* in the case of bacterial DyPs [35,61–63]. In particulary, these enzymes are considered promising biocatalysts for a variety of industrial applications due to their catalytic ability to degrade synthetic dyes and lignin-related products [44,50,60–69], which indicates that DyPs can be used for bioremediation of dye-contaminated wastewater. Another application includes the biodegradation and/or valorization of lignocellulosic material that tends to be quite resistant to (bio)chemical degradation. Moreover, lignin is the second most abundant biopolymer (carbon source) and the largest source of natural phenolic compounds on Earth [44], which suggests that DyPs could have commercial value for lignin degradation. DyPs can also be useful in the food industry [61,70–72], especially in vanilla production [61,72], since there is a high demand for this flavor, which is challenging to produce in laboratories at large scale.

Additionally, some fungal DyPs are reported to be able to bleach β-carotene [70], which is sought after in the process of whitening of whey-containing foods and beverages. A recent study demonstrates that bacterial DyPs can also degrade different mycotoxins, sometimes present in animal feed and food [66]. If left untreated, these toxins can threaten the health of animals and humans, leading to significant economic losses. The potential use of bacterial DyPs in industrial applications is nowadays even more overreaching. These enzymes are easily genetically modifiable and many molecular tools are available for enzyme engineering, making it possible to obtain custom-tailored DyPs. This allows for the creation of highly efficient and stable biocatalysts that, depending on the envisioned application, can be further improved in terms of thermostability, resistance to organic solvents, increase/decrease pH_{opt} for enzymatic activity, or reduce substrate inhibition. Indeed, several DyPs were successfully engineered towards improved thermostability, enhanced H_2O_2 resistance, increased catalytic efficiency for target substrates or a shifted acidic pH_{opt} to a neutral one [45,64,73–79].

To further broaden the use of DyPs in biotechnological applications, we need to consider another important factor which is their immobilization. Diverse immobilization strategies have been developed to improve enzyme stability, activity and bypass the use of co-substrates. Immobilization of the biocatalyst also offers the possibility to reuse the respective enzyme with the added advantage of easy separation of the biocatalyst and products, which is crucial for enzymatic industrial processes. So far, only a few immobilized DyPs have been tested for biotechnological applications (Table 1.1), particularly for dye-bioremediation [80-84]. DyP from *B. amyloliquefaciens* (BaDyP) has been immobilized in dopamine-modified porous microspheres of halloysite nanotubes [80]. Compared to solution assays, immobilized BaDyP showed better stability across a wide range of pH values and temperatures. Moreover, the reusability of BaDyP is also enhanced by immobilization, showing that the enzyme can retain ~58% of the initial decolorizing activity after six recycling batches. Additionally, this study showed that the treatment of dyeing effluent with immobilized BaDyP reduces bacterial growth, implying that, after the treatment, the dyeing effluent is less toxic [80]. Entrapment of DyPs from *P. fluorescens* Pf-01 or Pf-5 (PfDyP B2 and Pf-5 DyP1B) in calcium-alginate beads was shown to be beneficial for their activity and stability [81,82], as in the case of BaDyP. The optimal activity of immobilized Pf-5 DyP1B shifted from pH 5.5 and 30 °C to pH 7 and 40 °C. The reusability studies demonstrated that, after five cycles, the system retained 58% of its initial activity. Another immobilization strategy took advantage of the fact that DyPs are physiologic cargo proteins of encapsulin [83]. In this study, DyP from *Saccharomonospora viridis* (SviDyP) was packed in the encapsulin from the mesothermophile bacterium *Mycolicibacterium hassiacum*. The packed DyP had comparable activity with the enzyme in solution but higher thermostability at 40 °C, which is 50 times better than the free enzyme. All these studies demonstrate how beneficial immobilization of DyPs can be for the bioremediation of dyes. However, in all tested applications, H_2O_2 had to be added for enzymatic activity, which could affect the overall cost of the industrial enzymatic process.

Table 1.1 - Biotechnological applications of immobilized DyPs.

Enzyme[a]	Immobilization	Biotechnological application	Ref.
BaDyP	Dopamine-modified porous microspheres of halloysite nanotubes	Decolorizing activity for ABTS as for a dye mixture consisting of azo dye, triphenylmethane dye, anthraquinone dye, and anionic dye	[80]
PfDyP B2	Entrapment in calcium-alginate beads	Decolorizing activity for ABTS	[81]
Pf-5 DyP1B	Entrapment in magnetic calcium-alginate beads	Decolorizing activity for reactive Blue 5	[82]
SviDyP	Entrapment in an encapsulin	Decolorizing activity for ABTS	[83]
BsDyP	Covalent attachment to biocompatible coated gold electrodes	Decolorizing activity for ABTS, Reactive Blue 19, Reactive Black 5, and triarylmethane dye malachite green. Oxidation of 2,6-dimethoxyphenol	[84]
PpDyP	Adsorption onto biocompatible silver electrodes	H_2O_2 biosensor	[85]

[a] - BaDyP - *B. amyloliquefaciens*; PfDyP B2 - *P. fluorescens* Pf-01; Pf-5-DyP1B - *P. fluorescens* Pf-5; SviDyP - *S. viridis;* BsDyP - *B. subtillis* and PpDyP - *P. putida.*

Recently, it was shown that BsDyP covalently attached to biocompatible gold coated electrodes showed dye-decoloring activity without adding H_2O_2 [84]. Instead, the immobilized enzyme is electrochemically activated and shows higher catalytic performance than the soluble enzyme towards a variety of dyes. Additionally, the enzyme shows broader pH activity profiles, with the acidic pH shifting towards more neutral and alkaline pH [84].

Similarly to classical peroxidases, DyPs can also be used as immobilized biocatalysts for biosensing applications. Our group was the first to explore DyP from *P. putida* MET94, PpDyP, as an immobilized biocatalyst in H_2O_2 biosensors, which was evaluated by immobilizing the enzyme onto self-assembled monolayer (SAM) coated Ag electrodes [85]. We demonstrated that immobilized PpDyP showed good stability, shorter response times and higher sensitivity compared to other H_2O_2 biosensors reported in the literature, which use HRP as the biocatalyst [85]. Optimization was attempted to further improve the constructed biodevice, using enzyme variants obtained through directed evolution, displaying increased resistance to H_2O_2

inactivation in solution. The biosensor based on a variant harboring two mutations at the second shell of the heme cavity showed improved storage stability compared with the WT PpDyP [85].

1.3. Amperometric enzyme biosensors

A biosensor is an analytical device that can detect and quantify the presence of a target analyte in complex matrices, *in situ* and preferably without sample preparation. The device consists of a biological component (e.g., antibody, cell, DNA, enzyme, tissue), specific for the analyte, in direct contact with a physicochemical transducer (e.g. electrochemical, magnetic, optical, piezoelectric, thermal), which translates the signal obtained through the bio-recognition of the biological component with its target analyte, into a measurable signal (Figure 1.8) [30,86,87]. Due to their diversity of potential targets, sensitive quantification, and ease of use, biosensors are highly sought in, e.g., medicine, industry, and agriculture.

Enzyme-based electrochemical biosensors are the most widespread. These devices combine enzyme's selectivity and high turnover rates with the advantages of electroanalytic methods, such as high sensitivity, simplicity, low cost, the potential for miniaturization, and portability of devices [30,87–93]. Depending on the physicochemical signal that is generated by the bio-recognition reaction, electrochemical biosensors can be classified as (i) potentiometric, which detect charge accumulation or cell potential; (ii) conductometric, which monitor conductivity changes; (iii) impedimetric, which probe resistance and capacitance variations; or (iv) amperometric, which monitor the current variation when a fixed potential is applied [87,90,93,94]. Enzyme-based amperometric biosensors have been widely explored over the last few decades [88,95] and are the focus of this thesis. They are robust, easy to miniaturize, and operate with small sample volumes of rather complex matrices. A typical enzyme-based amperometric biosensor consists of a thin layer of enzyme immobilized on the surface of a conductive material such as platinum, silver, gold, or carbon (e.g., graphite - G, glassy carbon - GC, carbon nanotubes - CNTs), which acts as the working electrode (WE) and ensures the enzyme's connection to the electrochemical transducer.

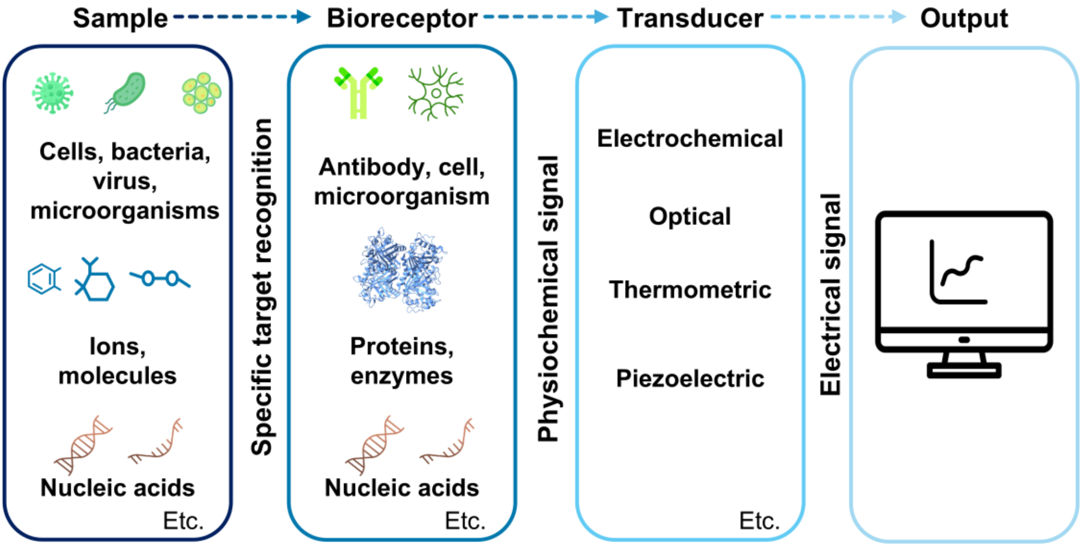

Figure 1.8 - Schematic representation of the working principle of biosensors.

The choice of the WE is important since the electrochemical measurements often depend on the used material [87–90,93,96]. The attachment of the enzyme to the electrode can be achieved through a variety of immobilization methods. Immobilization is a crucial step in biosensor development since analyte detection, efficient signal transduction, and reusability of the biocatalyst depend on efficient enzyme immobilization. Nevertheless, this process may cause undesirable structural changes to the biocatalyst affecting its catalytic activity (cf. Chapter 1.4).

1.3.1. Amperometric enzyme biosensors

Amperometric enzyme biosensors can be of the first-, second- or third-generation based on the mode of electron transfer (ET) between the enzyme and the electrode (Figure 1.9) [88,93,95,97,98]:

(i) In *First-generation biosensors*, the substrate or the product of the enzymatic reaction is directly measured electrochemically. This class of biosensors is mainly based on O_2-dependent enzymes, particularly oxygenases and oxidases

[88,95,99,100]. The latter can monitor either the production of H_2O_2 by applying a fixed anodic potential (+500 mV vs. NHE) or the oxygen consumption by applying a fixed cathodic potential (−500 mV vs. NHE). Although the detection mode is quite simple, they have some drawbacks, such as the need for an abundant amount of O_2 to ensure that enzyme activity is not limited by the lack of the co-substrate or by its variation in the sample, which can impair the sensor's response and reproducibility. In addition, since high operation potentials are employed, the oxidation of interfering species present in the sample can also occur, which may result in low sensitivity [88,94,99,100].

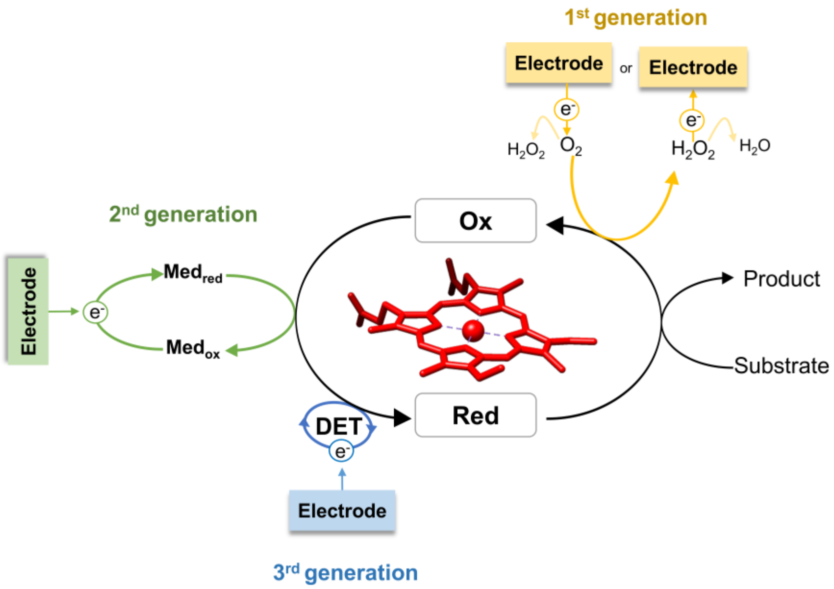

Figure 1.9 - Schematic representation of different ET modes in amperometric enzyme biosensors. In first-generation biosensors (yellow), the co-substrate (O_2) or product (H_2O_2) of the enzymatic reaction are detected directly at the electrode. In second-generation biosensors (green), the amperometric signal arises from the reduction of the mediator following ET to the enzyme. Third-generation biosensors (blue) measure the direct reduction of the enzyme redox center by the electrode. Med-mediator; Red-reduced; Ox-oxidized; DET-direct ET.

(ii) Second-generation biosensors use mediators for the ET (MET-mediated ET), enabling the detection of the target analyte at low potentials without oxygen dependence [88,95]. This broadens the range of applicable enzymes and measurable

analytes compared to first-generation biosensors. Mediators facilitate reversible electrochemistry and efficient ET between the enzyme and electrode, which generates a current proportional to the analyte concentration [93,94,98]. Common mediators include quinone derivates, ferrocene and ferricyanide [101]. Some ET proteins like cytochromes can also be used, potentially improving the selectivity of the device when they are the immobilized biocatalyst's physiological partner [102]. The mediators can be added to the sample or immobilized on the electrode surface. In the latter case, the mediator must be entrapped close to the enzyme. However, a common issue is mediator leakage, which limits continuous use and reusability [93,98,101]. This problem can be overcome by the use of redox polymers, amd modified enzymes (e.g., ferrocene-modified glucose oxidase), or by reconstituted enzymes on functionalized electrodes, which, although reducing or even eliminating mediator leakage, may affect enzyme activity [93,98,101].

(iii) Third-generation biosensors rely on the bioelectrocatalysis that results from the direct ET (DET) between the enzyme and the electrochemical transducer upon the interaction of the enzyme with its substrate. For this reason, these devices have a simplified design as redox mediators or co-substrates are not required [11,88,91,93,95,98,103,104]. Third-generation biosensors usually also offer superior selectivity. However, the establishment of DET is not always straightforward. The redox centers can be buried in the enzyme matrix making the ET with the electrode difficult or, the enzyme matrix may act like an isolating barrier hindering the ET process with the electrode. Moreover, direct contact with the electrode may change the enzyme's conformation, causing denaturation and activity loss [93,98,104]. Despite these concerns, several oxidoreductases, e.g, laccases, peroxidases, alcohol and cellobiose dehydrogenases [88,93,105,106], display efficient DET upon immobilization on electrode surfaces. Recently, third-generation biosensors have gained popularity due to the latest advancements in material science and protein engineering techniques. Novel conductive nanomaterials that can facilitate interfacial ET and provide high-surface-area electrodes are being developed, resulting in higher enzyme loading, which leads to the improvement of the overall sensitivity of the

biosensor [93,107,108] (cf. Chapter 1.4). Additionally, protein engineering targeting (i) improved biomolecular recognition of the substrate, (ii) increased rate of heterogeneous ET, and (iii) enhanced stability of the enzyme upon immobilization [93,109] have revealed beneficial for the biosensor development by increasing selectivity, sensitivity, and the overall stability of the device.

1.3.2. Peroxidase-based amperometric biosensors

In the past 30 years, peroxidase-based biosensors have been widely used for the detection of H_2O_2 in physiological and food samples, while at the same time, many of them have also been proposed for detecting organic hydroperoxides, phenols, aromatic amides, and non-typical peroxidase substrates, such as uric acid, trichloroacetic acid (TCA), and nitrite or hazardous compounds (e.g., potassium cyanide) [29,30,104]. In most cases, the electrocatalytic activity (Figure 1.10) is monitored through MET or DET (in second- or third-generation biosensors, respectively) via an increase of cathodic current, which is related to the substrate concentration in solution.

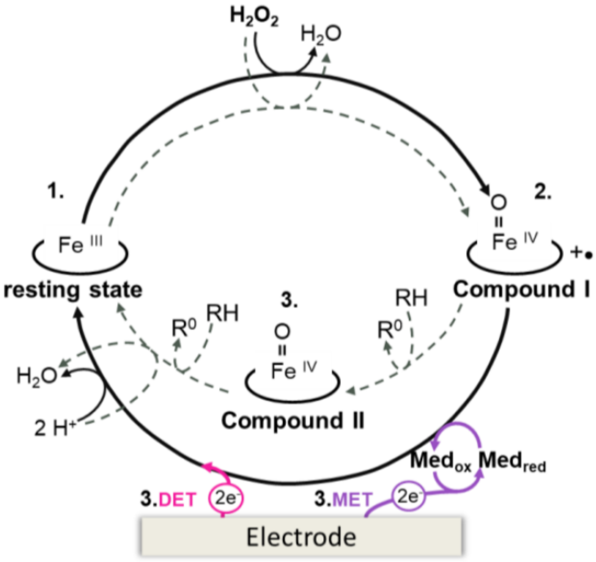

Figure 1.10 - Reaction scheme of peroxidase-based electrochemical biosensors (solid lines) and of the native catalytic cycle (dashed lines), with the following designations: RH - substrate; R° - product; Med_{ox} - oxidized mediator; Med_{red} - reduced mediator; DET - direct electron transfer; MET - mediated electron transfer.

The most frequently employed enzymes for the construction of peroxide-based biodevices are plant peroxidases, in particular HRP and TOP, as well as barley, peanut, guinea grass and soybean peroxidases. HRP is one of the most explored enzymes for the development of amperometric biosensors due to (i) commercial availability, (ii) low production cost, (iii) high stability under standard conditions, (iv) high activity towards H_2O_2 and a broad range of phenolic compounds as aromatic amines, and (v) well understood catalytic and structural properties [30,110–112]. Nevertheless, there are some drawbacks to using HRP in amperometric biosensors, which are related to substrate inhibition (H_2O_2) and to the high level of enzyme glycosylation. Around 25% of the HRP molecular weight is associated with the carbohydrates present on its surface. Glycosylation can affect the binding and electronic wiring of the enzyme to the electrode and DET [6,113]. In recent years, natural and synthetic materials with peroxidase-like activity have been explored in search for alternatives to classical plant peroxidases. For instance, globins and microperoxidases that, under certain conditions, display peroxidase-like activity have also been explored for biosensing applications [114–116]. Moreover, an increasing trend is the use of nanostructured materials with peroxidase-like activity, called artificial peroxidases, such as metal oxide nanoparticles. Nevertheless, these materials still face a challenge regarding their low selectivity compared to natural enzymes [29,117–119].

1.3.2.1 H_2O_2 detection

H_2O_2 is a small inorganic molecule with strong oxidizing properties and is commonly used in pharmaceutical, clinical, environmental, mining, textile, and food manufacturing applications [120–124], especially for whitening or sterilization purposes [120–124]. In humans, this reactive oxygen species is present throughout the body and has a variety of roles in physiological processes such as cellular signaling, through which it can regulate cell growth, immune activation, and apoptosis. In breath and body fluids such as urine and blood plasma, H_2O_2 concentrations can indicate metabolic disorders associated with diabetes, pulmonary diseases, or other health conditions [122,123]. The safe concentration range of H_2O_2 for biological entities, in general, depends not only on the media but also on cellular metabolism and/or method of exposure, which can span from ~100 nm for seawater to ~1 mM for the aquaculture industry (Figure 1.11) [123].

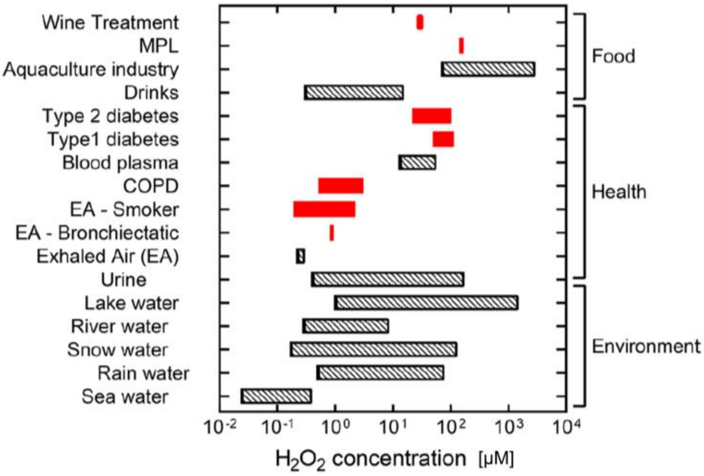

Figure 1.11 - Relevant concentration range of H_2O_2 in environmental, biomedical and food samples. The black bars refer to safe ranges, red bars represent the hazardous ranges (i.e., any value inside these ranges is indicative of condition or a disease. Levels for diabetes refer to concentration in blood. COPD stands for "Chronic Obstructive Pulmonary Disease". MPL stands for "Maximum Permitted Level". For MPL and wine treatment, the maximum permitted level is indicated. Reprinted from [123].

Given the importance of H_2O_2 in industrial and biological processes, a variety of methods for its detection and quantification have been in use for many years, including colorimetric titration, chromatography, and light detection (fluorimetry, chemiluminescence, fluorescence or spectrophotometry). However, these conventional techniques are complex, costly and time-consuming [123]. In comparison, electrochemical (bio)sensors can offer simple, rapid, sensitive and cost-effective ways of detecting H_2O_2 [121,123,124]. The discussion in this thesis will focus on DET biosensors that employ peroxidase-based amperometric constructs.

1.3.2.2. H_2O_2 peroxidase-based biosensors

The simplest third-generation plant peroxidase-based biosensors are made by the direct adsorption of the peroxidase on the electrode interface. The electrocatalytic activity of the immobilized enzyme has been observed in materials like modified graphite [113,125–127], graphene thick films [128], and gold [129–131] (Table 1.2).

However, this strategy is commonly linked with slow ET rates because of (i) the deeply buried heme in the enzyme matrix, (ii) the presence of a high percentage of non-active enzyme population due to sub-optimal orientation and/or altered conformation structure, and (iii) the high glycosylation [132]. The presence of the carbohydrates on the enzyme surface not only forms an insulating barrier but also increases the distance between the electrode and the heme site, reducing the ET efficiency [113]. One way to overcome this problem is by using recombinant non-glycosylated HRP and TOP that favor the adsorption and uniform orientation on the carbon electrode surface, resulting in improved ET rates and overall bioelectrode performance [113,127,129,130]. However, the production of recombinant plant peroxidases is neither straightforward nor consistently successful [113,127,129,130].

To facilitate the electron exchange between plant peroxidases and electrodes, the use of conducting and non-conducting polymers, detergents, SAMs, ionic liquids and nanomaterials, among others, has been tested (Table 1.2) [93,120,124].

Classical plant peroxidases have been physically entrapped or chemically attached to polymer films that can mimic the interactions in the physiological environment, promoting the native configuration of the enzyme [93]. In these cases, the redox polymer has a dual role since it physically and electrically connects the enzyme to the electrode. Both single polymeric materials and composite matrices incorporating carbon nanotubes have been explored, demonstrating that favorable electrostatic interactions between the HRP and the polymer films are important for the performance of the biosensors [93].

Cytochrome *c* peroxidase is another peroxidase whose electrochemical response towards H_2O_2 was demonstrated at pyrolytic graphite (PG) and Au surfaces [143–146]. However, these enzymes are less sought after for biosensing applications due to their complex activation mechanisms and limited substrate range compared to plant peroxidases [146]. As mentioned in Chapter 1.2.3. PpDyP was also used by our group to develop a DET-based H_2O_2 biosensor by attaching the bacterial DyP enzyme onto biocompatible SAM-coated Ag electrodes [85].

Table 1.2 - Peroxidase-based biosensors for H_2O_2 detection.

Enzyme	Electron Transfer	Electrode modification	Ref.
HRP	DET	PNM/GC	[133]
		MTAu/GC	[134]
		HA-HRP–CdS–IL/CILE	[135]
		DNA-SWCNT/GC	[136]
		AuNPs	[137]
		Pan/MWCNTCOOH/Au	[138]
		G	[126]
		AuNPs/CESM/GC	[139]
	MET	GNP-TNT/HIL/GC	[140]
		Nano-Au/CCE/GC	[141]
		Os(dmp)PVI]$^{+/2}$ + PEGDGE/G	[142]
TOP	MET	Os(dmp)PVI]$^{+/2}$ + PEGDGE/G	[142]
Cytochrome *c* peroxidase	DET	AUME	[143]
		PGE	[144]
DyP	DET	SAM/Ag	[85]

AuNPs - gold nanoparticles; CCE - carbon ceramic electrode; MWCNTs-COOH - carboxy-functionalized multiwalled carbon nanotubes; nano-Au - nano-scaled particulate gold; AuME - Gold membrane electrode; CESM - Carbonized chicken eggshell membrane; G - graphite electrode; GC - glassy carbon; HIL - hydrophobic ionic liquid; MTAu - multiwalled carbon nanotube/thionine/Au; NP-TNT - gold nanoparticle dotted TiO_2 nanotubes; Os(dmp)PVI]$^{+/2}$ - osmium redox polymer; PEGDGE - poly(ethyleneglycol) diglycidyl ether; PGE - pyrolytic grafide electrode; PNM - N-isopropylacyamide-co-3-methacryloxy-propyltrimethoxysilane; SAM - Self assembled monolayers; SWCNT - single walled carbon nanotubes.

The mechanistic pathway in all the examples given above (Table 1.2) proceeds by the following steps: the ferric [Fe(III)] resting state peroxidase is first oxidized by H_2O_2, leading to the formation of Cpd I (cf. Figure 1.10, solid line). The intermediate Cpd I is then reduced, and the ferric enzyme is restored via heterogeneous ET directly from the electrode. Typically, the catalytic currents are measured by amperometric methods at working potentials between +150 and +500 mV (vs. NHE), due to the high

$E^{0'}$ of the catalytic redox couples [Fe(III) / Cpd I, Cpd I / CpII, Cpd II / Fe (III)] [134,147,148]. Nevertheless, the cathodic currents are often observed at much lower potentials, consistent with the Fe(III) / Fe(II) redox transition [9]. This likely occurs since H_2O_2 reduction may follow an alternative non-native route that goes through the formation of the ferrous [Fe(II)] enzyme. This “low potential cycle” of peroxidase electrocatalysis has been associated with a non-native enzyme state and transient formation of inactive catalytic intermediates, as for example, Fe(II)-O_2, which can also be formed in the presence of high concentrations of H_2O_2 [9,11,142,149]. Due to the very efficient redox chemistry of the heme, it was proposed that this non-physiological process can be the cause of the electrocatalytic response of different heme-based electrodes [150–152]. Various DET mechanisms are proposed to rationalize these experimental findings [149]; we highlight one that postulates that the alternative electrocatalytic reaction follows a catalase-like mechanism, where H_2O_2 acts as an oxidant and a reductant. According to this scenario, the generated Cpd I can be reduced by H_2O_2, returning the peroxidase to the Fe(III) state and producing O_2 (Equation 1.1). After the reduction of the Fe(III) enzyme at the electrode (Equation 1.2), O_2 reacts with the ferrous peroxidase (Equation 1.3) to form Fe(II)-O_2 oxy-peroxidase, which in turn undergoes electrochemical reduction at the electrode (Equation 1.4), at the potential of Fe (III) / Fe(II) reduction.

$$\text{Cpd I} + H_2O_2 \rightarrow \text{Fe(III)} + O_2 + H_2O \qquad (1.1)$$

$$\text{Fe(III)} + H^+ + e^- + H_2O \rightarrow \text{Fe(II)}, \text{ at electrode} \qquad (1.2)$$

$$\text{Fe(II)} + O_2 \rightarrow \text{Fe(II)-}O_2 \qquad (1.3)$$

$$\text{Fe(II)-}O_2 + 2H^+ + 2e^- \rightarrow \text{Fe(II)} + H_2O_2, \text{ at electrode} \qquad (1.4)$$

1.3.2.3. Other substrates

Peroxidase-based biosensors are also employed for the detection of organic hydroperoxides, enzyme-reducing substrates, including numerous phenolic compounds, and aromatic amines, as well as non-typical substrates such as uric acid, TCA and nitrite. The electrocatalytic activity of the immobilized enzyme is monitored either by MET [125,154–156] or DET [135,157–159].

1.4. Biosensor construction: empirical vs. rational design

The most common methods for enzyme immobilization are physical adsorption, encapsulation (behind or within a porous membrane, polymer, clay paste or ink) and chemical binding, especially covalent coupling and cross-linking (Figure 1.12) [87,93,96].

The best immobilization strategy for a particular enzyme often results from the combination of several of these methods. Covalent attachment is known to be the most stable. However, the formation of the covalent link often damages the native configuration of the enzyme, which affects both stability and catalytic activity [87,93,96].

Physical adsorption based on weak non-specific forces, such as van der Waals bonds, hydrophobic interactions, hydrogen bonds or electrostatic interactions between the enzyme and the electrode is the simplest method for enzyme immobilization. However, this approach may lead to enzyme denaturation upon contact with metal or carbon surfaces [87,93,96]. This strategy also often results in bioelectrodes prone to leaching, detachment of the enzyme from the electrode, and fouling, that may occur when proteins non-uniformly aggregate on the electrode surface, which can partially block the electrode.

The encapsulation/entrapment of the enzyme into a porous matrix is also an attractive approach, as it can retain the biomolecules on the electrode support while ideally still allowing substrate access to the enzyme. In this manner, the stability and lifetime of the biosensor can usually be increased due to the reduced leakage of enzymes and the prevention of non-specific adsorption of fouling agents.

Overall, the enzyme immobilization strategy chosen for the construction of a third-generation biosensor should guarantee biocompatibility, efficient electrical contact between the enzyme and the electrode, and preservation of the enzyme's catalytic activity.

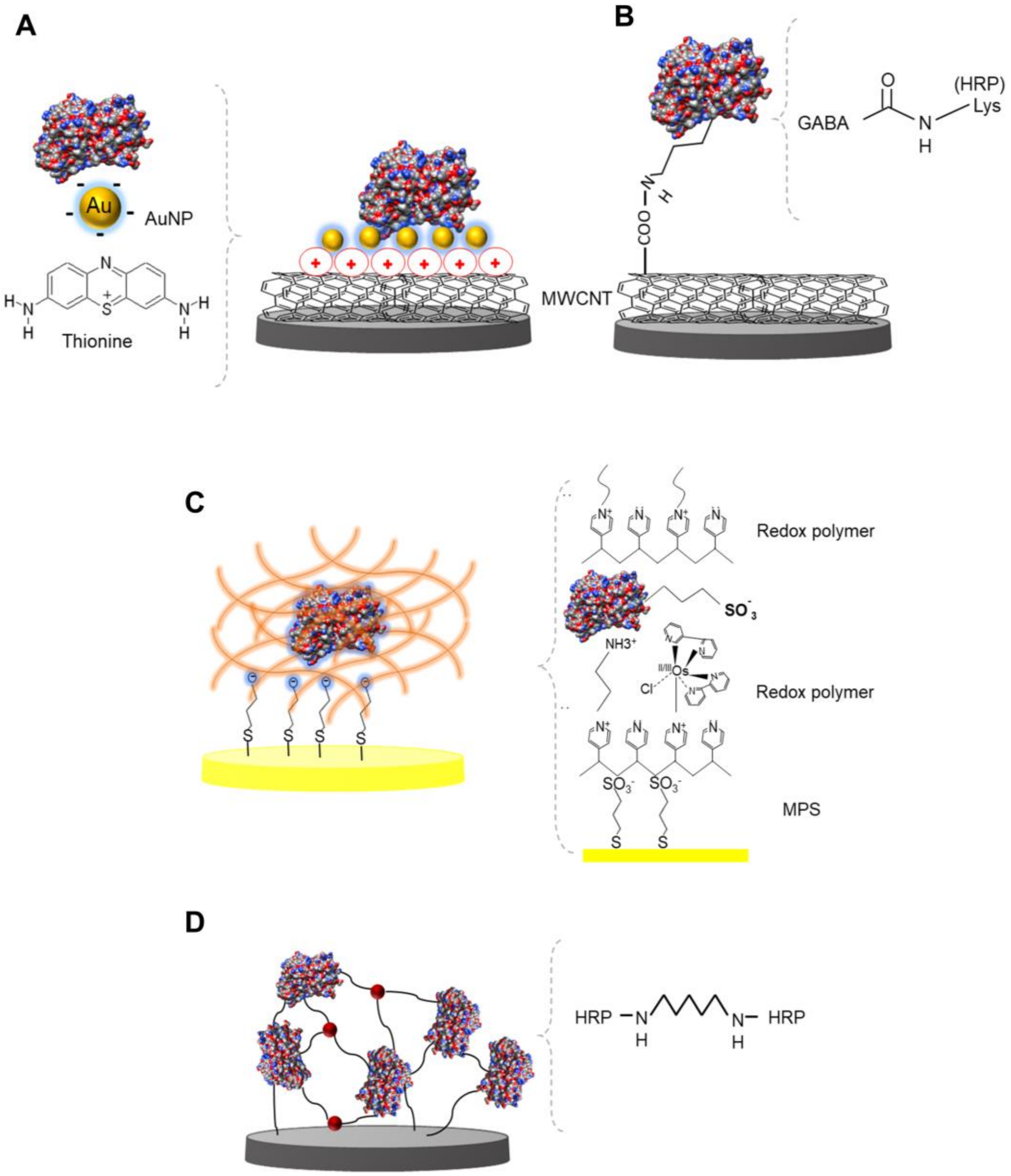

Figure 1.12 - Enzyme immobilization methods. (**A**) Adsorption onto a multi-walled carbon nanotubes (MWCNTs)/thionine/Au nanoparticles (NPs) composite film on glassy carbon (GC) [134]; (**B**) covalent binding onto functionalized MWCNTs deposited on GC [160]; (**C**) entrapment of chemically modified enzyme within a positively charged redox hydrogel deposited on Au coated with a negatively charged SAM [161]; (**D**) glutaraldehyde cross-linking of enzyme and bovine serum albumin (BSA) on a silica-dextran nanocomposite sol-gel deposited on GC [162]. HRP - horseradish peroxidase. HRP structure - image generated using Chimera X.

There is a continuous research effort dedicated to parallel investigations of (i) novel immobilization materials and matrices, including biocompatible coatings, (ii) methodologies for sensitive monitoring of the immobilization process at different levels (e.g. solid support, coating, enzyme orientation, enzyme structure) and (iii) design of robust biocatalysts.

1.4.1. Nanomaterials and coatings for surface modification in third-generation biosensors

Nanostructure development and applications represent a part of many fields of fundamental and applied science, and we will only mention those relevant to the work described in this thesis. In the development of biosensors, the use of different nanostructures, such as NP, nanotubes, nanowires or nanorods, that are commonly deposited on the electrode surface has significantly contributed to the improvement and creation of new electrode interfaces. Moreover, their use usually results in a biodevice with increased enzyme surface coverage compared with non-modified surfaces [88,91,93,108]. This usually leads to an improved overall electrochemical analytical performance of the modified biosensor [88,91,93,108]. Moreover, some nanostructures offer the added advantage of allowing for the coupling of electrochemistry with spectroscopy, which can provide valuable information about the structure of the adsorbed biocatalyst on the electrode surface [1,163].

Noble metal nanostructures have unique optical properties, including the capacity to create localized plasmon resonances upon illumination. These nanostructures allow us to study biocatalysts adsorbed on the electrode surface by surface-enhanced (SE) spectroscopies [1,163]. The most commonly used bulk surfaces are silver (Ag) and gold (Au), whose specific plasmonic properties can be created by electrochemical roughening or electrodeposition [1,163]. These surfaces can simultaneously work as electrodes and provide SE effect of the spectroscopic signal of the attached species. For protein immobilization, the metal surface needs to be biocompatible which can be achieved by coating it with, e.g., alkanethiol SAMs (Figure 1.13) [1,163]. This has been one of the most common strategies for modification of Au, Ag or platinum surfaces [93,108], since the thiol group of the alkanethiols has a high affinity for metals, which will ensure covalent binding, while the head group (carrying e.g., thiols, disulphides, amines, acids or silanes) promotes the anchoring of the enzyme to the modified electrode [1,163]. Modifying metallic surfaces with SAMs has made an important contribution to the direct electrochemistry of enzymes. This results mainly from the optimization of DET routes by making the enzyme adopt a favorable and uniform orientation and adjusting the distance between the enzyme and the electrode [93,108], by selecting the length of the spacer group (Figure 1.13). The properties of the modified surface can be tailored to match the enzyme surface charge distribution by employing the head groups of different SAMs. The enzymes can be bound to the modified metal surfaces by adsorption based on weak non-specific forces or covalently [93,108]. The latter ensures a robust enzyme immobilization but may result in altered native conformation. On the other hand, attachment of the biocatalyst through weak forces is less likely to lead to structural disruption of the immobilized enzyme [93,108].

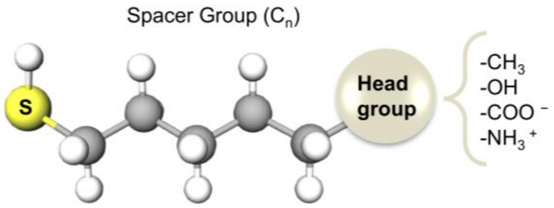

Figure 1.13 - Schematic representation of a metal surface covered with SAMs. The number (n) of CH_2 in the spacer group can vary most commonly between 2 and 16.

Despite the above-mentioned advantages of metal nanostructures, carbon-based nanostructures are more frequently chosen for electrode modification due to their large surface area, chemical inertness, and electrical conductivity [108,164,165]. Modification of the electrode with carbon-based nanoparticles increases the surface area for enzyme loading, and due to their high conductivity, facilitates the DET between the enzyme and the electrode surface [108,164,165].

1.4.2. Characterization of biosensor surface morphology

Characterization of the electrode's surface morphology can provide important information related to the homogeneity and reproducibility of the method used for surface modification. The most widely used techniques are atomic force and scanning electron microscopies (AFM and SEM, respectively) that provide information on enzyme distribution on the electrode and the homogeneity of the films [165–167]. Additionally, surface-enhanced Raman (SER) spectroscopy can be used to identify functional groups present on the surface [167–169].

1.4.3. Structural characterization of immobilized heme enzymes

Electrochemical biosensors are in the majority of cases constructed by a trial-and-error strategy that is based on probing different parameters to find the best combination of electrode support, immobilization method, and enzyme. In this manner, the performance of the biodevice is assessed using typically either voltammetry or chronoamperometry, that reveal which construct shows the best bioelectrochemical response [93]. This strategy is hereinafter called the **empirical approach**. These methods allow for the *in situ* monitoring of the redox process occurring at the electrode surface, as well as the electrochemical system responsiveness and reaction reversibility [30,93,94]. However, using only electrochemical methods for the biosensor characterization does not provide a complete picture of the enzyme-electrode interface since no structural information about the immobilized enzyme can be obtained. Moreover, because the structural features of the immobilized enzyme influence the analytical and kinetic performance of the biosensor, it is crucial to gain information about enzyme loading, structure of the electroactive species and conformation in the immobilized state, which can be achieved by coupling spectroscopy with electrochemistry. This strategy, which is hereinafter referred to as the **rational design approach**, is the main tool of choice in the work presented in this thesis and will be explained in more detail below.

1.4.3.1. Rational design approaches - structural and redox properties of the immobilized enzyme

Spectroscopic techniques can reveal insights into the enzyme-electrode interface at a molecular level. For heme enzymes, usually UV-Vis absorption, resonance Raman (RR) and Surface-enhanced RR (SERR) spectroscopies are used to probe the heme active site [167], while circular dichroism (CD) and Fourier-transform infrared spectroscopies give information about the enzyme secondary structure upon immobilization [170]. A transparent electrode needs to be used for CD and UV-vis absorption, which limits the choice of the electrode material. Among the above listed techniques, SERR spectroelectrochemistry, which couples electrochemistry with SERR spectroscopy, is the only experimental approach that allows for the simultaneous structural characterization and $E^{0'}$ determination of the immobilized heme enzyme *in situ* [1]. The requirement of a plasmonic electrode surface limits the application of SERR spectroscopy of heme enzymes to nanostructured Ag electrodes [1] since this technique combines the SE effect with the RR spectroscopy. The latter is a powerful tool to probe the structure of heme enzymes [1,8]. The RR spectra obtained by excitation in resonance with the Soret band of the heme display core-size marker bands (ν_4, ν_3, ν_2, ν_{10}), with their frequencies being indicative of the redox, spin and coordination state of the heme, Figure 1.4 [1,8]. SERR spectroscopy selectively enhances the RR signal of the heme-containing enzyme (Figure 1.14) attached in close proximity of the plasmonic Ag surface, making this technique extremely sensitive [1]. Comparison of the RR spectra of the enzyme in solution with the SERR spectra of the immobilized enzyme provides information about the possible effects of the immobilization on the structural features of the heme group [171,172]. In this manner, we can disclose fine details of eventual active site alterations upon immobilization, which can influence the catalytic and thermodynamic properties of immobilized heme proteins [171–173]. Simultaneously, the catalytic performance of the immobilized enzyme can be monitored by electrochemistry since the SERR active substrate simultaneously acts as an electrode. SERR spectroelectrochemistry has been used to study membrane proteins in a physiological-like environment, e.g., oxygen and nitrite reductases, among many others [174-176]. Moreover, it has been applied to evaluate the potential of several heme enzymes for the development of biotechnological applications that rely on immobilized biocatalysts such as cytochrome P450 (P450), microperoxidases, and more recently, DyPs [85,172,177-178].

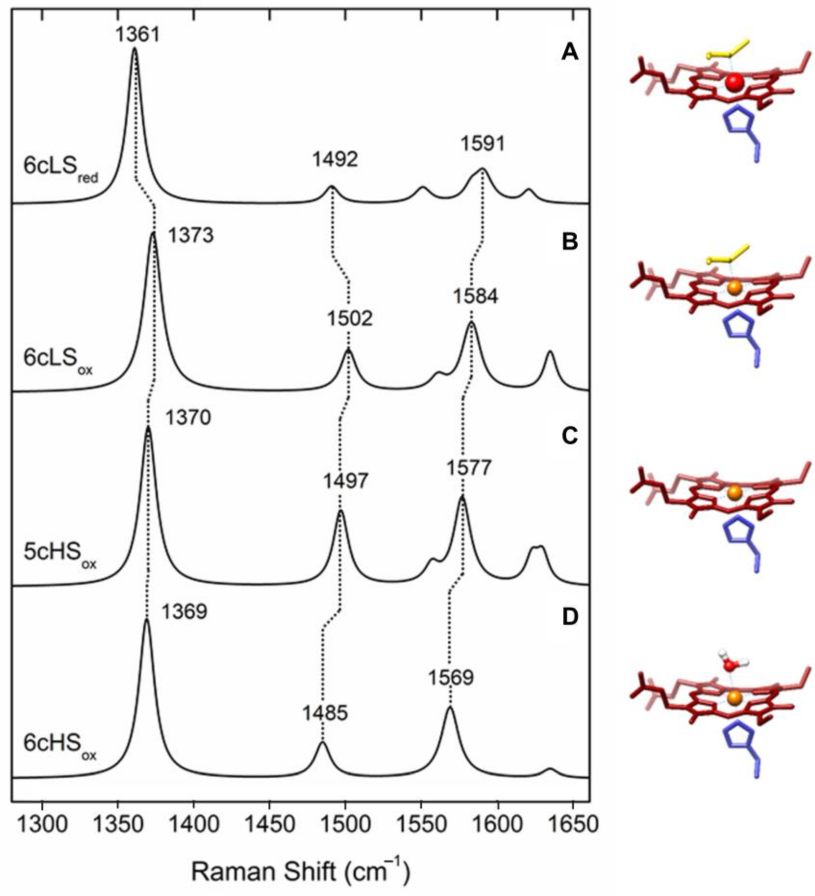

Figure 1.14 - Resonance Raman (RR) spectra of cytochrome *c* in different oxidation, spin, and coordination states with depicted marker bands (black trace line), left, and corresponding heme configurations, right. (**A**) Ferrous (Fe(II)) heme in 6cLS state, coordinated by distal Met and proximal His. (**B**) Ferric (Fe(III)) heme in 6cLS state, coordinated by distal Met and proximal His. (**C**) Ferric heme in a 5cHS state, coordinated by proximal His and vacant 6th axial position. (**D**) Ferric heme in 6cHS state, coordinated by a distal water molecule and proximal His.

1.5. Biosensor Performance

Enzyme-based amperometric biosensors are devices that detect the target analyte, typically the enzyme's substrate, by measuring the current generated by the oxidation or reduction of the enzyme, which allows the detection and quantification of the analyte present in the sample. To fully evaluate the biodevice, it is necessary to understand the analytical and kinetic parameters that influence its performance. The most commonly used methods for obtaining these parameters and measuring the electrochemical response of the immobilized enzyme are chronoamperometry (cAmp) or potential scanning techniques, such as cyclic, differential pulse and square-wave voltammetry.

In *chronoamperometric detection*, the electrode is poised at a fixed potential (the working potential of the biosensor), and the current observed upon injection of the analyte is monitored over time. The current change is proportional to the analyte concentration in the solution. This technique is the most used in practical applications due to its simplicity, low background signals and detection limits [93]. In *voltammetric detection*, the potential is scanned over a specific range while the current obtained upon injection of the analyte is measured as a function of the applied potential. Usually, the catalytic current response is a peak or a plateau that is proportional to the concentration of the analyte [93,105,179]. The cyclic voltammetry (CV), in particular, is very useful in the development stage of the biosensors, due to its simplicity and well-known theoretical framework [93,105,179]. Furthermore, if enzyme DET response (cf. Chapter 1.3.1.) is observed in the absence of analyte, i.e., the non-catalytic signal can be measured, the $E^{0'}$ of the immobilized enzyme ($E^{0'}_{imm}$) can be determined by CV [105,180]. Note that the $E^{0'}_{imm}$ could differ from the $E^{0'}$ of the enzyme in solution ($E^{0'}_{sol}$), which may suggest that the electrocatalytic response can be due to possibly denatured enzyme species. The comparison of the $E^{0'}_{imm}$ with the $E^{0'}_{sol}$ is a reliable indicator of immobilization-induced alteration of the enzyme. Nonetheless, spectroscopy/structural characterization of the immobilized enzyme (cf. section 1.4.3.1) allows for an accurate identification of non-native states.

The *kinetic parameters* of the biosensor can be estimated if the enzyme reaction at the electrode surface follows a Michaelis-Menten-type kinetic behavior [93,105,179,181]. In this case, the catalytic currents are fitted by a modified Michaelis-Menten equation (Equation 1.5):

$$I_{cat}=\frac{I_{max}\times[S]}{K_M^{app}+[S]} \qquad (1.5)$$

I_{cat} is the catalytic current, I_{max} is the maximum I_{cat} observed at enzyme saturating conditions, [S] is the target analyte concentration, and K_M^{app} is the apparent Michaelis-Menten constant. The value of K_M^{app} can be determined by taking the concentration value corresponding to half of the maximum current. A low K_M^{app} value indicates a high affinity between the enzyme and the analyte, leading to a higher reaction rate, while a high K_M^{app} value can indicate a lower affinity for the substrate and/or that there is a significant analyte diffusion barrier between the electrode and the enzyme [93,105,179,181]. This can be caused by restricted access of the analyte to the active site of the enzyme due to the low permeability of the biosensor film and/or unfavorable orientation of the enzyme on the electrode surface. Additionally, the eventual immobilization-induced conformation changes can decrease the enzyme affinity towards the substrate (increasing K_M^{app}) or cause partial or total inactivation (decreased I_{max}) [93,105,179,181].

The performance of the biosensor is evaluated by a series of analytical parameters: sensitivity, linear concentration range, the limit of detection (LOD), reproducibility, selectivity/response to interferences, stability and response time [182].

The slope of the calibration curve ($\Delta I_{cat}/\Delta[S]$) at first-order kinetics represents the *sensitivity* of the biosensor, expressed in $A \cdot M^{-1}$ or $A \cdot M^{-1} \cdot cm^{-2}$ [182]. This is the most common parameter to evaluate and compare performances of different biosensors.

The *linear range* is the range of analyte concentrations in which the biosensor shows a linear response. This parameter corresponds to the concentration values (maximum and minimum) used to calculate the calibration curve. Ideally, a biosensor should have a wide linear working range to avoid sample dilution or pre-concentration steps [182].

The *limit of detection* (LOD) is defined as the minimum analyte concentration detected but not necessarily quantified by the biosensor. According to IUPAC, the LOD of an analytical method is related to the background signal and its fluctuation [183]. For biosensors, it is estimated from the calibration of curve typically as the analyte concentration, at a signal-to-noise ratio of 3 [182].

Reproducibility is related to the ability of a biosensor to generate the same response in repeated experiments. Commonly, it is estimated as the relative standard deviation (RSD) of the current response at a specific analyte concentration (in the linear range) or the sensitivity of multiple biosensor preparations [182].

Selectivity is correlated with the biosensor's ability to identify the target analyte in a complex sample. It is usually expressed as the percentage of response variation upon adding potential interfering species to the solution [182].

Response time is the time the biosensor takes to reach 95% of the maximum current signal after adding the analyte to the solution. This parameter depends on the diffusion rates of the compounds involved in the detection reaction (either the analyte, product or redox mediators), and can be affected by the speed at which the solution is homogenized. The response time is usually proportional to the turnover rate of the enzyme, meaning that a fast turnover results in short response times [182].

The *stability* can be estimated from activity measurements for one analyte concentration or by the sensitivity of different biosensors over time, compared with the initial value. The stability of the biosensor is usually evaluated in terms of operation lifetime (repeated measurements using the same electrode) and storage stability or shelf-life (analysis of electrode batches at different times) [182].

In this work, in the search for the most promising construct for the development of a H_2O_2 *biosensor, we aim to identify the best DyP to act as an immobilized biocatalyst in a third-generation configuration, which will be revealed by analysis of the structural features of the immobilized enzyme and the analytical parameters of the produced biodevice.*

1.6. Aim and outline of the thesis

This thesis focuses on constructing third-generation amperometric devices for H_2O_2 detection using bacterial DyP as the immobilized biocatalyst. It contains five chapters, organized as a pipeline of requirements that must be fulfilled for a successful rational design of biosensors. **Chapter 1** explains the general concepts needed for the understanding of this thesis, including the importance of developing H_2O_2 biosensors, enzyme immobilization, and methodological approaches used in this work.

Chapter 2 explores recombinant DyPs from different bacterial organisms: *S. coelicolor* (ScoDyP), *T. fusca* (TfuDyP), *C. bogoriensis* (CboDyP), *S. viridis* (SviDyP), *E. coli* (Yfex), *T. cellulosilytica* (TceDyP), and *P. putida* (PpDyP). Here, we describe their structural and redox properties in **solution**, and several variants designed for improved catalysis. This chapter highlights SviDyP, ScoDyP, CboDyP, PpDyP, the distal CboDyP, and PpDyP (R214W), as well as the *in silico* designed PpDyP variants, as the most promising candidates to be used for further studies.

In **Chapter 3**, we explore different **immobilization strategies** for constructing third-generation H_2O_2 biosensors. Using the *rational design approach*, the immobilized enzymes are characterized by SERR spectroscopy and electrochemistry, elucidating the fine details about the enzyme's structural and electrochemical properties upon attachment to the electrode support. Simultaneously, an *empirical approach* is explored in which the DyP-based biodevice was characterized using only electrochemical methods. We conclude Chapter 3 by selecting the biodevices based on PpDyP *in silico* variants, designed using the *rational approach* for further studies. These devices presented improved analytical parameters in comparison to so far reported HRP-based devices and the devices constructed following the *empirical approach.*

Chapter 4 describes the development of a **miniaturized**, disposable, and user-friendly third-generation electrochemical biosensor for H_2O_2 detection in air-exposed samples using modified screen-printed electrodes (SPE). It brings together the results from Chapters 2 and 3 in terms of the choice of the biocatalyst and the immobilization strategy. It results from transposing our approach employed in Chapter 3 in a laboratory set-up to modified commercially available SPEs. The developed biosensor is based on DyP immobilized on nanostructure-modified SPEs. We show that it has improved performance compared to other miniaturized HRP/SPE-based biosensors reported in the literature, with the added advantage of operating in air-exposed samples.

Chapter 5 comprises the overall conclusion of this thesis and the possible future perspectives. In this chapter, a flowchart highlighting the main conclusions of each milestone achieved through this thesis is presented (Thesis work flowchart). Overall, the developed biosensor using PpDyP that has been characterized by a *rational design* showed improved performance compared to HRP-based biosensors reported in the literature either in the laboratory setup (Chapter 3) or miniaturized setup (Chapter 4). We are confident that the development of DyP-based biosensors will likely increase in the future because these bacterial enzymes lack glycosylation and can easily be genetically modified to attain variant forms with improved catalytic and stability properties for the envisioned applications.

1.7. References

[1] F. Siebert, P. Hildebrandt, Vibrational Spectroscopy in Life Science, Wiley, 2007. https://doi.org/10.1002/9783527621347.

[2] T.L. Poulos, Heme Enzyme Structure and Function, Chem Rev 114 (2014) 3919–3962. https://doi.org/10.1021/cr400415k.

[3] T.G. Spiro, A.A. Jarzecki, Heme-Based Sensors: Theoretical Modeling of Heme-Ligand–Protein Interactions, Curr Opin Chem Biol 5 (2001) 715–723. https://doi.org/10.1016/S1367-5931(01)00271-X.

[4] E. Raven, B. Dunford, Heme Peroxidases, The Royal Society of Chemistry ebook, 2016. https://doi.org/10.1039/9781782622628.

[5] G. Smulevich, A. Feis, B.D. Howes, A. Ivancich, Structure-Function Relationships Among Heme Peroxidases: New Insights from Electronic Absorption, Resonance Raman and Multifrequency Electron Paramagnetic Resonance Spectroscopies, In: Handbook of Porphyrin Science, 2010: pp. 367–453. https://doi.org/10.1142/9789814307246_0003.

[6] E. Torres, M. Ayala, Biocatalysis Based on Heme Peroxidases, Springer (2010) 1–358. https://doi.org/10.1007/978-3-642-12627-7.

[7] B. Bhaskar, L. Lad, T.L. Poulos, Iron: Heme Proteins, Peroxidases, Catalases &; Catalase-Peroxidases, Based in part on the article Iron: Heme Proteins, Peroxidases, & Catalases by Ann M. English which appeared in the *Encyclopedia of Inorganic Chemistry, First Edition* ., In: Encyclopedia of Inorganic Chemistry, Wiley, 2005. https://doi.org/10.1002/0470862106.ia106.

[8] G. Smulevich, A. Feis, B.D. Howes, Fifteen Years of Raman Spectroscopy of Engineered Heme Containing Peroxidases: What Have We Learned?, Acc Chem Res 38 (2005) 433–440. https://doi.org/10.1021/ar020112q.

[9] G. Battistuzzi, M. Bellei, C.A. Bortolotti, M. Sola, Redox Properties of Heme Peroxidases, Arch Biochem Biophys 500 (2010) 21–36. https://doi.org/10.1016/j.abb.2010.03.002.

[10] P. Jones, H.B. Dunford, The Mechanism of Compound I Formation Revisited, J Inorg Biochem 99 (2005) 2292–2298. https://doi.org/10.1016/j.jinorgbio.2005.08.009.

[11] E.E. Ferapontova, Direct Peroxidase Bioelectrocatalysis on A Variety of Electrode Materials, Electroanalysis 16 (2004) 1101–1112. https://doi.org/10.1002/elan.200403003.

[12] A.G. Mauk, G.R. Moore, Control of Metalloprotein Redox Potentials: What Does Site-Directed Mutagenesis of Hemoproteins Tell Us?, J Biol Inorg Chem 2 (1997) 119–125. https://doi.org/10.1007/s007750050115.

[13] M. Ayala, R. Roman, R. Vazquez-Duhalt, A Catalytic Approach to Estimate the Redox Potential of Heme-Peroxidases, Biochem Biophys Res Commun 357 (2007) 804–808. https://doi.org/10.1016/j.bbrc.2007.04.020.

[14] M.S. Mondal, H.A. Fuller, F.A. Armstrong, Direct Measurement of the Reduction Potential of Catalytically Active Cytochrome *c* Peroxidase Compound I: Voltammetric Detection of a Reversible, Cooperative Two-Electron Transfer Reaction, J Am Chem Soc 118 (1996) 263–264. https://doi.org/10.1021/ja952489f.

[15] M. Tanaka, K. Ishimori, I. Morishima, Luminol Activity of Horseradish Peroxidase Mutants Mimicking a Proposed Binding Site for Luminol in *Arthromyces ramosus* Peroxidase, Biochem 38 (1999) 10463–10473. https://doi.org/10.1021/bi9907328.

[16] M. Torimura, M. Mochizuki, K. Kano, T. Ikeda, T. Ueda, Mediator-Assisted Continuous-Flow Column Electrolytic Spectroelectrochemical Technique for the Measurement of Protein Redox Potentials. Application to Peroxidase, Anal Chem 70 (1998) 4690–4695. https://doi.org/10.1021/ac980621z.

[17] Y. Hayashi, I. Yamazaki, The Oxidation-Reduction Potentials of Compound I/Compound II and Compound II/Ferric Couples of Horseradish Peroxidases A_2 and C., J Biol Chem 254 (1979) 9101–9106. https://doi.org/10.1016/S0021-9258(19)86816-3.

[18] K. Ambert-Balay, M. Dougherty, M. Tien, Reactivity of Manganese Peroxidase: Site-Directed Mutagenesis of Residues in Proximity to the Porphyrin Ring, Arch Biochem Biophys 382 (2000) 89–94. https://doi.org/10.1006/abbi.2000.2000.

[19] Z.S. Farhangrazi, B.R. Copeland, T. Nakayama, T. Amachi, I. Yamazaki, L.S. Powers, Oxidation-Reduction Properties of Compounds I and II of *Arthromyces ramosus* Peroxidase, Biochem 33 (1994) 5647–5652. https://doi.org/10.1021/bi00184a038.

[20] I. Efimov, N.D. Papadopoulou, K.J. McLean, S.K. Badyal, I.K. Macdonald, A.W. Munro, P.C.E. Moody, E.L. Raven, The Redox Properties of Ascorbate Peroxidase, Biochem 46 (2007) 8017–8023. https://doi.org/10.1021/bi7006492.

[21] M.S. Mondal, D.B. Goodin, F.A. Armstrong, Simultaneous Voltammetric Comparisons of Reduction Potentials, Reactivities, and Stabilities of the High-Potential Catalytic States of Wild-Type and Distal-Pocket Mutant (W51F) Yeast Cytochrome *c* Peroxidase, J Am Chem Soc 120 (1998) 6270–6276. https://doi.org/10.1021/ja980197j.

[22] A.W. Bott, Redox Properties of Electron Transfer Metalloproteins, Curr Sep 18 (1999) 47–54.

[23] C. Olea, J. Kuriyan, M.A. Marletta, Modulating Heme Redox Potential through Protein-Induced Porphyrin Distortion, J Am Chem Soc 132 (2010) 12794–12795. https://doi.org/10.1021/ja106252b.

[24] M. Paoli, J. Marles-Wright, A. Smith, Structure–Function Relationships in Heme-Proteins, DNA Cell Biol 21 (2002) 271–280. https://doi.org/10.1089/104454902753759690.

[25] J. Mao, K. Hauser, M.R. Gunner, How Cytochromes with Different Folds Control Heme Redox Potentials, Biochem 42 (2003) 9829–9840. https://doi.org/10.1021/bi027288k.

[26] N.C. Veitch, Structural Determinants of Plant Peroxidase Function, Phytochem Rev 3 (2004) 3–18. https://doi.org/10.1023/B:PHYT.0000047799.17604.94.

[27] K. Sellami, A. Couvert, N. Nasrallah, R. Maachi, M. Abouseoud, A. Amrane, Peroxidase Enzymes as Green Catalysts for Bioremediation and Biotechnological Applications: A Review, Sci Total Environ 806 (2022) 150500. https://doi.org/10.1016/j.scitotenv.2021.150500.

[28] M. Hamid, Khalil-ur-Rehman, Potential Applications of Peroxidases, Food Chem 115 (2009) 1177–1186. https://doi.org/10.1016/j.foodchem.2009.02.035.

[29] B. Neumann, U. Wollenberger, Electrochemical Biosensors Employing Natural and Artificial Heme Peroxidases on Semiconductors, Sens 20 (2020) 3692. https://doi.org/10.3390/s20133692.

[30] A. Navaee, A. Salimi, Enzyme-Based Electrochemical Biosensors. In: Electrochemical Biosensors, Elsevier, 2019: pp. 167–211. https://doi.org/10.1016/B978-0-12-816491-4.00007-3.

[31] Y. Sugano, Dyp-Type Peroxidases Comprise a Novel Heme Peroxidase Family, Cell Mol Life Sci 66 (2009) 1387–1403. https://doi.org/10.1007/s00018-008-8651-8.

[32] T. Yoshida, Y. Sugano, Unexpected Diversity of Dye-Decolorizing Peroxidases, Biochem Biophys Rep 33 (2023) 101401. https://doi.org/10.1016/j.bbrep.2022.101401.

[33] T. Yoshida, Y. Sugano, A Structural and Functional Perspective of Dyp-Type Peroxidase Family, Arch Biochem Biophys 574 (2015) 49–55. https://doi.org/10.1016/j.abb.2015.01.022.

[34] Y. Sugano, R. Muramatsu, A. Ichiyanagi, T. Sato, M. Shoda, Dyp, a Unique Dye-Decolorizing Peroxidase, Represents a Novel Heme Peroxidase Family: ASP171 Replaces the Distal Histidine of Classical Peroxidases, J Biol Chem 282 (2007) 36652–36658. https://doi.org/10.1074/jbc.M706996200.

[35] D.I. Colpa, M.W. Fraaije, E. van Bloois, Dyp-Type Peroxidases: a Promising and Versatile Class Of Enzymes, J. Ind. Microbiol. Biotechnol. 41 (2014) 1–7. https://doi.org/10.1007/s10295-013-1371-6.

[36] S.J. Kim, M. Shoda, Purification and Characterization of a Novel Peroxidase from *Geotrichum candidum* Dec 1 Involved in Decolorization of Dyes, Appl Environ Microbiol 65 (1999) 1029–1035. https://doi.org/10.1128/AEM.65.3.1029-1035.1999.

[37] Y. Sugano, K. Sasaki, M. Shoda, cDNA Cloning and Genetic Analysis of a Novel Decolorizing Enzyme, Peroxidase Gene Dyp from *Geotrichum candidum* Dec 1, J Biosci Bioeng 87 (1999) 411–417. https://doi.org/10.1016/S1389-1723(99)80087-5.

[38] M.L.C. Petrus, E. Vijgenboom, A.K. Chaplin, J.A.R. Worrall, G.P. van Wezel, D. Claessen, The Dyp-Type Peroxidase Dtpa is a Tat-Substrate Required for Glxa Maturation and Morphogenesis in *Streptomyces*, Open Biol 6 (2016) 150149. https://doi.org/10.1098/rsob.150149.

[39] K.A. Lien, K. Dinshaw, R.J. Nichols, C. Cassidy-Amstutz, M. Knight, R. Singh, L.D. Eltis, D.F. Savage, S.A. Stanley, A Nanocompartment System Contributes to Defense Against Oxidative Stress in *Mycobacterium tuberculosis*, Elife 10 (2021) e74358. https://doi.org/10.7554/eLife.74358.

[40] K. Sugawara, E. Igeta, Y. Amano, M. Hyuga, Y. Sugano, Degradation of Antifungal Anthraquinone Compounds is a Probable Physiological Role of Dyp Secreted by *Bjerkandera adusta*, AMB Express 9 (2019) 56. https://doi.org/10.1186/s13568-019-0779-4.

[41] A. Kaur, P.T. Van, C.R. Busch, C.K. Robinson, M. Pan, W.L. Pang, D.J. Reiss, J. DiRuggiero, N.S. Baliga, Coordination of Frontline Defense Mechanisms Under Severe Oxidative Stress, Mol Syst Biol 6 (2010) 393. https://doi.org/10.1038/msb.2010.50.

[42] C. Liers, M.J. Pecyna, H. Kellner, A. Worrich, H. Zorn, K.T. Steffen, M. Hofrichter, R. Ullrich, Substrate Oxidation by Dye-Decolorizing Peroxidases (Dyps) from Wood- and Litter-Degrading Agaricomycetes Compared to Other Fungal and Plant Heme-Peroxidases, Appl Microbiol Biotechnol 97 (2013) 5839–5849. https://doi.org/10.1007/s00253-012-4521-2.

[43] K.M. DeAngelis, D. Sharma, R. Varney, B. Simmons, N.G. Isern, L.M. Markilllie, C. Nicora, A.D. Norbeck, R.C. Taylor, J.T. Aldrich, E.W. Robinson, Evidence Supporting Dissimilatory and Assimilatory Lignin Degradation in *Enterobacter lignolyticus* SCF1, Front Microbiol 4 (2013) 280. https://doi.org/10.3389/fmicb.2013.00280.

[44] D. Silva, C.F. Rodrigues, C. Lorena, P.T. Borges, L.O. Martins, Biocatalysis for Biorefineries: the Case of Dye-Decolorizing Peroxidases, Biotechnol Adv 65 (2023). https://doi.org/10.1016/j.biotechadv.2023.108153.

[45] C.F. Rodrigues, P.T. Borges, M.F. Scocozza, D. Silva, A. Taborda, V. Brissos, C. Frazão, L.O. Martins, Loops Around the Heme Pocket Have a Critical Role in the Function and Stability of BsDyP from *Bacillus subtilis*, Int J Mol Sci 22 (2021) 10862. https://doi.org/10.3390/ijms221910862.

[46] J. Li, C. Liu, B. Li, H. Yuan, J. Yang, B. Zheng, Identification and Molecular Characterization of a Novel DyP-Type Peroxidase from *Pseudomonas aeruginosa* PKE117, Appl Biochem Biotechnol 166 (2012) 774–785. https://doi.org/10.1007/s12010-011-9466-x.

[47] X. Liu, Q. Du, Z. Wang, D. Zhu, Y. Huang, N. Li, T. Wei, S. Xu, L. Gu, Crystal Structure and Biochemical Features of EfeB/YcdB from Escherichia coli O157, J Biol Chem 286 (2011) 14922–14931. https://doi.org/10.1074/jbc.M110.197780.

[48] T. Johjima, M. Ohkuma, T. Kudo, Isolation and cDNA Cloning of Novel Hydrogen Peroxide-Dependent Phenol Oxidase from the Basidiomycete *Termitomyces albuminosus*, Appl Microbiol Biotechnol 61 (2003) 220–225. https://doi.org/10.1007/s00253-003-1236-4.

[49] U.A. Zitare, M.H. Habib, H. Rozeboom, M.L. Mascotti, S. Todorovic, M.W. Fraaije, Mutational and Structural Analysis of an Ancestral Fungal Dye-Decolorizing Peroxidase, FEBS Journal 288 (2021) 3602–3618. https://doi.org/10.1111/febs.15687.

[50] T. Uchida, M. Sasaki, Y. Tanaka, K. Ishimori, A Dye-Decolorizing Peroxidase from *Vibrio cholerae*, Biochem 54 (2015) 6610–6621. https://doi.org/10.1021/acs.biochem.5b00952.

[51] C.M. Silveira, E. Moe, M. Fraaije, L.O. Martins, S. Todorovic, Resonance Raman View of the Active Site Architecture in Bacterial Dyp-Type Peroxidases, RSC Adv 10 (2020) 11095–11104. https://doi.org/10.1039/D0RA00950D.

[52] S. Todorovic, P. Hildebrandt, L.O. Martins, Surface Enhanced Resonance Raman Detection of a Catalytic Intermediate of Dyp-Type Peroxidase, Phys. Chem. Chem. Phys. 17 (2015) 11954–11957. https://doi.org/10.1039/c5cp01283j.

[53] M. Lučić, M.T. Wilson, T. Tosha, H. Sugimoto, A. Shilova, D. Axford, R.L. Owen, M.A. Hough, J.A.R. Worrall, Serial Femtosecond Crystallography Reveals the Role of Water in the One- or Two-Electron Redox Chemistry of Compound I in the Catalytic Cycle of the B-Type Dye-Decolorizing Peroxidase DtpB, ACS Catal 12 (2022) 13349–13359. https://doi.org/10.1021/acscatal.2c03754.

[54] Y. Sugano, Y. Matsushima, K. Tsuchiya, H. Aoki, M. Hirai, M. Shoda, Degradation Pathway of an Anthraquinone Dye Catalyzed by a Unique Peroxidase Dyp from *Thanatephorus cucumeris* Dec 1, Biodegradation 20 (2009) 433–440. https://doi.org/10.1007/s10532-008-9234-y.

[55] S. Mendes, T. Catarino, C. Silveira, S. Todorovic, L.O. Martins, The Catalytic Mechanism of A-Type Dye-Decolourising Peroxidase BsDyp: Neither Aspartate nor Arginine is Individually Essential for Peroxidase Activity, Catal Sci Technol 5 (2015) 5196–5207. https://doi.org/10.1039/C5CY00478K.

[56] S. Mendes, V. Brissos, A. Gabriel, T. Catarino, D.L. Turner, S. Todorovic, L.O. Martins, An Integrated View of Redox and Catalytic Properties of B-type PpDyP from *Pseudomonas putida* MET94 and its Distal Variants, Arch. Biochem. Biophy. 574 (2015) 99–107. https://doi.org/10.1016/j.abb.2015.03.009.

[57] R. Singh, J.C. Grigg, Z. Armstrong, M.E.P. Murphy, L.D. Eltis, Distal Heme Pocket Residues of B-Type Dye-Decolorizing Peroxidase: Arginine but not Aspartate is Essential for Peroxidase Activity, Journal of Biological Chemistry 287 (2012) 10623–10630. https://doi.org/10.1074/jbc.M111.332171.

[58] M. Lučić, M.T. Wilson, D.A. Svistunenko, R.L. Owen, M.A. Hough, J.A.R. Worrall, Aspartate or Arginine? Validated Redox State X-ray Structures Elucidate Mechanistic Subtleties of $Fe^{IV} = O$ Formation in Bacterial Dye-Decolorizing Peroxidases, J Biol Inorg Chem 26 (2021) 743–761. https://doi.org/10.1007/s00775-021-01896-2.

[59] M. Lučić, D.A. Svistunenko, M.T. Wilson, A.K. Chaplin, B. Davy, A. Ebrahim, D. Axford, T. Tosha, H. Sugimoto, S. Owada, F.S.N. Dworkowski, I. Tews, R.L. Owen, M.A. Hough, J.A.R. Worrall, Serial Femtosecond Zero Dose Crystallography Captures a Water-Free Distal Heme Site in a Dye-Decolorising Peroxidase to Reveal a Catalytic Role for an Arginine in $Fe^{IV}=O$ Formation, Angew Chem, Int 59 (2020) 21656–21662. https://doi.org/10.1002/anie.202008622.

[60] R. Singh, L.D. Eltis, The Multihued Palette of Dye-Decolorizing Peroxidases, Arch Biochem Biophys 574 (2015) 56–65. https://doi.org/10.1016/j.abb.2015.01.014.

[61] N. Lončar, D.I. Colpa, M.W. Fraaije, Exploring the Biocatalytic Potential of a DyP-Type Peroxidase by Profiling the Substrate Acceptance of *Thermobifida fusca* DyP Peroxidase, Tetrahedron (2016). https://doi.org/10.1016/j.tet.2015.12.078.

[62] M.H. Habib, H.J. Rozeboom, M.W. Fraaije, Characterization of a New DyP-Peroxidase from the Alkaliphilic Cellulomonad, *Cellulomonas bogoriensis*, Molecules 24 (2019) 1208. https://doi.org/10.3390/molecules24071208.

[63] A. Santos, S. Mendes, V. Brissos, L.O. Martins, New Dye-Decolorizing Peroxidases from *Bacillus subtilis* and *Pseudomonas putida* MET94: Towards Biotechnological Applications, Appl. Microbiol. Biotechnol. 98 (2014) 2053–2065. https://doi.org/10.1007/s00253-013-5041-4.

[64] V. Brissos, D. Tavares, A.C. Sousa, M.P. Robalo, L.O. Martins, Engineering a Bacterial DyP-Type Peroxidase for Enhanced Oxidation of Lignin-Related Phenolics at Alkaline pH, ACS Catal. 5 (2017) 3454–3465. https://doi.org/10.1021/acscatal.6b03331.

[65] R. Rahmanpour, T.D.H. Bugg, Characterization of Dyp-Type Peroxidases from *Pseudomonas fluorescens* Pf-5: Oxidation of Mn(II) and Polymeric Lignin by Dyp1B, Arch Biochem Biophys 574 (2015) 93–98. https://doi.org/10.1016/j.abb.2014.12.022.

[66] X. Qin, Y. Xin, X. Su, X. Wang, Y. Wang, J. Zhang, T. Tu, B. Yao, H. Luo, H. Huang, Efficient Degradation of Zearalenone by Dye-Decolorizing Peroxidase from *Streptomyces thermocarboxydus* Combining Catalytic Properties of Manganese Peroxidase and Laccase, Toxins 13 (2021) 602. https://doi.org/10.3390/toxins13090602.

[67] G. Huang, R. Shrestha, K. Jia, B. V. Geisbrecht, P. Li, Enantioselective Synthesis of Dilignol Model Compounds and their Stereodiscrimination Study with a Dye-Decolorizing Peroxidase, Org Lett 19 (2017) 1820–1823. https://doi.org/10.1021/acs.orglett.7b00587.

[68] J.N. Roberts, R. Singh, J.C. Grigg, M.E.P. Murphy, T.D.H. Bugg, L.D. Eltis, Characterization of Dye-Decolorizing Peroxidases from *Rhodococcus jostii* RHA1, Biochem 50 (2011) 5108–5119. https://doi.org/10.1021/bi200427h.

[69] C. Chen, T. Li, Bacterial Dye-Decolorizing Peroxidases: Biochemical Properties and Biotechnological Opportunities, Phys Sci Rev 1 (2016) 1–15. https://doi.org/10.1515/psr-2016-0051.

[70] N.-K. Krahe, R.G. Berger, F. Ersoy, A DyP-Type Peroxidase of *Pleurotus sapidus* with Alkene Cleaving Activity, Molecules 25 (2020) 1536. https://doi.org/10.3390/molecules25071536.

[71] J. Kolwek, C. Behrens, D. Linke, U. Krings, R.G. Berger, Cell-Free One-Pot Conversion of (+)-Valencene to (+)-Nootkatone by a Unique Dye-decolorizing peroxidase combined with a laccase from *Funalia trogii*, J Ind Microbiol Biotechnol 45 (2018) 89–101. https://doi.org/10.1007/s10295-017-1998-9.

[72] D.I. Colpa, N. Lončar, M. Schmidt, M.W. Fraaije, Creating Oxidase–Peroxidase Fusion Enzymes as a Toolbox for Cascade Reactions, ChemBioChem 18 (2017) 2226–2230. https://doi.org/10.1002/cbic.201700478.

[73] R. Singh, J.C. Grigg, W. Qin, J.F. Kadla, M.E.P. Murphy, L.D. Eltis, Improved Manganese-Oxidizing Activity of DypB, a Peroxidase from a Lignolytic Bacterium, ACS Chem Biol 8 (2013) 700–706. https://doi.org/10.1021/cb300608x.

[74] J.R. Cherry, M.H. Lamsa, P. Schneider, J. Vind, A. Svendsen, A. Jones, A.H. Pedersen, Directed Evolution of a Fungal Peroxidase, Nat Biotechnol 17 (1999) 379–384. https://doi.org/10.1038/7939.

[75] H.J.O. Ogola, N. Hashimoto, S. Miyabe, H. Ashida, T. Ishikawa, H. Shibata, Y. Sawa, Enhancement of Hydrogen Peroxide Stability of a Novel Anabaena sp. DyP-Type Peroxidase by Site-Directed Mutagenesis of methionine residues, Appl Microbiol Biotechnol 87 (2010) 1727–1736. https://doi.org/10.1007/s00253-010-2603-6.

[76] D. Linde, M. Cañellas, C. Coscolín, I. Davó-Siguero, A. Romero, F. Lucas, F.J. Ruiz-Dueñas, V. Guallar, A.T. Martínez, Asymmetric sulfoxidation by Engineering the Heme Pocket of a Dye-Decolorizing Peroxidase, Catal Sci Technol 6 (2016) 6277–6285. https://doi.org/10.1039/C6CY00539J.

[77] A.H.A. Alessa, K.L. Tee, D. Gonzalez-Perez, H.E.M. Omar Ali, C.A. Evans, A. Trevaskis, J.-H. Xu, T.S. Wong, Accelerated Directed Evolution of Dye-Decolorizing Peroxidase Using a Bacterial Extracellular Protein Secretion System (BENNY), Bioresour Bioprocess 6 (2019) 20. https://doi.org/10.1186/s40643-019-0255-7.

[78] N.-K. Krahe, R.G. Berger, M. Witt, H. Zorn, A.B. Omarini, F. Ersoy, Monokaryotic *Pleurotus sapidus* Strains with Intraspecific Variability of an Alkene Cleaving DyP-Type Peroxidase Activity as a Result of Gene Mutation and Differential Gene Expression, Int J Mol Sci 22 (2021) 1363. https://doi.org/10.3390/ijms22031363.

[79] R. Rahman Pour, A. Ehibhatiomhan, Y. Huang, B. Ashley, G.M. Rashid, S. Mendel-Williams, T.D.H. Bugg, Protein engineering of *Pseudomonas fluorescens peroxidase* Dyp1B for Oxidation of Phenolic and Polymeric Lignin Substrates, Enzyme Microb Technol 123 (2019) 21–29. https://doi.org/10.1016/j.enzmictec.2019.01.002.

[80] J. Ren, J. Huo, Q. Wang, Z. Liu, S. Li, S. Wang, W. Guo, H. Li, Characteristics of Immobilized Dye-Decolorizing Peroxidase from *Bacillus amyloliquefaciens* and Application to the Bioremediation of Dyeing Effluent, Biochem Eng J 182 (2022) 108430. https://doi.org/10.1016/j.bej.2022.108430.

[81] A. Wasak, R. Drozd, Ł. Struk, B. Grygorcewicz, Entrapment of DyP-type Peroxidase from *Pseudomonas fluorescens* Pf-5 into Ca-alginate Magnetic Beads, Biotechnol Appl Biochem 65 (2018) 238–245. https://doi.org/10.1002/bab.1562.

[82] N. Lončar, N. Drašković, N. Božić, E. Romero, S. Simić, I. Opsenica, Z. Vujčić, M.W. Fraaije, Expression and Characterization of a Dye-Decolorizing Peroxidase from *Pseudomonas fluorescens* Pf0-1, Catalysts 9 (2019) 1–10. https://doi.org/10.3390/catal9050463.

[83] N. Lončar, H.J. Rozeboom, L.E. Franken, M.C.A. Stuart, M.W. Fraaije, Structure of a Robust Bacterial Protein Cage and its Application as a Versatile Biocatalytic Platform Through Enzyme Encapsulation, Biochem Biophys Res Commun 529 (2020) 548–553. https://doi.org/10.1016/j.bbrc.2020.06.059.

[84] M.F. Scocozza, L.O. Martins, D.H. Murgida, Direct Electrochemical Generation of Catalytically Competent Oxyferryl Species of Classes I and P Dye Decolorizing Peroxidases, Int J Mol Sci 22 (2021) 12532. https://doi.org/10.3390/ijms222212532.

[85] C. Barbosa, C.M. Silveira, D. Silva, V. Brissos, P. Hildebrandt, L.O. Martins, S. Todorovic, Immobilized Dye-Decolorizing Peroxidase (DyP) and Directed Evolution Variants for Hydrogen Peroxide Biosensing, Biosen Bioelectron 153 (2020) 112055. https://doi.org/10.1016/j.bios.2020.112055.

[86] A.P.F. Turner, Biosensors: Sense and Sensibility, Chem Soc Rev 42 (2013) 3184–3196. https://doi.org/10.1039/c3cs35528d.

[87] C. Karunakaran, T. Madasamy, N.K. Sethy, Enzymatic biosensors. In: Biosens Bioelectron, Elsevier, 2015: pp. 133–204. https://doi.org/10.1016/B978-0-12-803100-1.00003-7.

[88] P. Bollella, L. Gorton, Enzyme Based Amperometric Biosensors, Curr. Opin Electrochem 10 (2018) 157–173. https://doi.org/10.1016/j.coelec.2018.06.003.

[89] M. Kataria, M. Swati, T. Pathak, K. Kumar, Enzyme Based Biosensors and their Applications, Elsevier, 2014. https://doi.org/10.1016/b978-0-444-64114-4.00008-x.

[90] J.D. Newman, S.J. Setford, Enzymatic Biosensors, Mol. Biotechnol. 32 (2006) 249–268. https://doi.org/10.1385/MB:32:3:249.

[91] P. Das, M. Das, S.R. Chinnadayyala, I.M. Singha, P. Goswami, Recent Advances on Developing 3rd Generation Enzyme Electrode for Biosensor Applications, Biosens Bioelectron 79 (2016). https://doi.org/10.1016/j.bios.2015.12.055.

[92] D. Grieshaber, R. MacKenzie, J. Vörös, E. Reimhult, Electrochemical Biosensors - Sensor Principles and Architectures, Sensors 8 (2008) 1400–1458. https://doi.org/10.3390/s80314000.

[93] T. Monteiro, M.G. Almeida, Electrochemical Enzyme Biosensors Revisited: Old Solutions for New Problems, Crit Rev Anal Chem 49 (2019) 44–66. https://doi.org/10.1080/10408347.2018.1461552.

[94] N.J. Ronkainen, H.B. Halsall, W.R. Heineman, Electrochemical Biosensors, Chem Soc Rev 39 (2010) 1747–1763. https://doi.org/10.1039/b714449k.

[95] S.V. Dzyadevych, V.N. Arkhypova, A.P. Soldatkin, A.V. El'skaya, C. Martelet, N. Jaffrezic-Renault, Amperometric Enzyme Biosensors: Past, Present and Future, IRBM 29 (2008) 171–180. https://doi.org/10.1016/j.rbmret.2007.11.007.

[96] A. Sassolas, L.J. Blum, B.D. Leca-Bouvier, Immobilization Strategies to Develop Enzymatic Biosensors, Biotechnol Adv 30 (2012) 489–511. https://doi.org/10.1016/j.biotechadv.2011.09.003.

[97] K. Habermüller, M. Mosbach, W. Schuhmann, Electron-Transfer Mechanisms in Amperometric Biosensors, Fresenius J Anal Chem 366 (2000) 560–568. https://doi.org/10.1007/s002160051551.

[98] G. Rocchitta, A. Spanu, S. Babudieri, G. Latte, G. Madeddu, G. Galleri, S. Nuvoli, P. Bagella, M. Demartis, V. Fiore, R. Manetti, P. Serra, Enzyme Biosensors for Biomedical Applications: Strategies for Safeguarding Analytical Performances in Biological Fluids, Sensors 16 (2016) 780. https://doi.org/10.3390/s16060780.

[99] J. Wang, Electrochemical Glucose Biosensors, Chem Rev 108 (2008) 814–825. https://doi.org/10.1021/cr068123a.

[100] V.B. Juska, M.E. Pemble, A Critical Review of Electrochemical Glucose Sensing: Evolution of Biosensor Platforms Based on Advanced Nanosystems, Sensors 20 (2020) 6013. https://doi.org/10.3390/s20216013.

[101] A. Chaubey, B.D. Malhotra, Mediated Biosensors, Biosens Bioelectron 17 (2002) 441–456. https://doi.org/10.1016/S0956-5663(01)00313-X.

[102] C.M. Silveira, M.G. Almeida, Small Electron-Transfer Proteins as Mediators in Enzymatic Electrochemical Biosensors, Anal Bioanal Chem 405 (2013) 3619–3635. https://doi.org/10.1007/s00216-013-6786-4.

[103] Y. Wu, S. Hu, Biosensors Based on Direct Electron Transfer in Redox Proteins, Microchimica Acta 159 (2007) 1–17. https://doi.org/10.1007/s00604-007-0749-4.

[104] L. Gorton, A. Lindgren, T. Larsson, F.D. Munteanu, T. Ruzgas, I. Gazaryan, Direct Electron Transfer Between Heme-Containing Enzymes and Electrodes as Basis for Third Generation Biosensors, Anal Chim Acta 400 (1999) 91–108. https://doi.org/10.1016/S0003-2670(99)00610-8.

[105] C. Léger, P. Bertrand, Direct Electrochemistry of Redox Enzymes as a Tool for Mechanistic Studies, Chem Rev 108 (2008) 2379–2438. https://doi.org/10.1021/cr0680742.

[106] T. Nöll, G. Nöll, Strategies for "Wiring" Redox-Active Proteins to Electrodes and Applications in Biosensors, Biofuel Cells, and Nanotechnology, Chem Soc Rev 40 (2011) 3564–3576. https://doi.org/10.1039/c1cs15030h.

[107] N.M. Kilic, S. Singh, G. Keles, S. Cinti, S. Kurbanoglu, D. Odaci, Novel Approaches to Enzyme-Based Electrochemical Nanobiosensors, Biosensors 13 (2023) 622. https://doi.org/10.3390/bios13060622.

[108] M. Song, X. Lin, Z. Peng, S. Xu, L. Jin, X. Zheng, H. Luo, Materials and Methods of Biosensor Interfaces With Stability, Front Mater 7 (2021). https://doi.org/10.3389/fmats.2020.583739.

[109] S. Campuzano, J.M. Pingarrón, Electrochemical Bioanalysis: All that Still Hides the Tip of the Iceberg, Curr Opin Electrochem 41 (2023). https://doi.org/10.1016/j.coelec.2023.101359.

[110] T.L. Poulos, Thirty Years of Heme Peroxidase Structural Biology, Arch Biochem Biophys 500 (2010) 3–12. https://doi.org/10.1016/j.abb.2010.02.008.

[111] T. Ruzgasa, E. Csregib, J. Emn, L. Gortonb, Peroxidase-Modified Electrodes : Fundamentals and Application, 330 (1996) 123–138.

[112] F.W. Krainer, A. Glieder, An Updated View on Horseradish Peroxidases: Recombinant Production and Biotechnological Applications, Appl Microbiol Biotechnol 99 (2015) 1611–1625. https://doi.org/10.1007/s00253-014-6346-7.

[113] A. Lindgren, M. Tanaka, T. Ruzgas, L. Gorton, I. Gazaryan, K. Ishimori, I. Morishima, Direct Electron Transfer Catalyzed by Recombinant Forms of Horseradish Peroxidase: Insight into the Mechanism, Electrochem Commun 1 (1999) 171–175. https://doi.org/10.1016/S1388-2481(99)00033-8.

[114] A.C. Onuoha, X. Zu, J.F. Rusling, Electrochemical Generation and Reactions of Ferrylmyoglobins in Water and Microemulsions, J Am Chem Soc 119 (1997) 3979–3986. https://doi.org/10.1021/ja964007l.

[115] D. Keilin, E.F. Hartree, Reaction of Methæmoglobin with Hydrogen Peroxide, Nature 166 (1950) 513–514. https://doi.org/10.1038/166513a0.

[116] X. Zu, Z. Lu, Z. Zhang, J.B. Schenkman, J.F. Rusling, Electroenzyme-Catalyzed Oxidation of Styrene and *cis* -β-Methylstyrene Using Thin Films of Cytochrome P450cam and Myoglobin, Langmuir 15 (1999) 7372–7377. https://doi.org/10.1021/la990685k.

[117] S. Ji, B. Jiang, H. Hao, Y. Chen, J. Dong, Y. Mao, Z. Zhang, R. Gao, W. Chen, R. Zhang, Q. Liang, H. Li, S. Liu, Y. Wang, Q. Zhang, L. Gu, D. Duan, M. Liang, D. Wang, X. Yan, Y. Li, Matching the Kinetics of Natural Enzymes with a Single-Atom Iron Nanozyme, Nat Catal 4 (2021) 407–417. https://doi.org/10.1038/s41929-021-00609-x.

[118] L. Huang, J. Chen, L. Gan, J. Wang, S. Dong, Single-Atom Nanozymes, Sci Adv 5 (2019) eaav5490. https://doi.org/10.1126/sciadv.aav5490.

[119] C.P. Kurup, M.U. Ahmed, Nanozymes towards Personalized Diagnostics: A Recent Progress in Biosensing, Biosensors 13 (2023) 461. https://doi.org/10.3390/bios13040461.

[120] W. Chen, S. Cai, Q.Q. Ren, W. Wen, Y. Di Zhao, Recent Advances in Electrochemical Sensing for Hydrogen Peroxide: A review, Analyst 137 (2012) 49–58. https://doi.org/10.1039/c1an15738h.

[121] J. Meier, E. M Hofferber, J. A Stapleton, N. M Iverson, Hydrogen Peroxide Sensors for Biomedical Applications, Chemosensors 7 (2019) 64. https://doi.org/10.3390/chemosensors7040064.

[122] B. Halliwell, M.V. Clement, L.H. Long, Hydrogen Peroxide in the Human Body, FEBS Lett 486 (2000) 10–13. https://doi.org/10.1016/S0014-5793(00)02197-9.

[123] J.E. Giaretta, H. Duan, F. Oveissi, S. Farajikhah, F. Dehghani, S. Naficy, Flexible Sensors for Hydrogen Peroxide Detection: A Critical Review, ACS Appl Mater Interfaces 14 (2022) 20491–20505. https://doi.org/10.1021/acsami.1c24727.

[124] T. Ahmad, A. Iqbal, S.A. Halim, J. Uddin, A. Khan, S. El Deeb, A. Al-Harrasi, Recent Advances in Electrochemical Sensing of Hydrogen Peroxide (H_2O_2) Released from Cancer Cells, Nanomaterials 12 (2022) 1475. https://doi.org/10.3390/nano12091475.

[125] T. Ruzgas, J. Emnéus, L. Gorton, G. Marko-Varga, The Development of a Peroxidase Biosensor for Monitoring Phenol and Related Aromatic Compounds, Anal Chim Acta 311 (1995) 245–253. https://doi.org/10.1016/0003-2670(95)00047-4.

[126] S. Gaspar, Biosensors Based on Novel Plant Peroxidases: a Comparative Study, Electrochim Acta 46 (2000) 255–264. https://doi.org/10.1016/S0013-4686(00)00580-6.

[127] J. Castillo, E. Ferapontova, D. Hushpulian, F. Tasca, V. Tishkov, T. Chubar, I. Gazaryan, L. Gorton, Direct Electrochemistry and Bioelectrocatalysis of H_2O_2 Reduction of Recombinant Tobacco Peroxidase On Graphite. Effect Of Peroxidase Single-Point Mutation On Ca^{2+}-Modulated Catalytic Activity, J Electroanal Chem 588 (2006) 112–121. https://doi.org/10.1016/j.jelechem.2005.12.010.

[128] D.A. Centeno, X.H. Solano, J.J. Castillo, A New Peroxidase from Leaves of Guinea Grass (*Panicum maximum*): A potential biocatalyst to build amperometric biosensors, Bioelectrochemistry 116 (2017) 33–38. https://doi.org/10.1016/j.bioelechem.2017.03.005.

[129] E. Ferapontova, L. Gorton, Effect of pH on Direct Electron Transfer in the System Gold Electrode–Recombinant Horseradish Peroxidase, Bioelectrochemistry 55 (2002) 83–87. https://doi.org/10.1016/S1567-5394(01)00158-X.

[130] E.E. Ferapontova, V.G. Grigorenko, A.M. Egorov, T. Börchers, T. Ruzgas, L. Gorton, Mediatorless Biosensor for H_2O_2 Based on Recombinant Forms of Horseradish Peroxidase Directly Adsorbed on Polycrystalline Gold, Biosens Bioelectron 16 (2001) 147–157. https://doi.org/10.1016/S0956-5663(01)00134-8.

[131] G. Presnova, V. Grigorenko, A. Egorov, T. Ruzgas, A. Lindgren, L. Gorton, T. Börchers, Direct Heterogeneous Electron Transfer of Recombinant Horseradish Peroxidases on Gold, Faraday Discuss 116 (2000) 281–289. https://doi.org/10.1039/b001645o.

[132] R. Andreu, E.E. Ferapontova, L. Gorton, J.J. Calvente, Direct Electron Transfer Kinetics in Horseradish Peroxidase Electrocatalysis, J Phys Chem B 111 (2007) 469–477. https://doi.org/10.1021/jp064277i.

[133] Y.-X. Sun, J.-T. Zhang, S.-W. Huang, S.-F. Wang, Hydrogen peroxide Biosensor Based on the Bioelectrocatalysis of Horseradish Peroxidase Incorporated in a new Hydrogel Film, Sens Actuators B Chem 124 (2007) 494–500. https://doi.org/10.1016/j.snb.2007.01.012.

[134] Z. Wang, M. Li, P. Su, Y. Zhang, Y. Shen, D. Han, A. Ivaska, L. Niu, Direct Electron Transfer of Horseradish Peroxidase and its Electrocatalysis Based on Carbon Nanotube/Thionine/Gold Composites, Electrochem Commun 10 (2008) 306–310. https://doi.org/10.1016/j.elecom.2007.12.011.

[135] Z. Zhu, X. Li, Y. Wang, Y. Zeng, W. Sun, X. Huang, Direct Electrochemistry and Electrocatalysis of Horseradish Peroxidase with Hyaluronic Acid-Ionic Liquid-Cadmium Sulfide Nanorod Composite Material, Anal Chim Acta 670 (2010) 51–56. https://doi.org/10.1016/j.aca.2010.04.061.

[136] X. Zeng, X. Li, X. Liu, Y. Liu, S. Luo, B. Kong, S. Yang, W. Wei, A Third-Generation Hydrogen Peroxide Biosensor Based on Horseradish Peroxidase Immobilized on DNA Functionalized Carbon Nanotubes, Biosens Bioelectron 25 (2009) 896–900. https://doi.org/10.1016/j.bios.2009.09.003.

[137] J.S. Narayanan, G. Slaughter, Towards a Dual in-line Electrochemical Biosensor for the Determination Of Glucose And Hydrogen Peroxide, Bioelectrochemistry 128 (2019) 56–65. https://doi.org/10.1016/j.bioelechem.2019.03.005.

[138] M.-Y. Hua, Y.-C. Lin, R.-Y. Tsai, H.-C. Chen, Y.-C. Liu, A hydrogen Peroxide Sensor Based on a Horseradish Peroxidase/Polyaniline/Carboxy-Functionalized Multiwalled Carbon Nanotube Modified Gold Electrode, Electrochim Acta 56 (2011) 9488–9495. https://doi.org/10.1016/j.electacta.2011.08.043.

[139] D. Zhang, H. Zhao, Z. Fan, M. Li, P. Du, C. Liu, Y. Li, H. Li, H. Cao, A Highly Sensitive and Selective Hydrogen Peroxide Biosensor Based on Gold Nanoparticles and Three-Dimensional Porous Carbonized Chicken Eggshell Membrane, PLoS One 10 (2015) e0130156. https://doi.org/10.1371/journal.pone.0130156.

[140] X. Liu, H. Feng, J. Zhang, R. Zhao, X. Liu, D.K.Y. Wong, Hydrogen Peroxide Detection at a Horseradish Peroxidase Biosensor with a Au Nanoparticle–Dotted Titanate Nanotube|Hydrophobic Ionic Liquid Scaffold, Biosens Bioelectron 32 (2012) 188–194. https://doi.org/10.1016/j.bios.2011.12.002.

[141] C.-X. Lei, S.-Q. Hu, N. Gao, G.-L. Shen, R.-Q. Yu, An Amperometric Hydrogen Peroxide Biosensor Based on Immobilizing Horseradish Peroxidase to a nano-Au Monolayer Supported by Sol–Gel Derived Carbon Ceramic Electrode, Bioelectrochemistry 65 (2004) 33–39. https://doi.org/10.1016/j.bioelechem.2004.06.002.

[142] P. Bollella, L. Medici, M. Tessema, A.A. Poloznikov, D.M. Hushpulian, V.I. Tishkov, R. Andreu, D. Leech, N. Megersa, M. Marcaccio, L. Gorton, R. Antiochia, Highly Sensitive, Stable and Selective Hydrogen Peroxide Amperometric Biosensors Based on Peroxidases from Different Sources Wired by Os-polymer: A Comparative Study, Solid State Ion 314 (2018) 178–186. https://doi.org/10.1016/j.ssi.2017.10.015.

[143] K. De Wael, H. Buschop, H.A. Heering, L. De Smet, J. Van Beeumen, B. Devreese, A. Adriaens, Electrochemical Determination of Hydrogen Peroxide Using *Rhodobacter capsulatus* Cytochrome *c* Peroxidase at a Gold Electrode, Microchimica Acta 162 (2008) 65–71. https://doi.org/10.1007/s00604-007-0878-9.

[144] P.M. Paes de Sousa, S.R. Pauleta, M.L. Simões Gonçalves, G.W. Pettigrew, I. Moura, M.M. Correia dos Santos, J.J.G. Moura, Mediated Catalysis of *Paracoccus pantotrophus* cytochrome *c* peroxidase by *P. pantotrophus* pseudoazurin: Kinetics Of Intermolecular Electron Transfer, J Biol Inorg Chem 12 (2007) 691–698. https://doi.org/10.1007/s00775-007-0219-9.

[145] C.F. Becker, N.J. Watmough, S.J. Elliott, Electrochemical Evidence for Multiple Peroxidatic Heme States of the Diheme Cytochrome *c* Peroxidase of *Pseudomonas aeruginosa*, Biochem 48 (2009) 87–95. https://doi.org/10.1021/bi801699m.

[146] K.E. Ellis, J. Seidel, O. Einsle, S.J. Elliott, *Geobacter sulfurreducens* Cytochrome *c* Peroxidases: Electrochemical Classification of Catalytic Mechanisms, Biochem 50 (2011) 4513–4520. https://doi.org/10.1021/bi200399h.

[147] A. Narváez, G. Suárez, I.C. Popescu, I. Katakis, E. Domínguez, Reagentless Biosensors Based on Self-Deposited Redox Polyelectrolyte-Oxidoreductases Architectures, Biosens Bioelectron 15 (2000) 43–52. https://doi.org/10.1016/S0956-5663(00)00049-X.

[148] Y. Okawa, N. Yokoyama, Y. Sakai, F. Shiba, Direct Electron Transfer Biosensor for Hydrogen Peroxide Carrying Nanocomplex Composed of Horseradish Peroxidase and Au-nanoparticle – Characterization and Application to Bienzyme Systems, Anal Chem Res 5 (2015) 1–8. https://doi.org/10.1016/j.ancr.2015.05.001.

[149] J.L. Olloqui-Sariego, G.S. Zakharova, A.A. Poloznikov, J.J. Calvente, D.M. Hushpulian, L. Gorton, R. Andreu, Fenton-like Inactivation of Tobacco Peroxidase Electrocatalysis at Negative Potentials, ACS Catal 6 (2016) 7452–7457. https://doi.org/10.1021/acscatal.6b01839.

[150] J.F. Rusling, Enzyme Bioelectrochemistry in Cast Biomembrane-Like Films, Acc Chem Res 31 (1998) 363–369. https://doi.org/10.1021/ar970254y.

[151] G.A. Huerta-Miranda, A.A. Arrocha-Arcos, M. Miranda-Hernández, Gold Nanoparticles/4-Aminothiophenol Interfaces for Direct Electron Transfer of Horseradish Peroxidase: Enzymatic Orientation and Modulation of Sensitivity Towards Hydrogen Peroxide Detection, Bioelectrochemistry 122 (2018) 77–83. https://doi.org/10.1016/j.bioelechem.2018.03.004.

[152] X. Chen, X. Peng, J. Kong, J. Deng, Facilitated Electron Transfer from an Electrode to Horseradish Peroxidase in a Biomembrane-like Surfactant Film, J Electroanal Chem 480 (2000) 26–33. https://doi.org/10.1016/S0022-0728(99)00441-6.

[153] Y. Zhang, P. He, N. Hu, Horseradish Peroxidase Immobilized in TiO_2 Nanoparticle Films on Pyrolytic Graphite Electrodes: Direct Electrochemistry and Bioelectrocatalysis, Electrochim Acta 49 (2004) 1981–1988. https://doi.org/10.1016/j.electacta.2003.12.028.

[154] R. Mossanha, C.A. Erdmann, C.S. Santos, K. Wohnrath, S.T. Fujiwara, C.A. Pessoa, Construction of a Biosensor Based on SAM of Thiolactic Acid on Gold Nanoparticles Stabilized by Silsesquioxane Polyelectrolyte for Cathecol Determination, Sens Actuators B Chem 252 (2017) 747–756. https://doi.org/10.1016/j.snb.2017.06.001.

[155] A. Kermad, S. Sam, N. Ghellai, K. Khaldi, N. Gabouze, Horseradish Peroxidase-Modified Porous Silicon for Phenol Monitoring, Materials Science and Engineering: B 178 (2013) 1159–1164. https://doi.org/10.1016/j.mseb.2013.07.010.

[156] T.J. Castilho, M. del P.T. Sotomayor, L.T. Kubota, Amperometric Biosensor Based On Horseradish Peroxidase for Biogenic Amine Determinations in Biological Samples, J Pharm Biomed Anal 37 (2005) 785–791. https://doi.org/10.1016/j.jpba.2004.11.043.

[157] W. Sun, Y. Guo, T. Li, X. Ju, J. Lou, C. Ruan, Electrochemistry of Horseradish Peroxidase Entrapped in Graphene and dsDNA Composite Modified Carbon Ionic Liquid Electrode, Electrochim Acta 75 (2012) 381–386. https://doi.org/10.1016/j.electacta.2012.05.018.

[158] Y. Niu, J. Liu, W. Chen, C. Yin, W. Weng, X. Li, X. Wang, G. Li, W. Sun, A direct Electron Transfer Biosensor Based on a Horseradish Peroxidase and Gold Nanotriangle Modified Electrode and Electrocatalysis, Anal Methods 10 (2018) 5297–5304. https://doi.org/10.1039/C8AY01980K.

[159] H. Liu, K. Guo, J. Lv, Y. Gao, C. Duan, L. Deng, Z. Zhu, A Novel Nitrite Biosensor Based on the Direct Electrochemistry of Horseradish Peroxidase Immobilized on Porous Co_3O_4 Nanosheets and Reduced Graphene Oxide Composite Modified Electrode, Sens Actuators B Chem 238 (2017) 249–256. https://doi.org/10.1016/j.snb.2016.07.073.

[160] M. Feizabadi, A. Soleymanpour, H. Faridnouri, D. Ajloo, Improving Stability of Biosensor Based on Covalent Immobilization Of Horseradish Peroxidase by γ-Aminobutyric Acid and Application in Detection of H_2O_2, Int J Biol Macromol 136 (2019) 597–606. https://doi.org/10.1016/j.ijbiomac.2019.06.103.

[161] V. Rosca, I. Catalin Popescu, Kinetic Analysis of Horseradish Peroxidase “Wiring” in Redox Polyelectrolyte–Peroxidase Multilayer Assemblies, Electrochem Commun 4 (2002) 904–911. https://doi.org/10.1016/S1388-2481(02)00486-1.

[162] R.K. Satvekar, S.S. Rohiwal, A. V. Raut, V.A. Karande, B.M. Tiwale, S.H. Pawar, A Silica-Dextran Nanocomposite as a Novel Matrix for Immobilization of Horseradish Peroxidase, and its Application to Sensing Hydrogen Peroxide, Microchimica Acta 181 (2014) 71–77. https://doi.org/10.1007/s00604-013-1065-9.

[163] I.M. Weidinger, Plasmonic Nanostructured Supports for Spectro-Electrochemistry of Enzymes on Electrodes. In: Handbook of Nanoelectrochemistry, Springer, Cham, 2015: pp. 1–16. https://doi.org/10.1007/978-3-319-15207-3_43-1.

[164] S. Gupta, C.N. Murthy, C.R. Prabha, Recent Advances in Carbon Nanotube Based Electrochemical Biosensors, Int J Biol Macromol 108 (2018) 687–703. https://doi.org/10.1016/j.ijbiomac.2017.12.038.

[165] M. Sharafeldin, J.J. Davis, Characterising the Biosensing Interface, Anal Chim Acta 1216 (2022) 339759. https://doi.org/10.1016/j.aca.2022.339759.

[166] N.R. Mohamad, N.H.C. Marzuki, N.A. Buang, F. Huyop, R.A. Wahab, An Overview of Technologies for Immobilization of Enzymes and Surface Analysis Techniques for Immobilized Enzymes, Biotechnol. Biotechnol. Equip 29 (2015) 205–220. https://doi.org/10.1080/13102818.2015.1008192.

[167] N. Kornienko, K.H. Ly, W.E. Robinson, N. Heidary, J.Z. Zhang, E. Reisner, Advancing Techniques for Investigating the Enzyme-Electrode Interface, Acc Chem Res 52 (2019) 1439–1448. https://doi.org/10.1021/acs.accounts.9b00087.

[168] D.H. Murgida, P. Hildebrandt, S. Todorovic, Immobilized Redox Proteins: Mimicking Basic Features of Physiological Membranes and Interfaces. In: Biomimetics Learning from Nature, InTech, 2010: pp. 21–48. https://doi.org/10.5772/8778.

[169] S. Todorovic, D.H. Murgida, Surface-Enhanced Raman Scattering of Biological Materials. In Encyclopedia of Analytical Chemistry, R.A. Meyers 2016: pp. 1–29. https://doi.org/10.1002/9780470027318.a9574.

[170] D. Zigah, E. Lojou, A. de Poulpiquet, Micro- and Nanoscopic Imaging of Enzymatic Electrodes: A Review, ChemElectroChem 6 (2019) 5524–5546. https://doi.org/10.1002/celc.201901065.

[171] D.H. Murgida, P. Hildebrandt, Heterogeneous Electron Transfer of Cytochrome *c* on Coated Silver Electrodes. Electric Field Effects On Structure and Redox Potential, J Phys Chem B 105 (2001) 1578–1586. https://doi.org/10.1021/jp003742n.

[172] S. Todorovic, C. Jung, P. Hildebrandt, D.H. Murgida, Conformational Transitions and Redox Potential Shifts of Cytochrome P450 Induced by Immobilization, J Biol Inorg Chem 11 (2006) 119–127. https://doi.org/10.1007/s00775-005-0054-9.

[173] D.H. Murgida, P. Hildebrandt, Electron-Transfer Processes of Cytochrome *c* at Interfaces. New Insights by Surface-enhanced Resonance Raman Spectroscopy, Acc. Chem. Res. 37 (2004) 854–861. https://doi.org/10.1021/ar0400443.

[174] S. Todorovic, A. Verissimo, N. Wisitruangsakul, I. Zebger, P. Hildebrandt, M.M. Pereira, M. Teixeira, D.H. Murgida, SERR-Spectroelectrochemical Study of a cbb_3 Oxygen Reductase in a Biomimetic Construct, J Phys Chem B 112 (2008) 16952–16959. https://doi.org/10.1021/jp807862m.

[175] C.M. Silveira, P.O. Quintas, I. Moura, J.J.G. Moura, P. Hildebrandt, M.G. Almeida, S. Todorovic, SERR Spectroelectrochemical Study of Cytochrome cd_1 Nitrite Reductase Co-Immobilized with Physiological Redox Partner Cytochrome c_{552} on Biocompatible Metal Electrodes, PLoS One 10 (2015) e0129940. https://doi.org/10.1371/journal.pone.0129940.

[176] S. Todorovic, M.M. Pereira, T.M. Bandeiras, M. Teixeira, P. Hildebrandt, D.H. Murgida, Midpoint Potentials of Hemes *a* and a_3 in the Quinol Oxidase from *Acidianus ambivalens* are Inverted, J Am Chem Soc 127 (2005) 13561–13566. https://doi.org/10.1021/ja052921l.

[177] M. Sezer, T. Genebra, S. Mendes, L.O. Martins, S. Todorovic, A DyP-Type Peroxidase at a Bio-Compatible Interface: Structural and Mechanistic Insights, Soft Matter 8 (2012) 10314–10321. https://doi.org/10.1039/c2sm26310f.

[178] C.M. Silveira, M.A. Castro, J.M. Dantas, C. Salgueiro, D.H. Murgida, S. Todorovic, Structure, Electrocatalysis and Dynamics of Immobilized Cytochrome PccH and its Microperoxidase, Phys Chem Chem Phys. 19 (2017) 8908–8918. https://doi.org/10.1039/c6cp08361g.

[179] C. Léger, An Introduction to Electrochemical Methods for the Functional Analysis of Metalloproteins. In: Practical Approaches to Biological Inorganic Chemistry, Elsevier Inc., 2013: pp. 179–216. https://doi.org/10.1016/B978-0-444-56351-4.00008-7.

[180] V. Fourmond, C. Léger, An introduction to electrochemical methods for the functional analysis of metalloproteins. In: Practical Approaches to Biological Inorganic Chemistry, Elsevier, 2020: pp. 325–373. https://doi.org/10.1016/B978-0-444-64225-7.00009-2.

[181] J.F. Rusling, B. Wang, S. Yun, Electrochemistry of Redox Enzymes. In: Bioelectrochemistry, Wiley, 2008: pp. 39–85. https://doi.org/10.1002/9780470753842.ch2.

[182] D.R. Thévenot, K. Toth, R.A. Durst, G.S. Wilson, Electrochemical Biosensors: Recommended Definitions and Classification, Anal Lett 34 (2001) 635–659. https://doi.org/10.1081/AL-100103209.

[183] A.D. McNaught, A. Wilkinson, IUPAC Compendium of Chemical Terminology, 2nd ed., Blackwell Scientific Publications, Oxford, 1997.

Chapter 2 In Search for Promising Biocatalysts for Use in Biotechnological Applications - Characterization of DyPs in Solution

This chapter contains data published in:

Lidia Zuccarello, **Catarina Barbosa**, Edilson Galdino, Nicola Lončar, Célia M. Silveira, Marco W. Fraaije, Smilja Todorovic. SERR Spectroelectrochemistry as a Guide for Rational Design of DyP-Based Bioelectronics Devices. *Int J Mol Sci* 22: 7998, 2021. Doi: 10.3390/ijms22157998.

Catarina Barbosa, Carolina F. Rodrigues, Nicola Lončar, Lígia O. Martins, Smilja Todorovic, Célia M. Silveira. Spectroelectrochemistry for Determination of the Redox Potential in Heme Enzymes: Dye-Decolorizing Peroxidases. *BBA Advances* 5: 100112, 2024. Doi: 10.1016/j.bbadva.2023.100112

Acknowledgments and contributions

In this chapter, Catarina Barbosa performed the overexpression and purification of WT: SviDyP, ScoDyP, TfuDyP, CboDyP, PpDyP and respective distal variants. She also recorded and interpreted resonance Raman (RR) spectra of WT: SviDyP, CboDyP, PpDyP and PpDyPs´ distal variants and determined the reduction potentials of WT SviDyP and ScoDyP by UV-spectroelectrohemistry.

Carolina F. Rodrigues has performed the site-direct mutagenesis of the PpDyP distal variants and overexpression and purification of PpDyP *in silico* variants. Caterina Martin helped in the construction of CboDyP distal variants. Lidia Zuccarello performed the RR spectra of ScoDyP and TfuDyP. Célia Silveira has determined the reduction potential of WT CboDyP, WT PpDyP, CboDyP and PpDyP distal variants, and PpDyP *in silico* engineering variants.

Abstract

In pursuing a suitable DyP candidate for biosensing applications, we begin by investigating seven WT DyPs from different bacterial sources. The heme cavity and active site structural properties of WT SviDyP, ScoDyP, TfuDyP, CboDyP, and PpDyP have been characterized using UV-vis absorption and RR spectroscopies. Additionally, we also studied PpDyP variants that were generated through *in silico* design (FireProt and PROSS), which exhibit enhanced catalytic properties in solution compared to the WT PpDyP, and distal variants of PpDyP and CboDyP (R30W/I and R214W/I, respectively) engineered targeting a reduction potential upshifting. Our findings suggest that WT SviDyP, ScoDyP, CboDyP, PpDyP, CboDyP R307W, PpDyP R214W, and *in silico* engineered variants of PpDyP all appear to be promising candidates for biosensing applications. This conclusion was based on the presence of catalytically competent species under physiological conditions. While the reduction potentials of the WT enzymes were comparable, the distal site variants demonstrated that site-specific substitutions influence the reduction potentials in a case-dependent manner.

2.1. Introduction

Bacterial DyPs are attractive targets for biotechnological applications due to their capacity to oxidize a broad range of structurally different substrates and their easy genetic manipulation, allowing for the construction of specific variants with tailored catalytic performance, high production yields and stability [1–5]. The configuration of the heme active site of DyPs in solution (i.e., physiological conditions) is most commonly revealed by UV-vis absorption spectroscopy [6–12]. However, this technique is not sensitive enough to fully characterize the different heme populations typically found in the heme active site of peroxidases, because the Soret and Q-bands of different populations usually overlap. Crystallography is also commonly used to address the active site configuration of DyPs [7,9,13,14]. Nevertheless, it is well known that the structural features of peroxidase crystals often differ from those in solution because the heme pocket is highly sensitive to chemical (e.g., pH or temperature) and physical (crystal vs. solution) conditions [15]. It is not uncommon to find contrasting information between crystallization and the spectroscopic data on enzymes in the literature. For instance, while the crystal structure of a peroxidase indicate that a solvent, water, or oxygen molecules are coordinating the heme, the solution characterization reveals that the sixth axial position is vacant [16]. Also, crystals may suffer from prolonged exposure to the X-ray beam, which can result in a photoproduced ferrous heme [17]. In addition, protein crystallization is usually performed in non-physiological conditions, such as a high salt concentration in the buffer solution, which may conceal the true heme coordination pattern, resulting in ions, such as chloride, coordinating the heme [12].

RR spectroscopy has proven to be a valuable tool for revealing detailed heme configuration and structure information. It also helped to understand the catalytic mechanisms by identifying the catalytic intermediaries in iron-porphyrin containing proteins, including DyPs [15,18,19]. A comparative RR study of several bacterial DyPs revealed that their heme architecture in solution is very diverse and class-independent [19]. The respective spin configurations could not be correlated with the conserved amino acids in the distal site of the heme pocket. Also, a high abundance of catalytically incompetent 6cLS population has been found in several DyPs at physiological pH [19]. This study highlights the strong pH dependence of spin state distribution and the crucial role of the second sphere arrangement in fine-tuning the pK_a of distal residues, which enable DyPs to bind and reduce H_2O_2. For instance, in the case of DyPs from *T. fusca* (TfuDyP) and *Deinococcus radiodurans* (DrDyP) in acidic conditions, $3.5 < pH < 5$, which are close to the respective pH optima [9,20], catalytically competent spin species are present (6cHS and 5cHS) [17]. At physiological pH, an increase or complete conversion to a catalytically incompetent population (6cLS) is observed in both cases [19]. These results indicate that the subtle structural changes linked to protonation effects in the distal heme pocket remarkably affect spin state configurations.

Heme proteins' coordination and spin states strongly influence the $E^{0\prime}$, which defines the range of oxidizable peroxidase substrates. The $E^{0\prime}_{Fe(III)\,/\,Fe(II)}$ redox couple ranges from −28 to −320 mV (vs. NHE) in heme peroxidases [21]. Although this redox couple is not directly involved in the reaction mechanism of peroxidases, the value of $E^{0\prime}_{Fe(III)\,/\,Fe(II)}$ is a good indicator of the stability and availability of the resting state Fe(III) for the catalytic reaction [21]. Also, the molecular factors that influence $E^{0\prime}_{Fe(III)\,/\,Fe(II)}$ value can influence the catalytic relevant redox couples Fe(III) / Compound I $[Fe(IV){=}O]^{+\bullet}$, Compound I / Compound II $[Fe(IV){=}O]^{+}$ and Compound II / Fe(III) [21]. Moreover, these catalytic intermediates have intrinsically very positive reduction potentials, ranging between +800 and +1,200 mV, which are often challenging to measure experimentally due to their instability and extreme reactivity [21,22].

The most common approaches for determination of the $E^{0\prime}_{Fe(III)\,/\,Fe(II)}$ of DyPs are (i) chemical redox titrations (referred to in the literature as potentiometric titrations), where the changes in the absorption spectra of the heme cofactor are followed during the stepwise chemical reduction or oxidation of the enzyme in solution [23,24]; (ii) electrochemical methods, for instance, CV [20,25], in which the electrode potential ramps linearly versus time in cyclical phases; and (iii) spectroelectrochemical methods (commonly UV-vis absorption- and SERR-based), in which spectroscopic changes of the enzyme are monitored along an electrochemical redox titration

[8,10,11,23]. Among these, spectroelectrochemical methods stand out because they allow for the identification of electroactive species of interest while simultaneously providing information about their molecular structure and redox state *in situ* [26]. So far, the $E^{0'}_{\mathrm{Fe(III)}/\mathrm{Fe(II)}}$ were determined for a few WT DyPs, with values ranging from −40 to −350 mV [8,10,20,23–25,27]. This wide range of redox values shows the importance of understanding the molecular factors that influence the $E^{0'}$ in DyPs.

This chapter presents a comparative study of DyPs from various bacterial organisms, which aims to identify the best candidates for their future use in biosensor development. To construct a DyP-based device for biotechnological applications, the best-performing candidate is selected first according to their solution characterization. Herein, spectroscopic insights into structural details of DyP active sites in solution employing UV-vis absorption and RR spectroscopy will be provided. Afterward, the redox properties of the studied DyPs will be characterized, and the structural basis for the significantly different redox properties of the studied enzymes will be discussed. Finally, we will describe the structural and redox properties of several variants genetically engineered for improved catalytic performance.

2.2. Materials and methods

2.2.1. Reagents and chemicals

All chemicals purchased from Sigma-Aldrich and were of the highest purity grade available. Solutions were prepared using deionized water from the Mili-Q Water Purification System (Merck Millipore).

2.2.2. Enzymes

2.2.2.1. Recombinant wild type: expression and purification

Recombinant wild type (WT) DyP from *S. coelicolor* (ScoDyP), *T. fusca* (TfuDyP), *C. bogoriensis* (CboDyP), *S. viridis* (SviDyP), *E. coli* (Yfex), *T.cellulosilytica* (TceDyP) and *P. putida* (PpDyP) were overexpressed and purified as previously described [7,28–30]. Briefly, E.coli strains, Tuner DE3, for WT PpDyP and NEB 10β, for all the other WT enzymes, were used to heterologously express the genes of each enzyme that were previously cloned in pET15b for WT PpDyP, pBAD-histag-SUMO for WT CboDyP and pBAD plasmids for the remaining enzymes. The recombinant WT enzymes were produced under the control of the T7lac, WT PpDyP, and araBAD, WT ScoDyP, TfuDyP, CboDyP, SviDyP, Yfex and TceDyP, promoters. Recombinant strains were cultivated in Luria-Bertani medium (LB) and Terrific Broth medium (TB), supplemented with 100 µg·mL-1 ampicillin. For the expression induction 0.1 mM IPTG (isopropyl β-D-1-thiogalactopyranoside) together with 75 µM hemin, for WT PpDyP, or 0.02% L-arabinose, for all the others enzymes, were added when OD600 reached the value of 0.6. Cells were harvested after 24h and disrupted using a French press, for PpDyP, or a sonicator, for ScoDyP, TfuDyP, CboDyP, SviDyP, Yfex and TceDyP.

SviDyP expression conditions were further optimized to increase its heme content. In comparison to the previously tested protocol [29], the expression host was changed from *E. coli* NEB 10β cells to *E. coli* Nissle 1917 cells, the growth media, TB, was changed to LB medium, and the L-Arabinose concentration decreased from 0.02% to 0.01%.

All the cell extracts were harvested by centrifugation. The cell crude extracts were loaded onto a pre-equilibrated 5 mL His-Trap HP column (GE Healthacare), the column was washed either with a) Buffer A (20 mM Tris-HCL pH 7.6, 0.2 M NaCl 50 mM) in the case of PpDyP or b) Buffer B (50 mM potassium phosphate, 0.5 M NaCl, pH 8) in the case of WT ScoDyP, TfuDyP, CboDyP, SviDyP, Yfex and TceDyP, followed by Buffer A or B each supplemented with 20 mM imidazole (in the case of a) and b), respectively). The enzynes were eluted by a 20 mM to 500 mM imidazole gradient in the respectives buffers [7,28–30], using an ÄKTA purifier (GE Healthcare) at room temperature.

2.2.2.2. Construction of cboDyP and ppDyP distal mutants and their overexpression and purification

Single amino acid replacements were created using the QuikChange site-directed mutagenesis protocol. For CboDyP variants, plasmid pBAD-histag-SUMO-*CboDyP* (containing the WT *cboDyP* sequence) was used as the template [7], and the primers were designed using the AA scan software [31]. For PpDyP variants, the plasmid of WT *ppDyP*, cloned in pET15b, was used as the template [25]. The primers, forward PpDyP_Opt_R214W_Fw 5’ CGGAAGCGTTTATGGTGTGGCGTAGCGTTAGCTGGG 3’ and reverse PpDyP_Opt_R214W_Rv 5’ CCCAGCTAACGCTACGCCACACCATAAACGCTTCCG 3’ were used to create the R214W mutation; forward PpDyP_Opt_R214I_Fw 5’ CGGAAGCGTTTATGGTGATTCGTAGCGTTAGCTGGG 3’ and PpDyP_Opt_R214I_Rv 5’ CCCAGCTAACGCTACGAATCACCATAAACGCTTCCG 3’ were used to create the R214I mutation. DNA sequence analysis was used to confirm the presence of the desired mutation in the resulting plasmids and the absence of unwanted mutations in other regions of the insert. The plasmids containing the *cboDyP* and *ppDyP* genes were transformed into NEB 10 β cells and *E. coli* Tuner strains, respectively. The recombinant CboDyP and PpDyP variants were produced under the control of the araBAD and T7lac promoters, respectively.

The proteins were expressed and purified as the WT enzymes (section 2.2.2.1).

2.2.2.3. Construction of the PpDyP in silico engineered mutants, overexpression and purification

PpDyP PROSS and PpDyP FireProt variants were designed *in silico* using the PROSS (https://pross.weizmann.ac.il/) and FireProt (https://loschmidt.chemi.muni.cz/fireprotweb/) algorithms. The submission was performed in standard settings, except for the conserved distal residues Asp 132 and Arg 214 and proximal His 197, which were fixed in the PROSS algorithm. The plasmid for WT ppDyPI, cloned in pET15b, was used as a template [3] to construct the *in silico* variants [32]. Enzyme expression and purification were performed for the WT enzyme [32]. The PpDyP-PROSS variant contained 29 mutations, while the PpDyP-FireProt variant contained 21. The biochemical characterization of both variants in solution showed increased protein expression levels, higher melting temperatures, lower susceptibility to aggregation and higher resistance to denaturing agents compared to the WT enzyme [33].

2.2.3. Heme content determination

The heme content of the DyPs was determined by the pyridine ferrohemochrome method using an extinction coefficient of $\varepsilon_{R\text{–}O\ 556\ nm} = 28.32\ mM^{-1}\ cm^{-1}$ [34]. The electronic absorption spectra of the purified enzymes were recorded on a UV-Vis absorption spectrophotometer Perkin Elmer Lambda 650.

2.2.4. Resonance Raman spectroscopy

RR spectra were acquired with a Raman spectrometer (Jobin Yvon LabRam 800 HR or a Jobin Yvon U1000) with a back-illuminated CCD detector cooled by liquid nitrogen; an Olympus 20x objective was used for laser focusing on the sample and light collection in the backscattering geometry. A 405 nm diode laser was used as an excitation source (Toptica Photonics AG).

RR spectra of the enzymes were measured at room temperature using a rotating quartz cuvette (Hellma) containing 60 - 100 µL of 20 - 80 µM DyP in 12.5 mM potassium phosphate buffer (PB) and 12.5 mM K_2SO_4 at pH 7.0. This rotating quartz cuvette was used to prevent prolonged sample exposure to the laser, as previously described [18]. The spectra were recorded using 1.8 - 3 mW laser power, and the accumulation times were 20 - 120 s. To improve the signal-to-noise (S/N) ratio, 32 spectra were co-added in each experiment. After polynomial baseline subtraction, all spectra were subjected to component analysis, as described previously [35].

ScoDyP spectra were acquired at low temperature using ca. 2 µL of the enzyme sample placed in a microscope stage (Linkham THMS 600) cooled to −50 °C with liquid N_2.

2.2.5. UV-vis absorption spectroelectrochemistry

UV-vis absorption-based spectroelectrochemical titrations of the DyPs in solution were carried out using a Pine Research Instrumentation spectroelectrochemistry kit (DRP10208). The enzyme solution (15 - 25 µM) in 50 mM phosphate buffer, 75 mM NaCl, pH 7.0 was purged with argon and kept under an argon atmosphere throughout the experiment. The following mediators were added to the enzyme solution in a maximum ratio of 1:1: trimethylhydroquinone (+115 mV), 1,4-naphthoquinone (+60 mV), duroquinone (+5 mV), indigo trisulphonate (−70 mV), indigo disulphonate (−125 mV), anthraquinone-2-sulphonate (−225 mV), safranine O (−284 mV), benzyl viologen (−345 mV), and methyl viologen (−440 mV). A gold screen-printed electrode card composed of a perforated honeycomb working and solid counter electrodes (Pine Research Instrumentation) was placed inside a quartz cell (optical path 1.7 mm) containing the enzyme/mediator solution; an Ag/AgCl electrode (3 M KCl, World Precision Instruments, WPI) was used as reference. The electrodes were connected to a Princeton Applied Research 263A potentiostat that controlled the potential applied to the cell. The UV-vis absorption spectra were recorded using a Sarspec STD spectrophotometer. Enzyme reduction (and oxidation) was monitored by the evolution of the ferrous Soret absorption band at 430 nm. Preliminary assays revealed that the reduction (reductive titration, from oxidized to reduced enzyme) and oxidation (oxidative titration, from reduced to oxidized enzyme) titration curves were not superimposable, with gaps between 60 to 100 mV observed between reductive and oxidative titrations for some enzymes (Figure S 2.1 A). To minimize this hysteresis effect, the mediators were used up to a max of 1:1 ratio (mediators:enzyme), which allowed for the obtainment of reversible redox titrations (Figure S 2.1 B) for all DyPs. Except for ScoDyP and SviDyP, the hysteresis effect was still observed, even with an equimolar concentration of enzymes and mediators (Figure S 2.2). When using the 1:1 ratio, the mediators absorption influenced the measurement of Soret band intensities; therefore, the latter were corrected by subtraction of the absorbance of control spectra from titrations performed with mediators only. The reduction potentials of the redox couple Fe(III) / Fe(II) at pH 7 ($E^{0'}_{Fe(III)/Fe(II)}$) were obtained by fitting the Nernst equation (Equation 2.1) to the potential-dependent corrected and normalized absorption at 430 nm

$$E=E^{0'}+\frac{RT}{nF}\ln\frac{[Ox]}{[Red]} \qquad (2.1)$$

in which R is the universal gas constant, T is the temperature, n is the number of electrons involved in the reaction, F is the Faraday constant, and [Ox] and [Red] represent the concentrations of oxidized and reduced species, respectively.

2.3. Results and discussion

2.3.1. Heme incorporation in DyPs

Recombinant production of heme enzymes in *E. coli* has been the most common, efficient, and cost-saving method for producing high amounts of these enzymes. However, the production of heme enzymes is often limited by heme biosynthesis in *E. coli*, which can result in partially assembled holo-heme enzymes [36] or enzymes containing the iron-deficient heme precursor protoporphyrin IX, i.e. metal-free protoporphyrin, instead of the heme cofactor [29]. For the herein purified DyPs, we first determined their UV-vis spectroscopic properties to verify if the enzymes contained the heme cofactor. The heme content was estimated based on the extinction coefficient of pyridine hemochrome *b* [34] .

The UV-vis absorption spectra of WT SviDyP$_D$ (depleted SviDyP), TceDyP, and Yfex revealed apparent differences in the Q-band region (450 - 700 nm) compared to the other purified DyPs (Figure 2.1). In this region, a heme-containing DyP revealed a broad peak between 450 and 650 nm as represented by WT SviDyP (red trace, Figure 2.1), while WT SviDyP$_D$, TceDyP and Yfex presented four bands at 509, 546, 568 and 621 nm, Figure 2.1. The latter spectra were identical to the typical spectrum of metal-free porphyrin that comprises a four-band in the UV-vis absorption spectrum of moderate intensity in the 500 to 660 nm region and an extremely strong Soret band at 400 nm [37,38]. The heme content was estimated to be 0.10 to 0.20 mol of heme *b* per mol of the enzyme, indicating that only 10% to 20% of the purified enzymes are heme-loaded. These results led us to conclude that WT SviDyP$_D$, TceDyP, and Yfex were significantly iron-depleted, which was further corroborated by the absence of spectral changes in the presence of sodium dithionite (Figure S 2.3). This finding aligns with the report of Colpa et al. [26], which demonstrated that a high overexpression level of DyPs leads to the incorporation of metal-free porphyrin. Since a previous study showed that SviDyP has higher activity than some other DyPs [39], we decided to focus on improving the expression condition of this enzyme. To produce a fully heme-loaded enzyme, we changed the expression system to *E. coli* Nissle

1917 cells [36], which were developed specifically to be a suitable host for the recombinant production of heme proteins.

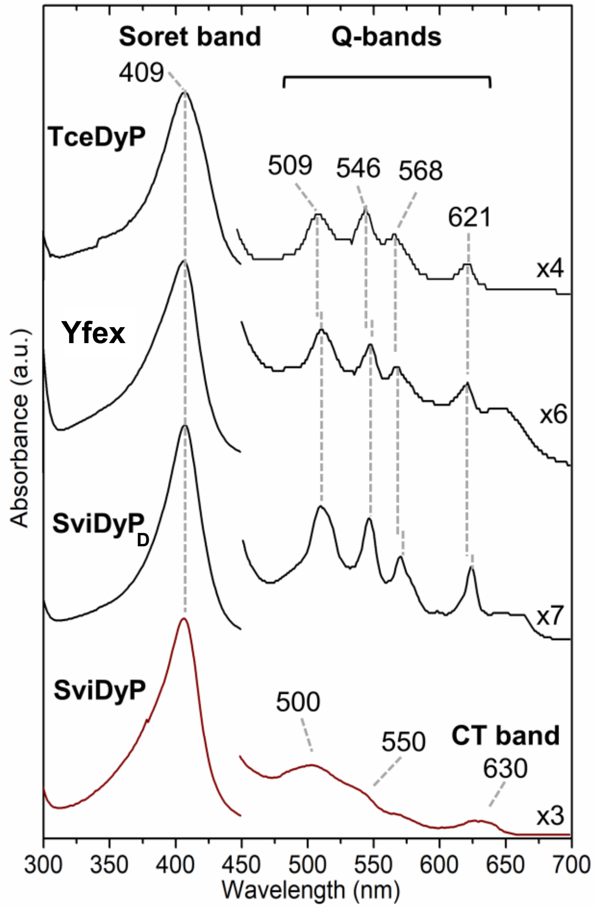

Figure 2.1 - UV-vis absorption spectra of metal-free protoporphyrin containing DyPs (black traces): TceDyP, Yfex, and SviDyP$_D$; and heme-containing ferric SviDyP (red trace). CT band - Charge-transfer band.

In contrast to other laboratory *E. coli* strains, this strain can take up heme from the environment through the heme receptor ChuA [36] which allows for higher availability of the heme cofactor in the cell cytoplasm to be incorporated in the proteins. The overexpression of SviDyP was, in this way, reduced by changing the growth medium from Terrific Broth to a less rich Luria-Bertani medium, aiming at an improved heme/metal-free porphyrin-enzyme ratio [29]. This strategy resulted in a recombinant enzyme with 60% heme loading, herein designated as SviDyP. The enzyme revealed a UV-vis absorption fingerprint characteristic of a heme *b*-containing protein, with no contributions from the metal-free porphyrin (Figure 1, red trace).

All other purified WT DyPs (ScoDyP, TfuDyP, CboDyP, and PpDyP) were obtained as heme-containing enzymes with the heme content estimated to be 0.8 to 1.1 mol of heme *b* per mole of protein, which will be discussed further in the next section. In our search for a promising biocatalyst for biotechnological applications, we further focused our studies on WT: SviDyP, ScoDyP, CboDyP, TfuDyP, and PpDyP. The WT TceDyP and Yfex were discarded because they were purified as metal-free porphyrin-containing enzymes.

2.3.2. Structural characterization of DyP active site

To better understand the molecular details of the enzymes' heme site architecture, the resting states of the ferric enzymes were characterized by UV-vis absorption and RR spectroscopies in solution. UV-vis absorption spectroscopy can provide information about the oxidation state of the cofactor. The high-frequency region (1300 - 1700 cm^{-1}) of RR spectra contains marker bands (ν_i) that are highly sensitive to oxidation (ν_4) and spin/coordination state (ν_3 and ν_2) of the heme cofactor [18]. The UV-vis absorption spectra of WT SviDyP, ScoDyP, and CboDyP revealed a Soret band around 410 nm, Q-bands at approximately 500 and 550 nm, and a charge-transfer (CT) band at 630 nm (Figure 2.2 A). The CT band suggested the presence of HS heme species. The high frequency region of the RR spectra, Figure 2.2 B, showed the presence of a 6cHS species, revealed by ν_4, ν_3 and ν_2 marker bands at 1370, 1481, and 1560 cm^{-1}, respectively, Table S 2.1.The UV-vis absorption spectra of TfuDyP showed the Soret band at 411 nm, Q-bands at 540 nm and 575 nm, and the absence of the CT bands, Figure 2.2 A. The lack of CT bands indicated the presence of LS heme species, which is corroborated by the RR spectrum, Figure 2.2 B, that demonstrates a homogeneous 6cLS population with characteristic ν_4, ν_3, and ν_2 marker bands at 1378, 1509, and 1585 cm^{-1}, Table S 2.1.

The UV-vis absorption spectrum of PpDyP showed Soret, Q- and CT bands at 406, 506 and 636 nm, respectively (Figure S 2.4 D). A fingerprint indicative of two co-existing ferric heme species was revealed by the RR spectra, showing the presence of the well-distinguished ν_3 bands at 1493 cm^{-1} and 1502 cm^{-1}, characteristic for a

5cHS and a 5-coordinated quantum mechanically mixed-spin (5cQS), respectively (Table S 2.2) [22].

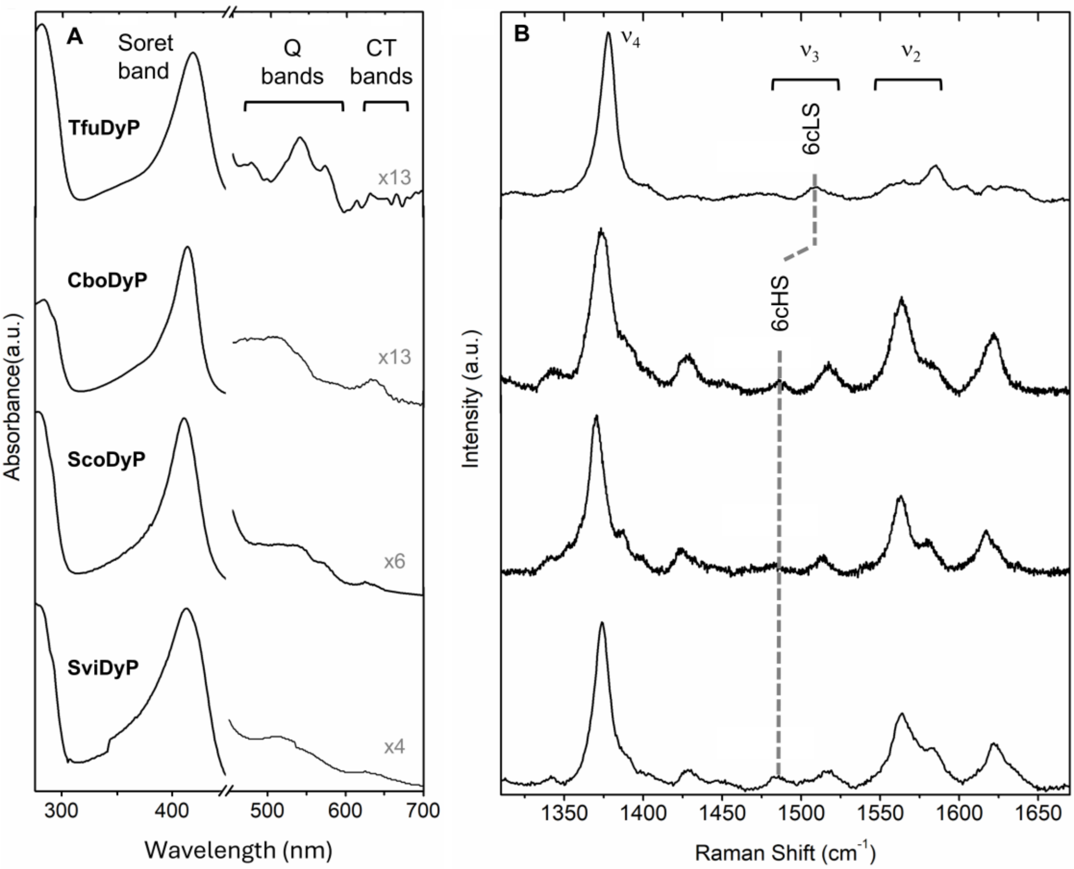

Figure 2.2 - Spectroscopic characterization of ferric WT: TfuDyP, CboDyP, ScoDyP and SviDyP (**A**) UV-vis absorption spectra at pH 8 and (**B**) High-frequency region of the RR spectra. All the RR spectra were acquired at 21 °C except for the spectra of ScoDyP (−50 °C). A 405 nm excitation was used to acquire the RR spectra except for TfuDyP, which was obtained with 413 nm excitation. Experimental details can be found in materials and methods.

In search of the most promising DyP candidate for biotechnological applications, only the enzymes with an active site structure indicative of catalytically competent heme species (5cHS, 6cHS, or 5cQS) were considered. Spectroscopic characterization showed that this criterion was fulfilled by SviDyP, ScoDyP, and CboDyP and PpDyP.

2.2.3. Redox properties of DyPs

Herein, the $E^{0'}_{Fe(III)/Fe(II)}$ of the studied DyPs in solution was probed by monitoring the heme reduction/oxidation using UV-vis absorption spectroelectrochemistry via the changes in the Soret bands as a function of applied potential (Figure 2.3). This value is important as indicates the stability and availability of the resting-state ferric enzyme [Fe(III)] for the catalytic reaction [21].

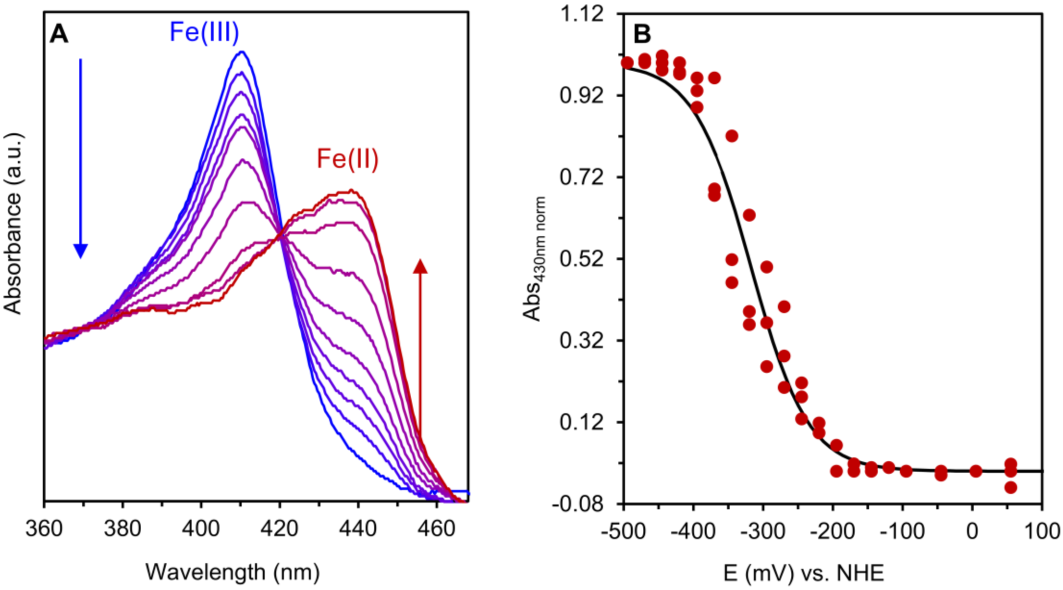

Figure 2.3 - (A) UV-vis absorption spectral changes along the reductive titration of SviDyP performed from +305 mV (blue line) to −490 mV (red line). **(B)** The relative absorption of ferrous protein at 430 nm plotted as a function of cell potential; data was collected from three independent titrations. The solid line represented the fit of the experiment data to the Nernst equation, yielding $E^{0'} = -320 \pm 3$ mV.

Both reductive and oxidative titration were monitored to ensure that no hysteresis occurred, meaning that the $E^{0'}_{Fe(III)/Fe(II)}$ values were consistent and independent of the titration direction. However, despite using equimolar concentrations of enzymes and mediators, hysteresis was observed in the case of WT ScoDyP and SviDyP (Figure S 2.2). For these cases, the titration that, upon the fit of the experimental data to the Nerst equation (Equation 2.1), gave a number of electrons (n) ~1 (Equation 2.1) was chosen as the representative of the $E^{0'}$ of the enzymes. Hysteresis is hypothesized to result from the combination of two factors: the presence of residual

O_2 in the solution and conformational changes in the enzyme due to possible interaction with the mediators [40].

$E^{0'}_{Fe(III) / Fe(II)}$ of WT SviDyP, CboDyP, TfuDyP and PpDyP all fall around −320 mV, Table 2.1, and are among the lowest reported for DyPs (Table 2.1); ScoDyP presents a more positive $E^{0'}_{Fe(III) / Fe(II)}$ (−170 ± 2 mV, Table 2.1). The $E^{0'}$ of the DyPs studied here, together with those reported for other bacterial DyPs, revealed a wide range of potentials (−40 to −320 mV, Table 2.1) that aligns well with other peroxidases [21], which is interesting given the apparent lack of sequence or structural homology between the enzymes [14]. This broad range of $E^{0'}$ highlights the significant role of the protein matrix in fine-tuning the heme group's redox properties, which in turn influences the catalytic specificity of these enzymes.

Table 2.1 - Reduction potentials ($E^{0'}$) of WT DyPs.

Enzyme[a]	**$E^{o'}$ / mV (vs. NHE)**	**Ref.**
SviDyP	−320 ± 3	This work
ScoDyP	−170 ± 2	
TfuDyP	−325 ± 24	
CboDyP	−320 ± 10	
PpDyP	−290 ± 5	
BsDyP	−40	[24]
DrDyP	−81	[20]
DyP2	−85	[27]
TcDyP	−136	[8]
KpDyP	−350	[11]

[a] Recombinant DyPs from different organisms: *S. viridis* (SviDyP); *S.coelicolor* (ScoDyP); *T. fusca* (TfuDyP); *C. bogoriensis* (CboDyP); *P. putida* (PpDyP); *B. subtilis* (BsDyP); *D. radiodurans* (DrDyP); *Amycolatopsis* sp. 75iv2 (DyP2); *T. curvata* (TcDyP) and *K. pneumoniae* (KpDyP).

2.2.3.1. *DyP engineered variants*

Enzyme engineering enables the customization of DyPs for specific applications [1]. Common strategies include site-directed mutagenesis, often used to assess the role of specific amino acids in the DyP catalytic cycle [8,10,11,25,41−43], as well as directed evolution [1] and *in silico* protein design [33], both of which aim to create highly efficient and stable enzymes.

In this work, site-directed mutagenesis was used to create distal variants of CboDyP and PpDyP in an attempt to upshift their $E^{0'}_{Fe(III)\,/\,Fe(II)}$. The *in silico* engineering was used to create variants of PpDyP (PpPyP FireProt and PpDyP PROSS) that show higher thermostability than the WT PpDyP. The biochemical characterization in solution of these variants revealed that they have improved catalytic properties, i.e., higher activity towards H_2O_2 and stability, compared to the WT PpDyP [33].

2.2.3.1.a. Targeting improved redox properties

The conserved distal Arg, R307 in CboDyP and R214 in PpDyP, were substituted by hydrophobic residues: either the non-polar Ile or the amphipathic Trp (Figure 2.4). Due to their hydrophobicity, these residues were selected as likely candidates capable of upshifting the $E^{0'}_{Fe(III)\,/\,Fe(II)}$ of CboDyP and PpDyP.

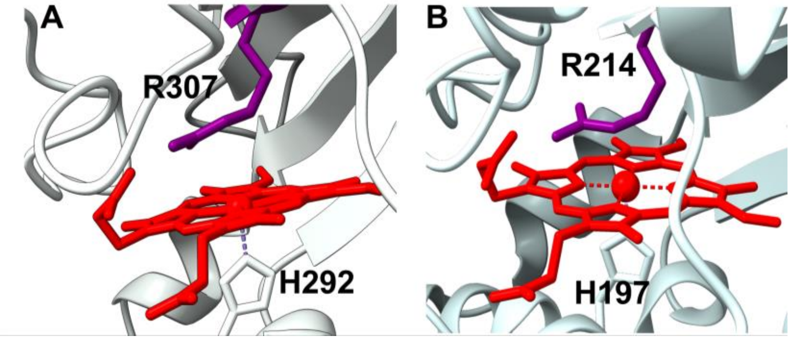

Figure 2.4 - Structural details of the heme cavity of (**A**) WT CboDyP (PDB code:6QZO) and (**B**) WT PpDyP (PDB code: 7QYQ) highlighting the mutated distal arginine (purple). Image generated using Chimera X.

Although the role of the conserved distal Arg in the catalytic cycle of DyPs is not fully understood, it appears to be a critical amino acid for some DyPs, including WT PpDyP, being involved in the formation of Compound I (cf. Chapter 1.2.2). The UV-vis absorption spectra of CboDyP R307W and R307I variants were identical to those of the WT CboDyP, Figure S 2.4 A-C, suggesting that no major alterations occured in the active site. RR spectroscopy indicated that CboDyP R307W indeed possessed a uniform 6cHS population, with the ν_4, ν_3 and ν_2 marker bands centered at 1373, 1483 and 1563 cm^{-1} (Figure 2.5 B, and Table S 2.3), respectively, as previously observed for the WT enzyme [19]. Component analysis of the RR spectrum of the CboDyP R307I variant indicated the presence of a predominant 6cHS species but also an additional 6cLS population (ν_4, ν_3 and ν_2 bands at 1375, 1508 and 1582 cm^{-1}) with a relative abundance ca. 25 % (Figure 2.6 C, Table 2.2 and S 2.2).

Table 2.2 - Relative intensities of the ν_3 modes of each spin population observed in the RR spectra of the ferric CboDyP and PpDyP distal variants *From Sezer et al. [24].

	CboDyP			**PpDyP**		
	WT	**R307W**	**R307I**	**WT***	**R214W**	**R214I**
6cHS	100	100	75	6	60	-
6cLS	-	-	25	2	40	100
5cQS	-	-	-	63	-	-
5cHS	-	-	-	29	-	-

The UV-vis absorption spectra of PpDyP variants indicated that the heme structure is strongly affected by the R214 substitution, Figure S 2.4 D-F. The Soret and the Q-bands red-shifts 8 - 14 and ca. 30 nm in the variant's spectra compared with WT enzyme [25]. The absence of CT bands in the PpDyP R214I spectrum suggested that in contrast to WT enzyme, HS heme species are absent. The RR spectra of PpDyP R214W and R214I revealed that the two major species identified in the RR spectrum of WT PpDyP, i.e., the 5cHS and 5cQS populations, were absent in the spectra of the variants (Figure 2.6, Table 2.2).

RR spectra of PpDyP R214W showed the presence of 6cHS and 6cLS populations (ν_4, ν_3 and ν_2 bands centered at 1372, 1483 and 1564 cm^{-1} and at 1375, 1507 and 1582 cm^{-1}, respectively), while PpDyP R214I variant revealed a uniform 6cLS population (ν_4, ν_3, and ν_2 marker bands centered at 1376, 1507 and 1581 cm^{-1}; Figure

2.7, Table 2.2 and Table S2.2). These species represented only minor contributions (< 10 %) in the RR spectra of WT PpDyP [24], which is consistent with drastic structural alterations of the distal heme pocket of PpDyP variants.

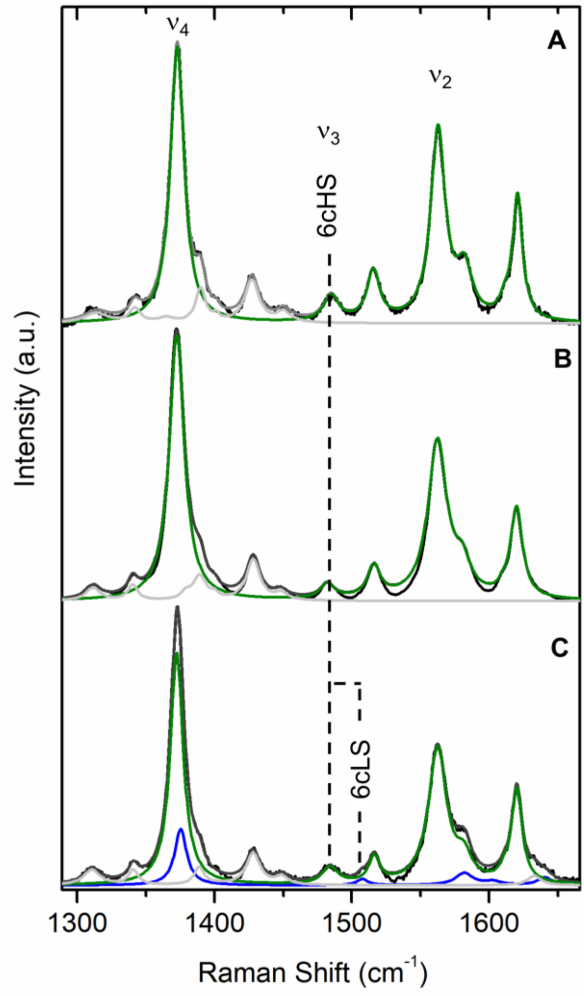

Figure 2.5 - Experimental and component RR spectra of ferric CboDyP and variants. **(A)** WT, **(B)** R307W, and **(C)** R307I. The component spectra representing 6cHS (green) and 6cLS (blue) heme species and non-assigned bands (light grey) are fitted to the experimental spectra (black); the overall component spectra are depicted in dark grey. The spectra of 20 - 80 μM proteins were measured with 405 nm excitation and 3 mW laser power.

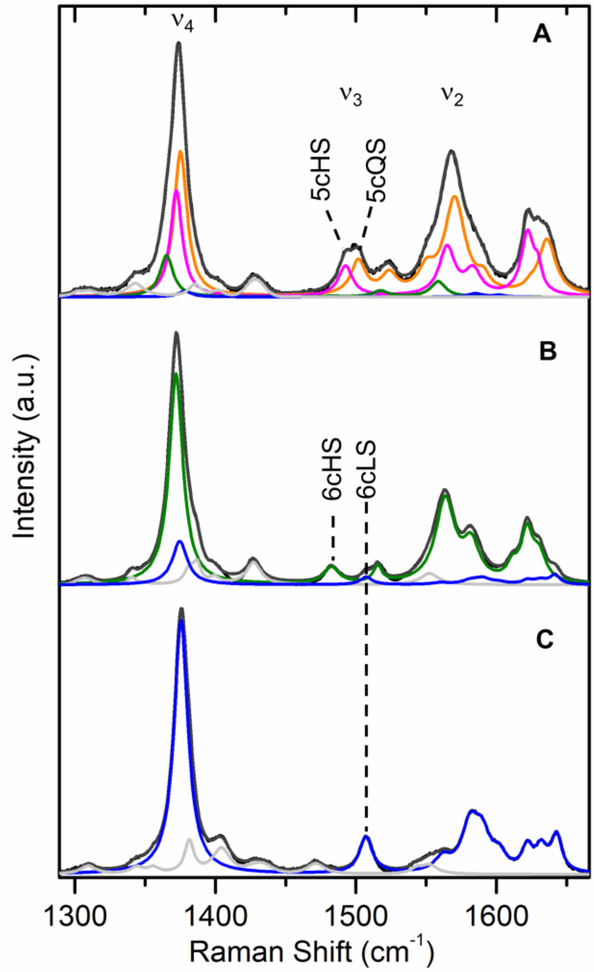

Figure 2.6 - Experimental and component RR spectra of ferric WT PpDyP and variants. (**A**) WT; (**B**) R214W and (**C**) R214I. The component spectra representing 6cHS (green), 6cLS (blue), 5cHS (magenta), and 5cQS (orange) heme species and non-assigned bands (light grey) are fitted to the experimental spectra (black); the overall component spectra are depicted in dark grey. Spectra of 20-80 µM proteins were measured at 405 nm excitation and 3 mW laser power.

We demonstrated here that the replacement of the distal Arg in PpDyP variants (and to a lower extent also in CboDyP) led to the formation of 6cHS and 6cLS, carrying a thus far unknown distal ligand since neither Ile or Trp are likely to coordinate the heme iron. The formation of these heme species results from the highly flexible heme pocket observed in resting state peroxidases, which can adopt different configurations. Usually, peroxidases have a 5cHS heme iron with a sixth axial position vacant for H_2O_2 binding and/or a 6cHS configuration in which the heme carries a loosely bound axial ligand [44].

Owing to its importance for catalysis (cf Chapter 1.2.2), Arg variants of DyPs from different organisms have been previously studied. The substitution of the Arg residue was shown to have a variable effect on the heme cavity structure. Moderate to complete attenuation of CT bands in the UV-vis absorption spectra was observed in the case of Arg/Leu substituted PpDyP and DyPB from *Rhodococcus jostii* RHA1 [25,41], which is indicative of a formation of LS species. On the other hand, in the case of Arg/Ala variants of BsDyP from *B. subtilis*, KpDyP from *K. pneumoniae*, TcDyP from *T. curvata* and ElDyP from *Enterobacter lignolyticus* [8,10,11,42,43] very subtle or no spectral differences were reported, indicative that substitution of the Arg did not influence the heme pocket.

From the evaluation of the active site structure, it could be concluded that both CboDyP variants and PpDyP R214W were promising biocatalysts for biotechnological applications, since they can readily bind H_2O_2. In contrast, the PpDyP R214I variant was discarded at this point since it had a homogenous 6cLS heme population that is catalytically incompetent.

Probing the $E^{0'}_{Fe(III)\,/\,Fe(II)}$ of CboDyP and PpDyP variants. The CboDyP R307W/I revealed a comparable $E^{0'}_{Fe(III)\,/\,Fe(II)}$ (−160 ± 12 mV for R307W and −155 ± 20 mV for R307I), which were nevertheless significantly upshifted compared to the WT enzyme ($E^{0'}_{Fe(III)\,/\,Fe(II)}$ = −320 ± 10 mV, Table 2.3). Based on pure electrostatic effects, removing the positively charged Arg should contribute to the stabilization of the Fe(III) form, thereby decreasing the $E^{0'}_{Fe(III)\,/\,Fe(II)}$ of the variants. We propose that the upshifted $E^{0'}_{Fe(III)\,/\,Fe(II)}$ is a consequence of decreased hydration of the heme environment due to the introduction of the hydrophobic Trp and Ile residues in the heme cavity. According to the Kassner relation, the increase in hydrophobicity can account for up to 200 mV upshifts of $E^{0'}_{Fe(III)\,/\,Fe(II)}$ in heme proteins [45]. The $E^{0'}_{Fe(III)\,/\,Fe(II)}$ values of the two PpDyP variants did not show significant differences (−270 ± 10 mV and −260 ± 10 mV for PpDyP R214W and R214I, respectively) and were comparable to the $E^{0'}$ of the WT PpDyP (Table 2.3). This case-dependent influence of the Arg substitution on $E^{0'}$, observed for CboDyP and PpDyP, was in agreement with the previous studies, which demonstrated that in other DyPs, different outcomes of the Arg substitution were observed. In KpDyP, a negligible $\Delta E^{0'}$ was observed for Arg/Leu substitution [11]; in BsDyP, a negative shifted $E^{0'}$ was determined for the Arg/Leu variant [43] and in the Arg/Ala variant of TcDyP [8].

Table 2.3 - $E^{0'}$ of CboDyP, PpDyP and other reported distal variants.

		Enzyme	**$E^{0'}_{Fe(III)/Fe(II)}$/ mV (vs. NHE)**	**Reference**
CboDyP	**Distal variants**	**R307W**	−160 ± 12	This work
		R307I	−155 ± 20	
PpDyP	**Distal variants**	**R214I**	−270 ± 10	
		R214W	−260 ± 10	
	***in silico* variants**	**FireProt**	−300 ± 20	
		PROSS	−310	
BsDyP variants			–70 to – 120	[43]
TcDyP variants			–130 to –210	[8]
KpDyP variants			–300 to –350	[11]

Notably, compared to the WT enzymes all distal variants present decreased catalytic activity for ABTS oxidation, a common compound used to probe the activity of DyPs, (Figure S 2.5).

2.2.3.1.b. Targeting improved catalytic properties and stability of PpDyP

Variants of PpDyP were engineered following *in silico* design targeting higher thermostability, employing two different algorithms called FireProt and PROSS. PpDyP FireProt contained 21 mutations, while PpDyP PROSS contained 29 mutations (Figure 2.7) [33], dispersed across the enzyme structure, mainly presented at its surface.

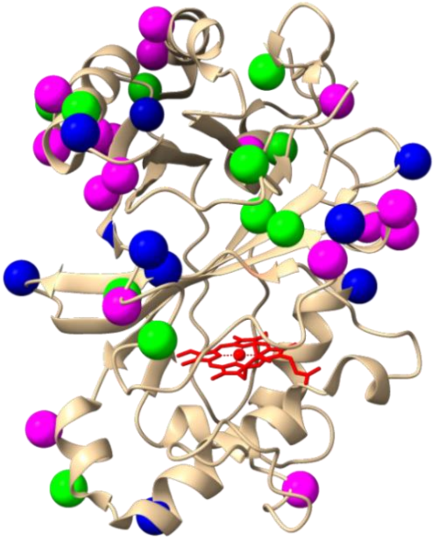

Figure 2.7 - PpDyP structure with substituted positions in the *in silico* design variants highlighted. Magenta colored spheres are the replaced amino acids suggested by PROSS, green by FireProt algorithms, and blue suggested by both algorithms. Image generated using Chimera X.

Nevertheless, both algorithms suggested substitutions at 11 - 12 Å distance from the heme (two in the case of FireProt and one in the case of PROSS). The two algorithms indicate the substitution of V217M and also, in the case of the FireProt, the H125R [33], which introduced a sulfur-containing amino acid (Met) and an additional positively charged amino acid (Arg) near the heme active site. Given that both substitutions involve relatively bulky amino acids, it is expected that structural changes in the heme cavity are likely to occur. Biochemical characterization of the variants in solution showed that both variants exhibited increased protein expression and stability, including higher melting temperatures and delayed aggregation while showing increased activity for H_2O_2 compared to the WT PpDyP [33].

UV-vis absorption (Figure S 2.6) and RR spectroscopic characterization (Figure 2.8) demonstrated that both variants displayed similar spectral features to those of the WT enzyme. The Soret band was found at 404 nm, Q-bands at 503 and 534 nm, and a CT band at 640 nm (Figure S 2.6). The RR spectra revealed the presence of the same two significant heme populations as in WT PpDyP, 5cQS (ν_4, ν_3, and ν_2 1376, 1502 and 1572 cm^{-1}, respectively), and 5cHS (ν_4, ν_3, and ν_2 1372, 1493 and 1565 cm^{-1}, respectively) (Figure 2.8 and Table S 2.2). However, the relative abundance of each heme species differs between PpDyP FireProt, PpDyP PROSS and the WT enzyme

(Table 2.4), which can be attributed to the subtle influence of the amino acid substitution near the active site. Due to the presence of the catalytically competent heme species, both variants represented promising candidates to be explored as immobilized biocatalysts for biosensing applications.

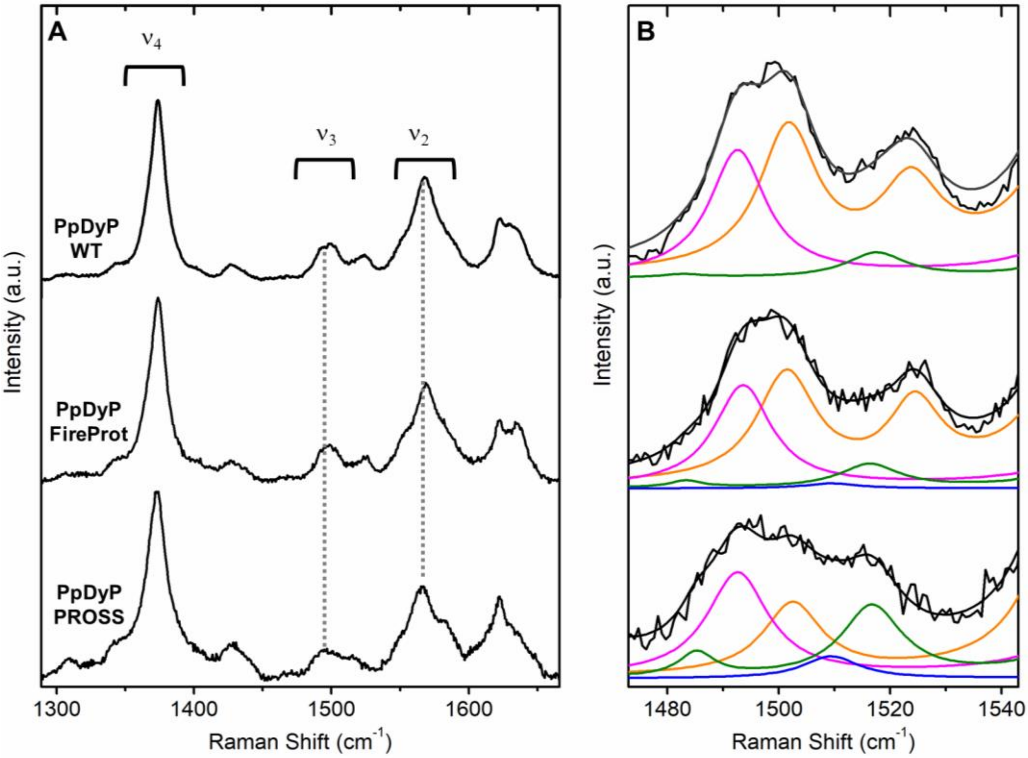

Figure 2.8 - (**A**) High frequency RR spectra of ferric PpDyP WT and variants at pH 7.6. (**B**) Component analysis of the respective ν_3/ν_{38} region. The component spectra represent the 5cQS (orange), 5cHS (magenta), 6cHS (green), and 6cLS (blue) heme species.The 20 - 80 µM protein spectra were measured with 405 nm excitation and 3 mW laser power

Probing the $E^{0'}_{Fe(III) / Fe(II)}$ of the "in silico" variants. Despite the presence of a large number of amino acids replaced in the structure of PpDyP FireProt and PROSS, their $E^{0'}_{Fe(III) / Fe(II)}$ −300 ± 20 and −310 ± 15 , respectively, were comparable to that of the WT enzyme (–290 ± 5 mV, Table 2.3). Interestingly, all PpDyP variants studied in this work, distal and *in silico* engineered, presented an $E^{0'}_{Fe(III) / Fe(II)}$ comparable to that of the WT enzyme. This is possibly due to the highly flexible heme cavity (more evident for the distal variants), which could stabilize the same ferric species as the WT and preserve its redox properties, Table 2.3. Notably, it was previously shown that the $E^{0'}_{Fe(III)\,/\,Fe(II)}$ of a directed evolution variant (6E10), which has four substitutions on the second shell of the heme cavity, actually has a reduction potential up-shifted ca. ~ 200 mV ($E^{0'}_{Fe(III)\,/\,Fe(II)} = -60$ mV) when compared to the WT enzyme [3]. The comparison of the upshift of potential for the 6E10 variant with either the herein studied *in silico* design or the distal variants highlights the importance of the electrostatic and hydrogen bond network of the second coordination shell of the active site of PpDyP.

2.4. Concluding remarks

In our search for the best DyP candidate for biosensing applications, we started with DyPs from seven bacterial sources. Among these, $SviDyP_D$, Yfex, and TceDyP were purified mainly as metal-free porphyrin-containing enzymes, while ScoDyP, TfuDyP, CboDyP, and PpDyP were obtained as heme-containing enzymes.

Our RR spectroscopic analysis indicated that WT SviDyP, ScoDyP, CboDyP, PpDyP, the distal variants of CboDyP and PpDyP (R214W), together with the *in silico* engineered variants of PpDyP, all appear to be promising candidates to be used as biocatalysts in biosensing applications since they retained catalytically compotent active site structure under physiological conditions.

The determination of the $E^{0'}_{Fe(III)\,/\,Fe(II)}$ in solution of WT SviDyP, ScoDyP, TfuDyP, CboDyP, and PpDyP revealed that their values were comparable. This indicated that the reduction potential was not the determinant factor when choosing the most promising DyP candidate for further development of biosensing devices. Interestingly, the Nernst curves obtained for all probed enzymes, including those that existed as a mixture of spin populations, i.e., CboDyP R307I, PpDyP FireProt, PpDyP PROSS, and PpDyP R214W, revealed a single redox transition, which suggested that the $E^{0'}$ values of the different populations are probably very close.

2.5. References

[1] Y. Sugano, Dyp-Type Peroxidases Comprise a Novel Heme Peroxidase Family, Cell Mol Life Sci 66 (2009) 1387–1403. https://doi.org/10.1007/s00018-008-8651-8.

[2] T. Yoshida, Y. Sugano, A Structural and Functional Perspective of Dyp-Type Peroxidase Family, Arch Biochem Biophys 574 (2015) 49–55. https://doi.org/10.1016/j.abb.2015.01.022.

[3] V. Brissos, D. Tavares, A.C. Sousa, M.P. Robalo, L.O. Martins, Engineering a Bacterial Dyp-Type Peroxidase for Enhanced Oxidation of Lignin-Related Phenolics at Alkaline pH, ACS Catal. 5 (2017) 3454–3465. https://doi.org/10.1021/acscatal.6b03331.

[4] D.I. Colpa, M.W. Fraaije, E. van Bloois, Dyp-Type Peroxidases: a Promising and Versatile Class of Enzymes, J Ind Microbiol Biotechnol 41 (2014) 1–7. https://doi.org/10.1007/s10295-013-1371-6.

[5] D. Silva, C.F. Rodrigues, C. Lorena, P.T. Borges, L.O. Martins, Biocatalysis for Biorefineries: the Case of Dye-Decolorizing Peroxidases, Biotechnol Adv 65 (2023). https://doi.org/10.1016/j.biotechadv.2023.108153.

[6] J.N. Roberts, R. Singh, J.C. Grigg, M.E.P. Murphy, T.D.H. Bugg, L.D. Eltis, Characterization of Dye-Decolorizing Peroxidases from *Rhodococcus jostii* RHA1, Biochem 50 (2011) 5108–5119. https://doi.org/10.1021/bi200427h.

[7] M.H. Habib, H.J. Rozeboom, M.W. Fraaije, Characterization of a New DyP-Peroxidase from the Alkaliphilic Cellulomonad, Cellulomonas bogoriensis, Molecules 24 (2019) 1208. https://doi.org/10.3390/molecules24071208

[8] C. Chen, R. Shrestha, K. Jia, P.F. Gao, B. V. Geisbrecht, S.H. Bossmann, J. Shi, P. Li, Characterization of Dye-Decolorizing Peroxidase (DyP) from *Thermomonospora curvata* reveals unique catalytic properties of A-type DyPs, J Biol Chem 290 (2015) 23447–23463. https://doi.org/10.1074/jbc.M115.658807.

[9] E. Van Bloois, D.E. Torres Pazmiño, R.T. Winter, M.W. Fraaije, A Robust and Extracellular Heme-Containing Peroxidase from *Thermobifida fusca* as Prototype of a Bacterial Peroxidase Superfamily, Appl Microbiol Biotechnol 86 (2010) 1419–1430. https://doi.org/10.1007/s00253-009-2369-x.

[10] V. Pfanzagl, M. Bellei, S. Hofbauer, C.V.F.P. Laurent, P.G. Furtmüller, C. Oostenbrink, G. Battistuzzi, C. Obinger, Redox thermodynamics of B-class Dye-Decolorizing Peroxidases, J Inorg Biochem 199 (2019) 110761. https://doi.org/10.1016/j.jinorgbio.2019.110761

[11] V. Pfanzagl, K. Nys, M. Bellei, H. Michlits, G. Mlynek, G. Battistuzzi, K. Djinovic-Carugo, S. Van Doorslaer, P.G. Furtmüller, S. Hofbauer, C. Obinger, Roles of Distal Aspartate and Arginine of B-class Dye-Decolorizing Peroxidase in Heterolytic Hydrogen Peroxide Cleavage, J Biol Chem 293 (2018) 14823–14838. https://doi.org/10.1074/jbc.RA118.004773.

[12] R. Singh, J.C. Grigg, Z. Armstrong, M.E.P. Murphy, L.D. Eltis, Distal Heme Pocket Residues of B-type Dye-Decolorizing Peroxidase: Arginine but not Aspartate is Essential for Peroxidase Activity, J Biol Chem 287 (2012) 10623–10630. https://doi.org/10.1074/jbc.M111.332171.

[13] C. Zubieta, S.S. Krishna, M. Kapoor, P. Kozbial, D. McMullan, H.L. Axelrod, M.D. Miller, P. Abdubek, E. Ambing, T. Astakhova, D. Carlton, H. Chiu, T. Clayton, M.C. Deller, L. Duan, M. Elsliger, J. Feuerhelm, S.K. Grzechnik, J. Hale, E. Hampton, G.W. Han, L. Jaroszewski, K.K. Jin, H.E. Klock, M.W. Knuth, A. Kumar, D. Marciano, A.T. Morse, E. Nigoghossian, L. Okach, S. Oommachen, R. Reyes, C.L. Rife, P. Schimmel, H. van den Bedem, D. Weekes, A. White, Q. Xu, K.O. Hodgson, J. Wooley, A.M. Deacon, A. Godzik, S.A. Lesley, I.A. Wilson, Crystal Structures of two Novel Dye-Decolorizing Peroxidases Reveal a β-barrel Fold with a Conserved Heme-Binding Motif, Proteins: Struct Funct, Bioinform 69 (2007) 223–233. https://doi.org/10.1002/prot.21550.

[14] T. Yoshida, Y. Sugano, Unexpected diversity of dye-decolorizing peroxidases, Biochem Biophys Rep 33 (2023) 101401. https://doi.org/10.1016/j.bbrep.2022.101401.

[15] G. Smulevich, A. Feis, B.D. Howes, Fifteen Years of Raman Spectroscopy of Engineered Heme Containing Peroxidases: What Have We Learned?, Acc Chem Res 38 (2005) 433–440. https://doi.org/10.1021/ar020112q.

[16] X. Liu, Q. Du, Z. Wang, D. Zhu, Y. Huang, N. Li, T. Wei, S. Xu, L. Gu, Crystal Structure and Biochemical Features of EfeB/YcdB from *Escherichia coli* O157, J Bio Chem 286 (2011) 14922–14931. https://doi.org/10.1074/jbc.M110.197780.

[17] A. Sturm, A. Schierhorn, U. Lindenstrauss, H. Lilie, T. Brüser, YcdB from *Escherichia coli* Reveals a Novel Class of Tat-dependently Translocated Hemoproteins, J Bio Chem 281 (2006) 13972–13978. https://doi.org/10.1074/jbc.M511891200.

[18] F. Siebert, P. Hildebrandt, Vibrational Spectroscopy in Life Science. Wiley, 2007. https://doi.org/10.1002/9783527621347.

[19] C.M. Silveira, E. Moe, M. Fraaije, L.O. Martins, S. Todorovic, Resonance Raman View of the Active Site Architecture in Bacterial Dyp-Type Peroxidases, RSC Adv 10 (2020) 11095–11104. https://doi.org/10.1039/D0RA00950D.

[20] K. Frade, C.M. Silveira, B.A. Salgueiro, S. Mendes, L.O. Martins, C. Frazão, S. Todorovic, E. Moe, Biochemical, Biophysical, and Structural Analysis of an Unusual DyP from the Extremophile *Deinococcus radiodurans*, Molecules 29 (2024) 358. https://doi.org/10.3390/molecules29020358.

[21] G. Battistuzzi, M. Bellei, C.A. Bortolotti, M. Sola, Redox Properties of Heme Peroxidases, Arch Biochem Biophys 500 (2010) 21–36. https://doi.org/10.1016/j.abb.2010.03.002.

[22] M.S. Mondal, H.A. Fuller, F.A. Armstrong, Direct Measurement of the Reduction Potential of Catalytically Active Cytochrome *c* Peroxidase Compound I: Voltammetric Detection of a Reversible, Cooperative Two-Electron Transfer Reaction, J Am Chem Soc 118 (1996) 263–264. https://doi.org/10.1021/ja952489f.

[23] M. Sezer, T. Genebra, S. Mendes, L.O. Martins, S. Todorovic, A DyP-type Peroxidase at a Bio-Compatible Interface: Structural and Mechanistic Insights, Soft Matter 8 (2012) 10314–10321. https://doi.org/10.1039/c2sm26310f.

[24] M. Sezer, A. Santos, P. Kielb, T. Pinto, L.O. Martins, S. Todorovic, Distinct Structural and Redox Properties of the Heme Active Site in Bacterial Dye Decolorizing Peroxidase-Type Peroxidases from Two Subfamilies: Resonance Raman and Electrochemical Study, Biochem 52 (2013) 3074–3084. https://doi.org/10.1021/bi301630a.

[25] S. Mendes, V. Brissos, A. Gabriel, T. Catarino, D.L. Turner, S. Todorovic, L.O. Martins, An Integrated View of Redox and Catalytic Properties of B-type PpDyP from *Pseudomonas putida* MET94 and its distal variants, Arch Biochem Biophys 574 (2015) 99–107. https://doi.org/10.1016/j.abb.2015.03.009.

[26] D.H. Murgida, P. Hildebrandt, S. Todorovic, Immobilized Redox Proteins: Mimicking Basic Features of Physiological Membranes and Interfaces, in: Biomimetics Learning from Nature, InTech, 2010: pp. 21–48. https://doi.org/10.5772/8778.

[27] M.E. Brown, T. Barros, M.C.Y. Chang, Identification and Characterization of a Multifunctional Dye Peroxidase from a Lignin-Reactive Bacterium, ACS Chem Biol 7 (2012) 2074–2081. https://doi.org/10.1021/cb300383y.

[28] C. Barbosa, C.M. Silveira, D. Silva, V. Brissos, P. Hildebrandt, L.O. Martins, S. Todorovic, Immobilized Dye-Decolorizing Peroxidase (DyP) and Directed Evolution Variants for Hydrogen Peroxide Biosensing, Biosen. Bioelectron. 153 (2020) 112055. https://doi.org/10.1016/j.bios.2020.112055.

[29] D.I. Colpa, M.W. Fraaije, High overexpression of dye decolorizing peroxidase TfuDyP leads to the incorporation of heme precursor protoporphyrin IX, J Mol Catal B Enzym 134 (2016) 372–377. https://doi.org/10.1016/j.molcatb.2016.08.017.

[30] N. Lončar, D.I. Colpa, M.W. Fraaije, Exploring the Biocatalytic Potential of a DyP-type Peroxidase by Profiling the Substrate Acceptance of *Thermobifida fusca* DyP peroxidase, Tetrahedron (2016). https://doi.org/10.1016/j.tet.2015.12.078.

[31] D. Sun, M.K. Ostermaier, F.M. Heydenreich, D. Mayer, R. Jaussi, J. Standfuss, D.B. Veprintsev, AAscan, PCRdesign and MutantChecker: A Suite of Programs for Primer Design and Sequence Analysis for High-Throughput Scanning Mutagenesis, PLoS One 8 (2013) e78878. https://doi.org/10.1371/journal.pone.0078878.

[32] A. Santos, S. Mendes, V. Brissos, L.O. Martins, New Dye-Decolorizing Peroxidases from *Bacillus subtilis* and *Pseudomonas putida* MET94: Towards Biotechnological Applications, Appl. Microbiol. Biotechnol. 98 (2014) 2053–2065. https://doi.org/10.1007/s00253-013-5041-4.

[33] D. Silva, A Closer Look at a Potential Biocatalyst: Unravelling the Catalytic, Stability and Structural Features of PpDyP, a DyP-type Peroxidase. Doctoral dissertation, Universidade Nova de Lisboa, 2022. https://hdl.handle.net/10362/158343.

[34] E.A. Berry, B.L. Trumpower, Simultaneous Determination of Hemes *a*, *b*, and *c* from Pyridine Hemochrome Spectra, Anal Biochem 161 (1987) 1–15. https://doi.org/10.1016/0003-2697(87)90643-9.

[35] S. Döpner, P. Hildebrandt, A.G. Mauk, H. Lenk, W. Stempfle, Analysis of Vibrational Spectra of Multicomponent Systems. Application to pH-Dependent Resonance Raman Spectra of Ferricytochrome *c*, Spectrochim Acta A 51 (1996) 573–584.

[36] K. Fiege, C.J. Querebillo, P. Hildebrandt, N. Frankenberg-Dinkel, Improved Method for the Incorporation of Heme Cofactors into Recombinant Proteins Using Escherichia coli Nissle 1917, Biochem 57 (2018) 2747–2755. https://doi.org/10.1021/acs.biochem.8b00242.

[37] M. Gouterman, Optical Spectra and Electronic Structure of Porphyrins and Related Rings. In: The Porphyrins, Elsevier, 1978: pp. 1–165. https://doi.org/10.1016/b978-0-12-220103-5.50008-8.

[38] B.F. Kim, J. Bohandy, Spectroscopy of Porphyrins., Johns Hopkins APL Technical Digest 2 (1981) 153–163.

[39] W. Yu, W. Liu, H. Huang, F. Zheng, X. Wang, Y. Wu, K. Li, X. Xie, Y. Jin, Application of a Novel Alkali-Tolerant Thermostable DyP-type Peroxidase from *Saccharomonospora viridis* DSM 43017 in Biobleaching of Eucalyptus Kraft Pulp, PLoS One 9 (2014) 1–11. https://doi.org/10.1371/journal.pone.0110319.

[40] Y. Jiang, X. Li, B.R. Morrow, A. Pothukuchy, J. Gollihar, R. Novak, C.B. Reilly, A.D. Ellington, D.R. Walt, Single-Molecule Mechanistic Study of Enzyme Hysteresis, ACS Cent Sci 5 (2019) 1691–1698. https://doi.org/10.1021/acscentsci.9b00718.

[41] R. Shrestha, K. Jia, S. Khadka, L.D. Eltis, P. Li, Mechanistic Insights into DyPB from *Rhodococcus jostii* RHA1 via Kinetic Characterization, ACS Catal 11 (2021) 5486–5495. https://doi.org/10.1021/acscatal.1c00703.

[42] R. Shrestha, G. Huang, D.A. Meekins, B. V. Geisbrecht, P. Li, Mechanistic Insights into Dye-Decolorizing Peroxidase Revealed by Solvent Isotope and Viscosity Effects, ACS Catal 7 (2017) 6352–6364. https://doi.org/10.1021/acscatal.7b01861.

[43] S. Mendes, T. Catarino, C. Silveira, S. Todorovic, L.O. Martins, The Catalytic Mechanism of A-type Dye-Decolorizing Peroxidase BsDyP: Neither Aspartate nor Arginine is Individually Essential for Peroxidase Activity, Catal Sci Technol 5 (2015) 5196–5207. https://doi.org/10.1039/C5CY00478K.

[44] G. Smulevich, A. Feis, B.D. Howes, A. Ivancich, Structure-Function Relationships Among Heme Peroxidases: New Insights from Electronic Absorption, Resonance Raman and Multifrequency Electron Paramagnetic Resonance Spectroscopies. In: Handbook of Porphyrin Science, 2010: pp. 367–453. https://doi.org/10.1142/9789814307246_0003.

[45] R.J. Kassner, Theoretical Model for the Effects of Local Nonpolar Heme Environments on the Redox Potentials in Cytochromes, J Am Chem Soc 95 (1973) 2674–2677. https://doi.org/10.1021/ja00789a044.

Supporting Information

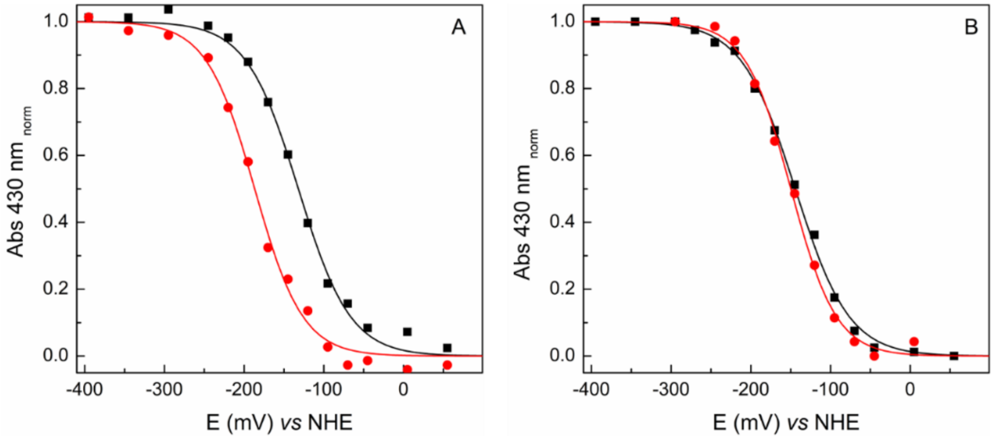

Figure S 2.1 - Oxidative (black squares) and reductive (red circles) titrations of CboDyP variants performed using (**A**) 2:1 and (**B**) 1:1 enzyme:mediator concentration ratio, revealing up to 80 mV shifts in the former case. The relative absorption of the ferrous enzymes at 430 nm is plotted as a function of the cell potential. Solid lines represent the fit of the Nernst equation to the experimental data. When a 2:1 enzyme mediator ratio is used the E°'$_{Fe(III)\,/\,Fe(II)}$ determined from the reductive and oxidative titrations show up to 80 mV differences, while when 1:1 ratio was used both titrations are superimposable.

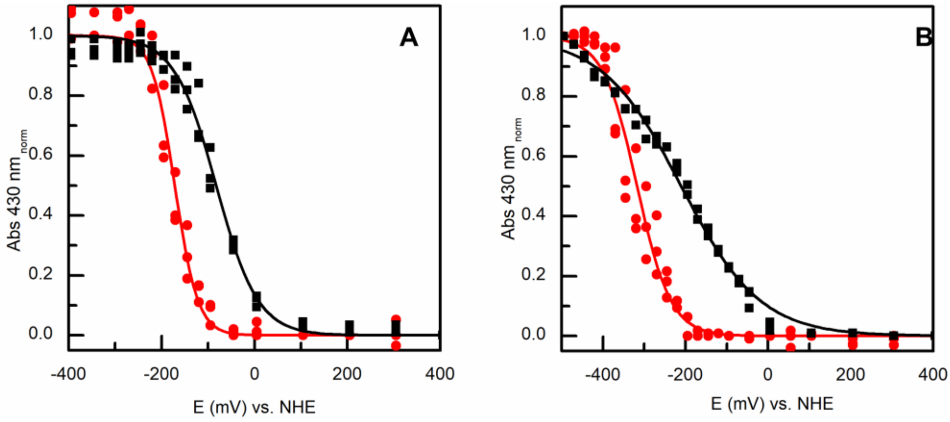

Figure S 2.2 - Oxidative (black squares) and reductive (red circles) titrations of (**A**) ScoDyP and (**B**) SviDyP performed using a 1:1 enzyme:mediator concentration ratio. The relative absorption of the ferrous enzymes at 430 nm is plotted as a function of the cell potential. Solid lines represent the fit of the Nernst equation to the experimental data. The data shown corresponds to three independent titrations for each enzyme. When a 1:1 enzyme mediator ratio is used, the E°'$_{Fe(III)\,/\,Fe(II)}$ determined from the reductive and oxidative titrations show up to 100 mV differences.

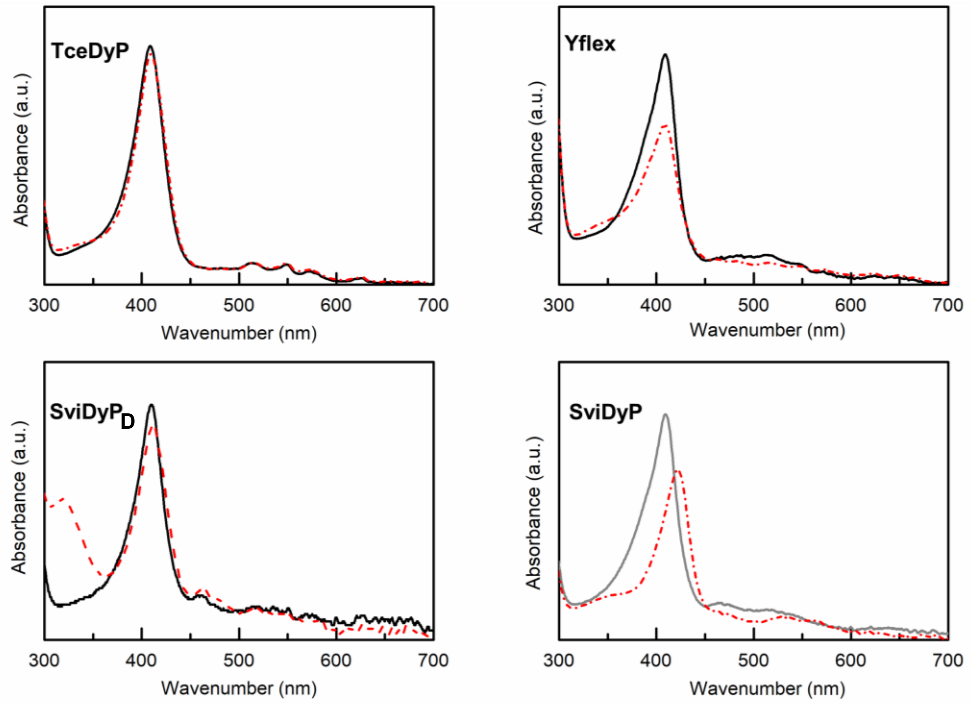

Figure S 2.3 - UV-Vis absorption spectra of metal-free protoporphyrin containing DyPs (black trace): TceDyP, Yfex, and SviDyP$_D$; and heme-containing ferric SviDyP (grey trace) in the absence and presence of sodium dithionite in excess (dashed red trace).

Table S 2.1 - RR marker band modes (νi) for 5cHS,5cQS,6cHS and 6cLS populations in SviDyP,ScoDyP, TfuDyP and CboDyP, determined from the component analysis of the RR spectra of the ferric DyPs. $^{+}$data from [1].

νi (cm^{-1})	SviDyP	ScoDyP*	TfuDyP^{+}	CboDyP^{+}
	6cHS	6cHS	6cLS	6cHS
ν_4	1374	1370	1378	1371
ν_3	1485	1481	1509	1481
ν_2	1565	1562	1585	1561
$\nu_{C=C}$	1620	1615	1629 1640	1619
ν_{10}	-	-	1640	-

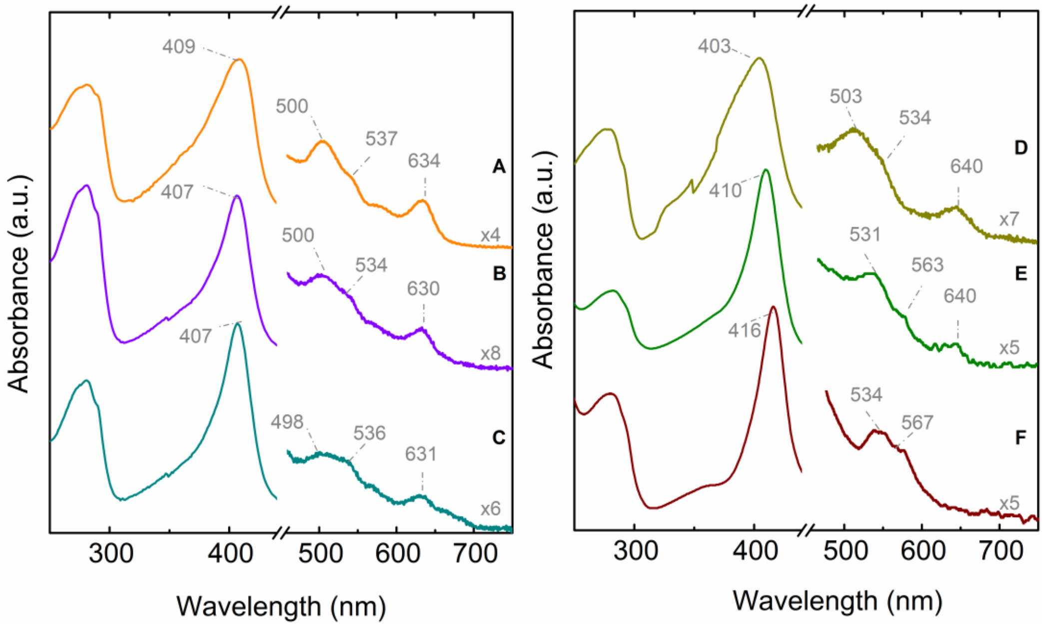

Figure S 2.4 - UV-vis absorption spectra of CboDyP (**A**) WT, (**B**) R307W, (**C**) R307I and PpDyP (**D**) WT, (**E**) R214W, (**F**) R214I.

Table S 2.2 - RR marker band modes (ν_i) for 5cHS,5cQS,6cHS and 6cLS populations in PpDyPs : WT, *in silico* engineered, FireProt and PROSS, and distal variants: R214W and R214I determined from the component analysis of the experimental spectra of the ferric enzymes.

ν_i (cm^{-1})	**PpDyP**						
	WT / FireProt / PROSS				**R214W**		**R214I**
	5cQS	**5cHS**	**6cHS**	**6cLS**	**6cHS**	**6cLS**	**6cLS**
ν_4	1376	1372	1365	1378	1372	1375	1376
ν_3	1503	1493	1483	1509	1483	1507	1507
($^{a}I_{\text{rel }\nu_3}$)	(63/51/47)	(29/44/33)	(6/5/11)	(2/-/9)	(60)	(40)	(100)
ν_2	1572	1565	1518	-	1564	1582	1581
$\nu_{C=C}$	1625	1622	1559	-	-	1622	1622
ν_{10}	1636	1631	-	-	-	1642	1643

$^{a}I_{\text{rel }\nu_3}$ designates the relative intensities of the each ν_3 bands determine from the component analysis with the overall intensity of the ν_3 band observed in the RR spectra of the respective of the ferric DyPs.

Table S 2.3 - RR marker band modes (νi) for 5cHS,5cQS,6cHS and 6cLS populations in CboDyP distal variants determined from the component analysis of the experimental.

	CboDyP		
νi (cm^{-1})	**R307W**	**R307I**	
	6cHS	**6cHS**	**6cLS**
ν_4	1373	1372	1375
ν_3	1483	1484	1508
ν_2	1562	1563	1582
$\nu_{C=C}$	1620	1620	-
ν_{10}	-		1640

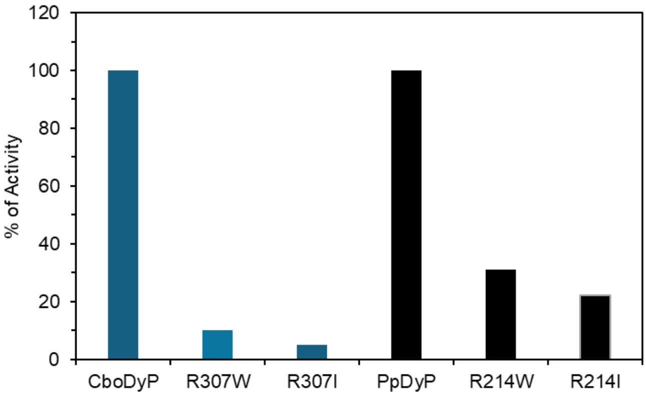

Figure S 2.5 - Percentage of catalytic activity of PpDyP and CboDyP distal variants in comparison with the WT enzymes.

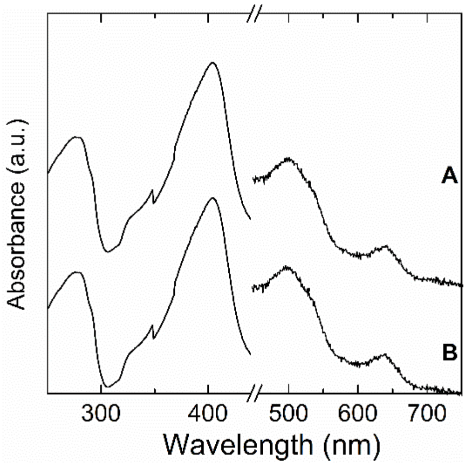

Figure S 2.6 - UV-Vis absorption spectra of PpDyP (**A**)FireProt and (**B**) PROSS.

References

[1] C.M. Silveira, E. Moe, M. Fraaije, L.O. Martins, S. Todorovic, Resonance Raman View of the Active Site Architecture in Bacterial Dyp-Type Peroxidases, RSC Adv 10 (2020) 11095–11104. https://doi.org/10.1039/D0RA00950D.

Chapter 3 Exploring immobilization strategies for the development of amperometric biosensors - Immobilized DyPs

This chapter contains data published in :

Lidia Zuccarello, **Catarina Barbosa**, Edilson Galdino, Nicola Lončar, Célia M. Silveira, Marco W. Fraaije, Smilja Todorovic. SERR Spectroelectrochemistry as a Guide for Rational Design of DyP-Based Bioelectronics Devices. *Int J Mol Sci* 22: 7998, 2021. Doi: 10.3390/ijms22157998.

Catarina Barbosa, Carolina F. Rodrigues, Nicola Lončar, Lígia O. Martins, Smilja Todorovic, Célia M. Silveira. Spectroelectrochemistry for Determination of the Redox Potential in Heme Enzymes: Dye-Decolorizing Peroxidases. *BBA Advances* 5: 100112, 2024. Doi: 10.1016/j.bbadva.2023.100112

Acknowledgments and contributions

In this chapter, Catarina Barbosa performed the overexpression and purification of WT: SviDyP, ScoDyP, TfuDyP, CboDyP, CboDyP, PpDyP and respective distal variants. She recorded and interpreted resonance Raman (RR) spectra of WT: SviDyP, CboDyP, PpDP and their distal variants and analysed surface-enhanced resonance Raman (SERR) spectra of immobilized distal variants and determined their reduction potentials. She also conducted the immobilization studies of WT CboDyP and WT PpDyP on different carbon nanomaterials and determined their electrocatalytic activity.

Carolina F. Rodrigues performed the site-direct mutagenesis of the PpDyP distal variants and overexpressed and purified PpDyP *in silico* variants. Caterina Martin helped in the construction of CboDyP distal variants. Lidia Zuccarello and Edilson Galdino performed the immobilization studies of WT: ScoDyP, TfuDyP, and CboDyP on different coated electrodes and assessed the DyPs heme structure cavity upon immobilization by SERR spectroscopy. Lidia Zuccarello conducted the reduction potential determination of immobilized WT CboDyP. Célia Silveira determined the electrocatalytic activity of immobilized PpDyP FireProt and PpDyP PROSS and performed their stability assays.

Abstract

After concluding that WT SviDyP, TScoyP, TfuDyP, CboDyP, and PpDyP, together with CboDyP R307W/I, PpDyP R214W and PpDyP *in silico* engineered variants were the most promising DyPs to be used in biosensing applications, we proceeded to their immobilization to develop third-generation H_2O_2 biosensors. For this application, DyPs must retain their native properties upon immobilization on electrode surfaces. In this study, we explored the development and characterization of H_2O_2 biosensors by empirical strategy or rational design. In the former approach DyPs were immobilized on glassy carbon electrodes, and modified with carbon nanotubes. Their redox and catalytic properties were assessed through electrochemical techniques. In the rational design approach, DyPs were immobilized on biocompatible SAM-coated Ag electrodes, and their structural integrity, redox characteristics, and catalytic activity were evaluated using SERR spectroscopy and electrochemical methods. Our results showed that DyP constructs developed through the rational design outperformed existing HRP-based biosensors. Moreover, this approach provided more profound insights into the structural properties of the immobilized DyPs, which is a critical parameter for developing a functional biosensor.

3.1. Introduction

Electrochemical enzyme-based biosensors are commonly developed using empirical approaches, where various combinations of electrode materials, immobilization methods, and matrices are tested in a trial-and-error manner to identify the optimal combination for the best electrochemical response [1,2]. Electrochemical techniques, such as CV, cAmp, or others [1,2], are the most commonly used to evaluate the performance of electrochemical biosensors. When a good, stable and reproducible electrocatalytic response of the immobilized enzyme is achieved, these biosensors usually offer excellent performance, characterized by high sensitivity, selectivity, reproducibility, good operational and storage stability, and short response time [1]. Nevertheless, the development of a third-generation biosensor is not a straightforward process since direct enzyme immobilization on the surface of the electrode may result in conformational changes, which can affect the overall performance of the biodevice [1,3–5]. The electrochemical methods used to characterize these devices enable the *in situ* control and monitoring of redox processes occurring at the electrode surface. However, these methods lack structural information about enzymes upon immobilization which, as noted above, is essential for developing functional third-generation biosensors. Take the case of the development of biosensing devices using immobilized cytochrome P450 (P450) as an example [6–8]. These enzymes play key roles in biosynthesis, including fatty acids and endogenous steroids, and in the metabolism of xenobiotics, including drugs, pesticides, and carcinogens [6–8]. Moreover, they catalyze diverse reactions, such as hydroxylation, sulfoxidation, epoxidation, deamination, and N-oxide reductions. For all these reasons, enormous efforts have been focused on the use of this enzyme in bioelectrocatalysis, either in chemical syntheses or in biosensing applications, but independent of the approach, they were unsuccessful [6–8]. Despite their clear potential, the application of P450-based biocatalytic devices has been hampered by key limitations linked to enzyme immobilization which, regardless of the employed strategies, results in altered redox and catalytic properties in comparison to the enzyme in solution [6–8]. This is related to the fact that P450 undergoes structural conformational changes resulting in the conversion of the native enzyme to the inactive P420 form [5]. This was revealed by coupling electrochemistry with SERR spectroscopy, where it was possible to correlate the redox properties with the structural features of the newly formed species upon immobilization [5]. The above example demonstrates clear drawbacks of using only electrochemical methods for third-generation biosensor characterization. The coupling of electrochemical methods with SERR spectroscopy for developing enzyme-based electrochemical biosensors, herein referred to as the rational design, provides information about the structure and redox properties of the immobilized enzyme. This strategy was employed to evaluate other heme enzymes, including nitrite reductases, microperoxidases, and DyPs, upon immobilization [9–15]. We have previously reported that PpDyP is an excellent candidate for constructing a third-generation electrochemical H_2O_2 biosensor using this approach [9]. The previously constructed PpDyP-biodevice outperformed biosensors developed with HRP immobilized on modified electrodes, such as those incorporating carbon/metal nanostructures and quantum dots, among others [5].

In this chapter, we will describe different strategies for characterizing a DyP-based biosensor: DyPs from different bacterial organisms will be immobilized on biocompatible coated Ag-electrodes, where electrochemical techniques will be coupled with SERR spectroscopy following a rational design approach. In parallel, DyPs will be immobilized on a mixture of CNT, and the constructs will be characterized by electrochemical methods only.

3.2. Materials and methods

3.2.1. Reagents, chemicals and enzymes

8-Amino-1-octanethiol hydrochloride (AOT), 6-mercapto-1-hexanol (MOH), 1-undecanethiol (1-UDT), 11-mercaptoundecanoic (MUA) and 11-mercapto-1-undecanol (MUD) were purchased from Sigma-Aldrich. 11-amino-1-undecanethiol hydrochloride (AUT) was purchased from Sigma-Aldrich and Dojindo. Single-walled Carbon nanotubes ink (SWCNTs-Ink) 0.2 mg/mL, SWCNTs amine functionalized ($SWCNTs-NH_2$) , multiwalled CNTs either COOH or OH functionalized (MWCNTs-

COOH and MWCNTs-OH), as all the other chemicals, were purchased from Sigma-Aldrich and were of the highest purity grade available. Solutions were prepared using deionized water from Mili-Q® water system.

Enzymes used in this chapter were purified as described in Chapter 2.2.2.

3.2.2. Enzyme immobilization

SAM coated Ag-electrodes: Ag electrodes (geometric area 0.7 ± 0.05 cm^2) were prepared as previously described [11,16]. Briefly, the surface of the Ag electrodes was mechanically polished and then electrochemically roughened in 0.1 M KCl to create a plasmon-active surface. Following an initial potential step at 2,205 mV (40 s), the electrodes were treated with three repetitive oxidation/reduction cycles at +505/−505 mV (vs. NHE) (1st cycle 60 s, 2nd 30 s, and 3rd, 30 s oxidation and reduction steps, respectively and lastly a 300 s step for reduction). The electrodes were then incubated in a 1 mM ethanolic solution of alkanethiol self-assembled monolayers (SAMs) overnight. For the immobilization of WT: SviDyP, ScoDyP, TfuDyP, and CboDyP, the following SAMs were tested: pure 1-UDT, AUT, MUA, and MUD; and mixed 1-UDT/MUA (M:M, 1:1), 1-UDT/MUD (M:M, 3:1), 1-UDT/AUT. WT PpDyP and its variants were immobilized in SAM mixture previously optimized for WT enzyme: AOT/MOH (M:M, 1:3) [9]. Prior to SERR experiments, the DyPs were immobilized on the SAM coated electrodes, either by i) immersion into a DyP solution (final concentration 0.3 - 0.5 μM) prepared in 12.5 mM PB and 12.5 mM K_2SO_4, pH 7, supporting electrolyte buffer, for 15 - 30 min and rinsing with buffer prior to use or ii) by injecting the enzyme into the SERR cell containing the same buffer (10 mL) with the electrode poised at 0.250 V vs. NHE. All potentials in this work are referenced to NHE.

CNT modified GC electrodes: Prior to electrode modification, the GC working electrode (Ø = 3 mm, BASI) was sequentially polished with alumina slurry 0.5 and 0.3 μm for 3 min. The electrodes were then thoroughly washed with water and ethanol and ultra-sonicated for 5 min. Finally, the electrodes were washed with water and dried with compressed air. SWCNTs-ink was ultra-sonicated for 1 min prior to use.

CboDyP and PpDyP (100 μM) in supporting electrolyte buffer were mixed with SWCNTs-Ink (1:1, v/v). The DyP:SWCNTs-Ink electrode modification was made by depositing 3 successive layers of 5 μL of the mixture and drying each layer, one by one, at room temperature under an N_2 atmosphere. For immobilization of PpDyP, other CNTs were also tested including: SWCNT-NH_2 prepared in tetrahydrofuran (THF), MWCNTs-COOH and MWCNTs-OH prepared in polyallylamine hydrochloride (PAH). In the case of PpDyP/SWCNTs-NH_2/GC, 3 layers of 5 μL of the SWCNTs-NH_2 were deposited on the electrode surface followed by a drop of 5 μL of PpDyP (100 μM). Between each layer the electrode surface was dried as described for SWCNTs-Ink. The GC modification using MWCNTs-COOH/PAH or MWCNTs-OH/PAH was performed as described for the PpDyP/SWCNTs-Ink mix.

3.2.3. Surface enhanced resonance Raman (SERR) spectroscopy

SERR spectra were acquired with a Raman spectrometer (Jobin Yvon U1000 or Jobin Yvon LabRam 800 HR) equipped with a 1200 lines/mm grating and a back-illuminated CCD detector cooled by liquid nitrogen, which was coupled to a confocal microscope. An Olympus 20× objective was used for laser focusing onto the sample and light collection in the backscattering. A 405 nm diode laser was used as an excitation source (Toptica Photonics AG). To prevent prolonged exposure of individual enzyme molecules to laser irradiation the electrode was kept under constant rotation (2600 rpm) [17].

SERR experiments were performed in a SERR cell (see below) with 1.3 - 1.4 mW laser power. The accumulation times were 20 - 40 s; to improve the signal-to-noise (S/N) ratio, 4 - 16 spectra were co-added in each experiment. After polynomial baseline subtraction, all spectra were subjected to component analysis, as described previously [18].

3.2.4. SERR spectroelectrochemistry

Potential-dependent SERR experiments were performed using a home-built spectroelectrochemical cell equipped with three-electrode arrangement: the enzyme/SAM modified Ag working electrode, a reference electrode (Ag/AgCl 3 M KCl, WPI) and a platinum wire counter electrode (Goodfellow). A Princeton Applied Research 263A potentiostat was used to control the electrode potentials. The experiments were carried out in argon-purged supporting electrolyte buffer to avoid the formation of O_2 reduction products that could interact with the immobilized enzymes. Spectra acquisition was the same as described above (cf. section 3.2.3). Determination of the $E^{0'}$ for the different spin species was based on the relative SERR intensities of a single oxidation state marker obtained from the component analysis either for the native ferric and/or ferrous spin species (ν_3 mode was used for PpDyP R214W and, while for PpDyP R214I, FireProt, PROSS and CboDyP, due to the lower spectral quality, the most intense ν_4 mode was used for). The $E^{0'}$ were obtained by fitting the Nerst equation (cf. section 2.2.5 Equation 2.1) to the potential dependent relative SERR intensities of each species [11].

3.2.5. Electrochemistry assays

Cyclic voltammetry (I vs. E; CV) experiments were performed either in the SERR spectroelectrochemical cell, composed as described above (cf section 3.2.4) or in a classical three-electrodes electrochemical cell, using the modified GC electrode as the working electrode, a reference electrode (Ag/AgCl 3 M KCl, WPI), and a platinum counter electrode (Radiometer). Prior to the measurements, the supporting electrolyte buffer was purged by bubbling argon for 15 min. In all experiments, the cells were maintained under an argon atmosphere. CVs were recorded in a range between +400 to −600 mV at a scan rate of 50 mV/s. The chronoamperometry (I vs. t; cAmp) experiments were performed in the SERR spectroelectrochemical cell under argon purging at an applied potential of +100 mV with the modified Ag electrode rotating at 2600 rpm.

To evaluate the electrocatalytic response of the enzyme electrodes to H_2O_2, previously deoxygenated stock solutions (10 and 100 mM) were successively injected into the cells. The catalytic currents (I_{cat}) were corrected by subtracting the current measured in the absence of substrate. The concentration of the H_2O_2 stock solutions were determined spectrophotometrically using a molar absorption coefficient of

43.6 $M^{-1} \cdot cm^{-1}$ at 240 nm [19]. Kinetic data were fitted with the electrochemical Michaelis-Menten equation (cf. Equation 1.5):

$$I_{cat} = \frac{I_{max} \times [S]}{K_M^{app} + [S]} \qquad \text{(cf. 1.5)}$$

in which I_{cat} is the catalytic current, I_{max} is the maximum I_{cat} observed at enzyme saturating conditions, [S] is the target analyte concentration, K_M^{app} is the apparent Michaelis-Menten constant.

3.3. Results and Discussion

3.3.1. Immobilization strategies

In Chapter 2 we identified the following WT DyPs: TfuDyP, CboDyP, ScoDyP, SviDyP, and PpDyP, PpDyP FireProt and PpDyP PROSS as potentially promising biocatalysts to be used in biosensing applications. In parallel, the distal variants of CboDyP and PpDyP were also studied despite their non-optimal catalytic performance in solution. This chapter will explore different immobilization strategies employing SAMs-coated Ag electrodes and CNTs-modified GC electrodes.

3.3.1.a. Structural characterization of DyP immobilized on SAMs-coated Ag electrodes

First, the $E^{0'}_{Fe(III)\ /\ Fe(II)}$ and catalytic activity of the WT DyPs attached to modified biocompatible Ag electrodes were explored.

Surface charge distribution analysis. To create a biocompatible environment for immobilizing DyPs Ag electrodes were coated with SAMs. For each studied enzyme, the choice of the SAMs followed an initial consideration of the DyPs' surface charge distribution (Figure 3.1).

The WT SviDyP structure model (generated using the Swiss Model algorithm) and the crystal structures of WT ScoDyP and WT TfuDyP (Figure 3.1 A-B) showed that these enzymes have a homogenous distribution of hydrophobic and charged residues on their surface.

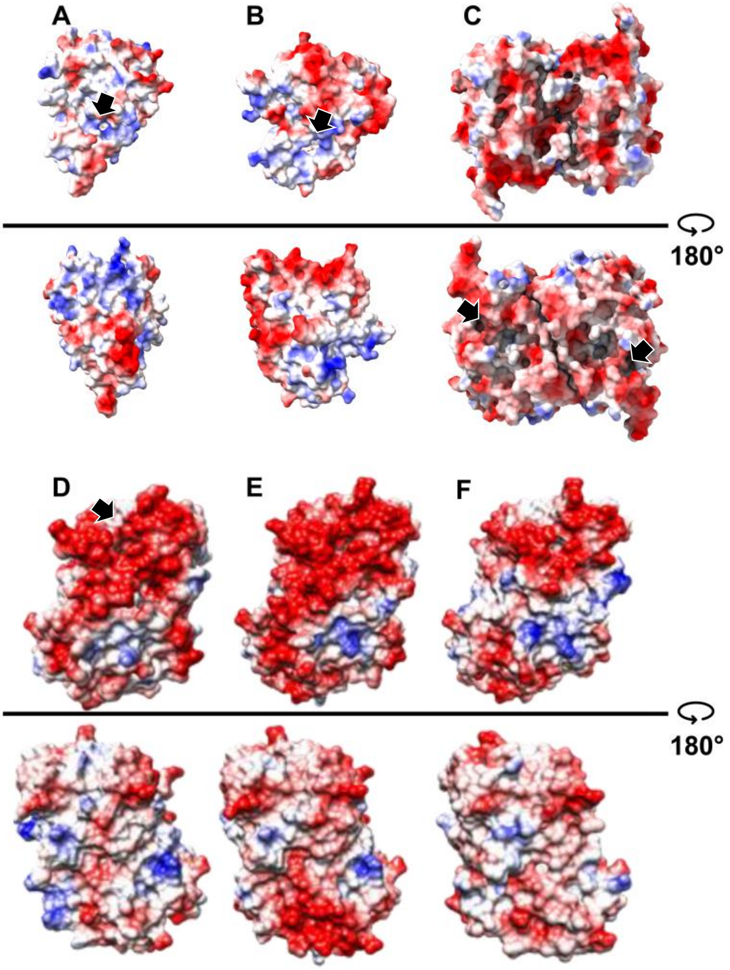

Figure 3.1 - Surface electrostatic potential distribution obtained from the DyP crystal structures available. (**A**) WT ScoDyP (monomer; PDB code: 4GT2), (**B**) WT TfuDyP (monomer; PDB code: 5FW4, (**C**) WT CboDyP (dimer; PDB code: 6QZO), (**D**) WT PpDyP (monomer; PDB code. 7QYQ). For the PpDyP *in silico* variants (**E**) PpDyP PROSS and (**F**) PpDyP FireProt the surface electrostatic potential distribution was obtained from the model structures [20]. Surface electrostatic potential was calculated with Coulombic surface coloring in Chimera X. Potential is colored on a scale from -10 kcal/mol (red, negatively charged regions) to +10.0 kcal/mol (blue, positively charged regions). The heme position in the different structures is indicated with the black arrow except for the in silico variants (E, F), in which it is the same as in the WT PpDyP (D).

For these reasons, hydrophobic (-CH_3) and charged (positive - NH_3^+ or negative -COO^-) SAMs were chosen in the first attempt. Surface charge distribution of WT CboDyP showed well-defined negatively charged patches mixed with hydrophobic surface residues (Figure 3.1 C), which suggested that a positively charged electrode surface (-NH_3^+ - terminated SAM) could favor electrostatic interactions with the enzyme. The immobilization of WT SviDyP, WT ScoDyP, WT TfuDyP, and WT CboDyP was attempted using either pure -CH_3, -NH_3^+, and -COO-terminated alkanethiols or mixtures of CH_3 with NH_3^+ or -COO^--terminated SAMs. In the case of WT CboDyP and WT ScoDyP, pure -OH and mixed -OH/-CH_3 terminated SAM were also tested.

The surface charge distribution of WT PpDyP (Figure 3.1 D) revealed a relatively well-defined negatively charged patch counterbalanced with a hydrophobic surface that contains positively and negatively charged residues. Surprisingly, PpDyP FireProt and PpDyP PROSS, which carry an elevated number of amino acid substitutions (21 and 29, respectively) across their structure [20], showed a surface-charged distribution comparable with that of the WT enzyme (Figure 3.1 D-F). Hence, all PpDyP variants were immobilized in the SAM mixture, AOT/MOH (1:3, M:M), previously optimized for the WT PpDyP [9].

For each DyP immobilization, the SAM-coated Ag electrodes were incubated in the enzyme solution (0.3 - 0.5 μM) during variable time intervals (cf. section 3.2.2). For each DyP/SAM/Ag construct, the ferric SERR spectrum was compared with the RR spectrum of the resting state enzyme in solution to evaluate the DyP active site upon immobilization.

(i) Fully preserved active site structure: PpDyP FireProt and PpDyP PROSS. As previously demonstrated for the immobilized WT PpDyP [9], the *in silico*-engineered PpDyP variants revealed in the high-frequency region of the SERR spectra the core-size marker bands (ν_4, ν_3, ν_2, and ν_{10}) at the same positions as in the RR spectra measured for each enzyme in solution. The SERR spectra of both variants showed multiple co-existing heme species. The two major heme populations were attributed to 5cHS and 5cQS species, evidenced by the analysis of the ν_3 mode at 1491 and 1500 cm^{-1}, respectively (Figure 3.2), as in the case of immobilized WT PpDyP. The comparison of RR with the SERR spectra showed no significant changes in the heme architecture or emergence of new heme species in the immobilized state.

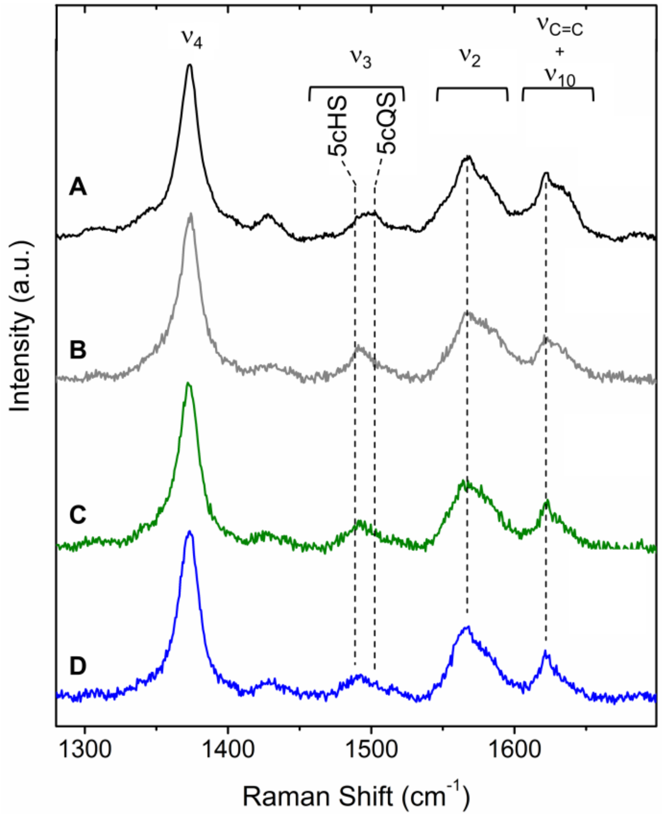

Figure 3.2 - RR spectra (solution) and SERR spectra (immobilized) of PpDyPs. (**A**) RR spectra of ferric of the WT PpDyP (black) and (**B-D**) SERR spectra of WT PpDyP (grey); FireProt (green) and PROSS (blue). SERR spectra of PpDyPs immobilized on Ag electrodes coated with AOT:MOH SAM at pH 7, recorded at +250 mV electrode poised. The spectra were measured with 405 nm excitation at RT, laser power and accumulation time of 3 mW and 30 s (RR) and 1.4 mW and 30 s (SERR).

(ii) Partial-preserved active site structure: WT CboDyP and PpDyP R214W. The comparison of the SERR spectra with the respective RR spectra demonstrated that WT CboDyP and PpDyP R214W undergo minor structural conformational changes upon immobilization (Figure 3.3 and Figure S 3.2 A-B). The SERR spectra revealed, in both cases, the presence of a 5cHS heme species, identified by the ν_3 mode at 1492 cm^{-1} with a relative contribution of 35% and 30% for WT CboDyP and PpDyP R214W. In addition to the native 6cHS and 6cLS heme species, the SERR spectra showed the characteristic marker bands ν_4, ν_3 and ν_2 at the same position as in the RR spectra (Table S 2.1, Figure 3.3). In the SERR spectra of CboDyP, an additional minor species, approximately 10% of ν_4 band area, centered at 1358 cm^{-1} could be identified, indicative of reduced (ferrous) enzyme. Its origin is most likely due to the possible photoreduction of the immobilized enzyme during the SERR experiment. Note that although WT CboDyP could be immobilized in the native state, the widths

of the SERR component bands were approximately 1 - 2 cm^{-1} wider than those observed in the RR spectra, which could be due to the non-homogeneous orientation distribution of the enzyme on the electrode. For WT CboDyP under all other tested conditions, residual or no SERR signals were observed (Figure S 3.1) which indicated the absence of the enzyme at the electrode surface.

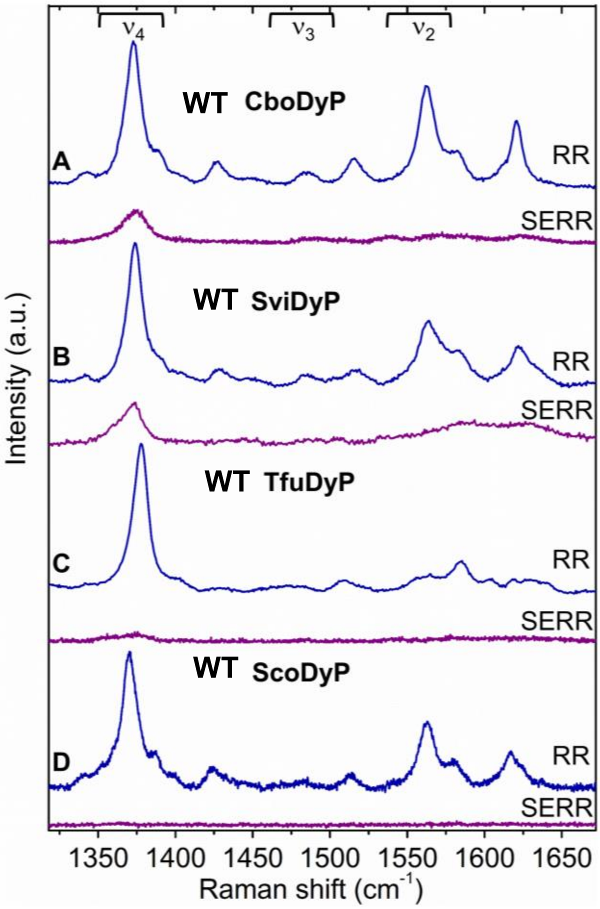

Figure 3.3 - RR (blue) and SERR (purple) spectra of ferric DyPs. (**A**) WT CboDyP (**B**) WT SviDyP (**C**) WT TfuDyP (**D**) ScoDyP. All RR spectra were measured at pH 8 and all the SERR spectra were recorded at pH 7, at poised electrode potential at +250 mV. For enzyme immobilization, Ag electrodes coated with 1-UDT:AUT were used for all enzymes except for ScoDyP, which was immobilized on 1-UDT. All spectra were acquired at 21 °C except for the RR spectra of WT SCoDyP (−50 °C). A 405 nm excitation was used to acquire all RR and SERR spectra except the RR spectra of WT TfuDyP, which was obtained with 413 nm excitation. Experimental details can be found in 2.2.4. for the RR spectra and 3.2.3 for SERR spectra.

(iii) Non-preserved active site structure: WT SviDyP, WT ScoDyP, WT TfuDyP, PpDyP R214I and CboDyP R307W/I. The SERR spectra of those enzymes were very different from their respective RR spectra, which revealed that they undergo major alterations of the heme pocket upon immobilization (Figure 3.3 and Figure S 3.2 C-D and S 3.3). SERR spectra of WT SviDyP and WT TfuDyP could be obtained when the enzymes were immobilized in mixed hydrophobic (-CH_3) and positively charged

(NH_3^+) terminated SAMs. As for WT CboDyP, under all other tested conditions, residual or no SERR signal was observed for WT SviDyP and WT TfuDyP (Figure S 3.1). In the case of WT SviDyP, three species were identified with different relative abundance: 44% native 6cHS species, 34% non-native 6cLS, and 21% reduced enzyme, possibly due to enzyme photoreduction during the SERR experiment. For immobilized WT TfuDyP HS species were identified, but with distinct frequencies, bandwidths, and relative intensities compared to those in solution [21]. CboDyP variants, R307W and R307I, and PpDyP R214I were immobilized on the same type of modified electrodes as the respective WT enzymes. Immobilized CboDyP variant revealed the presence of mostly non-native heme species (5cHS and 6cLS), losing nearly all the native 6cLS (Figure S 3.3), while WT retained over 50% of the native configuration. In PpDyP R214I, non-native 5cHS becomes predominant over the native 6cLS (Figure S 3.2 C-D).

(iv) Absence of enzyme attachment. For WT ScoDyP, the absence of a detectable SERR signal for the immobilized enzyme from all studied SAMs indicated that a suitable biocompatible environment for immobilization could not be achieved (Figure S 3.1 D).

3.3.1.b. Immobilization of DyP on CNTs-modified GC electrodes

Carbon-based nanomaterials are commonly used in electrochemical applications. They are typically associated with lower overpotentials and enhanced ET rates between the modified electrode and the immobilized enzyme [22–24]. For this reason, WT CboDyP and WT PpDyP were immobilized on GC-modified electrodes with single-walled CNTs-ink mixed with the enzyme solution. For immobilization of WT PpDyP, NH_2-SWCNTs prepared in THF, COOH-MWCNTs and OH-MWCNTs prepared in PAH were also tested. These constructs were characterized by electrochemical methods only.

3.3.2. Bioelectrode constructs based on immobilized DyPs

3.3.2.1. Redox properties

3.3.2.1.a. DyPs on SAM-coated Ag electrodes

Probing redox activity of immobilized DyPs. In the next step, we probed the redox behavior of the enzymes identified in section 3.3.1.a. (i.e., WT PpDyP, PpDyP *in silico* variants, PpDyP R214W and WT CboDyP) attached to SAM-coated Ag electrodes to evaluate the efficiency of the DET. The SERR spectra of the immobilized resting state DyPs were measured at a series of poised electrode potentials from 300 to −450 mV to perform the redox titration. The most negative potential applied to the SAM-coated Ag electrode was −450 mV due to the reductive desorption of the alkanethiol monolayer at more negative potentials. For immobilized CboDyP, the enzyme could not be further reduced at potentials below −150 mV. This was evident from the asymmetric redox-sensitive ν_4 band indicating the presence of redox-inactive species (Figure 3.4 A). Component analysis of the SERR spectrum of the reduced enzyme at −200 mV (Figure 3.4 B) revealed the presence of two distinct populations. The major one is identified as the ferrous 6cHS species with a ν_4 at 1359 ($\nu_{4\mathrm{ferric}}$ = 1371 cm^{-1}) and a ν_3 at 1475 cm^{-1} ($\nu_{3\mathrm{ferric}}$ = 1481 cm^{-1}). These changes in positions are characteristic of ferric-to-ferrous conversion in 6cHS species [17] indicating that this ferrous species is the reduced state of the native ferric 6cHS (Figure 3.5 B). The minor population identified at −200 mV was identical to the non-native 5cHS species observed in the SERR spectra of the ferric enzyme, which led us to conclude that this is a redox-inactive species formed upon attachment of CboDyP to the electrode.

The SERR spectra of immobilized PpDyP *in silico* variants at the most negative potential applied revealed an asymmetric ν_4 (Figure 3.5). Component analysis of the SERR spectra at −450 mV revealed the presence of a ferrous 5cHS (ν_4 at 1360 and a ν_3 at 1474 cm^{-1}) population and a redox-inactive species (ν_4 at 1365 cm^{-1}) (Figure 3.5 B) with the same marker bands previously described for the immobilized WT PpDyP [15].

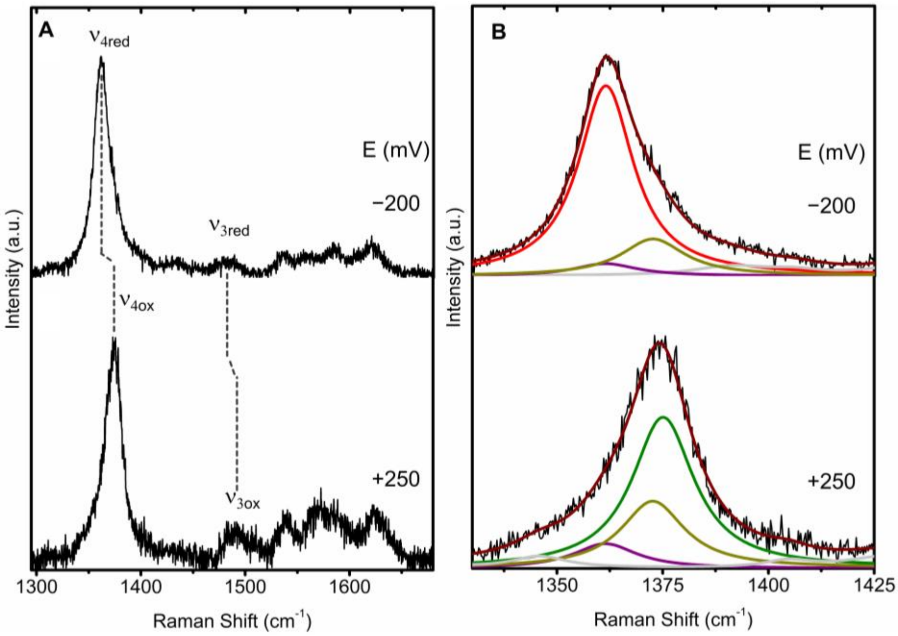

Figure 3.4 - SERR spectra of immobilized CboDyP on Ag electrodes coated with 1-UDT:AUT SAM at poised potentials of +250 mV and -200 mV. (**A**) High frequency region showing the overall changes of the SERR spectra. (**B**) Component spectra of the ν_4 region of CboDyP; the component spectra represent native ferric 6cHS (green), redox-inactive ferric 5cHS (dark yellow), ferrous 6cHS (red) and redox-inactive ferrous (purple) species, non-assigned bands (grey) and the overall fit (dark red). All spectra were obtained with 405 nm excitation at pH 7 and 21 °C.

The redox-inactive species in PpDyP *in silico* variants account for almost 40% overall ν_4 intensity (Figure 3.5 B and D) while in the case of the immobilized ferrous WT enzyme was only ca. ~20% [11]. Moreover, in these variants, in contrast with the WT, the complete reduction of the ferric species is not achieved (Figure 3.5 B and D, orange and pink traces). For the immobilized PpDyP distal variants at −400 mV (Figure S 3.4), in contrast with the WT PpDyP, a symmetrical ν_4 band is observed in the SERR spectra, which was attributed to the ferrous 5cHS population as previously observed in the same position as for WT enzyme (ν_4 at 1360 and a ν_3 at 1474 cm^{-1}) [11]. For all PpDyP variants the SERR signal intensity decreases after extended exposure of the enzymes to negataive potentials (Figure 3.5 A; 3.6 A and Figure S 3.4 A and C) as previously observed for the WT PpDyP [9, 11], implying that reduction- or potential-induced desorption of the enzymes occurred.

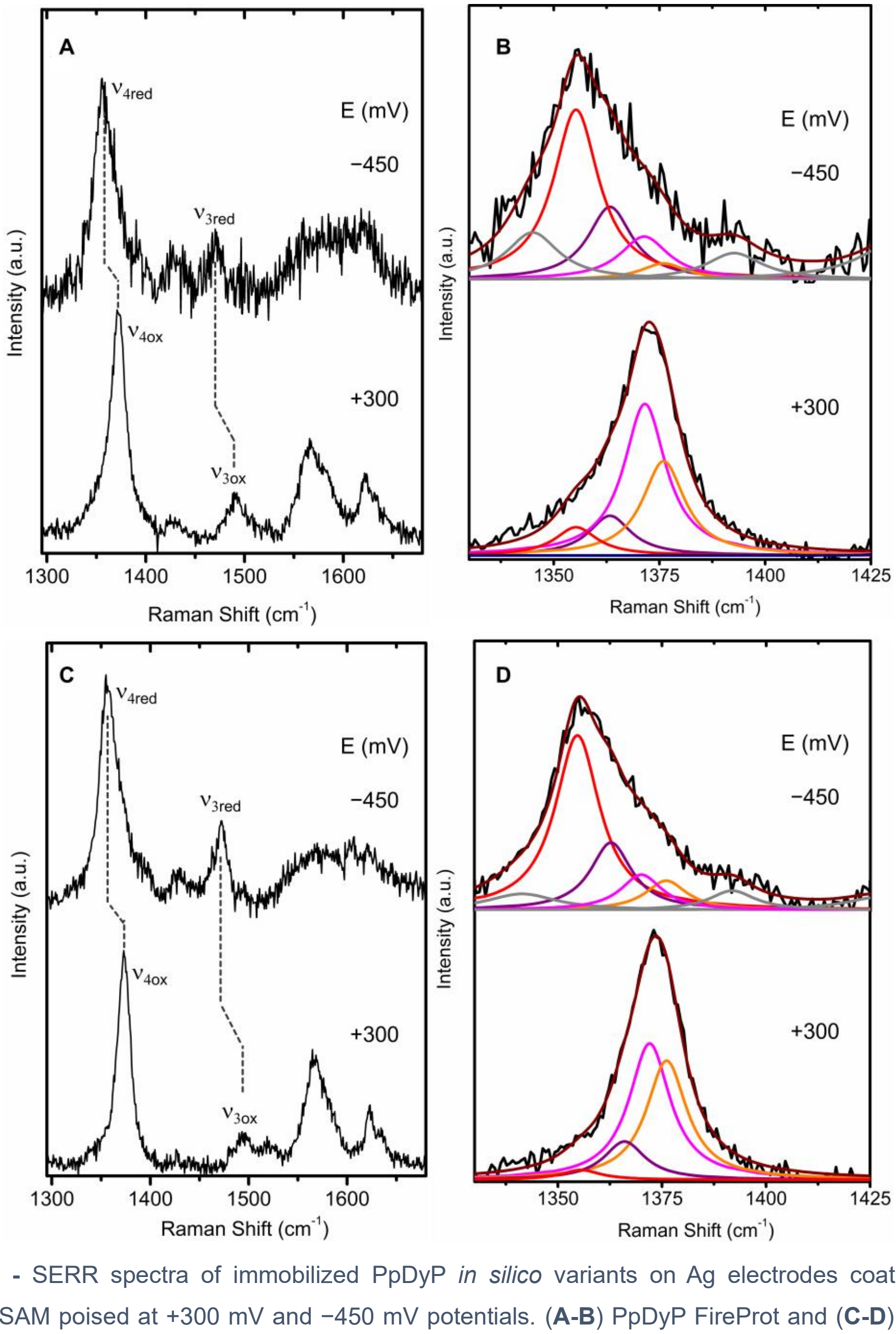

Figure 3.5 - SERR spectra of immobilized PpDyP *in silico* variants on Ag electrodes coated with AOT:MOH SAM poised at +300 mV and −450 mV potentials. (**A-B**) PpDyP FireProt and (**C-D**) PpDyP PROSS. (**B and D**) Component analysis of the ν_4 band of the respective spectra; the component spectra represents the native ferric 5cHS (magenta), ferric 5cQS (orange), redox-inactive (purple) and ferrous (red) specie, non-assigned bands (grey) and the overall fit (dark red). All spectra were obtained with 405 nm excitation at pH 7 and 21 °C.

Reduction potential determination. The $E^{0'}_{Fe(III)/Fe(II)}$ of the immobilized PpDyP variants, and WT CboDyP were determined in the next step. The contributions of the ferric and ferrous species were calculated from the component analysis of the potential-dependent SERR spectra (Figure 3.6 A) measured at a series of poised potentials.

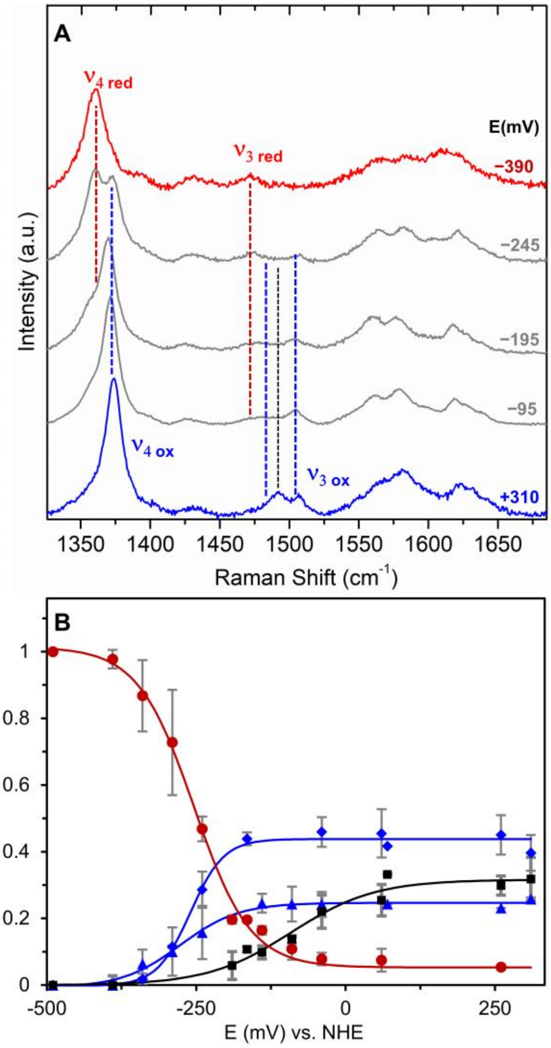

Figure 3.6 - Redox titration of PpDyP R214W. (**A**) SERR titration (represented by several selected spectra), performed from + 310 mV (ferric state, blue line) to −390 mV potential (ferrous state, red line. (**B**) Potential dependent relative SERR contributions of ν_3 mode [$I_{rel}(\nu_3)$] on the component analysis for ferrous 5cHS (red circles), ferric 6cLS (blue diamond), ferric 6cHS (blue triangles). Error bars (grey lines) of each point represent the standard deviation (SD) (n = 6) The solid lines represent the fits of the Nernst equation to the data, yielding $E^{0'} = -250 \pm 10$ mV for the ferrous 5cHS, $E^{0'} = -280 \pm 10$ mV for the ferric 6cHS, $E^{0'} = -260 \pm 5$ mV for the ferric 6cLS, and $E^{0'} = -70 \pm 20$ mV for the non-native ferric 5cHS populations. The black trace (dotted in (A) and solid in (B)) represent the non-native 5cHS specie.

The spectral parameters (band frequencies and widths) were kept constant for each spin population along the deconvolution procedure. The only variable for a SERR spectrum at a given potential was the intensity of the individual component bands, which is proportional to the species concentration and was fitted to the Nernst equation. Previously, a similar approach based on component analysis of the ν_3/ν_4 bands was successfully adopted to analyze the redox behavior of proteins containing multiple heme groups with/or different spin populations [11,13]. Potential dependence of the relative spectral contribution of the ferrous and ferric species identified in the SERR spectra of all the immobilized enzymes revealed a sigmoid shape (Figure 3.6 B).

The $E^{0'}_{imm}$, Table 3.1, determined for PpDyP variants, both distal (R214W and R214I, −250 ± 10; −190 ± 5 mV) and *in silico* engineered (PpDyP FireProt and PpDyP PROSS, −285 ± 20 and −330 ± 20 mV), were comparable to the respective $E^{0'}_{sol}$ determined ($E^{0'}_{sol}$, −270 ± 10; −260 ± 10, −300 ± 20 mV, respectively, cf. Table 2.3). Moreover, the obtained reduction potentials when the overall ferrous species was followed were comparable to the one previously determined for the WT enzyme ($E^{0'}_{imm}$ = −300 mV) [11].

For both distal variants, the $E^{0'}_{imm}$ of the non-native ferric species, which most likely resulted from immobilization-induced conformational changes in the heme cavity, are upshifted (−70 ± 20 mV and −125 ± 20 mV, PpDyP R214W and R214I respectively). The formation of these species likely resulted in an increased hydrophobicity of the heme cavity, which led to the formation of a denatured 5cHS form of the enzyme. The native 6cHS of the immobilized WT CboDyP revealed an $E^{0'}_{imm}$ with a difference of about +300 mV compared to the $E^{0'}_{sol}$, Table 3.1 (Figure S 3.5). The large discrepancy of $E^{0'}_{sol}$ vs. $E^{0'}_{imm}$ was attributed to a non-uniform orientation of the enzyme molecules on the electrode surface, revealed by the enlarged width of the SERR bands. This heterogeneous orientation could be due to the non-specific hydrophobic interaction between the enzyme and the coated electrode.The immobilization of WT CboDyP on a hydrophobic SAM likely reduces the polarity of the heme cavity, which could cause an increase in the reduction potential up to +200 mV, as predicted by the Kassner relation [25]. The change in polarity could induce subtle conformational changes that propagate to the active site, increasing the hydrophobicity of the heme cavity in WT CboDyP. This effect may not necessarily be followed by the exchange of heme ligands that can be detected spectroscopically.

Table 3.1 - Reduction potentials ($E^{\circ\prime}_{imm}$, mV vs. NHE) of the immobilized WT CboDyP and PpDyP variants obtained by SERR spectroelectrochemistry.

$E^{\circ\prime}_{imm}$				
WT CboDyP	**PpDyP**			
	R214W*	**R214I**	**FireProt**	**PROSS**
+15 ± 15	−250 ± 6	−190 ± 5	−285 + 20	−330 + 20
	−280 ± 10 (6cHS)	−230 ± 10 (6cLS)		
	−260 ± 5 (6cLS)	−125 ± 18 (Non-native 5cHS)		
	−70 ± 20 (Non-native 5cHS)	-		

The $E^{\circ\prime}_{imm}$ values were determined by fitting the potential dependent relative SERR contributions of the ν_4 mode [$I(\nu_4)$] of the ferrous heme species obtained from component analysis, for WT CboDyP, PpDyP FireProt and PpDyP PROSS to the Nernst equation. *The potential dependent SERR contributions of the ν_3 mode [$I(\nu_3)$] were used.

3.3.2.1.b. DyPs attached to SWCNTs-Ink/GC electrodes

WT CboDyP and WT PpDyP were also immobilized on SWCNTs-ink and the resulted constructs were analyzed by CV. The CV signals of the enzymes immobilized in SWCNTs-Ink/GC (WT CboDyP:SWCNTs-Ink/GC and WT PpDyP:SWCNTs-Ink/GC, respectively) showed distinct current peaks corresponding to the one-electron oxidation/reduction of the heme iron (Figure 3.7). This enabled the direct determination of the $E^{0'}_{Fe(III) / Fe(II)}$ from the CV data. The peak-to-peak separation was 40 and 14 mV, for CboDyP and PpDyP-based electrodes, (Figure 3.7), indicating a reversible redox process. However, for the PpDyP:SWCNTs-Ink/GC electrode, an unidentified peak near the anodic peak of the Fe(III) / Fe(II) redox couple was observed (Figure 3.7 A, marked +). Moreover, the non-turnover currents measured from GC electrodes modified with a mix of DyP:SWCNTs-ink reflect the amount of enzyme immobilized and its ability to interact with the modified electrode. Since both electrodes revealed comparable currents, we concluded that a similar amount of enzyme was immobilized on both electrodes. The peak currents were directly proportional to the applied scan rates, demonstrating that the enzymes were adsorbed on the modified electrodes, Figure S 3.6.

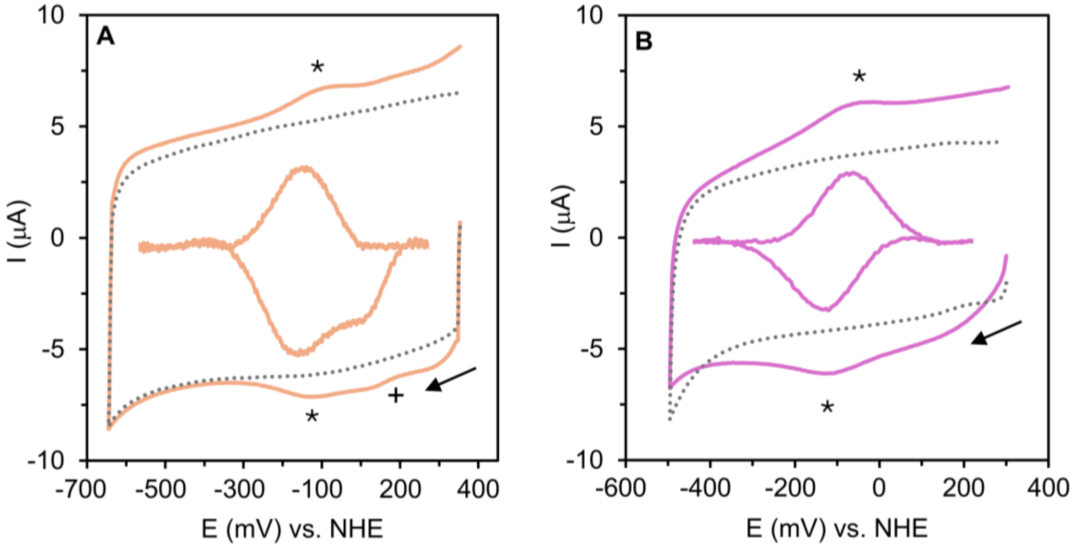

Figure 3.7 - Cyclic voltammograms of (**A**) PpDyP:SWCNTs-Ink/GC and (**B**) CboDyP:SWCNTs-Ink/GC constructs. (*) designated the Fe(III)/Fe(II) redox couple of the enzymes. (+) marked the unassigned peak. The control electrode prepared with buffer and SWCNTs-Ink is presented in the black line. Baseline subtracted currents are represented inside each CV. CVs were measured at 50 mV/s scan rate in 12.5 mM K_2SO_4 in 12.5 mM PB, pH 7.0.

The $E^{0'}_{Fe(III)\,/\,Fe(II)}$ of WT CboDyP immobilized on SWCNT-Ink/GC electrodes was found to be −90 ± 5 mV, while for WT PpDyP it was −70 ± 10 mV. These values are upshifted compared to the $E^{0'}_{sol}$ (−320 mV and −290 mV for WT CboDyP and WT PpDyP, respectively, cf. Chapter 2.3.2 Table 2.1). This upshift probably resulted from heterogeneous enzyme orientation at the electrode surface, likely due to interaction with the functional groups on the carbon nanotubes or unspecific physical adsorption. However, it could also result from a denatured enzyme. Namely, because the $E^{0'}$ was determined using electrochemical methods only, and the structural properties of the electroactive species could not be determined.

Other CNT-modified GC electrodes for WT PpDyP immobilization. For all the other CNT modifications tested, i.e., PpDyP adsorbed on SWCTs-NH_2/GC electrodes, and PpDyP entrapped in MWCNTs-COOH/PAH/GC or MWCNTs-OH/PAH/GC, the non-catalytic redox peaks could not be observed in the CVs (Figure S 3.7 A).

3.3.2.2. Electrocatalysis and analytical characterization of the developed biodevices

The electrocatalytic reduction of H_2O_2 by the immobilized DyPs on SAM-coated Ag electrodes or SWCNT-ink/GC electrodes was evaluated by CV and/or cAmp. In the case of a catalytically active immobilized enzyme that efficiently reduces H_2O_2, an increase of the cathodic current is expected upon H_2O_2 addition to the electrocatalytic cell due to the catalytic reduction by the immobilized enzyme. The cathodic currents are attributed to Compound I (the catalytic intermediate $[Fe\ (IV){=}O]^{+\bullet}$) formation that occurs when the ferric enzyme reacts with H_2O_2 being subsequently reduced by the electrode [9,11,26].

3.3.2.2.a. Bioelectrodes prepared using DyPs/SAM/Ag electrodes

The electrocatalytic reduction of H_2O_2 by the immobilized DyPs was evaluated by CV, for CboDyP and by cAmp, for PpDyP R314W, PpDyP FireProt and PpDyP PROSS. As previously observed for WT BsDyP and WT PpDyP when immobilized on SAM-coated Ag electrodes [9,12], the non-catalytic redox peaks could not be observed in the CVs, probably due to insufficient amount of enzymes on the electrode surface. Upon addition of increasing concentrations of H_2O_2, no catalytic signal could be detected in the case of the biodevices based on WT CboDyP or PpDyP R214W (Figure S 3.8). Therefore, we concluded that immobilized WT CboDyP and PpDyP R214W displayed no electrocatalytic activity. This was not surprising, for the PpDyP variant showed a drastic loss of activity in solution compared to the WT, while WT CboDyP, although immobilized in a native-like state, showed altered $E^{0'}_{imm}$.

The response of PpDyP FireProt and PpDyP PROSS electrodes to H_2O_2 was characterized by cAmp at a potential of +100 mV (Figure 3.8), since at these conditions, the non-enzymatic reduction of H_2O_2 by the Ag electrode is negligible [9].

The amperometric response was recorded upon successive addition of a purged stock solution of H_2O_2 to the cell, Figure 3.8.

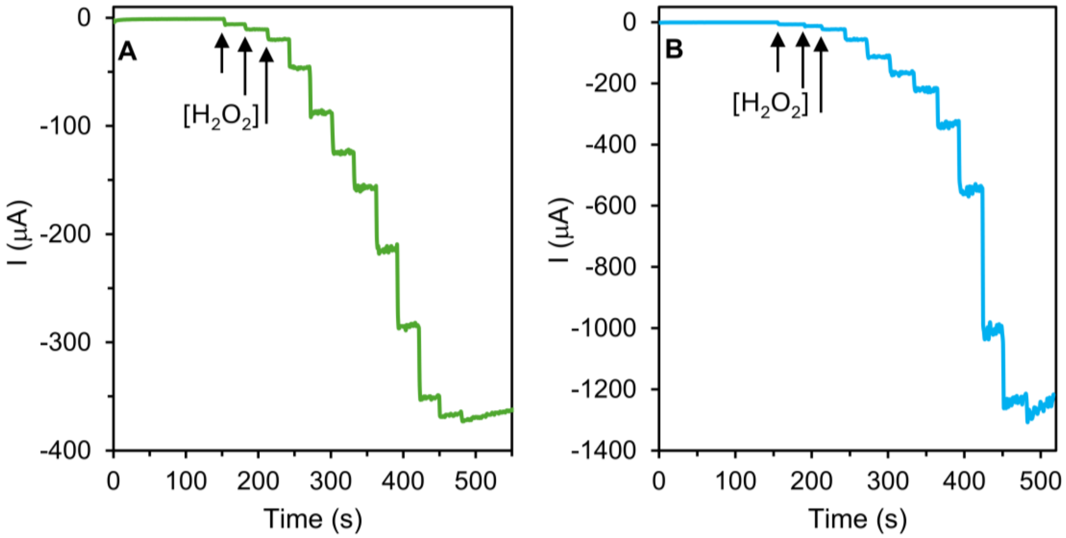

Figure 3.8 - Amperometric response of immobilized PpDyP *in silico* variants. (**A**) PpDyP FireProt/SAM/Ag and (**B**) PpDyP PROSS/SAM/Ag (blue line) electrodes response to increasing (0.005 - 1.6 mM) concentrations of H_2O_2 Measurements were performed in 12.5 mM K_2SO_4 in 12.5 mM PB, pH 7.0, at an applied potential of +100 mV. The electrode was rotated at 2600 rpm to minimize the effect of substrate mass transport to the immobilized enzyme.

We observe a stepwise increase of the catalytic current at a very short response time (< 3 s), indicative of efficient heterogeneous ET, as was previously reported for WT PpDyP [9]. The PpDyP FireProt and PpDyP PROSS bioelectrodes reached an activity plateau for a concentration of H_2O_2 higher than 1 mM (Figure 3.9 A), revealing a Michaelis-Menten-type enzyme kinetics, Figure 3.9. The K_M^{app} and maximum current density at saturating substrate concentration (J_{max}) were 0.3 ± 0.05 mM and -640 $\mu A/cm^{-2}$ for PpDyP FireProt and 1.6 ± 0.3 mM and -2,890 $\mu A/cm^{-2}$ for PpDyP PROSS. In solution, the analogous K_i and K_M values were 4.8 mM and 0.09 mM for PpDyP FireProt and 1.2 mM and 0.14 mM for PpDyP PROSS [20]. The results in solution indicate substrate-inhibited enzyme kinetics, allowing for the determination of inhibition constants. However, the low K_M value suggests that the enzymes also have a high affinity for H_2O_2, in the solution state. In the immobilized state, a decrease in the affinity for H_2O_2 was observed for both enzymes, as the K_M^{app} values are 3 and 11 times higher than the K_M values in solution for PpDyP FireProt and PpDyP PROSS, respectively.This is a typical behavior observed for immobilized enzymes on electrode surfaces and is typically attributed to a more limited diffusion of the substrate to the enzyme's active site.

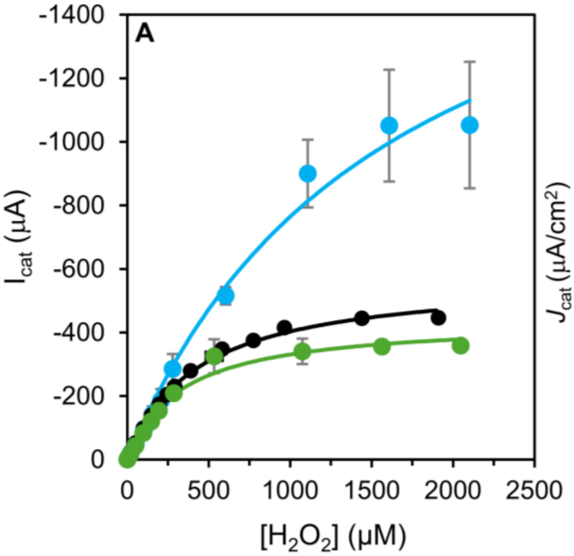

Figure 3.9 - Catalytic response of immobilized PpDyPs on Ag/SAM electrodes towards H_2O_2. (**A**) Michaelis–Menten plots of catalytic currents vs. H_2O_2 concentration for immobilized PpDyPs and (**B**) linear dependence of the catalytic current on H_2O_2 concentration (n = 8), with slope and r^2 of 1,150 ± 20 $mA{\cdot}M^{-1}{\cdot}cm^{-2}$ and 0.999 (PpDyP FireProt) and 1,420 ± 50 $mA{\cdot}M^{-1}{\cdot}cm^{-2}$ and 0.992 (PpDyP PROSS). Error bars represent the SD for each point, for PpDyP PROSS (blue circles), PpDyP FireProt (green circles) and WT PpFyP (black circles, [9]), immobilized on SAM/Ag electrodes.

Calculating the K_i constant for the immobilized enzymes was not possible, under the tested conditions, which suggested that H_2O_2 no longer inhibited the DyPs. This alteration of catalytic behavior could be explained by the fact that the attachment of an enzyme to an electrode may restrain the enzyme's rotational freedom, which could affect substrate accessibility. Additionally, the electrode provided the electrons for electroactivity measured for the immobilized enzyme. On that account, the ET pathways were most likely different from those in solution, as for the latter ABTS was used to monitor the steady-state kinetics.

The PpDyP *in silico* constructs showed a linear response to H_2O_2 from 5 - 195 µM and 5 - 278 µM for PpDyP FirePROT and PpDyP PROSS (Figure 3.9 B), respectively. The sensitivity, determined by the slope of the calibration curve where the catalytic response is linear to the substrate concentration, and the LOD, estimated at S/N of three, were 1,150 ± 20 $mA \cdot M^{-1} \cdot cm^{-2}$ and 7 µM respectively for PpDyP FirePROT and similarly 1,420 ± 50 $mA \cdot M^{-1} \cdot cm^{-2}$ and 12 µM for PpDyP PROSS. The sensor-to-sensor reproducibility determined by the measurement of the sensitivity of 7 bioelectrodes showed relative standard deviation (RSD) of ca.~ 10% and 17% for PpDyP FireProt and PpDyP PROSS, respectively. This low RSD demonstrated the robust construction of the biodevices. Both constructs presented a behavior similar to the WT construct in terms of electrochemical performance for H_2O_2 detection; however, PpDyP PROSS can reach higher maximum currents than the WT enzyme.

The stability of the PpDyP FireProt and PROSS bioelectrodes was evaluated by measuring the sensitivity of the biodevices in regular time intervals for one month, using electrodes that were stored at 4°C in supporting electrolyte buffer. After one month storage, both enzymes retain about 93 - 95% of their initial sensitivity, Figure S 3.9, which is slightly better than the WT PpDyP (85%) [9].

3.3.2.2.b. Biodevices prepared using DyP:SWCNTs-ink/GC

For the electrodes prepared by adsorption of WT CboDyP or WT PpDyP on SWCNTs-ink in the presence of H_2O_2, an increase in the cathodic current (Figure 3.10) was observed, which reflected the formation of Compound I upon the addition of H_2O_2 to the electrochemical cell. In both constructs, a steady increase of the catalytic current was observed, which was subtle in the WT PpDyP construct but very noticeable in the case of the WT CboDyP construct (Figure 3.10).

To determine the sensitivity, linear range, and LOD, the CVs were analyzed at −100 mV. This working potential was selected since the non-enzymatic reduction of H_2O_2 by the electrode is negligible at this potential (Figure S 3.10). The plots I_{cat} vs. $[H_2O_2]$, showed distinct dependence towards H_2O_2 concentrations for the studied enzymes (Figure 3.11) regarding the produced current and inhibition. The WT CboDyP construct revealed a higher current response and no inhibition, while the WT

PpDyP construct appeared prone to inhibition by the substrate above 500 µM H_2O_2 (Figure 3.11 A).

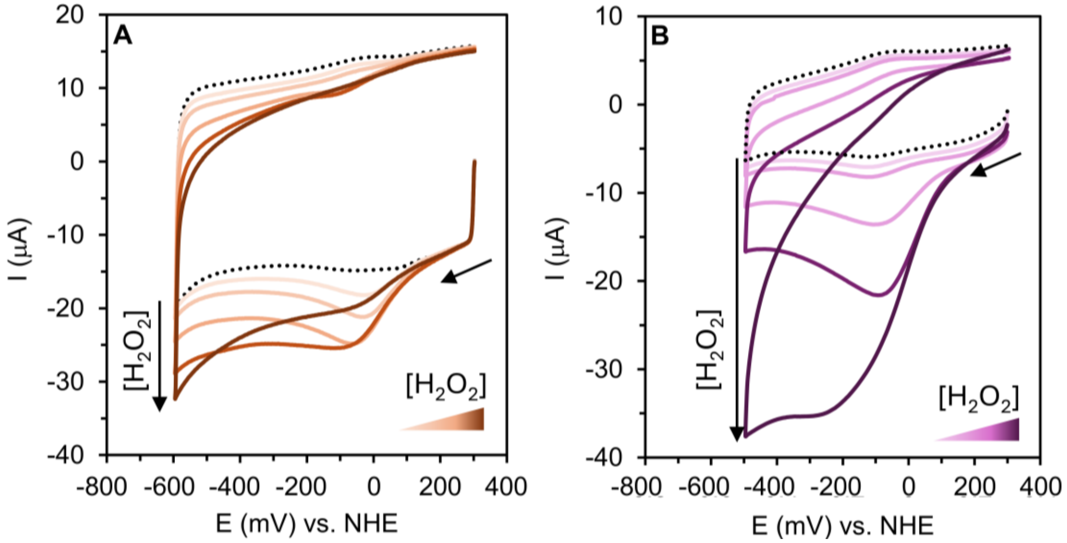

Figure 3.10 - Electrocatalytic response of DyP:SWCNTs-Ink/GC to H_2O_2. (**A**) WT PpDyP:SWCNTs-Ink/GC and (**B**) WT CboDyP:SWCNTs-Ink/GC electrodes in the absence (black trace) and presence of increasing (9 - 1268 µM) concentrations of H_2O_2; orange and magenta traces for WT CboDyP and WT PpDyP, respectively. The supporting electrolyte was 12.5 mM K_2SO_4 in 12.5 mM PB, pH 7.0. CVs were measured at 50 mV / s scan rate.

The response of the WT CboDyP:SWCNT-Ink/GC construct to H_2O_2 was linear from 9 - 400 µM while a narrower linear range was observed in the case of the PpDyP-SWCNT-Ink/GC construct (9 - 230 µM). The sensitivity, and the LOD were 550 ± 10 $mM \cdot M^{-1} \cdot cm^{-2}$ and 16 µM, respectively, for CboDyP:SWCNT-Ink/GC and similarly 610 ± 30 $mA \cdot M^{-1} \cdot cm^{-2}$ and 31 µA for the PpDyP modified electrode.

The reproducibility of each bioelectrode was calculated by comparing the sensitivity of 3 different electrodes, revealing an RSD of ca. 30%. This high RSD was not surprising, given the simplicity of the bioelectrode preparation. It only involves five consecutive steps of drop-casting the modification mixture and drying between each layer added, which could lead to different DyP:CNTs distribution on the electrode surface.

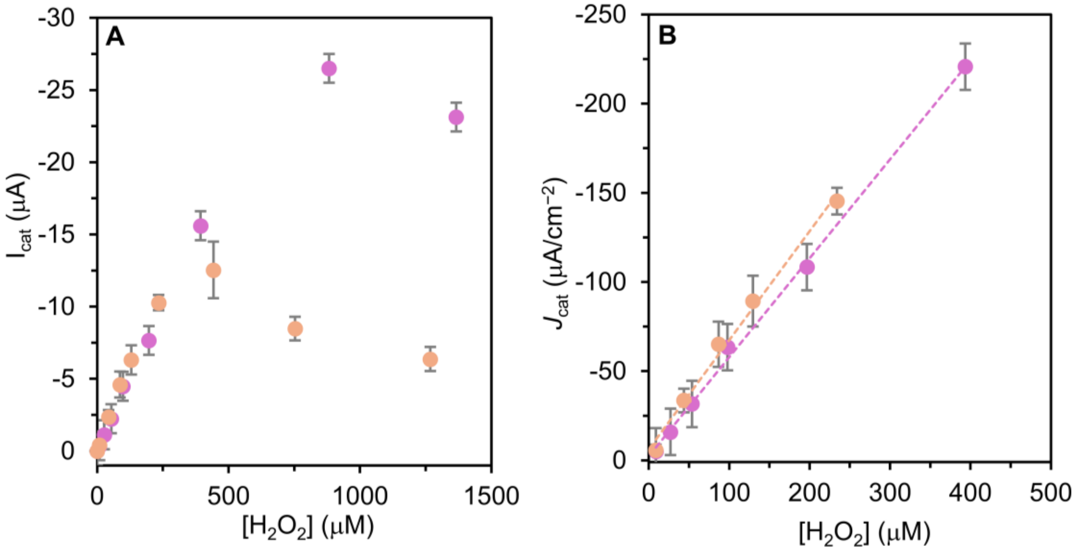

Figure 3.11 - Catalytic response of immobilized DyPs on SWCNTs-Ink/GC electrodes to H_2O_2. (**A**) Calibration plot for H_2O_2 response for WT CboDyP:SWCNTs-Ink/GC (pink circles) and WT PpDyP:SWCNTs-Ink/GC (orange circles) and the respective (**B**) linear dependence of the catalytic current on H_2O_2 concentration (n = 3) with their respective slopes (corrected for the electrode geometric area of 0.07 cm^2) and a r^2 of 555 ± 10 $mA·M^{-1}·cm^{-2}$ and 0.998 (pink) and the other 610 ± 30 $mA·M^{-1}·cm^{-2}$ and 0.992 (orange) for CboDyP and PpDyP constructs, respectively. Error bars represent the SD of each point.

Other CNT-modified GC electrodes for WT PpDyP immobilization. For all other CNTs modifications tested where WT PpDyP was either adsorbed on SWCTs-NH_2/GC electrodes or entrapped in MWCNTs-COOH/PAH/GC or MWCNTs-OH/PAH/GC, no catalytic activity was measured (Figure S 3.7) in the presence of increasing H_2O_2 concentrations.

3.3.3.3. Analysis of the analytical parameters compared to the HRP-based biosensors.

The biodevices developed herein showed good catalytic activity towards H_2O_2, including those designed using an empirical approach, i.e., WT CboDyP:SWCNTs-Ink/GC and WT PpDyP:SWCNTs-INK-Ink/GC, and those following a rational design, i.e., PpDyP FireProt/SAM/Ag and PpDyP PROSS/SAM/Ag (Table 3.2), except WT CboDyP/SAM/Ag.

The DyP:SWCNT-Ink/GC biodevices displayed comparable sensitivity and linear range with the most common HRP-based biosensors. Both WT CboDyP:SWCNTs-Ink/GC and WT PpDyP:SWCNTs-Ink/GC revealed a LOD of 30 and 16 µM for WT CboDyP and WT PpDyP, respectively. Although our developed devices have a higher LOD than the reported HRP-based devices, this is not necessarily a drawback. For instance, biodevices with these characteristics could be employed for medical applications where the concentration of H_2O_2 higher than 10 µM could harm the patient [27].

The PpDyP FireProt and PpDyP PROSS bioelectrodes showed several remarkable features compared to the HRP-based examples found in the literature. Their sensitivity is ca.~1,300 $mA\cdot M^{-1}\cdot cm^{-2}$, which is comparable to the previously developed (by us) WT PpDyP bioelectrode [4], with values of 1,150 ± 20 and 1,420 ± 50 $mA\cdot M^{-1}\cdot cm^{-2}$ for PpDyP FireProt and PpDyP PROSS, respectively, is up to four orders of magnitude higher than the reported values for HRP-based bioelectrodes (Table 3.2). The devices developed herein presented a fast response time (1.8 - 2.5 s), shorter than the reported values for HRP biodevices [28–35]. In terms of the LOD, both DyP-based bioelectrodes showed an average behavior falling in the range reported for HRP (0.02 - 86 µM). Both devices presented a comparable linear range (5 - 195 and 5 - 278 µM for PpDyP FireProt and PpDyP PROSS, respectively) to the WT PpDyP bioelectrode (1 - 200 µM) [9]. Taken together, from all the biodevices developed herein that displayed H_2O_2 activity, both WT CboDyP and PpDyPs (WT and *in silico* engineered variants) emerge as promising candidates for the construction of H_2O_2 biosensors. Nevertheless, the bioelectrodes constructed by the rational design, based on PpDyP FireProt and PpDyP PROSS as the immobilized biocatalyst, displayed superior analytical performance (Table 3.2).

Table 3.2 - Analytical parameters of electrochemical DyP- and HRP-based H_2O_2 biosensors

Bioelectrode	Method/E_w (vs. NHE)	LOD (µM)	Linear range (µM)	Response time (s)	Sensitivity ($mA \cdot M^{-1} \cdot cm^{-2}$) ($mA \cdot M^{-1}$)$^+$	Ref.
WT CboDyP:SWCNT-Ink/GC	CV/−100	16	9 - 500	-	555 ± 10	This work
WT PpDyP:SWCNT-Ink/GC	CV/−100	31	9 - 230	-	610 ± 30	
PpDyP FireProt/SAM/Ag	cAmp/+100	7	5 - 195	2.5	1,150 ± 20	
PpDyP PROSS/SAM/Ag	cAmp/+100	12	5 - 278	1.8	1,420 ± 50	
WT PpDyP/SAM/Ag	cAmp/+100	3.6	1 - 200	2	1,310	[4]
HRP/DNA-SWCNT/GC	cAmp/−100	0.3	0.6 - 1800	-	620	[28]
HRP/Pan/MWCNTCOOH/Au	cAmp/−100	86	86 -10000	2.9	195	[29]
HRP/polyAuNPs/Au	cAmp/+250	1.5	5 -1100	8	498	[30]
HRP/Ti_3C_2/Nafion/GC	DPV	1	5 - 8000	-	6.1^+	[31]
HRP/PDA-MNPs/(L-Arg/ Tb)/GC	cAmp/−700	0.23	0.5 - 30	-	95^+	[32]
HRP/TBA−COOH−IL/MWCNT/GC	cAmp/−195	6	20 - 4300	-	161	[33]
HEPNP/rGO/Au	CV/−245	0.01	0.01 -100	-	N.R.	[34]
HRP/HAp5-fCNT/GC	cAmp/0	1.9	10 - 350	-	62^+	[35]

E_W - Working Potential (mV); cAmp - Chronoamperometry, CV - Cyclic Voltammetry, LOD - Limit of Detection; L-Arg/Tb - Poly(l-arginine/toluidine Blue); MWCNTCOOH - Carboxy-functionalized Multiwalled Carbon Nanotube; rGO - Reduced Graphene Oxide; GC - Glassy Carbon; HAp5-fCNT - Hydroxyapatite Nanoparticles Functionalized Carbon Nanotubes; HEPNP - HRP Encapsulated Protein Panoparticles; OANW - Oleylamine-Stabilized Gold Nanowires; Pan - Polyaniline; PDA-MNPs - Polydopamine-Modified Magnetic Nanoparticles; PolyAuNPS - Olymerized Gold Nanoparticles; SAM - Self-Assemble Monolayer; SWCNT-Ink - Single Walled Carbon Nanotubes; TBA−COOH−IL - Quaternary Ammonium-Based Carboxyl Functionalized Ionic Liquid; Ti_3C_2 - MXene. + sensitivity values are reported in $mA \cdot M^{-1}$. All values refer to third-generation biosensors.

3.4. Concluding remarks

SERR spectroelectrochemistry demonstrated that, while WT CboDyP and PpDyP R214W were immobilized on SAM-coated electrodes in an apparently native-like structure, immobilized WT CboDyP did not preserve its catalytic activity and redox properties. In contrast, immobilized PpDyP R214W retained its reduction potential; however, as in solution, it presented diminished catalytic activity in the immobilized state. PpDyP FireProt and PpDyP PROSS retained their structure and redox properties while displaying catalytic activity towards H_2O_2.

The analytical parameters of the various biodevices developed herein showed that PpDyP FireProt/SAM/Ag and PpDyP PROSS/SAM/Ag constructs exhibited remarkable features, including high sensitivity and low LOD. Overall, this work demonstrated that coupling SERR spectroscopy with electrochemistry allowed the identification of the best candidates, pinpointing possible areas for improvement of the enzyme immobilization process. This strategy resulted in the development of enhanced third-generation electrochemical bioelectronic devices that outperform those characterized using the conventional trial-and-error strategy.

3.7. References

[1] T. Monteiro, M.G. Almeida, Electrochemical Enzyme Biosensors Revisited: Old Solutions for New Problems, Crit Rev Anal Chem 49 (2019) 44–66. https://doi.org/10.1080/10408347.2018.1461552.

[2] A. Sassolas, L.J. Blum, B.D. Leca-Bouvier, Immobilization Strategies to Develop Enzymatic Biosensors, Biotechnol Adv 30 (2012) 489–511. https://doi.org/10.1016/j.biotechadv.2011.09.003.

[3] N.M. Kilic, S. Singh, G. Keles, S. Cinti, S. Kurbanoglu, D. Odaci, Novel Approaches to Enzyme-Based Electrochemical Nanobiosensors, Biosensors 13 (2023) 622. https://doi.org/10.3390/bios13060622.

[4] F. Secundo, Conformational Changes of Enzymes Upon Immobilisation, Chem Soc Rev 42 (2013) 6250–6261. https://doi.org/10.1039/c3cs35495d.

[5] S. Todorovic, C. Jung, P. Hildebrandt, D.H. Murgida, Conformational Transitions and Redox Potential Shifts of Cytochrome P450 Induced by Immobilization, J Biol Inorg Chem. 11 (2006) 119–127. https://doi.org/10.1007/s00775-005-0054-9.

[6] D. Valikhani, J.M. Bolivar, J.N. Pelletier, An Overview of Cytochrome P450 Immobilization Strategies for Drug Metabolism Studies, Biosensing, and Biocatalytic Applications: Challenges and Opportunities, ACS Catal 11 (2021) 9418–9434. https://doi.org/10.1021/acscatal.1c02017.

[7] E. Schneider, D.S. Clark, Cytochrome P450 (CYP) Enzymes and the Development of CYP Biosensors, Biosens Bioelectron 39 (2013) 1–13. https://doi.org/10.1016/j.bios.2012.05.043.

[8] N. Bistolas, U. Wollenberger, C. Jung, F.W. Scheller, Cytochrome P450 Biosensors—a Review, Biosens Bioelectron 20 (2005) 2408–2423. https://doi.org/10.1016/j.bios.2004.11.023.

[9] C. Barbosa, C.M. Silveira, D. Silva, V. Brissos, P. Hildebrandt, L.O. Martins, S. Todorovic, Immobilized Dye-Decolorizing Peroxidase (DyP) and Directed Evolution Variants for Hydrogen Peroxide Biosensing, Biosen. Bioelectron. 153 (2020) 112055. https://doi.org/10.1016/j.bios.2020.112055.

[10] S. Todorovic, A. Verissimo, N. Wisitruangsakul, I. Zebger, P. Hildebrandt, M.M. Pereira, M. Teixeira, D.H. Murgida, SERR-Spectroelectrochemical Study of a cbb_3 Oxygen Reductase in a Biomimetic Construct, J Phys Chem B 112 (2008) 16952–16959. https://doi.org/10.1021/jp807862m.

[11] M. Sezer, T. Genebra, S. Mendes, L.O. Martins, S. Todorovic, A DyP-type Peroxidase at a Bio-Compatible Interface: Structural and Mechanistic Insights, Soft Matter 8 (2012) 10314–10321. https://doi.org/10.1039/c2sm26310f.

[12] M. Sezer, A. Santos, P. Kielb, T. Pinto, L.O. Martins, S. Todorovic, Distinct Structural and Redox Properties of the Heme Active Site in Bacterial Dye Decolorizing Peroxidase-Type Peroxidases from Two Subfamilies: Resonance Raman and Electrochemical Study, Biochem 52 (2013) 3074–3084. https://doi.org/10.1021/bi301630a.

[13] C.M. Silveira, M.A. Castro, J.M. Dantas, C. Salgueiro, D.H. Murgida, S. Todorovic, Structure, Electrocatalysis and Dynamics of Immobilized Cytochrome PccH and its Microperoxidase, Phys Chem Chem Phys 19 (2017) 8908–8918. https://doi.org/10.1039/c6cp08361g.

[14] C.M. Silveira, P.O. Quintas, I. Moura, J.J.G. Moura, P. Hildebrandt, M.G. Almeida, S. Todorovic, SERR Spectroelectrochemical Study of Cytochrome cd_1 Nitrite Reductase Co-Immobilized with Physiological Redox Partner Cytochrome c_{552} on Biocompatible Metal Electrodes, PLoS One 10 (2015) e0129940. https://doi.org/10.1371/journal.pone.0129940.

[15] S. Todorovic, M.M. Pereira, T.M. Bandeiras, M. Teixeira, P. Hildebrandt, D.H. Murgida, Midpoint Potentials of Hemes *a* and a_3 in the Quinol Oxidase from *Acidianus ambivalens* are Inverted, J Am Chem Soc 127 (2005) 13561–13566. https://doi.org/10.1021/ja052921l.

[16] D.H. Murgida, P. Hildebrandt, Heterogeneous Electron Transfer of Cytochrome *c* on Coated Silver Electrodes. Electric field effects on structure and redox potential, J Phys Chem B 105 (2001) 1578–1586. https://doi.org/10.1021/jp003742n.

[17] F. Siebert, P. Hildebrandt, Vibrational Spectroscopy in Life Science. Wiley, 2007. https://doi.org/10.1002/9783527621347.

[18] S. Döpner, P. Hildebrandt, A.G. Mauk, H. Lenk, W. Stempfle, Analysis of Vibrational Spectra of Multicomponent Systems. Application to pH-Dependent Resonance Raman Spectra of Ferricytochrome *c*, Spectrochim Acta A 51 (1996) 573–584.

[19] A.G. Hildebrandt, I. Roots, Reduced Nicotinamide Adenine Dinucleotide Phosphate (NADPH)-dependent Formation and breakdown of Hydrogen Peroxide during mixed Function Oxidation Reactions in liver Microsomes, Arch. Biochem. Biophys. 171 (1975) 385–397. https://doi.org/10.1016/0003-9861(75)90047-8.

[20] D. Silva, A Closer Look at a Potential Biocatalyst: Unravelling the Catalytic, Stability and Structural Features of PpDyP, a DyP-type Peroxidase. Doctoral dissertation, Universidade Nova de Lisboa, 2022. https://hdl.handle.net/10362/158343.

[21] C.M. Silveira, E. Moe, M. Fraaije, L.O. Martins, S. Todorovic, Resonance Raman View of the Active Site Architecture in Bacterial Dyp-Type Peroxidases, RSC Adv 10 (2020) 11095–11104. https://doi.org/10.1039/D0RA00950D.

[22] S. Marchesan, M. Prato, Under the lens: Carbon Nanotube and Protein Interaction at the Nanoscale, Chem Commun 51 (2015) 4347–4359. https://doi.org/10.1039/c4cc09173f.

[23] K. Gong, Y. Yan, M. Zhang, L. Su, S. Xiong, L. Mao, Electrochemistry and Electroanalytical Applications of Carbon Nanotubes: A Review, Anal Sci 21 (2005) 1383–1393. https://doi.org/10.2116/analsci.21.1383.

[24] S. Gupta, C.N. Murthy, C.R. Prabha, Recent Advances in carbon Nanotube Based Electrochemical Biosensors, Int J Biol Macromol 108 (2018) 687–703. https://doi.org/10.1016/j.ijbiomac.2017.12.038.

[25] R.J. Kassner, Theoretical Model for the Effects of Local Nonpolar Heme Environments on the Redox Potentials in Cytochromes, J Am Chem Soc 95 (1973) 2674–2677. https://doi.org/10.1021/ja00789a044.

[26] S. Todorovic, P. Hildebrandt, L.O. Martins, Surface Enhanced Resonance Raman Detection of a Catalytic Intermediate of DyP-type Peroxidase, Phys Chem Chem Phys 17 (2015) 11954–11957. https://doi.org/10.1039/c5cp01283j.

[27] J.E. Giaretta, H. Duan, F. Oveissi, S. Farajikhah, F. Dehghani, S. Naficy, Flexible Sensors for Hydrogen Peroxide Detection: A Critical Review, ACS Appl. Mater. Interfaces 14 (2022) 20491–20505. https://doi.org/10.1021/acsami.1c24727.

[28] X. Zeng, X. Li, X. Liu, Y. Liu, S. Luo, B. Kong, S. Yang, W. Wei, A Third-Generation Hydrogen Peroxide Biosensor Based on Horseradish Peroxidase Immobilized on DNA Functionalized Carbon Nanotubes, Biosens Bioelectron 25 (2009) 896–900. https://doi.org/10.1016/j.bios.2009.09.003.

[29] M.-Y. Hua, Y.-C. Lin, R.-Y. Tsai, H.-C. Chen, Y.-C. Liu, A Hydrogen Peroxide Sensor Based on a Horseradish Peroxidase/Polyaniline/Carboxy-Functionalized Multiwalled Carbon Nanotube Modified Gold Electrode, Electrochim Acta 56 (2011) 9488–9495. https://doi.org/10.1016/j.electacta.2011.08.043.

[30] R. Villalonga, P. Díez, P. Yáñez-Sedeño, J.M. Pingarrón, Wiring Horseradish Peroxidase on Gold Nanoparticles-Based Nanostructured Polymeric Network for the Construction of Mediatorless Hydrogen Peroxide Biosensor, Electrochim Acta 56 (2011) 4672–4677. https://doi.org/10.1016/j.electacta.2011.02.108.

[31] W. Xu, M. Sakran, J. Fei, X. Li, C. Weng, W. Yang, G. Zhu, W. Zhu, X. Zhou, Electrochemical Biosensor Based on HRP/Ti_3C_2 /Nafion Film for Determination of Hydrogen Peroxide in Serum Samples of Patients with Acute Myocardial Infarction, ACS Biomater Sci Eng 7 (2021) 2767–2773. https://doi.org/10.1021/acsbiomaterials.1c00242.

[32] S. Sardaremelli, M. Hasanzadeh, F. Seidi, Enzymatic Recognition of Hydrogen Peroxide (H_2O_2) in Human Plasma Samples using HRP> Immobilized on the Surface of Poly(arginine-toluidine blue)-Fe_3O_4 Nanoparticles Modified Polydopamine; A Novel Biosensor, J Mol Recognit 34 (2021). https://doi.org/10.1002/jmr.2928.

[33] M. Murphy, K. Theyagarajan, K. Thenmozhi, S. Senthilkumar, Quaternary Ammonium Based Carboxyl Functionalized Ionic Liquid for Covalent Immobilization of Horseradish Peroxidase and Development of Electrochemical Hydrogen Peroxide Biosensor, Electroanalysis 32 (2020) 2422–2430. https://doi.org/10.1002/elan.202060240.

[34] J.-H. Shin, M.-J. Lee, J.-H. Choi, J. Song, T.-H. Kim, B.-K. Oh, Electrochemical H_2O_2 Biosensor Based on Horseradish Peroxidase Encapsulated Protein Nanoparticles with Reduced Graphene Oxide-Modified Gold Electrode, Nano Converg 7 (2020) 39. https://doi.org/10.1186/s40580-020-00249-0.

[35] J. Alvarez-Paguay, L. Fernández, D. Bolaños-Méndez, G. González, P.J. Espinoza-Montero, Evaluation of an Electrochemical Biosensor Based on Carbon Nanotubes, Hydroxyapatite and Horseradish Peroxidase for the Detection of Hydrogen Peroxide, Sens Biosensing Res 37 (2022) 100514. https://doi.org/10.1016/j.sbsr.2022.100514.

Supporting Information

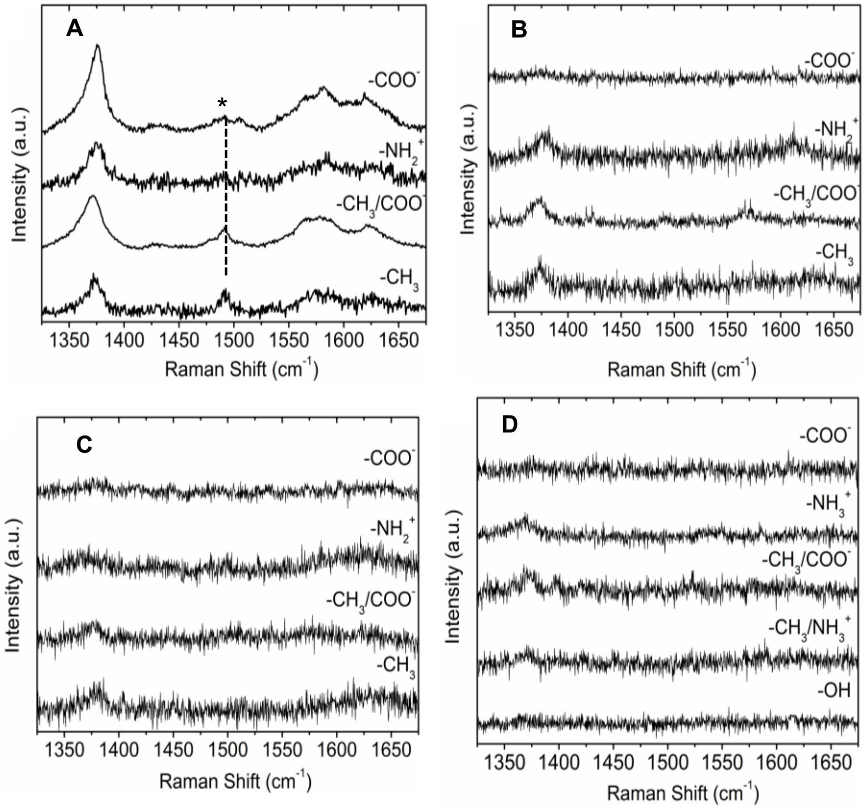

Figure S 3.1 - SERR spectra of the immobilized ferric DyPs. (**A**) WT SviDyP (**B**) WT CboDyP; (**C**) WT TfuDyP and (**D**) WT ScoDyP immobilized on Ag electrodes coated with pure and mixed alkanethiol ($HS(CH_2)_{n}$-X, X = OH, CH_3, COO^- , and NH_3^+) SAMs. For SviDyP the non-native 5cHS species is identified with (∗). All spectra were acquired with 405 nm excitation at RT pH 7, with a laser power and accumulation time of 1.3 mW and 30-40 s.

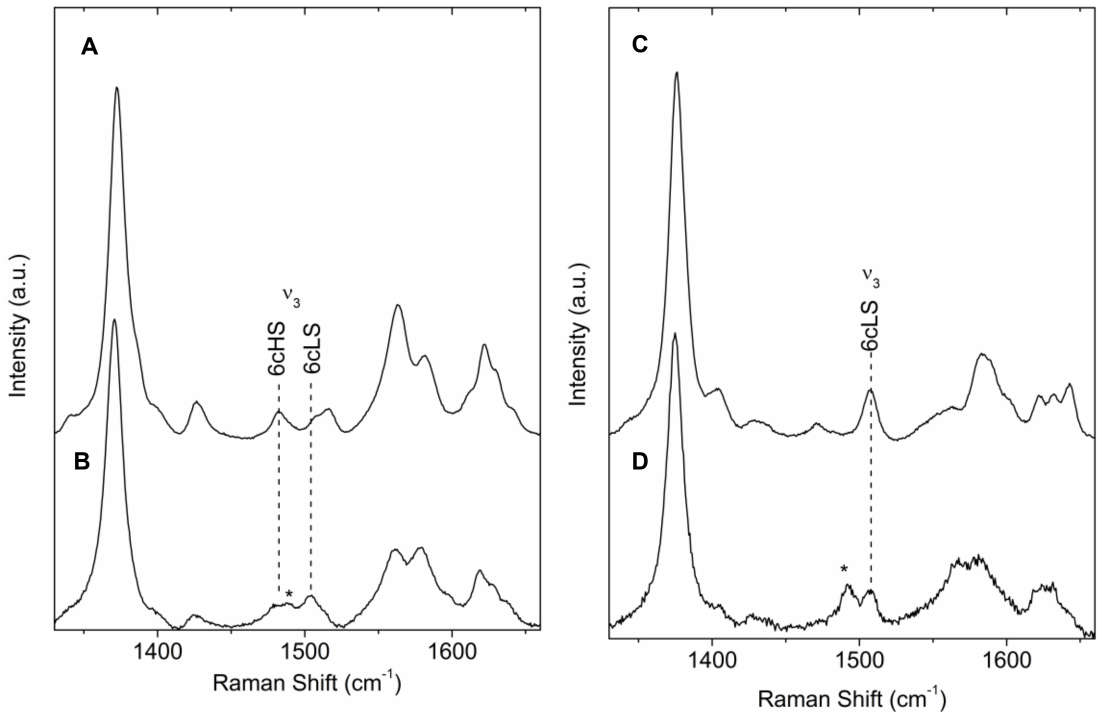

Figure S 3.2 - RR and SERR spectra of PpDyP distal variants. (**A**) RR and (**B**) SERR spectra of R214W variant; (**C**) RR and (**D**) SERR spectra of R214WI SERR spectra of each immobilized PpDyP variant on Ag electrodes coated with AOH:MOH at +0.250 V. The non-native 5cHS species is identified (∗). Measurements were done with a 405 nm excitation at RT, with laser power and accumulation time of 3 mW and 30 s (RR) and 1.4 mW and 30 s (SERR).

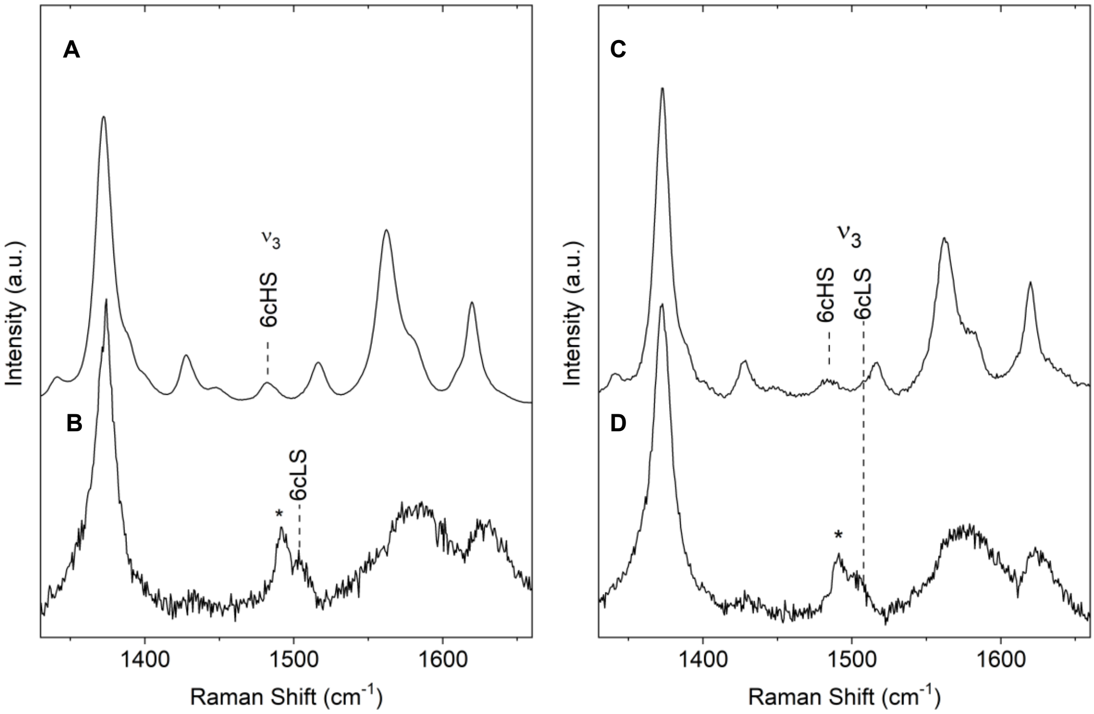

Figure S 3.3 - Comparison of the RR and SERR spectra of CboDyP distal variants. (**A**) RR and (**B**) SERR spectra of R307W variant; (**C**) RR and (**D**) SERR spectra of R307I variant. SERR spectra of immobilized CboDyP distal variants on Ag electrodes coated with 1-UDT: AUT SAMs at +0.250 V The non-native 5cHS species is identified (∗). Measurements done with a 405 nm excitation at RT, with laser power and accumulation time of 3 mW and 30 s (RR) and 1.4 mW and 30 s (SERR).

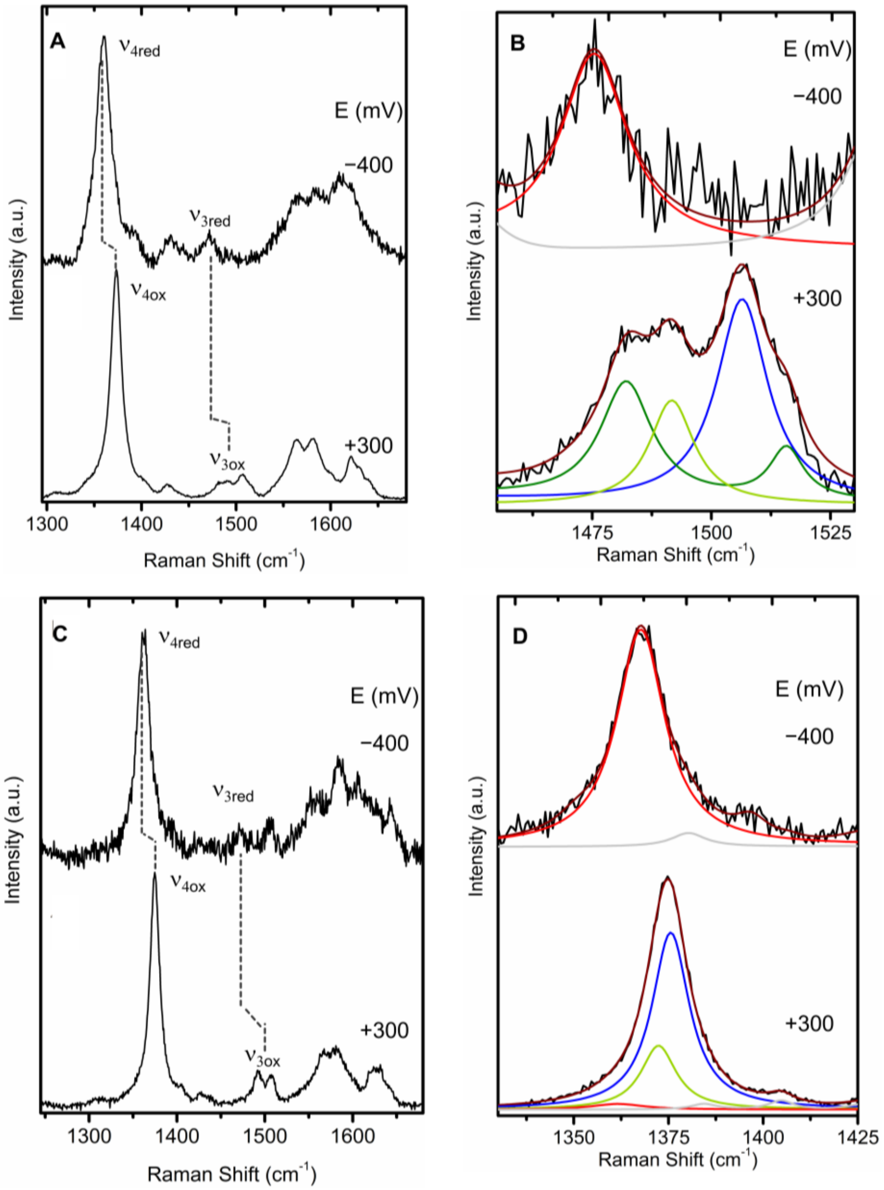

Figure S 3.4 - Spectra of immobilized (**A**) PpDyP R214W and (**C**) PpDyP R214I on Ag electrodes coated with AOT:MOH SAM at +300 mV and −400 mV. (**B**) Component analysis of ν_3/ν_{38} region for PpDyP R214W and (**D**) component analysis of ν_4 region for PpDyP R214I; the component spectra represent the native ferric populations: 6cHS (green), native 6cLS (blue), ferrous 5cHS (red) together with the non-native 5cHS (light green) and non-assigned bands (grey). The experimental spectra are depicted in black and the overall component spectra in dark red. Measurements were performed with 405 excitation and 1.4 mW laser power.

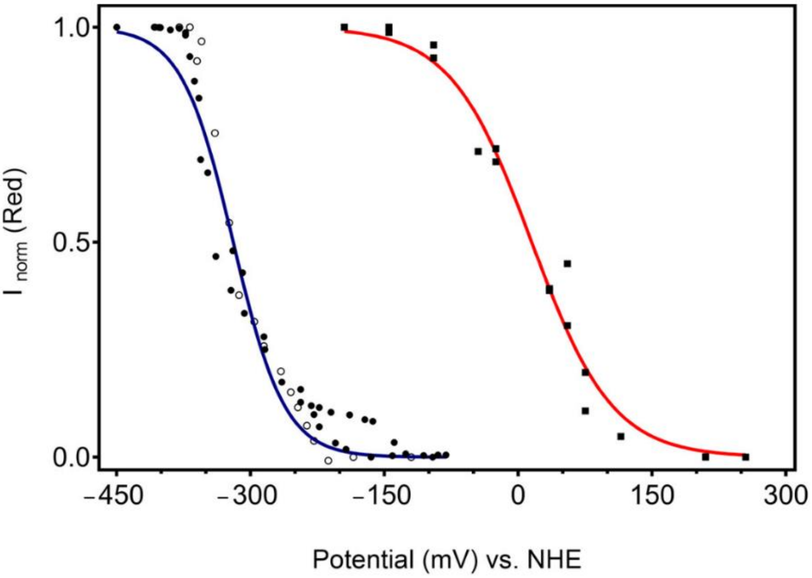

Figure S 3.5 - Redox titrations of WT CboDyP in solution and immobilized states. Left curve: potentiometric titration in solution monitored by UV-vis absorption spectroscopy. The circles represent the normalized absorption of the reduced population at 430 nm as a function of the solution potential for three independent experiments. Solid (and empty) symbols represent titrations by stepwise reduction (and oxidation) of the ferric (and ferrous) enzyme. Right curve: SERR spectroelectrochemical titration of CboDyP immobilized on electrodes coated with 1-UDT/AUT. The squares represent the relative contribution of the ferrous 6cHS population estimated from the v_4 band (1359 cm^{-1}) at variable electrode potentials for seven independent experiments. Solid lines represent fits of the Nernst equation to the experimental data points, yielding for solution enzyme, $E^{0'}_{sol}$ = −320 mV (blue line), and for immobilized enzyme, $E^{0'}_{imm}$ = +15 mV (red).

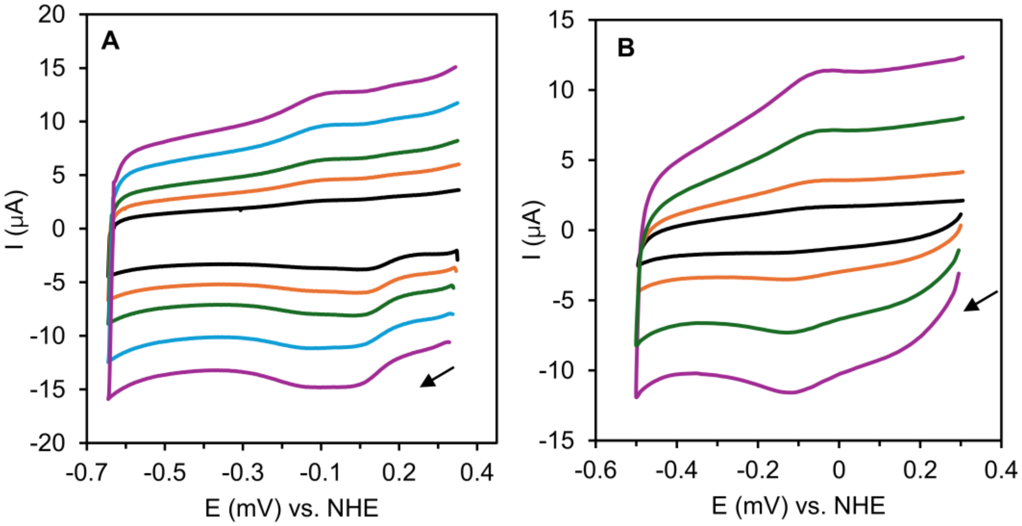

Figure S 3.6 - Electrochemical analysis CV of (**A**) WT PpDyP:SWCNT-Ink/GC and (**B**) WT CboDyP:SWCNT-Ink/GC, at scan rates of 20 (black line), 35 (orange line), 50 (green line), 75 (blue line) and 100 mV/s (purple line) (inner to outer scans).

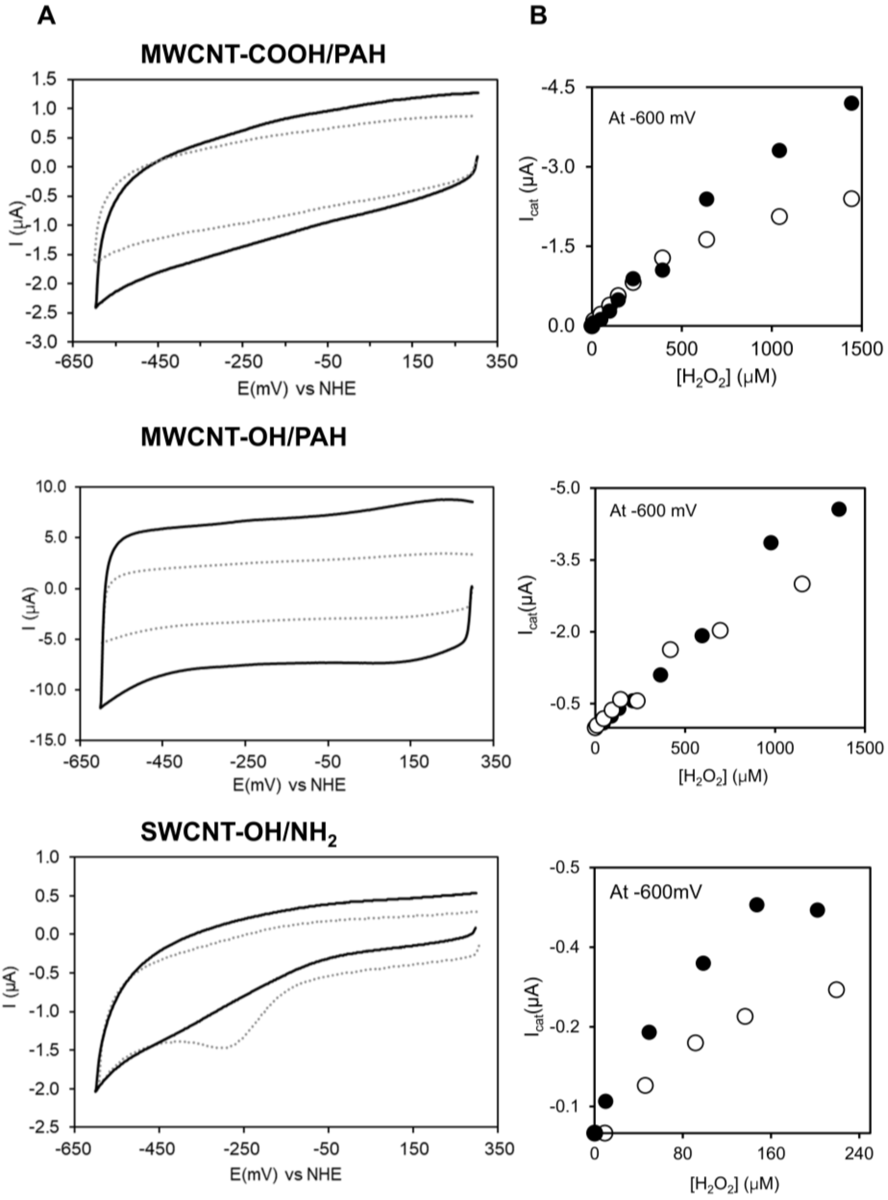

Figure S 3.7 - Electrocatlytic activity of PpDyP immobilized in different CNTs. (**A**) CV of WT PpDyP immobilized on the different CNT modified GC. (**B**) Calibration plot for H_2O_2 response for PpDyP immobilized on the different CNT modified GC (full black circles) and respective controls, electrodes prepared without the enzyme, (open black circles). The measurements were performed in 12.5 mM K_2SO_4 in 12.5 mM PB, pH 7.0. CV was performed at 50 mV/s.

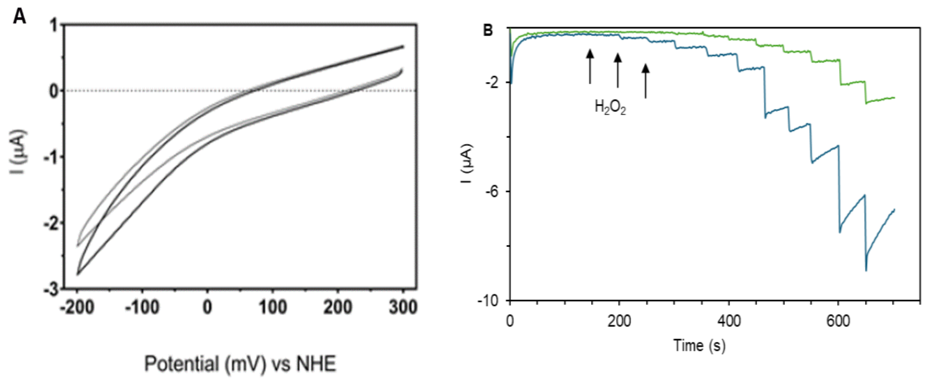

Figure S 3.8 - Electrochemical responses of (**A**) WT CboDy and (**B**) PpDyP distal variants (R214W/I) immobilized on SAM coated Ag electrodes. (**A**) CVs in the absence (black line) and presence (grey line) of 700 µM H_2O_2. (**B**) Chronoamperometry of PpDyP R214W (blue line) and PpDyP R214I (green line) in the presence of increasing concentrations of H_2O_2. The measurements were performed in 12.5 mM K_2SO_4 in 12.5 mM PB, pH 7.0. CV was performed at 50 mV/s, and cAmp was performed with the electrode rotating at 2600 rpm.

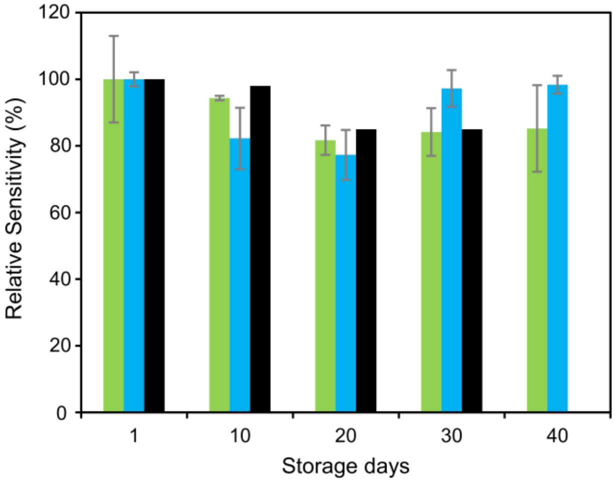

Figure S 3.9 - Stability of PpDyP FireProt/SAM/Ag (green), PpDyP PROSS/SAM/Ag (blue) and WT PpDyP/SAM/Ag (black, data from [4]) electrodes response to H_2O_2. Relative sensitivity during storage at 4 °C for 42 days measured on a batch of electrodes prepared on the same day (n = 12). Error bars represent the SD in percentage of each point.

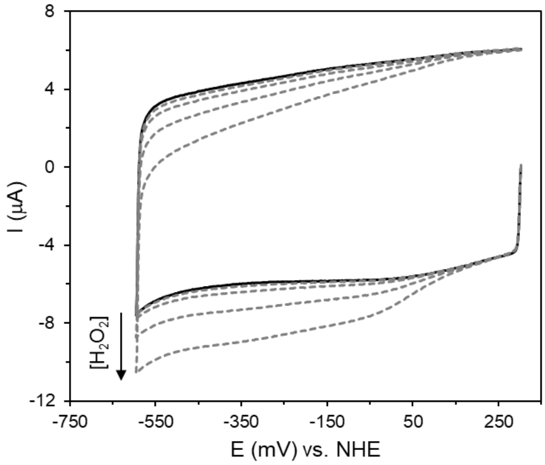

Figure S 3.10 - CVs of the control electrode buffer-SWCNTs-Ink/GC, prepared without DyPs (CboDyP or PpDyP), in the absence (black line) and presence (grey dashed lines) of increasing H_2O_2 concentrations (9 - 1267 μM). Cyclic voltammograms were measured at 50 mV/s scan rate in 12.5 mM K_2SO_4 in 12.5 mM PB.

Chapter 4 Construction of a miniaturized PpDyP-based H_2O_2 biosensor

This chapter contains data published in :

Catarina Barbosa, Maria C. Stefoni, Carolina F. Rodrigues, Lígia O. Martins, Daniel H. Murgida, Smilja Todorovic, Célia M. Silveira. Miniaturized Dyp Peroxidase-Based Biosensor for on-site Open-Air Use. ACS Omega 10: 8736–8744, 2025. Doi: 10.1021/acsomega.5c00461.

Acknowledgments and contributions

In this chapter, Catarina Barbosa performed the immobilization studies of WT PpDyP on all tested modified SPE, and evaluated the electrocatalytic activity of the immobilized enzyme on these electrodes. She performed the stability and recovery tests. Finally, she conducted the assays (electroactivity, stability, and recovery tests) using PpDyP PROSS as the biocatalyst.

Carolina Rodrigues performed the overexpression and purification of PpDyP PROSS. Maria Stefoni helped prepare the modified surface of the working electrode using electrodeposition of nanoparticles. Maria Marchi from the UBA SEM service acquired the scanning electron microscopy images.

Abstract

We report the construction of a miniaturized, disposable third-generation electrochemical PpDyP-based biosensor for H_2O_2 detection, using nanostructure-modified screen-printed electrodes (SPEs). Gold nanospheres (AuNPs) are electrodeposited on commercially available SPEs to increase enzyme loading. The PpDyP/SAM/AuNP/C-SPE biosensor has a linear response range to H_2O_2 from 30 to 475 µM, a sensitivity of 230 ± 10 $mA \cdot M^{-1} \cdot cm^{-2}$, and a limit of detection of 3.5 µM, determined in open air conditions. This single-use device is suitable for on-site measurements of H_2O_2 in air-exposed samples, such as physiological fluids. It has the potential for customization and improvement due to the easy production and genetic manipulation of the employed biocatalyst, PpDyP.

4.1. Introduction

Nowadays, there is an increasing interest in low-cost, compact and easy-to-use analytical devices that can quickly provide on-site detection of important analytes such as environmental pollutants or biomarkers in medical diagnostics. These types of devices are highly sought after in different fields, from clinical and biomedical applications [1–4] to food analysis, quality control [5,6] and environmental monitoring [7–9]. One promising solution to meet this need is using SPEs that enable the construction of miniaturized enzyme-based electrochemical devices with improved performance compared to traditional analytical techniques such as high-performance liquid chromatography. Enzyme-based SPE devices are favorable as they can ensure rapid, specific, sensitive, and precise analyte detection. Moreover, these devices are portable and can be used by non specialists for on-site detection. SPEs are strip electrodes that can work as compact electrochemical cells, typically featuring a three-electrode configuration (working, counter and reference electrode, WE, CE, and RE, respectively). They can be printed on plastic, ceramic, and, more recently, on paper substrates [2,10–16]. Another advantage of using SPEs to develop biodevices is their low cost and ease of mass production using thick film technology compared to classical pen electrodes commonly used in electrochemistry [2,10–17]. These miniaturized biodevices can work with a few microliters of sample volume drop on their surface (75 - 100 µL), or be used in a small 2.5 to 5 mL electrochemical cell [12]. These biodevices can be connected to a portable potentiostat, allowing on-site determination of the target analytes. The surface of the SPEs can be easily modified with biomolecules, nanoparticles and polymers, among others, depending on the desired application [4,18,19]. SPEs are often comparable with the use of organic solvents, which are commonly employed to prepare NP dispersions and dissolve water-insoluble organic molecules needed for the WE modification; or in the preparation of the target analyte before measurement. However, organic solvents may limit the use of SPEs since these solvents can dissolve the inks used in the SPE printing process, and thus compromising the biosensor's performance [16].

Silver inks are mainly used as the conductive track, while the WE is usually made with graphite inks. Other materials, such as gold or platinum, can be used in the SPE preparation [2,10–16]. The RE is commonly made from silver inks, resulting in a pseudo-reference (“false” reference) or a quasi-reference (“almost” or “essentially” reference) electrode [20]. They lack thermodynamic equilibrium; therefore, one cannot calculate its potential, which can be overcome by, for example, using internal standards such as ferricyanide [20]. Moreover, these pseudo-references are not ideally nonpolarizable (their potential shifts during the measurements depending on the current density applied) and work over a limited range of conditions, e.g., pH or temperature. Nevertheless, their potential can be surprisingly constant during the experiments under selected conditions [20].

Carbon ink is a commonly used material as the WE in electrochemical biosensing applications of SPEs due to chemical inertness, low background currents, wide potential windows, and ease of modification. Metal inks, such as gold, can offer other advantages, as they can be modified using SAMs of alkanethiols, enhancing the applicability of Au-SPEs for the development of enzymatic electrochemical biosensors [2,10–16] by providing a biocompatible environment for the biocatalyst attachment at the electrode surface [21].

(Bio/nano)modifiers can be added to the WE during or after screen-printing [3,4,12,13,15,16,22,23]. Nanomaterials such as Au, Ag, Pt, Pb, or other metal NP, CNTs, or graphene-based inks can accelerate the ET rate at the electrode surface between the enzyme and the WE [16]. The most common methods for modifying the WE of the SPEs after the screen-printing process are drop casting or electrodeposition of metal NPs. The former involves drying a NP solution/dispersion on the WE surface; this process nevertheless has a major drawback since metal NPs (especially AgNP) tend to aggregate during drying. In contrast, electrochemical deposition allows for precise control over the morphology of the metal NPs on the WE [15,18].

Due to the properties discussed above, SPEs have helped considerably in transitioning from the classic electrochemical cell to miniaturized and portable electrochemical biodevices that can be used for on-site analysis [24,25].

In this chapter, we describe a miniaturized third-generation electrochemical biosensor suitable for accurately quantifying H_2O_2 in small volumes of air-exposed samples. That is developed by immobilizing PpDyP selected in the previous chapter(s) onto commercially available SPEs modified with metal NPs.

4.2. Materials and methods

4.2.1. Reagents and solutions

8-Amino-1-octanethiol (AOT), 6-mercapto-1-hexanol (MOH), silver nanoparticles (AgNP,), Ø = 40 nm; 1 mg/mL in aqueous sodium citrate, gold (III) chloride trihydrate, Sigmatrix Urine Diluent and Serum Replacement were purchased from Sigma-Aldrich. Serum Replacement (50×) was diluted to 1× before the use in phosphate saline buffer pH 7.4. Sulfuric acid (96%) was purchased from Panreac AppliChem. Hydrogen peroxide (30% w/w) was obtained from Honeywell. All other chemicals were obtained from Sigma-Aldrich and had the highest purity grade available. Solutions were prepared using deionized water from a Milli-Q® Water Purification System (Merck Millipore).

The concentration of H_2O_2 stock solutions was determined spectrophotometrically using the molar absorption coefficient of $43.6\ M^{-1}\cdot cm^{-1}$ [26].

4.2.2. Overexpression and purification of recombinant wild-type PpDyP and variant

PpDyP and PpDyP PROSS expression and purification were performed as described in Chapter 2.2, following the previously optimized protocol [27].

4.2.3. Preparation of the PpDyP-modified electrodes

<u>Electrodes</u>. Carbon, gold and silver SPEs were purchased from Metrohm Dropsens. They present a three-electrode configuration printed on the same ceramic strip, with

carbon (C-SPE, DRP-C110), gold (AuSPE, DRP-C220BT) or silver (AgSPE, DRP-C010) working electrodes (WE, Ø = 4 mm), silver pseudo-reference electrode (+0.345 and +360 mV vs. NHE, for the C- and Au-SPE, respectively) and carbon (C- and Ag-SPE) or gold counter (Au-SPE) electrodes. All potentials herein report to NHE.

SPE cleaning. The C- , Ag- Au-SPE surfaces were cleaned by thoroughly rinsing with water and ethanol. The Au and Au modified WE was further electrochemically cleaned in 0.5 M H_2SO_4 by cyclic voltammetry in the +1,700 to +100 mV range at 100 mV/s scan rate (5 cycles).

4.2.3.1. Electrode modifications

Drop-casting of silver nanoparticles (AgNPs). Five consecutive layers of AgNPs were drop-casted (2 µL AgNP solution 1 mg/mL) on the C-SPE. Between each layer, the surface was dried inside an N_2-saturated chamber.

Electrodeposition of silver nanopillars (AgNPis). AgNPis were electrodeposited on the C-SPEs using a protocol adapted from Feng et al. [28]. In short, the WEs were poised at −0.3 V for 300 s in a solution containing 6 mM $AgNO_3$, 7 mM SDS, 130 mM NH_4CH_3COO, 0.3 mM NH_4OH, and 100 mM KNO_3. Afterward, the electrodes were thoroughly rinsed with water.

Electrodeposition of gold nanoparticles (AuNPs). The C/Au-SPEs were modified by electrodeposition of AuNPs following a previously described procedure [29]. Briefly, the WE of the SPE was immersed in a solution of 0.5 mM $HAuCl_4$ prepared in 0.5 M H_2SO_4, and the electrodeposition was carried out at −0.2 V for 5 min. Afterward, the modified AuNP/SPEs were cleaned electrochemically, as described above (4.3.2).

SAM formation and enzyme immobilization. Electrode functionalization with SAMs and enzyme immobilization were performed as described in section 3.2.2. Briefly, the metal or metal modified SPEs (Au-SPEs, AgNPi/SPEs and AuNP/SPEs) were incubated in 1 mM SAM solution AOT and MOH (1:3 v/v) in ethanol. The AgNP/C-SPEs were incubated on the same SAMs mixture prepared in water. The electrodes were incubated in the SAMs solution overnight or for 2 h 30 min depending on whether the SPE was used as the WE (anaerobic characterization) or as the whole electrochemical cell (aerobic characterization). For enzyme attachment, the SAM-coated electrodes were first rinsed with supporting electrolyte. Afterward, 75 μL of 0.5 - 5 μM PpDyP solution (in supporting electrolyte) was deposited on the surface of the WE and left incubating for 30 min, at 4 °C. Prior to measurements, the WE was rinsed with supporting electrolyte to remove loosely bound PpDyP molecules.

4.2.4. Electrochemical measurements

The electrochemical experiments were conducted using an Autolab PGSTAT204 potentiostat controlled with the NOVA 2.1 software (Metrohm).

Purged setup: The first characterization of the different constructs tested was made in a deoxygenated environment. A one-compartment electrochemical cell with a three-electrode system, composed of a RE (3 M Ag/AgCl, WPI), a Pt counter electrode (Radiometer) and the modified WE of the SPE strip, was used for electrode optimization steps *i.e.*, choice of SPE, nanostructure and enzyme concentration. In this set-up, the supporting electrolyte solution (10 mL) was deoxygenated by bubbling argon for 10 min before each experiment. These conditions were also used for the stability assays.

Open air setup: Following the optimization steps, the analytical characterization of the biosensor and sample analysis was performed using the SPE strip as the electrochemical cell. Experiments were done by placing the SPE inside an air-exposed cell containing 3 to 5 mL supporting electrolyte or sample.

PpDyP modified electrodes response to H_2O_2. The PpDyP-modified electrodes were characterized at room temperature by CV at 50 mV/s scan rate. Response to H_2O_2 was evaluated by successive substrate injections into the cell. The cyclic voltammograms were recorded in the range of +800 to 0 mV when using the external electrode cell and +750 to +150 V when using the reference electrode of the SPEs.

The cell solution was mixed by bubbling with argon or magnetic stirring for 35 s, for purged and open-air configurations, respectively.

Determination of the analytical parameters of the PpDyP modified electrodes for H_2O_2. The I_{cat} was measured at +100 mV; all values were corrected by subtracting the non-catalytic current measured without H_2O_2. Each assay was replicated at least three times.

The sensitivity was determined as the slope of the I_{cat} = f([H_2O_2] calibration curve), within the linear response range. The SPE's geometric area (0.11 cm^2) was used to convert the I_{cat} to current density (J_{cat}) values. The LOD was determined at a signal-to-noise ratio (S/N) of 3. The maximum current density (J_{max}) was determined at substrate-saturating concentrations, typically between 500 - 750 µM H_2O_2.

The long-term stability, i.e., storage stability, of the PpDyP electrode (PpDyP/SAM/AuNP/C-SPE) was evaluated via the analysis of the sensitivity of a batch of SPEs, prepared as described above and stored in supporting electrolyte at 4 °C for one month. Each electrode was tested once, at room temperature, which we refer to as single-use.

The reproducibility of the optimized PpDyP (PpDyP/SAM/AuNP/C-SPE) electrodes was determined as the RSD of the sensitivities of different electrode preparations (N=4).

Real sample analysis. Bottled water, synthetic urine and human serum replacement were used as purchased without any previous treatment. As described above, internal calibration curves in each matrix were performed in the SPE cell in open-air configuration. Each curve was replicated three times. The biosensor's response to H_2O_2 was measured using the standard addition method. The solutions were spiked with a given concentration of H_2O_2 (130 µM), and the recovery percentages were calculated (N = 3).

4.2.5. Electrode characterization

SEM. The SEM images were captured with a Carl Zeiss NTS Supra TM 40 FESEM using an electron high tension of 3 kV.

RR spectroscopy. RR spectra were acquired on a Raman spectrometer (Jobin Yvon LabRam 800 HR) with a back-illuminated CCD detector cooled by liquid nitrogen, equipped with a 1200 L/mm diffraction grating. An Olympus 20× objective was used for laser focusing on the sample and light collection in the backscattering geometry. The excitation source was a 405 nm diode laser (Toptica Photonics AG).

RR spectra of PpDyP in solution were recorded in a rotating cuvette (Hellma) containing 100 µL of 20 µM PpDyP in supporting electrolyte, pH 7. The RR spectra of the enzyme deposited on SAM/AuNP/C-SPEs were obtained from the surface of the electrode covered by a 100 µL drop of the enzyme (30 µM in supporting electrolyte). The spectra were recorded using 3 - 4 mW laser power and 25 - 30 s accumulation time. Four to eight spectra were co-added in each measurement to improve the S/N ratio.

SERR spectroscopy. SERR spectra of immobilized enzymes attached to the modified electrode were obtained with an Horiba LabRam HR Evolution stage 1 spectrometer, equipped with an 1800 L/mm diffraction grating and a Synapse detector, cooled by Peltier circuits. An Olympus 20× objective was used for laser focusing on the sample and light collection in the backscattering geometry. A 405 nm laser diode laser was used as an excitation source (Toptica Photonics AG). The spectra were recorded using laser power of 2 mW and accumulation time of 10 s. Four to eight spectra were co-added to improve the S/N ratio.

4.3. Results and discussion

After demonstrating that WT PpDyP and it's *in silico* engineered variant (PpDyP PROSS) are the most promising immobilized biocatalysts for H_2O_2 biosensing applications (cf. section 3.3.3.3, Table 3.3), a miniaturized prototype of a third-generation electrochemical device was developed. This was achieved by adapting the biodevice constructed with Ag bulk electrodes, i.e., PpDyP (PROSS)/SAM/Ag (cf. section 3.3.2.2.a) to SPEs.

The optimized PpDyP-based H_2O_2 biosensor was selected by evaluating the building blocks of the miniaturized construct, i.e., different types of SPE materials (Au-;C-; or Ag-) and nanostructures (silver nanoparticles - AgNP; gold nanoparticles - AuNP or silver nanopillars - AgNPi) conducted in anaerobic (Ar saturated) conditions, Figure 4.1. Afterward, the catalytic activity was also tested in aerobic (air-exposed) conditions. Prior to enzyme (WT or variant) immobilization, the WE (modified with nanostructures or not) was coated with a SAM to create a biocompatible environment for the attachment of PpDyP in the native structure, as described in Chapter 3.

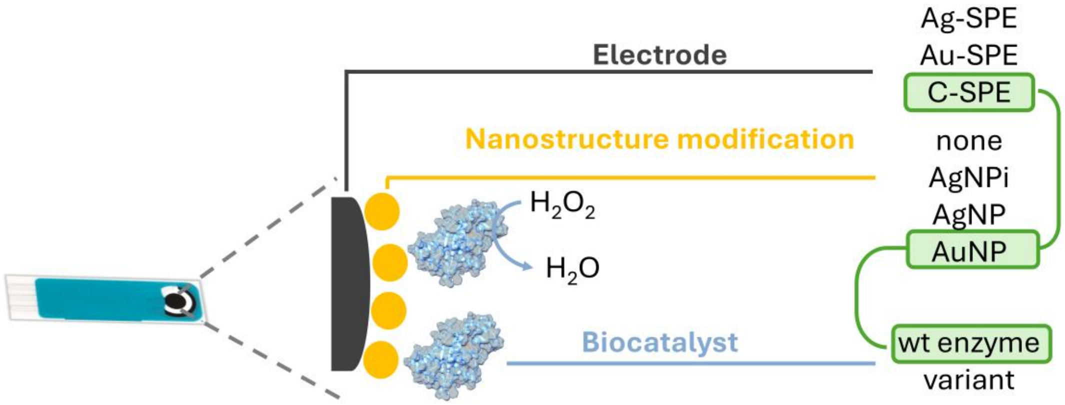

Figure 4.1 - Schematic representation of the modifications on the SPEs for constructing the miniaturized PpDyP biosensor. The modifications highlighted in green represent the optimized biosensor configuration.

4.3.1. PpDyP on Modified SPEs

4.3.1.1. Structural Characterization of the immobilized enzyme

AuNP/SPE. Electrodeposition of AuNPs on the WE of C-SPE(Figure 4.2) resulted in a high density of nanospheres, homogeneous in size and shape, covering the electrode surface, as revealed by SEM (Figure 4.2). The electrodeposition of AuNP on Au-SPE was also tested. Interestingly, the electrochemical surface area of these modified electrodes was revealed to be comparable as the AuNP/C-SPE one (Table

S 4.1), which indicated that the electrodeposition on both electrodes occurred in the same manner.

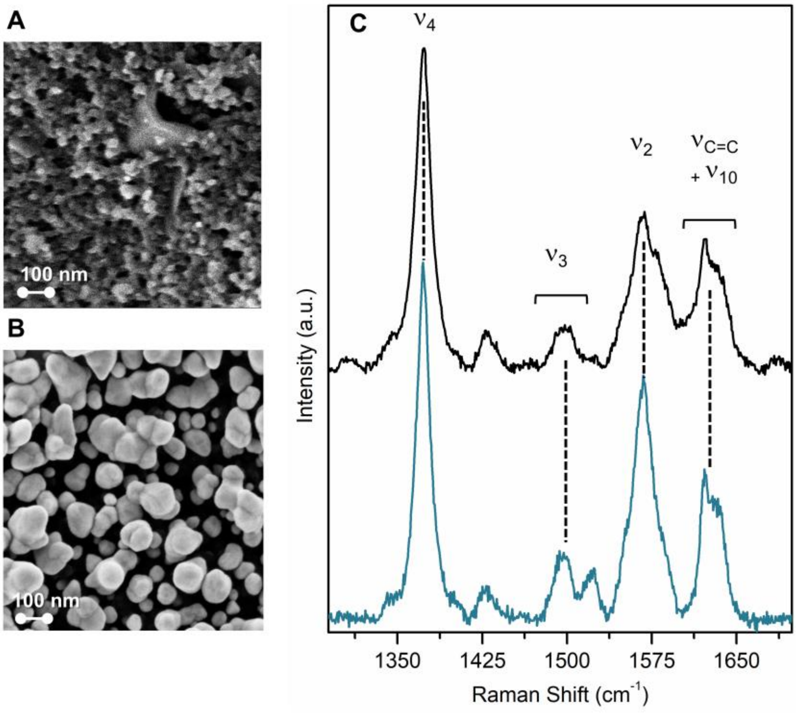

Figure 4.2 - Characterization of the WT PpDyP/SAM/AuNP/C-SPE biosensor components. (**A-B**) SEM images of C-SPE WE surface (**A**) before and (**B**) after AuNPs electrodeposition (magnification 100K× and 200K×, respectively). (**C**) RR spectra of WT PpDyP in solution (top trace) and immobilized on SAM/AuNP/C-SPE (bottom trace). Spectra were acquired with 405 nm excitation; laser power and accumulation times were 25 - 30 s and 3 - 4 mW, respectively.

The structural integrity of the heme active site of WT PpDyP attached to SAM/AuNP/C-SPE was probed by RR spectroscopy, which revealed the oxidation, coordination, and spin state of the heme group, based on the frequency of the marker bands, ν_i [30,31] (cf. Chapter 1.4.3.1). The comparison of the RR spectra of PpDyP in solution with the RR spectra obtained from the surface of modified C-SPEs, confirmed the presence of the same heme species in both cases. This was concluded from the position of the marker bands ν_4, ν_3, ν_2, ν_{10}, $\nu_{C=C}$, (Figure 4.2 C) and further confirmed by the component analysis of the spectra. The component analysis of RR spectra measured from the ferric enzyme in solution and at the electrode surface revealed the frequencies of the spin marker band ν_3 at 1500 cm^{-1}, 1494 cm^{-1}, and 1489 cm^{-1} (Figure S 4.1), which are characteristic of 5cQS, 5cHS and 6cHS species, respectively. It is noteworthy that the differences in the ν_2 region, i.e. a shoulder at 1570 cm^{-1}, observed in the RR spectra obtained from the C-SPE surface, can be attributed to the G peak (at ca. 1570 cm^{-1}) of the carbon electrode (Figure 4.2 C, bottom trace) [32]. For the SAM/AuNP/Au-SPE modified electrode, the attachment of the enzyme to the electrode surface most likely results in a native state of the enzyme as observed for the SAM/AuNP/C-SPE, since the AuNPs were coated in the same manner.

Silver-based modified (or non-modified) SPEs. Silver nanostructures, either AgNPi or AgNP, were also tested as WE modifications, aiming to increase the enzyme loading at the electrode surface while taking advantage of the silver nanostructures' plasmonic properties to enhance the RR signal of the immobilized enzyme. This would allow the monitoring of the active site architecture of the immobilized DyPs by SERR spectroscopy, which provides the same type of information as RR spectroscopy (cf. Chapter 1.4.3.1) but with several orders of magnitude higher sensitivity [30-31,33].

(i) AgNPi/C-SPE. Comparison of the RR spectra of WT PpDyP in its native ferric state in solution with SERR spectra of the immobilized ferric enzyme revealed the presence of the same heme species indicated by the identical positions of the marker bands (Figure 4.3 C). We can thus conclude that no structural conformational changes occurred in the heme pocket upon enzyme immobilization. However, the reproducibility of the AgNPis electrodeposition and the stability of the AgNPis solution was low, as demonstrated by the SEM images of different AgNPis/C-SPE preparations (Figure 4.3 A-B), which is a clear disadvantage compared to the good reproducibility of AuNPs electrodeposition.

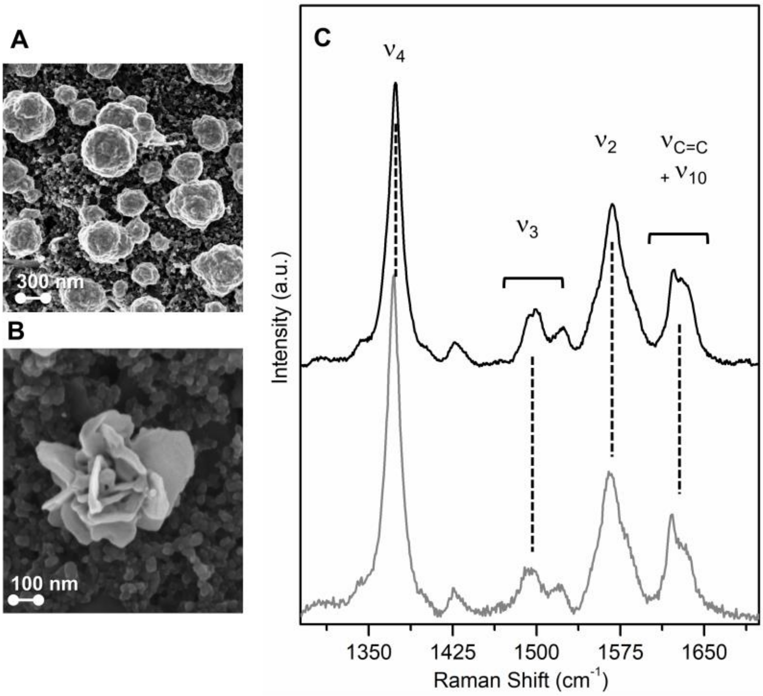

Figure 4.3 - Characterization of the WT PpDyP/SAM/AgNPi/C-SPE construct components. (**A**) and (**B**) SEM images of AgNPi prepared by independent electrodepositions on C-SPEs under identical experimental conditions. Magnification (a) 50K× and (b) 200K× (**C**) RR spectra of WT PpDyP in solution (top trace) and SERR spectra of WT PpDyP immobilized on SAM/AgNPi/C-SPE (bottom trace). RR and SERR spectra were measured using 20 μM and 5 μM WT PpDyP, with a 405 nm excitation, 3 - 2 mW laser power, and accumulation times 25 - 10 s.

(ii) AgNP/C-SPE and Ag-SPE. Two additional Ag substrates were also tested for biosensor development (Figure S 4.2 A-B). However, no (SE)RR spectra could measured either with the SAM/AgNP/C-SPE or SAM/Ag-SPE constructs, as shown by the lack of a (SE)RR signal of the immobilized WT PpDyP (Figure S 4.2 C), which prevented the evaluation of the heme active site's structural integrity. To understand if the lack of (SE)RR signal was due to the absence of bound protein to the electrode, measurement of the catalytic activity of these electrodes was performed (see below 4.3.1.2). C-SPE modified using drop-casted AgNP resulted in a non-homogenous coverage of the WE surface due to AgNP aggregation as revealed by SEM (Figure S 4.2.A).

4.3.1.2. Electrocatalytic characterization of immobilized PpDyP

The electrocatalytic properties of PpDyP immobilized on the SPEs (Ag-,Au-, C- SPE with or without nanostructures) were probed by CV. Upon addition of H_2O_2 to the electrochemical cell, the cathodic current increases due to the catalytic reduction by the enzyme attached to the WE, e.g., Figure 4.4 (color traces, Figure S 3), as expected.

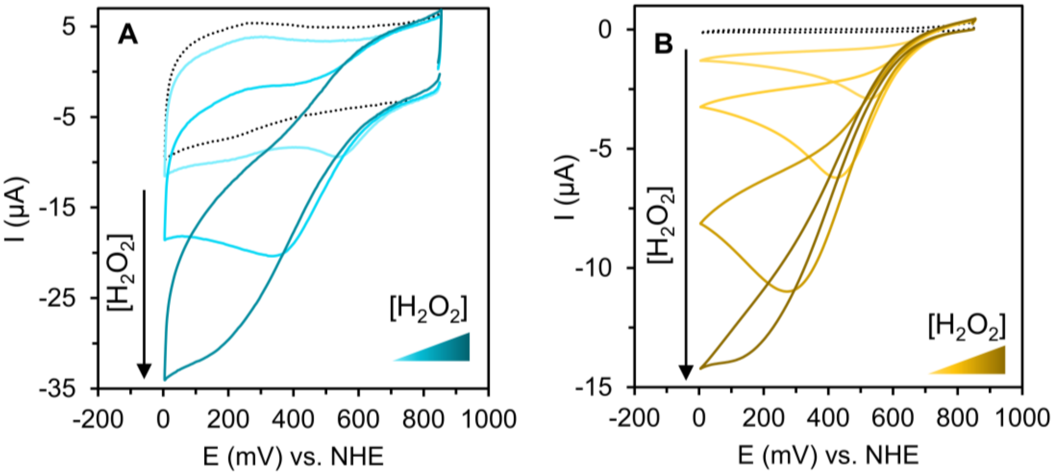

Figure 4.4 - Electrocatalytic response of WT PpDyP/SAM/AuNP/SPE constructs to H_2O_2 measured in anaerobic conditions. Cyclic voltammograms for each construct in the absences (black dotter traces) and presence of increasing concentration of H_2O_2 (color solid traces): (**A**) WT PpDyP/SAM/AuNP/C-SPE (increasing concentration of H_2O_2: 170 - 1140 μM); (**B**) WT PpDyP/SAM/AuNP/Au-SPE (increasing concentration of H_2O_2: 65 - 510 μM). Each electrode was prepared with (A) 0.5 and (B) 5 μM PpDyP. The supporting electrolyte was 12.5 mM K_2SO_4 in 12.5 mM PB, pH 7.0. Cyclic voltammograms were measured at 50 mV/s scan rate. The complete set of data of the assay can be found in Figure S 4.3.

As discussed, for the PpDyP *in silico*/SAM/Ag bulk constructs (cf. Chapter 3.3.2.2.a) these catalytic currents can be attributed to the formation of the catalytic intermediate $[Fe(IV)=O]^{+\bullet}$ (Cpd I), when the ferric PpDyP reacts with H_2O_2, which has been subsequently reduced by the electrode [27,34,35]. Note that, as in the case of the PpDyP/SAM/Ag constructs [27], the non-catalytic peaks could not be observed by CV in the absence of substrate (Figure 4.4 black dotted trace and S 4.4), which we correlated with insufficient enzyme loading (vide supra, Chapter 3.3.2.2.a).

As in the case of bulk Ag electrodes, the I_{cat} was determined at +100 mV (cf. Chapter 3.3.2.2.a). This working potential was selected because the catalytic currents were close to maximum at this potential (Figure 4.4), and the non-enzymatic reduction of H_2O_2 by the electrode was negligible (Figure 4.5 A, C, open circles and S 4.5 and S 4.6, open circles).

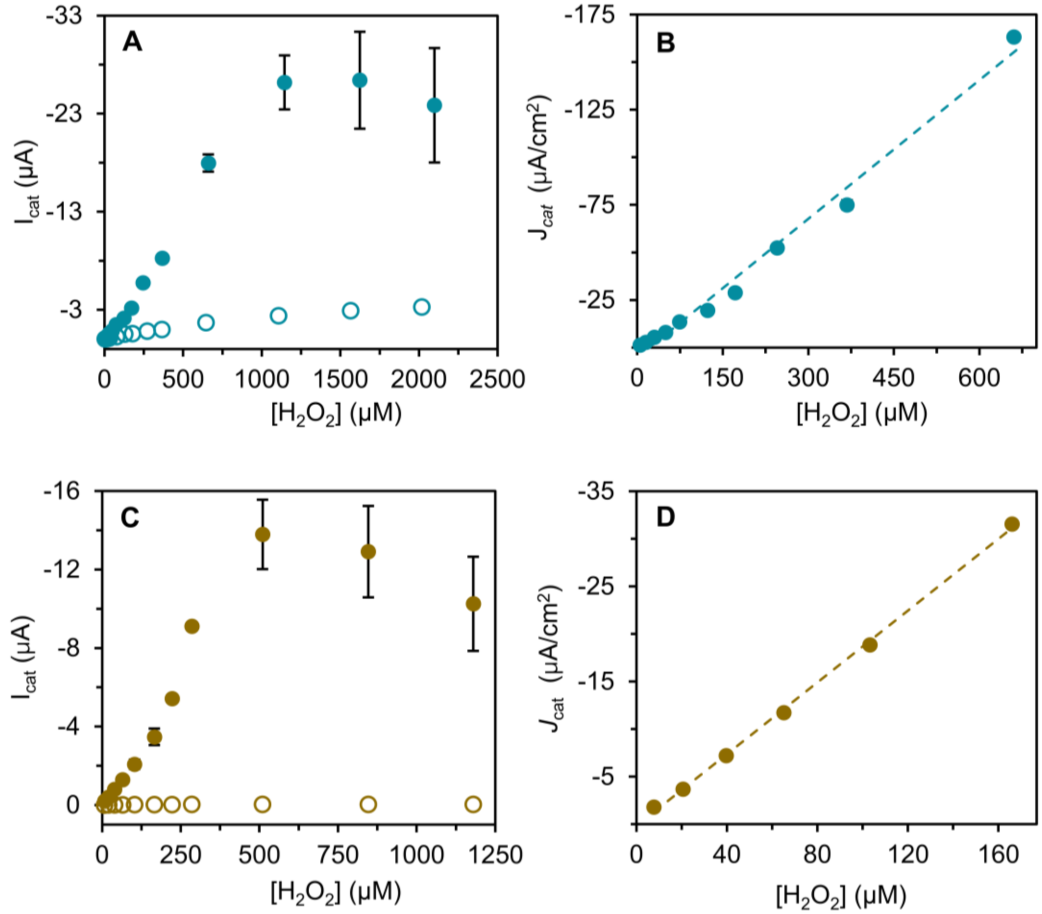

Figure 4.5 - Catalic current of PpDyP/SAM/AuNP/SPE in the presence of H_2O_2. (**A**) WT PpDyP/SAM/AuNP/C-SPE (solid circle), (**C**) WT PpDyP/SAM/AuNP/Au-SPE (solid circle). The respective response of the control (construct prepared without the enzyme) is represented by the open circles. (**B** and **D**). The corresponding linear dependence of the catalytic current density (corrected for the electrode geometric area of 0.11 cm^2) on H_2O_2 concentration, with slope and r^2 of (**B**) 215 ± 10 $mA \cdot M^{-1} \cdot cm^{-2}$ and 0.983, (**D**) 190 ± 5 $mA \cdot M^{-1} \cdot cm^{-2}$ and 0.998. Error bars represent the SD for each point (n = 4).

The segment of the plot of the I_{cat} vs. the H_2O_2 concentration in which response towards H_2O_2 is linear, was used to determine the sensitivity and the linear response range of biodevices. The majority of the developed constructs showed a good response to H_2O_2 with comparable analytical parameters and sensitivity ranging from 160 ± 4 to 215 ± 10 mA·M^{-1}·cm^{-2} (Table 4.1).

Table 4.1 - Analytical properties of the WT PpDyP modified electrodes prepared using different: SPEs, enzyme concentrations, and nanostructures determined under anaerobic conditions.

Electrode type	Modification	[WT PpDyP][a] µM	Sensitivity* (mA·M^{-1}·cm^{-2})	LR (µM)	LOD (µM)	J_{max} (µA/cm^2)
Au-SPE	AuNP/SAM	**0.5**	190 ± 10	5 - 170	12	−136
		5	190 ± 5	7 - 165	4	−136
	SAM	**0.5**	190 ± 5	8 - 220	6	−55
		5	190 ± 10	8 - 220	4	−64
C-SPE	AuNP/SAM	**0.5**	215 ± 10	5 - 750	11	−240
		5	160 ± 5	5 - 220	4	−255
	AgNP/SAM$^+$	**0.5**	185 ± 5	7 - 1400	20	N.D.
	AgNPi/SAM	**0.5**	N.D.	N.D.	N.D.	N.D.
Ag-SPE	SAM	**0.5**	N.D.	N.D.	N.D.	N.D.

[a] It was also observed that the enzyme concentration used in the electrode preparation did not influence the overall performance of the constructs using electrodeposited AuNP except in the case of SAM/AuNP/C-SPE; The sensitivity* was calculated using the geometric area of the SPEs (0.11 cm^2); $^+$SAM preparation of AgNP/C-SPE was performed in water; J_{max} - maximum current density; LR - linear Range; LOD - limit of detection; N.D. - non-determined.

<u>AuNP (or non) modified electrodes.</u> The Au- and C- SPE modified with AuNP, i.e. WT PpDyP/SAM/AuNP/Au-SPE and WT PpDyP/SAM/AuNP/C-SPE, had identical LODs (4 - 12 µM H_2O_2) and sensitivities as the WT PpDyP/SAM/Au-SPE (absence of nanostructures), Table 4.1. However, in the absence of the Au nanostructures, the linear response range was narrower, presenting a decreased J_{max} (approximately 50% lower), Table 4.1. The decreased analytical performance of this device demonstrates

that the use of AuNPs improves the biosensor analytical capacity, due to the higher amount of immobilized enzyme. We selected AuNP-modified electrodes, WT PpDyP/SAM/AuNP/Au-SPE and WT PpDyP/SAM/AuNP/C-SPE, for subsequent tests in an open-air setup.

Other constructs. The WT PpDyP/SAM/Ag-SPE and WT PpDyP/SAM/AgNP/C-SPE constructs were also characterized using the empirical strategy. In these cases, only analytical parameters were determined together with WT PpDyP/SAM/AgNPi/C-SPE designed by rational design. However, the latter and the PpDyP/SAM/Ag-SPE construct exhibited no electrocatalytic response. WT PpDyP/SAM/AgNP/SPE, on the other hand, presented a wider linear range response (up to 1400 μM H_2O_2) and a higher LOD (20 μM H_2O_2) when compared with the AuNP-modified constructs (Table 4.1, Figure S 4.5 B). However, the SEM surface characterization of the modified electrode with AgNP, Figure S 4.2 A, showed that the AgNPs are not homogeneously distributed, revealing NP aggregation. For this reason, this construct was not considered further for the following studies.

4.3.2. Performance of PpDyP/SAM/AuNP/C- or Au- SPE in open-air configuration

Given the good response of the AuNP-modified electrodes (C- and Au-SPE) to H_2O_2, their performance was further evaluated in an open-air configuration. This is a critical step for developing biosensors intended for on-site measurements, as it enables quick and straightforward assessment of the target analyte, H_2O_2, without the need for sample preparation, making these biosensors ideal for outside laboratory use.

4.3.2.1. Electrocatalysis and analytical characterization

In aerobic environment, the WT PpDyP/SAM/AuNP/C-SPE revealed a linear response to H_2O_2 from 30 to 475 μM, a sensitivity of 230 ± 10 $mA{\cdot}M^{-1}{\cdot}cm^{-2}$ and LOD of 3.5 μM, Table 4.2 and Figure 4.6, Figure S 3. Importantly, the analytical parameters were comparable to those obtained without O_2.

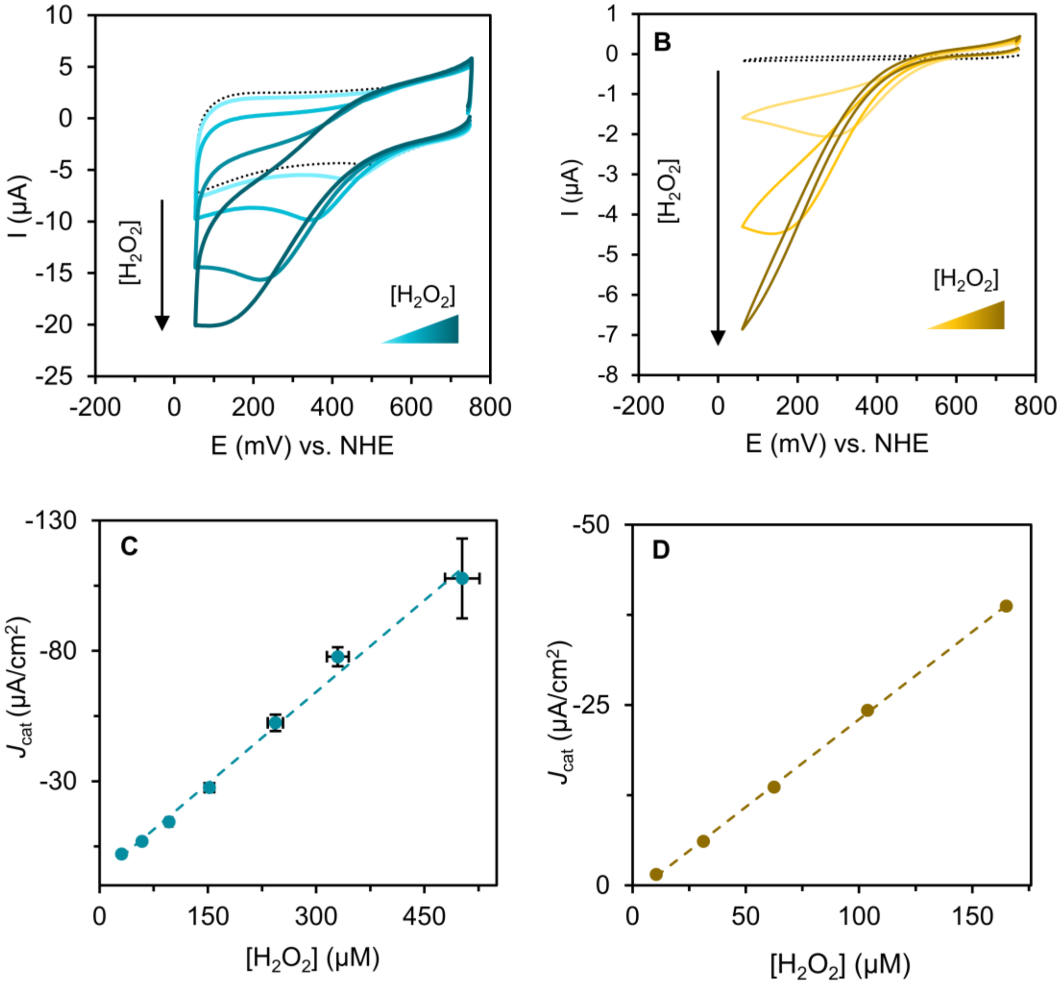

Figure 4.6 - Catalytic response of PpDyP/SAM/AuNP/SPE to H_2O_2 in open air conditions. Cyclic voltammograms of (**A**) WT PpDyP/SAM/AuNP/C-SPE and (**B**) WT PpDyP/SAM/AuNP/Au-SPE in the absence (black dotted traces) and presence (color solid traces) of increasing (30 - 500 μM and 60 - 385 μM, respectively) concentrations of H_2O_2. Electrodes were prepared with (A) 0.5 and (B) 5 μM PpDyP. The supporting electrolyte was 12.5 mM K_2SO_4 in 12.5 mM PB, pH 7.0. Cyclic voltammograms were measured at 50 mV/s scan rate. Linear dependence of the catalytic current density (corrected for the electrode geometric area of 0.11 cm^2) on H_2O_2 concentration, with slope and r^2 of (**C**) WT PpDyP/SAM/AuNP/C-SPE: 230 ± 10 $mA \cdot M^{-1} \cdot cm^{-2}$ and 0.992 and (**D**) WT PpDyP/SAM/AuNP/Au-SPE: 245 ± 5 $mA \cdot M^{-1} \cdot cm^{-2}$ and 0.999. The complete assay represented in A and B can be found in Figure S 4.3.

The control experiments, i.e, electrodes prepared without enzyme, showed no variation of the cathodic current upon adding H_2O_2 (Figure S 4.7), as observed in anaerobic environment.

The AuNP-modified C- and Au-SPE presented a comparable sensitivity, 230 ± 10 and 245 ± 5 $mA \cdot M^{-1} \cdot cm^{-2}$, respectively. Still, the analytical performance of the PpDyP/SAM/AuNP/C-SPE was superior due to its wider linear range (30 - 475 vs. 10 - 165 μM H_2O_2 for modified Au-SPE), with an estimated LOD of 3.5 μM H_2O_2. Moreover, the PpDyP/SAM/AuNP/C-SPE showed higher catalytic currents at saturating concentrations of H_2O_2 than the PpDyP/SAM/AuNP/Au-SPE (Figure S 4.8). Overall, these results established the C-SPEs modified with Au nanostructures as the best-performing for H_2O_2 biosensing, making them the constructs of choice for the stability assays and testing of their performance in complex samples.

Given the potential of the miniaturized device for commercialization, it was crucial to ensure that the devices fabricated using the same methodology showed reproducible analytical performance. Testing sensor-to-sensor reproducibility was, therefore, essential to validate the reliability of these devices. The comparison of 4 independent electrode preparations revealed a RSD of approximately 8%, demonstrating their robust construction. Furthermore, we tested the biosensor in a single-use configuration, which showed that it preserved 90% of its initial sensitivity following storage for 20 days, dropping to 70% afterward, Figure S 4.9.

The sensitivity of the miniaturized PpDyP-based device was nevertheless almost six times lower than that reported in our previous work using bulk Ag rotating electrodes in the laboratory setup (Table 4.2) [27]. To understand if the origin of this discrepancy is related to the SPE measuring setup (i.e., stationary electrode), in which the electrochemical response was controlled by the diffusion of the substrate to the electrode, a modified glassy carbon rotating disk electrode (GC-RDE) was prepared. This electrode was chosen to mimic the electrode material of the C-SPE. The GC-RDEs were modified and characterized by cAmp following the previously optimized protocols for SPEs and the bulk electrodes, respectively [27]. The amperometric response of the WT PpDyP/SAM/AuNP/GC-RDE constructs was analyzed upon successive injections of deoxygenated stock solution of H_2O_2 to the electrochemical cell. Chronoamperometric measurements revealed a stepwise increase of the catalytic current upon adding H_2O_2 in short response times, demonstrating an efficient heterogeneous ET between the immobilized enzyme and the electrode surface, Figure S 4.9 A. The WT PpDyP/SAM/AuNP/GC-RDE construct revealed a sensitivity of 1,335 $mA \cdot M^{-1} \cdot cm^{-2}$, linear response of 1 - 65 µM, and LOD of 5 µM (Figure 4.7 purple circles), which are comparable to those reported for bulk Ag electrodes (cf. section 3.3.3.3.). Moreover, when the RDE-modified electrode was used without rotation (Figure S 4.10 B), the construct displayed a similar sensitivity (200 ± 5 $mA \cdot M^{-1} \cdot cm^{-2}$) to the miniaturized device (230 ± 10 $mA \cdot M^{-1} \cdot cm^{-2}$), Figure 4.7 pink circles.

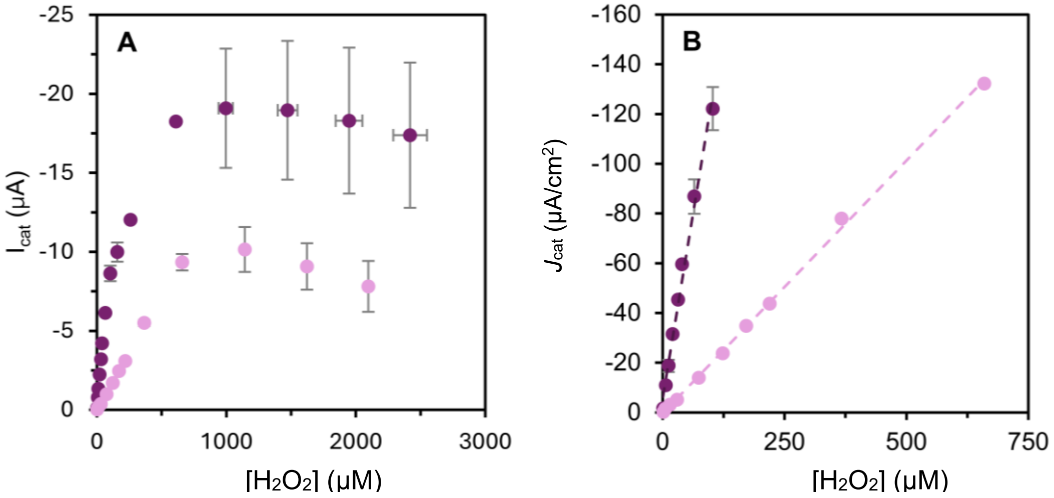

Figure 4.7 - Electrocatalytic response of WT PpDyP/SAM/AuNP/GC-RDE electrode with (purple circles) and without (pink circles) rotation. (**A**) catalytic currents vs. H_2O_2 and (**B**) linear dependance of the catalytic current density (corrected for the electrode geometric area, 0.07 cm^2) on H_2O_2 concentration with a slope and r^2 of 1,335 ± 40 $mA \cdot M^{-1} \cdot cm^{-2}$ and 0.990 for purple circles and 200 ± 5 $mA \cdot M^{-1} \cdot cm^{-2}$ and 0.998 for pink circles. Error bars represent the SD for each point (n = 3).

This proved that the diminished sensitivity of the SPE-based configuration was due to the stationary character of the setup, demonstrating a trade-off between the chosen measuring technique and the biosensor configuration.

4.3.2.2. PpDyP PROSS based miniaturized biosensor

As discussed in Chapter 3, the construct developed using the PpDyP *in silico* engineering variant, PpDyP PROSS, attached to bulk Ag rotating electrodes in the SERR electrochemical cell (PpDyP PROSS/SAM/Ag) revealed comparable analytical parameters to that of the WT PpDyP-based Ag construct (cf. Table 3.2), but with improved storage stability. For those reasons, once the best performing configuration for application in open air conditions was identified concerning the SPE material and nanostructure type (i.e., SAM/AuNP/C-SPE), we probed the analytical performance of constructs that instead of WT PpDyP carried the variant PpDyP PROSS. Overall, the analytical performance of the two devices was comparable (Table 4.2). However, PpDyP PROSS/SAM/AuNP/C-SPE presented a narrower linear range, downshifted when compared to the WT PpDyP/SAM/AuNP/C-SPE (5 - 245 vs. 30 - 475 µM H_2O_2, respectively) (Table 4.2). Hence, the two devices could be used for different applications (cf. Figure 1.11).

In terms of long-term stability, following an initial decrease, the PpDyP PROSS constructs maintain approximately 60% of the initial response sensitivity for up to 30 days, which revealed slightly lower stability than the WT PpDyP construct. Interestingly, this result contradicted the results from Chapter 3. In the assays performed using the SAM-coated Ag electrodes, the PpDyP PROSS had better storage stability than the WT PpDyP-based construct. We hypothesize that the decrease of the initial sensitivity in PpDyP (WT and PROSS) miniaturized devices could be related to the stability of the AuNPs rather than of the enzyme itself.

4.3.2.3. Analysis of the analytical parameters compared to other SPE-based H_2O_2 (bio)sensors

The bioelectrode developed herein showed comparable or better analytical performance than that of other SPE-based H_2O_2 (bio) sensors, designed with HRP [37–40] or artificial-peroxidases [41–43], Table 4.2. The latter are nowadays among the most used for H_2O_2 sensing. However, artificial peroxidases still need to overcome some issues, e.g. low selectivity and poor performance in complex matrices (for instance, due to sensor fouling from protein attachment) [44]. Furthermore, the miniaturized PpDyP-based biosensor performs exceptionally well in open air conditions (Table 4.2), which is an important added value.

4.3.2.4. Analytical applicability of the developed PpDyPs-based biosensor to real samples

In the next step, we proceeded to evaluate the analytical applicability of the PpDyP (PROSS)/SAM/AuNP/C-SPE biosensors to real samples, namely bottled water, synthetic urine, and human serum replacement under open-air conditions, using the standard addition method. The detection of H_2O_2 in these matrices is important for industrial (packaging) and medical fields (cf. Figure 1.11). Each solution was spiked with 130 µM H_2O_2, and the recovery percentage was calculated. We chose this concentration since only up to 100 µM H_2O_2 is considered safe for consumption in drinks, while for urine and blood, this value is considered normal [36]. We employed an internal calibration curve within each sample to assess the biosensor's accuracy in detecting H_2O_2 across the different solutions. The results were promising, with recovery rates of 99% (RSD 2%) for bottled water, 103% (RSD 12%) for synthetic urine, and 88% (RSD 20%) for serum (Table S 4.2). The PpDyP PROSS biosensor showed similar analytical performance to the WT PpDyP-based construct for quantifying H_2O_2 in bottled water and human serum replacement (Table S 4.2). These findings highlight the PpDyP (PROSS)/SAM/AuNP/C-SPE biosensor's ability to deliver reliable measurements of H_2O_2 in complex matrices, demonstrating consistent performance when calibration curves are tailored to each specific matrix.

Table 4.2 - Analytical performance of the previously and the herein developed PpDyP-based biosensors, HRP biosensors and artificial peroxidase-based sensors.

	(Bio)electrode	Method/ E_w (vs. NHE)	Purged/N_2 Saturated	Linear Range (μM)	Sensitivity ($mA \cdot M^{-1} \cdot cm^{-2}$)	LOD (μM)	Ref.
Biosensors	WT PpDyP/SAM/AuNP /C-SPE	CV/+100	No	30 - 475	230 ± 10	3.5	This work
	WT PpDyP/SAM/AuNS /Au-SPE	CV/+100	No	10 - 165	245 ± 5	N.D.	
	WT PpDyP/SAM/AuNP /GC-RDE	cAmp/+100	Yes	1 - 65	1,335 ± 40	5	
	PpDyP PROSS/SAM /AuNP/C-SPE	CV/+100	No	5 - 245	220 ± 5	2.4	
	WT PpDyP/SAM/Ag	cAmp/+100	Yes	1 - 200	1,310	3.6	[27]
	HRP-Nafion-C-SPE	cAmp/−145	Yes	6 - 35	143	0.5	[37]
	HRP/AuNP/CHIT/C-SPE	cAmp/−203	N.R.	10 - 13,300	0.176*	0.7	[38]
	HRP/Au/C-SPE	cAmp/−159	Yes	0.8 - 1,000	307	0.4	[39]
	HRP/PBS-C-SPE	cAmp/−400	N.R.	0 - 100	263	1.8	[40]
Sensors	PBNP-C-Grafite-SPE	cAmp/+250	N.R.	0.5 - 1000	73	0.2	[41]
	Pt-CuO@FCNF-SPE	cAmp/N.R.	N.R.	10 - 220	6.8*	3.3	[42]
	PAA/Au-SPE	cAmp/N.R.	Yes	50 - 500	899	2.0	[43]

AuNP - Au Nanoparticles; Au-SPE - Gold Screen-Printed Electrode; CHIT - Chitosan; C-SPE - Carbon Screen-Printed Electrode; CV - Cyclic Voltammetry; E_W - Working Potential vs. NHE; GC-RDE - Glassy Carbon Rotating Disk Electrode; LOD - Limit Of Detection; N.D. - Non Determined; N.R. - Not Reported; PAA - Polyamic Acid; PBNP - Prussian Blue Nanoparticles; PBS - $Cu_3(PO_4)_2$ Nanoflower; Pt -CuO@FCNF - Nanocrystal Interfacially Anchored On Functionalized Carbon Nanofiber; SAM - Self-Assembled Monolayer and SPE - Screen-Printed Electrode. *- sensitivity values are reported in $mA \cdot M^{-1}$

4.4. Concluding remarks

In this chapter, we describe the development of a miniaturized third-generation PpDyP-based biosensor for on-site H_2O_2 detection. Our biosensor can detect the desired analyte in air-exposed samples, such as physiological fluids. The development of this device followed a pipeline process in which we optimized the electrode material (Ag-/Au-/C-SPE), the nanostructure modification of the electrode (none, AuNP, AgNP or AuNPi), and the biocatalyst (WT PpDyP or PpDyP PROSS), Figure 4.1. All the PpDyP-based miniaturized constructs revealed electrocatalytic activity towards H_2O_2, except the WT PpDyP/SAM/AgSPE and WT PpDyP/SAM/AgNPi/C-SPE. The optimized device that revealed the best performance was produced using commercially available, inexpensive C-SPEs modified by easily and reproducibly prepared AuNPs that were coated with SAMs to ensure biocompatibility for the biocatalyst attachment. The miniaturized WT PpDyP/SAM/AuNP/C-SPE construct detected H_2O_2 in aerobic conditions with high sensitivity (230 ± 10 $mA \cdot M^{-1} \cdot cm^{-2}$), showed a good linear response range (30 - 475 μM) and long-term stability (20 days). The PpDyP biosensor demonstrated comparable analytical performance to HRP/SPE-based devices [37–40] and several sensors constructed using artificial peroxidases [41–43]. This is of crucial importance since HRP has been so far most commonly used for the development of H_2O_2 biosensors, while artificial peroxidases, such as Prussian blue, metal and magnetic nanoparticles, which display intrinsic peroxidase activity, nowadays represent the newest trend for developing H_2O_2 sensing devices. The biosensor developed herein stands out in terms of fabrication and measuring set-up simplicity. A key advantage of using DyPs as the immobilized biocatalyst is its highly tunable nature, which can be easily engineered to enhance specific catalytic and stability properties, making it adaptable to a wide range of applications. Furthermore, if we compromised on the device's simplicity, which was emphasized in this work, and went for a non-diffusion-controlled design, our bioelectrodes would offer further improved sensitivity compared to the HRP-based ones.

References

[1] R.D. Crapnell, A. Garcia-Miranda Ferrari, N.C. Dempsey, C.E. Banks, Electroanalytical Overview: Screen-Printed Electrochemical Sensing Platforms for the Detection of Vital Cardiac, Cancer and Inflammatory Biomarkers, Sens Diagn 1 (2022) 405–428. https://doi.org/10.1039/D1SD00041A.

[2] N.-B. Mincu, V. Lazar, D. Stan, C.M. Mihailescu, R. Iosub, A.L. Mateescu, Screen-Printed Electrodes (SPE) for *in vitro* Diagnostic Purpose, Diagnostics 10 (2020) 517. https://doi.org/10.3390/diagnostics10080517.

[3] R.A.S. Couto, J.L.F.C. Lima, M.B. Quinaz, Recent Developments, Characteristics and Potential Applications of Screen-Printed Electrodes in Pharmaceutical and Biological Analysis, Talanta 146 (2016) 801–814. https://doi.org/10.1016/j.talanta.2015.06.011.

[4] P. Kelíšková, O. Matvieiev, L. Janíková, R. Šelešovská, Recent Advances in the Use Of Screen-Printed Electrodes in Drug Analysis: A Review, Curr Opin Electrochem 42 (2023) 101408. https://doi.org/10.1016/j.coelec.2023.101408.

[5] A. Smart, A. Crew, R. Pemberton, G. Hughes, O. Doran, J.P. Hart, Screen-Printed Carbon Based Biosensors and their Applications in Agri-Food Safety, TrAC Trends Anal Chem 127 (2020) 115898. https://doi.org/10.1016/j.trac.2020.115898.

[6] B. Pérez-Fernández, A. Costa-García, A. de la E.- Muñiz, Electrochemical (Bio)Sensors for Pesticides Detection Using Screen-Printed Electrodes, Biosensors 10 (2020) 32. https://doi.org/10.3390/bios10040032.

[7] M. Li, D.-W. Li, G. Xiu, Y.-T. Long, Applications of Screen-Printed Electrodes in Current Environmental Analysis, Curr Opin Electrochem 3 (2017) 137–143. https://doi.org/10.1016/j.coelec.2017.08.016.

[8] J. Barton, M.B.G. García, D.H. Santos, P. Fanjul-Bolado, A. Ribotti, M. McCaul, D. Diamond, P. Magni, Screen-Printed Electrodes for Environmental Monitoring of Heavy Metal Ions: A Review, Microchim Acta183 (2016) 503–517. https://doi.org/10.1007/s00604-015-1651-0.

[9] A. Rubino, R. Queirós, Electrochemical Determination of Heavy Metal Ions Applying Screen-Printed Electrodes Based Sensors. A Review on Water and Environmental Samples Analysis, Talanta Open 7 (2023) 100203. https://doi.org/10.1016/j.talo.2023.100203.

[10] N.F. Barros Azeredo, M.S. Ferreira Santos, J.R. Sempionatto, J. Wang, L. Angnes, Screen-Printed Technologies Combined with Flow Analysis Techniques: Moving from Benchtop to Everywhere, Anal Chem 94 (2022) 250–268. https://doi.org/10.1021/acs.analchem.1c02637.

[11] A. García-Miranda Ferrari, S.J. Rowley-Neale, C.E. Banks, Screen-printed electrodes: Transitioning the laboratory in-to-the field, Talanta Open 3 (2021) 100032. https://doi.org/10.1016/j.talo.2021.100032.

[12] K. Yamanaka, M. Vestergaard, E. Tamiya, Printable Electrochemical Biosensors: A Focus on Screen-Printed Electrodes and Their Application, Sensors 16 (2016) 1761. https://doi.org/10.3390/s16101761.

[13] E. Costa-Rama, M.T. Fernández-Abedul, Paper-Based Screen-Printed Electrodes: A New Generation of Low-Cost Electroanalytical Platforms, Biosensors (Basel) 11 (2021) 51. https://doi.org/10.3390/bios11020051.

[14] R.M. Silva, A.D. da Silva, J.R. Camargo, B.S. de Castro, L.M. Meireles, P.S. Silva, B.C. Janegitz, T.A. Silva, Carbon Nanomaterials-Based Screen-Printed Electrodes for Sensing Applications, Biosensor 13 (2023) 453. https://doi.org/10.3390/bios13040453.

[15] G. Paimard, E. Ghasali, M. Baeza, Screen-Printed Electrodes: Fabrication, Modification, and Biosensing Applications, Chemosensors 11 (2023) 113. https://doi.org/10.3390/chemosensors11020113.

[16] Z. Taleat, A. Khoshroo, M. Mazloum-Ardakani, Screen-Printed Electrodes for Biosensing: A Review (2008–2013), Microchim Acta 181 (2014) 865–891. https://doi.org/10.1007/s00604-014-1181-1.

[17] A.P.F. Turner, Biosensors: Sense and Sensibility, Chem Soc Rev 42 (2013) 3184–3196. https://doi.org/10.1039/c3cs35528d.

[18] D. Antuña-Jiménez, M.B. González-García, D. Hernández-Santos, P. Fanjul-Bolado, Screen-Printed Electrodes Modified with Metal Nanoparticles for Small Molecule Sensing, Biosensers 10 (2020) 9. https://doi.org/10.3390/bios10020009.

[19] G.F. Duffy, E.J. Moore, Electrochemical Immunosensors for Food Analysis: A Review of Recent Developments, Anal Lett 50 (2017) 1–32. https://doi.org/10.1080/00032719.2016.1167900.

[20] G. Inzelt, Pseudo-reference Electrodes, in: Handbook of Reference Electrodes, Springer Berlin Heidelberg, Berlin, Heidelberg, 2013: pp. 331–332. https://doi.org/10.1007/978-3-642-36188-3_14.

[21] D.H. Murgida, P. Hildebrandt, S. Todorovic, Immobilized Redox Proteins: Mimicking Basic Features of Physiological Membranes And Interfaces, in: Biomimetics Learning from Nature, InTech, 2010: pp. 21–48. https://doi.org/10.5772/8778.

[22] M. Trojanowicz, Impact Of Nanotechnology on Design of Advanced Screen-Printed Electrodes for Different Analytical Applications, TrAC Trends Anal Chem 84 (2016) 22–47. https://doi.org/10.1016/j.trac.2016.03.027.

[23] Z. Chu, J. Peng, W. Jin, Advanced Nanomaterial Inks for Screen-Printed Chemical Sensors, Sens Actuators B Chem 243 (2017) 919–926. https://doi.org/10.1016/j.snb.2016.12.022.

[24] J.M. Díaz-Cruz, N. Serrano, C. Pérez-Ràfols, C. Ariño, M. Esteban, Electroanalysis From the Past to the Twenty-First Century: Challenges And Perspectives, J Solid State Electrochem 24 (2020) 2653–2661. https://doi.org/10.1007/s10008-020-04733-9.

[25] M.U. Ahmed, M.M. Hossain, M. Safavieh, Y.L. Wong, I.A. Rahman, M. Zourob, E. Tamiya, Toward the Development of Smart and Low Cost Point-of-Care Biosensors Based on Screen Printed Electrodes, Crit Rev Biotechnol 36 (2016) 495–505. https://doi.org/10.3109/07388551.2014.992387.

[26] A.G. Hildebrandt, I. Roots, Reduced Nicotinamide Adenine Dinucleotide Phosphate (NADPH)-Dependent Formation and Breakdown of Hydrogen Peroxide During Mixed Function Oxidation Reactions in Liver Microsomes, Arch. Biochem. Biophys. 171 (1975) 385–397. https://doi.org/10.1016/0003-9861(75)90047-8.

[27] C. Barbosa, C.M. Silveira, D. Silva, V. Brissos, P. Hildebrandt, L.O. Martins, S. Todorovic, Immobilized Dye-Decolorizing Peroxidase (Dyp) and Directed Evolution Variants for Hydrogen Peroxide Biosensing, Biosen. Bioelectron. 153 (2020) 112055. https://doi.org/10.1016/j.bios.2020.112055.

[28] J.J. Feng, Y.H. Lu, U. Gernert, P. Hildebrandt, D.H. Murgida, Electrosynthesis of SER-Active Silver Nanopillar Electrode Arrays, J Phys Chem C 114 (2010) 7280–7284. https://doi.org/10.1021/jp9084469.

[29] A. Blidar, B. Feier, A. Pusta, A.-M. Drăgan, C. Cristea, Graphene–Gold Nanostructures Hybrid Composites Screen-Printed Electrode for the Sensitive Electrochemical Detection of Vancomycin, Coatings 9 (2019) 652. https://doi.org/10.3390/coatings9100652.

[30] F. Siebert, P. Hildebrandt, Vibrational Spectroscopy in Life Science, Wiley, Weinheim, 2007. https://doi.org/10.1002/9783527621347.

[31] P. Hildebrandt, Resonance Raman Spectroscopy of Protein–Cofactor Complexes, In: Encyclopedia of Biophysics, Springer Berlin Heidelberg, Berlin, Heidelberg, 2018: pp. 1–10. https://doi.org/10.1007/978-3-642-35943-9_131-1.

[32] A.P. Carapeto, A.P. Serro, B.M.F. Nunes, M.C.L. Martins, S. Todorovic, M.T. Duarte, V. André, R. Colaço, B. Saramago, Characterization of Two DLC Coatings for Joint Prosthesis: The Role Of Albumin on the Tribological Behavior, Surf. Coat. Technol. 204 (2010) 3451–3458. https://doi.org/10.1016/j.surfcoat.2010.04.022

[33] D.H. Murgida, P. Hildebrandt, Electron-Transfer Processes of Cytochrome *c* at Interfaces. New Insights by Surface-Enhanced Resonance Raman Spectroscopy, Acc Chem Res 37 (2004) 854–861. https://doi.org/10.1021/ar0400443.

[34] S. Todorovic, P. Hildebrandt, L.O. Martins, Surface Enhanced Resonance Raman Detection of a Catalytic Intermediate of Dyp-Type Peroxidase, Phys Chem Chem Phys 17 (2015) 11954–11957. https://doi.org/10.1039/c5cp01283j.

[35] M. Sezer, T. Genebra, S. Mendes, L.O. Martins, S. Todorovic, A Dyp-Type Peroxidase at a Bio-Compatible Interface: Structural and Mechanistic Insights, Soft Matter 8 (2012) 10314–10321. https://doi.org/10.1039/c2sm26310f.

[36] J.E. Giaretta, H. Duan, F. Oveissi, S. Farajikhah, F. Dehghani, S. Naficy, Flexible Sensors for Hydrogen Peroxide Detection: A Critical Review, ACS Appl. Mater. Interfaces 14 (2022) 20491–20505. https://doi.org/10.1021/acsami.1c24727.

[37] Y.J. Teng, S.H. Zuo, M.B. Lan, Direct Electron Transfer of Horseradish Peroxidase on Porous Structure of Screen-Printed Electrode, Biosens Bioelectron 24 (2009) 1353–1357. https://doi.org/10.1016/j.bios.2008.07.062.

[38] T. Tangkuaram, C. Ponchio, T. Kangkasomboon, P. Katikawong, W. Veerasai, Design and Development of a Highly Stable Hydrogen Peroxide Biosensor on Screen Printed Carbon Electrode Based on Horseradish Peroxidase Bound With Gold Nanoparticles in the Matrix of Chitosan, Biosens Bioelectron 22 (2007) 2071–2078. https://doi.org/10.1016/j.bios.2006.09.011.

[39] X. Xu, S. Liu, H. Ju, A Novel Hydrogen Peroxide Sensor Via the Direct Electrochemistry of Horseradish Peroxidase Immobilized on Colloidal Gold Modified Screen-Printed Electrode, Sensors 3 (2003) 350–360. https://doi.org/10.3390/s30900350.

[40] M. Luo, Y. Song, N. Ali Khan, W. Wei, Y. Lu, Q. Zhao, H. Jiang, M. Li, D. Wang, Facile Fabrication of HRP-$Cu_3(PO_4)_2$ Hybrid Nanoflowers on Screen-Printed Electrode for Electrochemical Detection of H_2O_2, Microchem J 197 (2024) 109845. https://doi.org/10.1016/j.microc.2023.109845.

[41] D. Vokhmyanina, E. Daboss, O. Sharapova, M. Mogilnikova, A. Karyakin, Single Printing Step Prussian Blue Bulk-Modified Transducers for Oxidase-Based Biosensors, Biosensors 13 (2023) 250. https://doi.org/10.3390/bios13020250.

[42] N. Zhang, M. Tong, Z. Shi, J. Yang, B. Chen, C. Li, C. Guo, Screen Printed Electrodes on Interfacial Pt–CuO/carbon Nanofiber Functional Ink for Real-Time Qualification of Cell Released Hydrogen Peroxide, Anal Chim Acta 1245 (2023) 340829. https://doi.org/10.1016/j.aca.2023.340829.

[43] L.-G. Zamfir, L. Rotariu, V.E. Marinescu, X.T. Simelane, P.G.L. Baker, E.I. Iwuoha, C. Bala, Non-Enzymatic Polyamic Acid Sensors for Hydrogen Peroxide Detection, Sens Actuators B Chem 226 (2016) 525–533. https://doi.org/10.1016/j.snb.2015.12.026.

[44] C.P. Kurup, M.U. Ahmed, Nanozymes towards Personalized Diagnostics: A Recent Progress in Biosensing, Biosensors 13 (2023) 461. https://doi.org/10.3390/bios13040461.

.

Supporting information

Table S 4.1 - Electrochemical active area from the different modified gold electrodes.

Electrode	Electroactive area (cm^2)[a]
Au-SPE	0.092 ± 0.01
AuNP/Au-SPE	0.468 ± 0.04
AuNP/C-SPE	0.700 ± 0.09

[a] calculated using the charge associated with the reduction of the gold oxide for 7-10 electrodes by integration [1], which is proportional to the real active surface area of the gold surface.

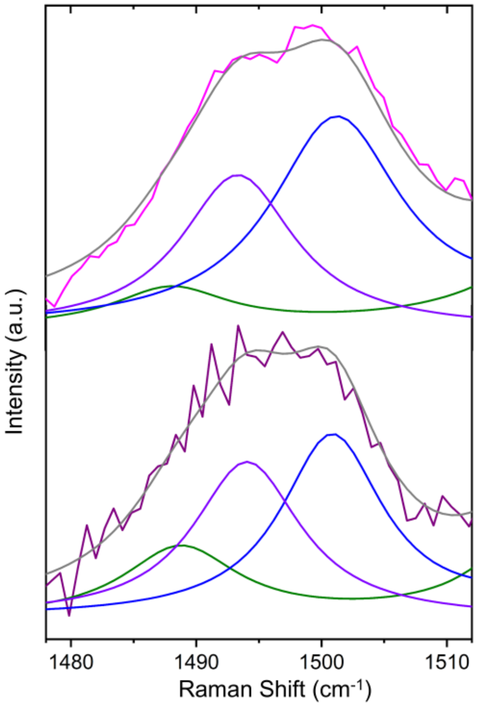

Figure S 4.1 - Experimental and deconvoluted ν_3 region of the RR spectra of WT PpDyP in solution (top trace) and immobilized on SAM/AuNP/C-SPE (bottom trace). Component analysis of the spectra reveals the presence of 6-coordinated high spin (green), 5-coordinated high spin (purple), and 5-coordinated quantum mechanically mixed spin (blue) species, according to the characteristic heme marker band frequencies. Spectra were measured with 405 nm excitation; laser power and accumulation times were 25 - 30 s and 3 - 4 mW, respectively.

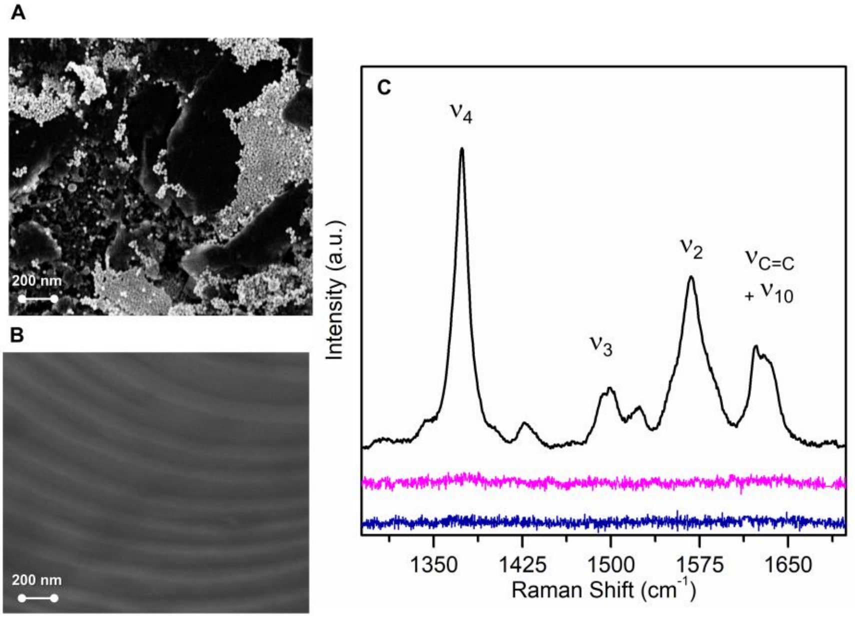

Figure S 4.2 - SEM images of WE surface of (**A**) drop-casted AgNP onto C-SPE and (**B**) Ag-SPE. Magnification 100K× , electron high tension of 3 kV. (**C**) RR spectra of PpDyP in solution (black trace) and SERR spectra of WT PpDyP immobilized on SAM/AgNP/SAM/C-SPE (purple trace) and SAM/Ag/SPE (blue trace) spectra were measured using 20 μM and 10 μM WT PpDyP, with a 405 nm excitation, 3 - 2 mW laser power, and accumulation times 25 - 10.

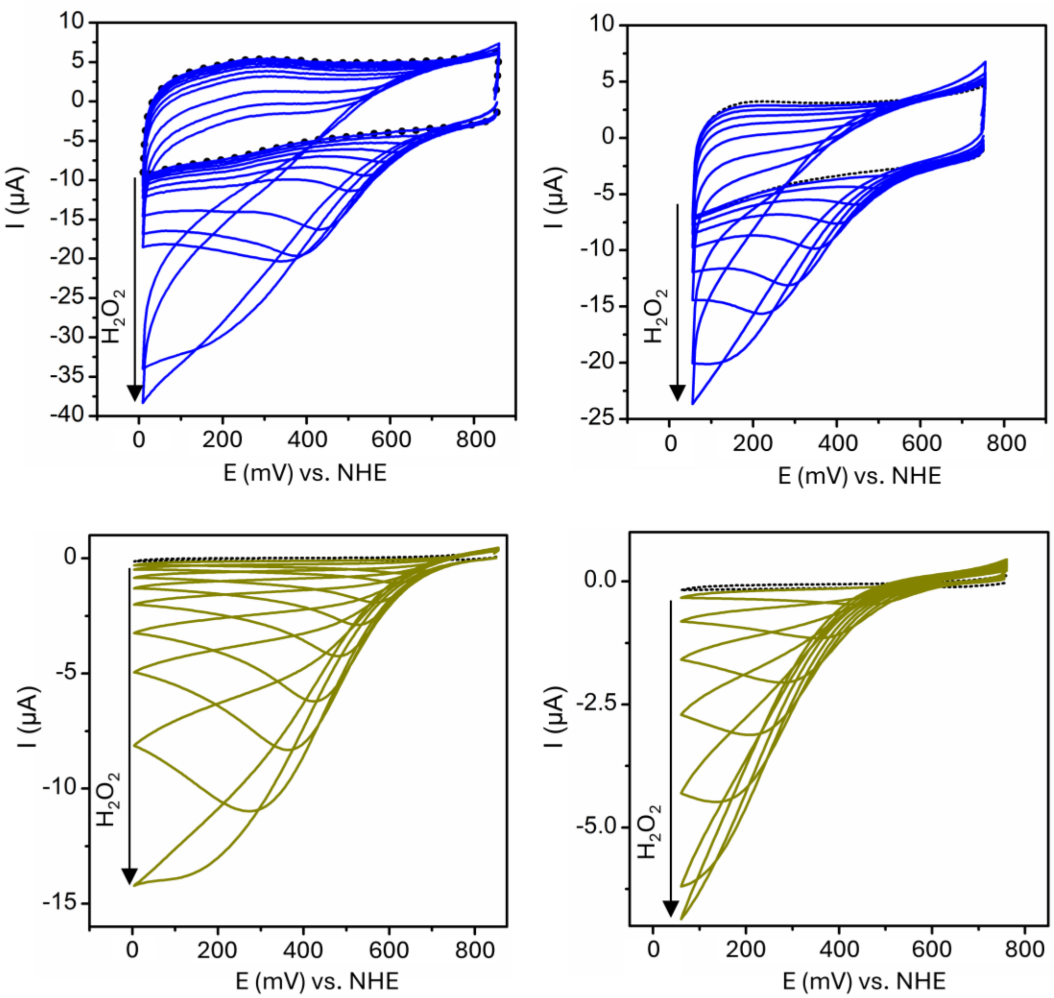

Figure S 4.3 - Cyclic voltammograms of WT PpDyP/SAM/AuNP/C-SPE (**A-B**) and WT PpDyP/SAM/AuNP/Au-SPE (**C-D**) in the absence (black dotted traces) and presence (color solid traces) of increasing concentrations of H_2O_2 (5 - 1360 μM ;5 - 1350 μM ; 5 - 1180 μM and 5 - 620 μM, respectively) in aeropic (A and C) and open air (B and D) conditions. Electrodes were prepared with (A and B) 0.5 and (C and D) 5 μM PpDyP. The supporting electrolyte was 12.5 mM K_2SO_4 in 12.5 mM PB, pH 7.0. Cyclic voltammograms were measured at 50 mV/s scan rate.

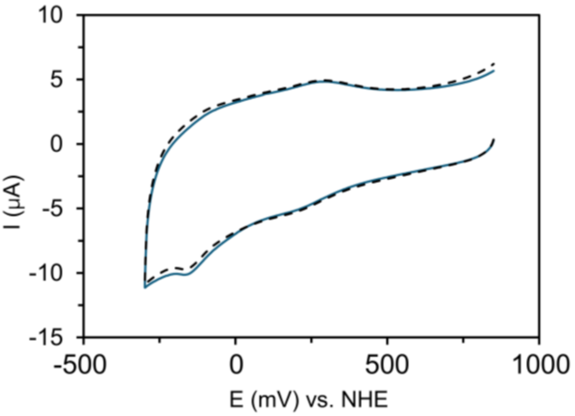

Figure S 4.4 - Cyclic voltammograms of PpDyP/SAM/AuNP/C-SPE (solid trace) and buffer/SAM/AuNP/C-SPE (control, dashed trace) in supporting electrolyte (12.5 mM K_2SO_4 in 12.5 mM PB, pH 7.0). Measurements performed at 30 mV/s scan rate under purged conditions. The enzyme electrode was prepared with 5 μM PpDyP. The small peaks observed in both control and enzyme-modified electrodes are due to surface redox reactions by oxygen-containing functional groups of the underlying C-SPE (e.g. carboxylic acid, quinone), which have been previously observed for other forms of carbon [2,3] and often occur when continuously cycling across large potential windows.

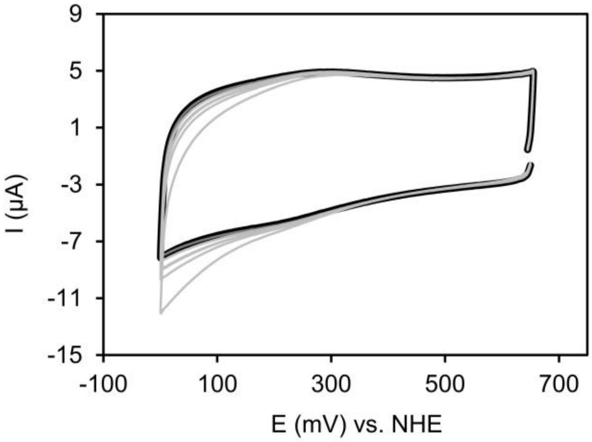

Figure S 4.5 - Cyclic voltammograms of the control electrode, buffer/SAM/AuNP/C-SPE, prepared without PpDyP, in the absence (black line) and presence (grey lines) of increasing H_2O_2 concentrations (5 -645 μM). Cyclic voltammograms were measured at 50 mV/s scan rate in 12.5 mM K_2SO_4 in 12.5 mM PB, pH 7.0, under anaerobic conditions.

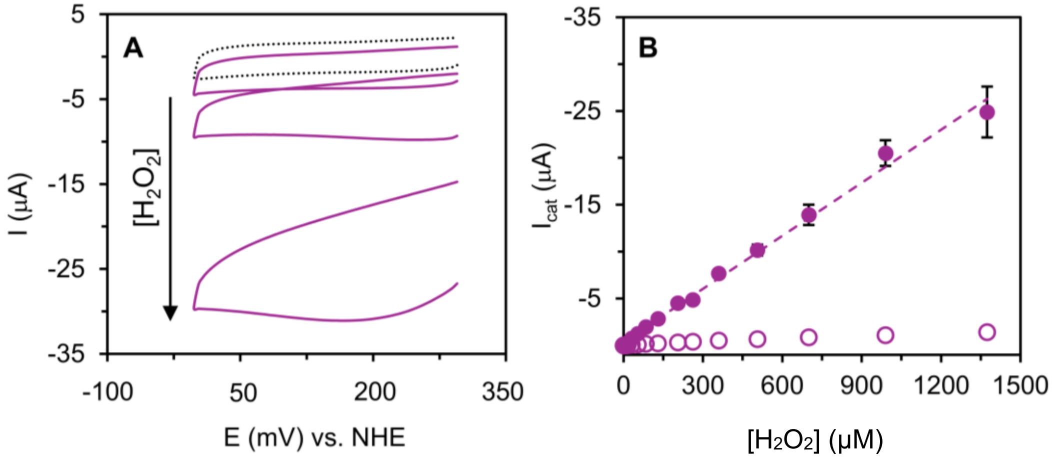

Figure S 4.6 - Electrocatalytic response of WT PpDyP/SAM/AgNP/C-SPE constructs to H_2O_2 measured in anaerobic conditions. (**A**) Cyclic voltammograms for each construct in the absences (black dotter traces) and presence of increasing concentration of H_2O_2 (5 - 1000 μM, color solid traces). Electrode prepared with 5 μM WT PpDyP. (**B**) Linear dependence of the catalytic current (corrected for the electrode geometric area of 0.11 cm^2) on H_2O_2 concentration, with slope and r^2 185 ± 3 $mA·M^{-1}·cm^{-2}$ and 0.993. The supporting electrolyte was 12.5 mM K_2SO_4 in 12.5 mM PB, pH 7.0. Cyclic voltammograms were measured at 50 mV/s scan rate. Error bars represent the SD of each point (n = 3).

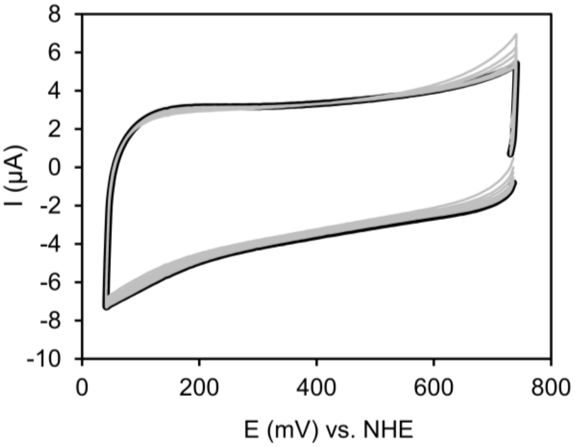

Figure S 4.7 - Cyclic voltammograms of the control electrode, buffer/SAM/AuNP/C-SPE, prepared without PpDyP, in the absence (black line) and presence (grey lines) of increasing H_2O_2 concentrations (5 - 450 μM). Cyclic voltammograms were measured at 50 mV/s scan rate in 12.5 mM K_2SO_4 in 12.5 mM PB, pH 7.0, under open air conditions.

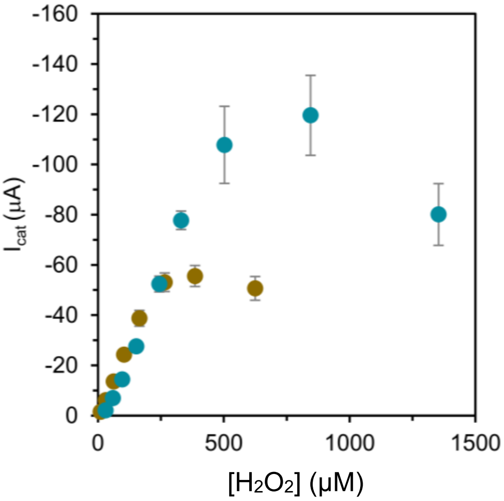

Figure S 4.8 - Electrocatalytic response of WT PpDyP/SAM/AuNP/C-SPE (blue circles) and WT PpDyP/SAM/AuNP/Au-SPE (dark yellow circles) in air-exposed samples.

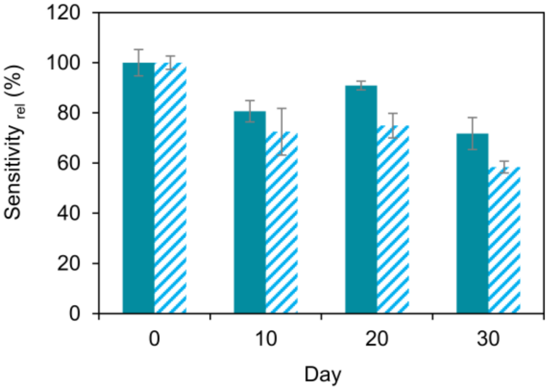

Figure S 4.9 - Stability of WT PpDyP/SAM/AuNP/C-SPE (cyan full bars) and PpDyP PROSS/SAM/AuNP/C-SPE (cyan dashed bars) electrodes response to H_2O_2. Relative sensitivity during storage at 4 °C for 30 days measured on a batch of electrodes prepared on the same day (n = 4). Error bars represent the SD in percentage of each point.

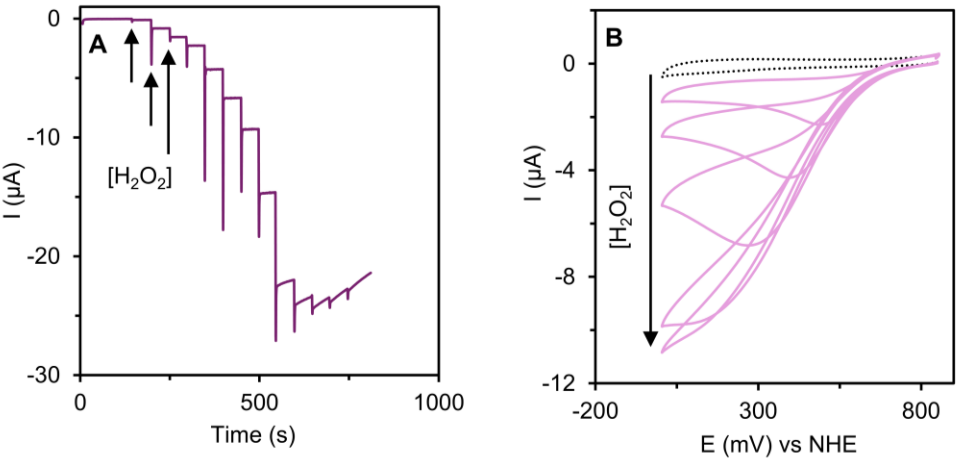

Figure S 4.10 - Amperometric response and CV of WT PpDyP/SAM/AuNP/GC-RDE with (**A**) and without (**B**) rotation to increasing H_2O_2 concentrations (0.001 - 2.6 mM). cAmp performed at an applied potential of +0.1 V and the electrode was rotated at 1800 rpm to minimize the effect of substrate mass transport to the immobilized enzyme. Electrodes prepared with 0.5 µM enzyme. Measurements performed in 12.5 mM K_2SO_4 in 12.5 mM PB, pH 7.0.

Table S 4.2 - Recovery percentage for 130 µM H_2O_2 added to samples determined using the WT PpDyP and PpDyP PROSS biosensors. N.D. - non-determined.

	Recovery (%) of 130 µM (RSD)		
	Bottled water	**Synthetic urine**	**Human serum**
WT PpDyP/SAM/AuNP/C-SPE	99 (2)	103 (12)	88 (20)
PpDyP PROSS/SAM/AuNP/C-SPE	114 (3)	N.D.	108 (5)

References

[1] Andoralov, V.M., Tarasevich, M.R., Tripachev, O.V. Oxygen reduction reaction on polycrystalline gold. Pathways of hydrogen peroxide transformation in the acidic medium. *Russ J Electrochem* 2011, 47, 1327–1336. https://doi.org/10.1134/S1023193511120020.

[2] Barisci, J. N.; Wallace, G. G.; Baughman, R. H. Electrochemical Characterization of Single-Walled Carbon Nanotube Electrodes. J. Electrochem. Soc. 2000, 147 (12), 4580. https://doi.org/10.1149/1.1394104.

[3] Che, G.; Lakshmi, B. B.; Fisher, E. R.; Martin, C. R. Carbon Nanotubule Membranes for Electrochemical Energy Storage and Production. Nature 1998, 393 (6683), 346–349. https://doi.org/10.1038/30694.

Chapter 5 Conclusions and Future Perspectives

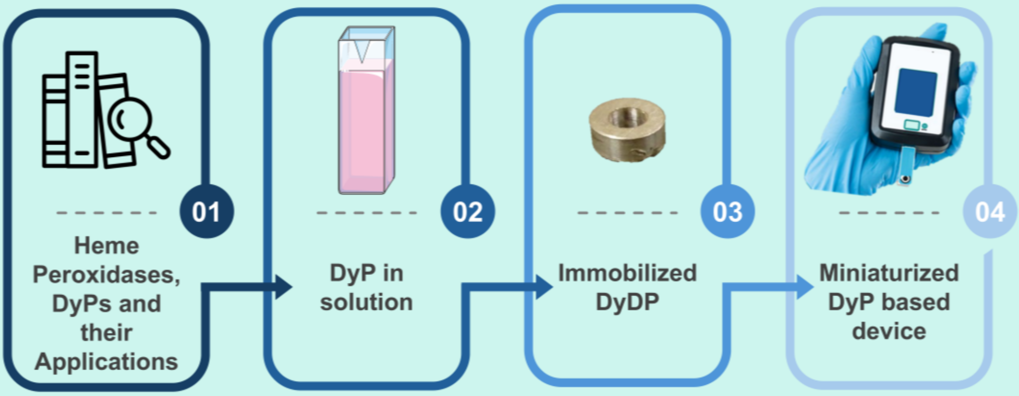

5.1. Main Conclusions

Heme peroxidases are commonly employed enzymes in biotechnological applications. These include, for example, ELISAs for analytical purposes. Moreover, peroxidases are desirable targets for constructing enzyme-based electrochemical biosensors for detecting H_2O_2, phenolic compounds, or aromatic amines. However, the development of biosensors using classical peroxidases is often hampered by the low stability of the biodevice and interference with reactive oxygen species. DyPs, a relatively recently discovered peroxidase family, represent an interesting alternative as immobilized biocatalysts in enzyme-based electrochemical biosensors. These enzymes demonstrate significant catalytic versatility because they can couple the reduction of H_2O_2 with the oxidation of a wide range of substrates, such as environmentally hazardous azo and anthraquinone derivatives phenolic compounds. Additionally, they remain highly stable under relatively high pressures and temperatures. Another appealing quality of these enzymes is the ease of their genetic engineering using techniques such as directed evolution or *in silico* design. This offers a promising future for developing variants with improved specific properties, such as higher thermostability or affinity for a substrate for a given application.

This thesis follows a pipeline of experimental considerations that allowed us to quickly and straightforwardly evaluate the potential of diverse DyPs for developing third-generation bioelectronic devices for H_2O_2 determination (thesis work flowchart). Our studies focus on several bacterial WT DyPs: ScoDyP, TfuDyP, CboDyP, SviDyP, Yfex, TceDyP and PpDyP and variants. According to their catalytic properties in solution (ability to oxidize ABTS at physiological pH and/or optimal pH), these enzymes all appear to be promising biocatalysts at first glance. This is not always the case, since there is a number of DyPs that are catalytically incompetent at physiological and even at optimal pH, such as the DyP from *D. radiodurans* .

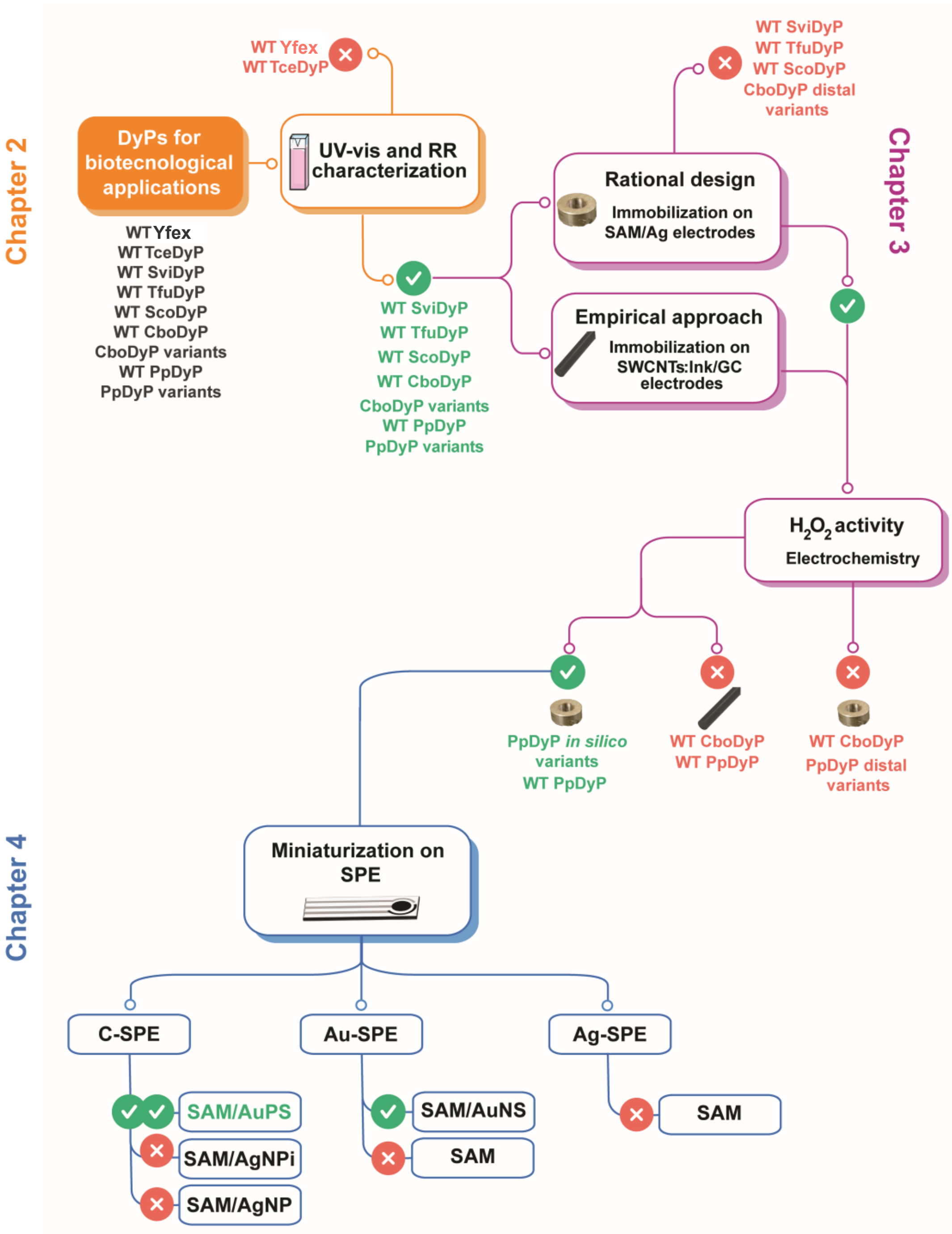

Thesis work flowchart

In **Chapter 2**, which focuses on the search for good DyP biocatalysts for biosensing applications, we characterize the heme structural properties and the redox properties of DyPs in solution, employing RR spectroscopy and UV-vis absorption spectroelectrochemistry, respectively. This comparative study allowed us, based on the evaluation of the heme cavity architecture and reduction potentials, to discard PpDyP R214I variant and proceed our studies with the WT: SviDyP, ScoDyP, TfuDyP, CboDyP, and PpDyP, together with CboDyP R307W/I and PpDyP R214W and with the PpDyP *in silico* engineered variants. **Chapter 3** describes the next step in constructing third-generation biosensors for H_2O_2 detection through the immobilization of DyP candidates selected in Chapter 2. Therein, we demonstrate that coupling SERR spectroscopy with electrochemistry (rational design approach), which provides a complete picture of the structure and activity of the immobilized enzymes, ensures a straightforward, economical, and efficient strategy for development of DyP-based devices. This approach allows for the easy identification of the parameters or steps that need to be optimized in the construction of the biosensor, e.g., the biocatalyst, immobilization matrix, electrode coating, and/or conditions (e.g., temperature, pH, enzyme incubation time and electrode rotation speed, among others). This is an advantage in comparison with the commonly used empirical strategies that follow trial-and-error process in the optimization of bioelectronic devices. The rational design approach helped us to identify two bioelectrodes carrying the *in silico* engineered PpDyP variants that display remarkable features, such as high sensitivity, rapid response, and longer storage stability compared to the WT-based construct. The analytical performance of the PpDyP *in silico* variant-based biodevices makes them excellent candidates for on-site measurements. In the next step, in **Chapter 4**, we set out to translate our biodevice developed using PpDyP attached to bulk silver electrodes modified with SAMs onto commercially available and inexpensive SPEs to create a miniaturized prototype of a third-generation amperometric device. This was done to fabricate a possible product for commercialization that is easy to manufacture, user-friendly, and works in air-exposed conditions, allowing for on-site measurements. For that end a number of SPE materials and WE modifications were tested for the attachment of WT PpDyP. The best-performing construct was composed of C-SPE modified with gold nanostructures coated with SAMs i.e. WT PpDyP/SAM/AuNP/C-SPE. The developed miniaturized construct is suitable for H_2O_2 determination in aerobic conditions, with high sensitivity and a broad linear response range. Both wild type PpDyP and the *in silico* engineered variant PpDyP PROSS display comparable analytical parameters. Importantly, we proved that the miniaturized devices can be used for H_2O_2 quantification in real air-exposed samples, outperforming HRP/SPE-based devices reported in the literature.

5.2. Future Perspetives

Future research on applications of immobilized DyPs can follow a number of directions:

(i) Improvement of the current miniaturized device. Although the developed miniaturized devices demonstrate impressive analytical performance for H_2O_2, several aspects can still be improved to enhance their applicability. These include measurement configuration, operating temperature, storage stability, and biocatalyst efficiency. For example, instead of having a disposable configuration, the devices could be designed for intermediate use, reducing the ecological footprint of biosensor production. Enhancing the long-term storage stability can be achieved by using engineered DyPs with improved stability or coating the device with a polymeric matrix to protect the potentially unstable AuNPs. The engineering of DyPs tailored for specific applications, such as lower LOD or increased resistance to H_2O_2 inhibition, could also be explored. Another parameter that is worth investigating about the biodevice is the operational temperature (i.e., > 21 °C), which will broaden its applicability in industrial settings. These improvements and optimizations can significantly enhance the biosensor's versatility, durability, and environmental impact, making the device more sustainable and effective for a variety of applications.

(ii) Exploring novel applications. Due to DyPs broad range of substrates, including environmentally persistent and harmful dyes and lignin, it could be extremely advantageous to develop devices for the degradation of these molecules for industrial

and environmental applications. These biodevices could be used to treat wastewater generated by various industries, e.g., textile, leather, food, paint, and varnish, where the DyP-based device would perform the dye degradation and removal from the contaminated water. Moreover, immobilized DyPs could be used in lignocellulose biorefineries, making use of their capacity to oxidize a variety of aromatic compounds. These DyP-based devices would be used to produce valuable compounds of economic interest, e.g., vanillin and aromatic acid phenols, among others. Overall, these applications of DyPs could improve sustainability and economic viability for industries focused on waste reduction and value-added chemical production, positioning DyPs as an essential tool for advancements in green chemistry.

(iii) ELISA tests. This work highlights the potential of DyPs as an alternative to traditional HRP enzymes due to their more straightforward production and enhanced sensitivity to H_2O_2. It would be interesting to explore the use of DyPs in ELISA assays instead of HRP to see if the assays' analytical sensitivity could be elevated. This would open exciting possibilities for more precise and reliable detection methods.

We believe that the development of DyP-based biosensors will increase in the future, as these bacterial enzymes, free from glycosylation, can easily be genetically modified to attain variant forms with tailored catalytic and stability properties for the envisioned application. As such, this thesis might serve as a guide for constructing improved DyP-based devices. Ultimately, we also highlight the potential for impactful applications that these biodevices may have. In particular, their use that could result in cleaner waters, production of added-value fine chemicals or improvement of analytical methods, all of which promise to contribute to a more sustainable and greener world.

.

ITQB NOVA, Avenida da República, 2780-157 Oeiras, Portugal | Tel +351 214 469 100 | itqb.unl.pt